Towards Zero-Inertia Power Systems: Stability Analysis, Control & Physics-Informed Neural Networks

Misyris, Georgios

Publication date:
2021

Document Version
Publisher's PDF, also known as Version of record

Center for Electric Power and Energy

Towards Zero-Inertia Power Systems: Stability Analysis, Control & Physics-Informed Neural Networks

Georgios Misyris

PhD Thesis, April 2021, Kongens Lyngby, Denmark

DANMARKS TEKNISKE UNIVERSITET
Center for Electric Power and Energy (CEE)
DTU Electrical Engineering

Towards Zero-Inertia Power Systems: Stability Analysis, Control & Physics-Informed Neural Networks

Dissertation, by Georgios Misyris

Supervisors:
Associate Professor Spyros Chatzivasileiadis, Technical University of Denmark
Consultant Grid Technology Tilman Weckesser, Danish Energy Association
Associate Professor Arne Hejde Nielsen, Technical University of Denmark

DTU – Technical University of Denmark, Kongens Lyngby – April 2021

Towards Zero-Inertia Power Systems: Stability Analysis, Control & Physics-Informed Neural Networks

This thesis was prepared by:
Georgios Misyris

Supervisors:
Associate Professor Spyros Chatzivasileiadis, Technical University of Denmark
Consultant Grid Technology Tilman Weckesser, Danish Energy Association
Associate Professor Arne Hejde Nielsen, Technical University of Denmark

Dissertation Examination Committee:
Professor Poul Sørensen
Department of Electrical Engineering, Technical University of Denmark, Denmark

Associate Professor Dirk Van Hertem
Electrical Energy Systems and Applications Group, University of Leuven, Belgium

Senior Lecturer Robin Preece
School of Electrical and Electronic Engineering, University of Manchester, United Kingdom

Center for Electric Power and Energy (CEE)
DTU Electrical Engineering
Elektrovej, Building 325
DK-2800 Kgs. Lyngby
Denmark

Tel: (+45) 4525 3500
Fax: (+45) 4588 6111
E-mail: cee@elektro.dtu.dk

Release date: April 2021

Edition: 1.0

Class: Internal

Field: Electrical Engineering

Remarks: The dissertation is presented to the Department of Electrical Engineering of the Technical University of Denmark in partial fulfillment of the requirements for the degree of Doctor of Philosophy.

ISBN: 000-00-00000-00-0

The unexamined life is
not worth living.

— Socrates

Preface

This thesis is prepared at the Department of Electrical Engineering of the Technical University of Denmark in partial fulfillment of the requirements for acquiring the degree of Doctor of Philosophy in Engineering. The Ph.D. project was part of the multiDC project funded by Innovation Fund Denmark, Grant No. 6154-00020B.

This dissertation summarizes the work carried out by the author during his Ph.D. project. It started on 1st January 2018, and it was completed on 2nd April 2021. During this period, the author was hired by the Technical University of Denmark as a Ph.D. student at the Center for Electric Power and Energy (CEE).

The thesis is composed of 4 chapters, which summarize 7 scientific papers, which are attached.

Georgios Misyris

Georgios Misyris
April, 2021

Acknowledgements

First, and foremost, I would like to express my gratitude to my supervisors Spyros Chatzivasileiads, Tilman Weckesser and Arne Nielsen for their extensive support, motivation, invaluable advice and providing me with the freedom to pursue different research directions during my Ph.D studies. A special thanks goes to the multiDC project team members at Energinet, Hitachi ABB Power Grids, RTE, KTH and Liége for stimulating input and discussions.

One of the most exciting aspects of my Ph.D. studies has been my fruitful collaboration with Thierry Van Cutsem. I would like to thank him for always being available when I needed his input and welcoming me at his group. I really admire his thoroughness, knowledge and modesty. He will remain a source of inspiration for the rest of my professional career. I would also like to extend my appreciation to the members of his group, Gilles Chaspierre and Bertrand Bastin for the insightful dicsussions. Thank you also for devoting your time and make me feel comfortable during my external stay.

I would like to thank many current and former DTU members, who played a vital role for making this Ph.D. journey enjoyable. Thank you Lejla, Florian, Amelie, Andrea Marin, Tiago, Anubhav, Morten (honorary greek guy, thank you also for translating my abstract to Danish), Fabio, Kanakesh, Ana, Daniel, Liyang, Li, Christos and Thanasis. I am grateful to Andreas and Jochen for taking the time to proof-read my thesis and provide constructive feedback on its structure. I would also like to thank both of you for our inspiring collaboration, our fruitful discussions and our friendship. I am deeply grateful to Dimitrios Doukas. Thanks to him, I applied for this Ph.D position three years ago and decided to pursue a science research career. My special thanks goes to Danilo for providing constructive feedback to my work and the memories we shared over the last three years.

Last but not least, special thanks goes to my good friend and great collaborator Andrea Tosatto. Your support over the last three years and especially the last six months was essential to make this Ph.D. journey joyful. I would like to thank Ida for her understanding, patience, help and unconditional love. I would also like to thank my good friends Marios Manolopoulos, Stamatis Nisirios, Michalis Kritharidis, Konstaninos Chatzidrosos, Kostas Kostikas, Dimitris Bloskas, Giorgos Koutis, Alexandros Ketikidis, Giorgos Mpampalis, Ilias Melas, Stefanos Kounelas, Andriana Dimitriou, Giorgos Gkelos, Vaggelis Koutsosimos, Manolis Zografos, Marios Tsantarliotis, Kostas Koutzias, Michele Luvisotto, Sophie Ellena, Nicola Viafora and Elisa Fedato, for always picking up the phone and being there for me. I hope I did not forget someone; and even if I did you should know that you have a special place within me. Finally, I am indebted to my parents, Spyros and Marina, and to my sister, Despina, for their encouragement and continuous support throughout my studies.

Georgios

Kgs. Lyngby, Denmark, April 2021

Table of Contents

List of Figures

List of Tables

Abstract

Large-scale integration of Renewable Energy Sources (RES) as well as the installation of new High Voltage Direct Current (HVDC) lines pose new technical challenges concerning the stability of the electrical power system, the accurate system modeling and the real-time dynamic security assessment. This is due to the lack of system inertia, limited overload capability of power electronic devices and fast power electronic interfaces. To ensure the secure and reliable operation of power systems with high penetration of RES and HVDC interconnectors, advanced control methods and new operational tools are required. The research aims of this PhD thesis are twofold: first, it investigates the effects of controller design of converters on the power system stability and proposes control designs and metrics to enable the secure integration of converter-based resources. Second, this thesis investigates analysis tools for time-domain simulations by evaluating the appropriateness of existing reduced complexity models for converters and by proposing the use of physics-informed neural networks which can provide fast and accurate solutions. Overall, this work approaches the fundamental challenge of low- and zero-inertia power systems from two distinct angles and proposes pragmatic solutions.

The first fundamental challenge concerns the replacement of conventional synchronous-based generation by renewable energy sources. This reduces the level of rotational inertia and introduces uncertainty in the dynamic behavior of the power grid due to their continuously varying power infeed. Consequently, the level of system inertia obtains a time-varying profile, which influences the frequency stability of the system. Two strategies are considered to tackle the problem of frequency stability. The first strategy leverages tools from control system theory and proposes a structured robust frequency control design that accounts for the impact of low inertia on frequency dynamics and aims to reduce the Rate Of Change Of Frequency (ROCOF) and frequency nadir. The second strategy focuses on utilizing HVDC systems interconnecting asynchronous areas and studies the exchange of frequency reserves in order to limit the maximum ROCOF and frequency nadir. Particularly, we extract expressions for the ROCOF, frequency nadir and maximum steady-state frequency deviation as a function of the system inertia and components' control parameters. These expressions are incorporated into the unit commitment problem as constraints. This enables the dispatch of enough generator-based units and the procurement of enough frequency reserves, to maintain the frequency stability of the system and allow for secure integration of RES into the power grid. Moreover, considering that converter-based resources are called to participate in grid-supporting services, we study how their operation mode, namely grid-forming and grid-following converter, affects the system stability and dynamic performance. Having as control objectives to avoid (i) induced instabilities caused by the converters and (ii) the saturation of converters in the event of a contingency, we propose methods for appropriate tuning of the converters' control parameters. This allows the safe and reliable integration of converter-based resources to power grid.

The second fundamental challenge relates to the system analyses based on time-domain simulations,

which is a critical tool for power system operators. To ensure the secure power system operation, transmission system operators evaluate a large number of scenarios that correspond to hundreds of thousands of operating points and different types of contingencies. Due to the increase of the number of generation units, mainly due to the large penetration of RES, the number of these scenarios dramatically increases, which in turn increases the computation time required for performing these dynamic security assessment studies. To this end, two methodologies are proposed. The first concerns the appropriateness of Root Mean Squared (RMS) models to assess the security of a power system with high penetration of RES. RES are usually connected to the grid over power electronic converters which introduce faster dynamics to the system response, that RMS models cannot always capture. Considering the key role grid-forming converters will play in the near future, we propose a loop-shaping control design, and derive sufficient conditions that determine the appropriateness of the RMS models of different classes of grid-forming converters, when simulating events where the power balance is disturbed, e.g. loss of load or generation. The second direction draws from recent developments in machine learning and neural networks for predicting solutions to systems of partial differential equations, ordinary differential equations and differential algebraic equations. This thesis proposes, for the first time, physics informed neural networks for power system applications and demonstrates how they can provide solutions for a system of differential algebraic equations at a fraction of the time required by traditional numerical solvers, while maintaing high accuracy.

Resumé

Integration af vedvarende energikilder (VE) i stor skala, så vel som installation af nye jævnstrøms højpændingsslinjer (HVDC), udgør nye tekniske udfordringer for stabiliteten i elsystemet, nøjagtig systemmodellering, samt dynamisk sikkerhedsvurdering i real-tid. Dette skyldes manglen på systeminerti, begrænset overbelastningskapacitet i de effektelektroniske enheder, samt hurtigtvirkende effektelektroniske interfaces. For at sikre sikker og pålidelig drift af elsystemer med høj indtrængen af vedvarende energi og HVDC interkonnektorer, er der behov for avancerede kontrolmetoder og nye operationelle værktøjer. Målet med forskningen i denne PhD afhandling er således tofold: I første omgang, undersøges effekterne af omformeres kontrolsystemsdesign på elsystemsstabiliteten og der foreslås kontrolsystemsdesign og metrikker der kan muliggøre sikker integration af omformerbaserede ressourcer. Dernæst, undersøger denne afhandling analyseværktøjer til tidsdomæne simuleringer, ved at evaluere hensigtsmæssigheden af eksisterende omformermodeller med reduceret kompleksitet og ved at foreslå brugen af fysik-informerede neurale netværk som giver nøjagtige og hurtige løsninger. Samlet set tilgår arbejdet i afhandlingen den fundamentale udfordring ved lav- og nulinerti elsystemer fra to distinkte vinkler og foreslår pragmatiske løsninger.

Den første fundamentale udfordring omhandler erstatning af konventionel synkronbaseret produktion med vedvarende energikilder. Dette reducerer mængden af roterende inerti and introducerer usikkerhed om den dynamiske opførsel af elnettet, grundet den kontinuerte indfødning af varierende effekt. Følgelig vil mængden af systeminerti få en tidsvarierende profil, hvilket påvirker frekvensstabiliteten i systemet. To strategier overvejes for at håndtere problemet med frekvensstabilitet. Den første strategi benytter værktøjer fra kontrolsystemsteori, og foreslår et struktureret robust design af frekvensregulering der tager højde for indvirkningen af lav inerti på frekvensdynamikker og har som målsætning at reducere både hurtigere frekvensændring (ROCOF) og frekvens nadir. Den anden strategi fokuserer på at udnytte HVDC systemers sammenkoblede asynkrone områder og studerer udvekslingen af frekvensreserver for mindske den maksimale ROCOF og frekvens nadir. I særdelshed, uddrager vi udtryk for ROCOF, frekvens nadir og maksimal steady-state afvigelse som en funktion af systeminertien og komponenters kontrolparametre. Disse udtryk bliver indarbejdet i unit commitment problemet som bi-betingelser. Dette muliggør at nok generator-baserede enheder dispatches og at der produceres nok frekvensreserver til at opretholde frekvensstabiliteten i systemet og tillader således sikker integration af VE i elnettet. Herudover, med tanke på at omformer-baserede ressourcer forventes at deltage i netunderstøttende services, undersøger vi først driftstilstandens indflydelse, navnlig net-dannende og net-følgende omformer, på systemets stabilitet og dynamiske ydeevne. Med kontrolmål om at undgå (i) inducerede ustabiliteter forårsaget af omformerne og (ii) mætning af omformere ved nødstilfælde, foreslår vi en passende tuning af omformernes kontrolparametre. Dette tillader sikker og pålidelig integration af omformerbaserede ressourcer i elnettet. — Den anden fundamentale udfordring angår systemanalyser baseret på tids-domæne simuleringer, hvilket er et kritisk værktøj for elsystemsoperatører. For at sikre sikker drift af elsystemer, udfører transmissionssystemsoperatører sikkerhedsvurderinger,

ved at evaluere store antal scenarier der svarer til forskellige driftstilstande, typer af forstyrrelser og tab af produktionsenheder. På grund af de øgede antal af produktionsenheder, hovedsagligt på grund af installation af talrige VE, øges antallet af disse scenarier dramatisk, hvilket igen øger den beregningstid det kræves for at udføre dynamisk sikkerhedsvurdering. Med henblik herpå, foreslås to metodologier. Den første, omhandler hensigtsmæssigheden af Root Mean Squared (RMS) modeller af elsystemer med høj penetration af VE. I betragtning af den nøglerolle net-dannende omformere får i den nære fremtid, foreslås et sløjfe-dannende kontrol design og nødvendige betingelser udledes, der bestemmer hensigtsmæssigheden af RMS modellerne, for forskellige klasser af net-dannende omformere ved simulering af hændelser, hvor effektbalancen forstyrres. Den anden retning, fokuserer på at udnytte nylige fremskridt indenfor maskinlæring og neurale netværk, til at løse systemer af partielle differentialligninger, ordinære differentialligninger og algebraiske differentialligninger. Denne afhandling foreslår, for første gang, fysik-informerede neurale netværk til elsystemsapplikationer og vi demonstrerer hvorledes de kan levere løsninger, til et system af algebraiske differentialligninger, på en brøkdel af den tid der kræves af traditionelle numeriske solvere, samtidig med at de opretholder høj nøjagtighed.

CHAPTER 1

Introduction

1.1 Background and motivation

To meet the targets of the Paris agreement [7], governments around the world have initiated a number of actions, which involve reducing the number of fossil fuel based generation units while increasing the penetration of renewable energy sources. In this regard, the European Clean Energy Package expects to deliver a 45 % reduction in greenhouse gases by 2030, and a reduction up to 90 % by 2050 [8]. This transition introduces a number of challenges in power system operation related to power system stability.

One aspect that Transmission System Operators (TSOs) assess, concerns the frequency stability of the system. This is defined as the ability of the system to maintain the balance between generation and demand, following a severe active power imbalance [9]. Due to the inclusion of intermittent power sources, preserving the balance between supply and demand becomes a much harder task [10]. Additionally, the inclusion of converter-based resources adds significant uncertainty to the system parameters, such as the system inertia which affects significantly the frequency stability [11]. This occurs because Renewable Energy Sources (RES) do not inherently contribute to frequency control, as synchronous machines do, since they are interfaced to the grid through power electronic devices and cannot store kinetic energy. However, with their main advantage being their fast control action, transmission system operators could potentially tackle the problem by introducing converter-based resources, such as High Voltage Direct Current links, batteries, wind turbines and solar panels into primary frequency control [12].

Among the different types of converter-based resources which can be used for frequency support, HVDC-links interconnecting asynchronous areas are a promising option [13, 14]. Considering the high number of interconnections formed by HVDC lines, especially in Europe [15], appropriate converter control tuning and better coordination between regional entities are required to handle system disturbances associated with frequency stability. However, to allow HVDC links to provide services such as active power balance restoration and limiting the instantaneous frequency deviation, other challenges need to be addressed. The replacement of conventional power plants combined with the opposition against installation of new AC overhead lines [16, 17], can lead to weaker AC systems, meaning that lower Short-Circuit Ratio (SCR) values and less stiff voltage are to be expected. Low SCR values can cause issues in the operation of HVDC links [16–18], which require extensive stability analysis to ensure their secure integration when providing grid support. The main issues are associated with the dynamic power transfer capability of the HVDC converter, as well as with the small-signal stability of the system.

Moreover, an example of a weak AC system is the North Sea Wind Power Hub (NSWPH) project, which was announced in 2017 by Energinet and TenneT, the Danish and Dutch transmission system operators. This project aims at installing more than 30 GW of offshore wind power in the North Sea. Artificial islands will collect the produced wind power and multiple inter-connectors

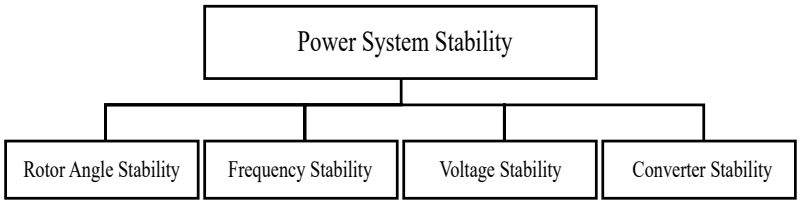

Figure 1.1: Classification of power system stability

will transmit it onshore [19, 20]. According to [21], the connections between the offshore system and onshore grids will be multiple point-to-point Voltage Source Converter (VSCs) HVDC links. Thus, the offshore system that could potentially be formed is an AC system with absence of stiff AC voltage and limited energy storage capability. Assessing the stability of such a system and designing appropriate controllers for converter-based resources are necessary for its realization and removing the barriers towards a carbon-free power grid.

Another barrier towards a carbon-free power grid concerns the ability of TSOs to continuously monitor the state of the system. Considering the continuously varying power infeed from RES, real-time situation awareness is necessary for ensuring the power system security [11, 22, 23]. Time-domain simulations play a vital role when performing dynamic security assessment. Up until now, due to the time-scale separation properties between synchronous generators and transmission line dynamics, transmission line dynamics were neglected and an algebraic model of the transmission network was used, i.e. Root Mean Square (RMS) modeling [24]. RMS modeling allows for large time-steps in numerical simulations and fast estimation of the dynamic state of the power system [25]. However, converter-based resources contain fast control systems with time constants similar to the time constants of the network line dynamics [1]. Thus, neglecting the network line dynamics when modeling converter-based resources and relying on RMS modeling of the power grid, leads to: (i) loss of information regarding the dynamic state of the system [26, 27] and (ii) inaccurate assessment of the stability boundaries [28]. Thus, in order for transmission system operators to ensure the power system security, a model that accounts for the electromagnetic dynamics is required, namely ElectroMagnetic Transient (EMT) model. The main limitation, however, of using EMT modeling is the small time-steps required for the numerical solutions of differential-algebraic equations, which increases the computational burden when performing dynamic security assessment. To this end, appropriate simulation tools are required to maintain secure operation of future power systems [27, 29, 30].

1.2 Research directions

Two research directions are defined in this thesis. The first one focuses on power system stability issues emerging from the integration of converter-based resources, as well as developing appropriate controllers to enhance the stability of power systems with varying penetration of RES. The second one focuses on identifying and developing appropriate simulation tools for performing dynamic security assessment of future power systems.

1.2.1 Enhancing stability in low- and zero-inertia power systems

The first research objective aims at identifying potential stability issues that can occur due to high penetration of RES and proposes appropriate solutions and control designs. Figure 1.1 depicts a

classification of the stability of future power systems containing a large number of converter-based resources [31, 32]. This thesis focuses on frequency and converter stability issues encompassing future power systems.

We first assess how different levels of system inertia affects the frequency stability of the system. Existing approaches in literature focus on two mitigation strategies for ensuring frequency stability. The first one concerns the development of fast frequency control schemes for improving the frequency stability of the system [33–36]. The second strategy focuses on the inclusion of frequency-related constraints, such as Rate Of Change Of Frequency (ROCOF), frequency nadir and steady state frequency deviation, in the unit commitment problem [37–40]. The idea is to include inertia requirements in the unit commitment problem. By doing that, TSOs can decide which units (synchronous generators or converter-based resources) are going to be dispatched for the sole purpose of providing frequency support. This allows for preserving the frequency stability of the system and ensuring secure integration of RES. This thesis aims at complementing these two strategies by proposing alternative fast frequency control schemes, and frequency-related constraints which can be included in the unit commitment problem.

Given that services, such as frequency support, will be provided by an increasing number of converter-based resources in the future, the dynamic properties of the power grid substantially change. This means that the challenge of large-scale integration is not limited to problems related to frequency stability, but also to the stable operation of the converter when connected to weak power grids. Particularly, it is well known that converters that operate in grid-following mode can lead to small-signal instability due to the inability of their Phase Locked Loop (PLL) controller to synchronize the converter with the grid under low SCR values [41]. Existing approaches in the literature investigates small-signal stability issues related to the operation of grid-following converters that are connected to weak grids [16–18, 42–44]. However, limited studies have been performed on the impact of converters that participate in frequency regulation, namely grid-supporting converters [41], on their dynamic transfer capability under large disturbances. For this reason the second objective of this work is to evaluate the impact of grid-supporting converters on the system stability.

As the share of RES increases, lower SCR values are expected. Due to poor dynamic performance of grid-following converters in weak grids, several options can be considered. The first solution is related to the operating mode of the converter. Grid-forming converters [41] appear as a suitable solution for integrating RES in weak grids. This is primarily due to their robust performance against low SCR values and their ability to regulate the frequency with fast active power injection [45, 46]. Although grid-forming converters are being used in parts of the world and mainly in microgrids, they have not been standardized by TSOs. The reason for that is that grid-forming converters cannot directly control the current. As described in [4, 5], this can lead to their saturation and loss of synchronism with the grid during large disturbances, i.e. overload incidents. Thus, it is still an open question of how secure a system consisting of numerous grid-forming converters is against large disturbances.

To answer this question, we perform two analyses. For the first analysis, we establish an alternative grid-forming pair [47], consisting of a synchronous condenser and a grid-following converter, and perform a comparative stability analysis of how the two grid-forming schemes (grid-forming converter and alternative grid-forming pair) respond to large disturbances. To the best of our knowledge, this is the first time that such an analysis is performed. For the second analysis,

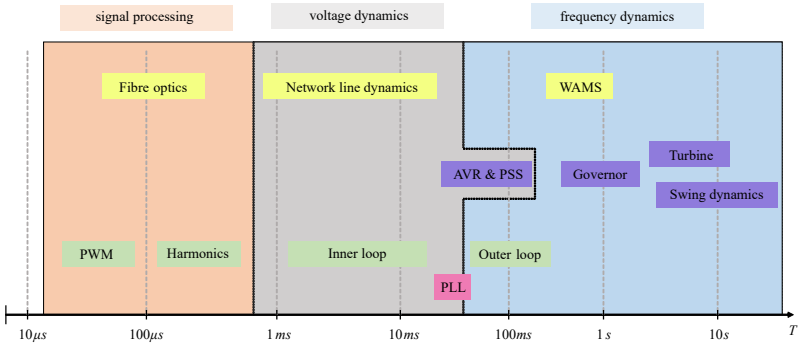

Figure 1.2: Timescale separation in future power systems. Adapted from [1].

this thesis studies the transient stability of a system “formed" only by grid-forming converters and develops a centralized control strategy that enhances the transient stability of grid-forming converters by avoiding current saturation and ensuring the N-1 criterion. Existing approaches in the literature [5, 48–50] develop control schemes that improve the transient stability, relying only on local measurements. Although the proposed schemes improve the transient performance of grid-forming converters, they have only been evaluated in systems containing an infinite bus or synchronous generators. As it will be demonstrated in Chapter 2.3.2, some of these control schemes still lead to transient instability in systems “formed" only by grid-forming converters. Consequently a centralized control strategy is necessary for ensuring the transient stability of the system in the event of a contingency. Last but not least, it should be mentioned that for the comparative analysis and the transient stability study, this thesis uses an offshore power system which is a representation of the NSWPH and comprises 100% converter-based resources.

1.2.2 Dynamic security assessment in future power systems

The second research direction investigates analysis tools for time-domain simulations. We first evaluate the appropriateness of existing reduced complexity models for converters. We propose the use of machine learning algorithms which provide mathematical representations of high dimensional functions that allow to solve computational problems at a fraction of the time required by traditional approaches.

The transition from synchronous generation units to converter-based units introduces rapid changes to power system dynamics. Figure 1.2 shows the time scale separation of physical and control dynamics in power systems that contain converter-based generation. The yellow, purple, pink and green colors correspond to grid, generator, PLL and converter dynamics, respectively. Unlike generator dynamics, converter dynamics overlap with the network line dynamics. Consequently, instability phenomena originating from LC resonances and inadequate tuning of converters control parameters, as well as low SCR cannot be captured. Thus, for these phenomena EMT simulations are necessary for accurate dynamic security assessment. Although RMS models are unable to capture fast dynamics, they can be appropriate for capturing slower dynamics. Given the need for fast and accurate time-domain simulations analysis, it is necessary to evaluate under which conditions RMS models can be used.

Existing approaches in the literature focus on determining the appropriateness of RMS modeling for converters based on time-domain simulation analysis [27, 29, 51, 52]. In [29], the appropriateness

of RMS modeling for grid-forming converters was evaluated for different types of disturbances, including faults and power imbalances occurring in the grid. A similar analysis has been conducted in [27], where the authors evaluate the validity of RMS models of both grid-forming and grid-following converters. In [51], the authors proposed an RMS model of grid-following converters which only accounts for the outer control loops of the converter, and disregards the network line dynamics, the PLL unit and the inner control loop. The results show a good accuracy of the RMS model when simulating generator and line tripping. In [52], the authors demonstrate the limitation of the proposed RMS model in [51] to be used in fault-ride through studies, mainly due to the significant influence of the PLL block and voltage controller parameters on the re-synchronization process of the converter after the fault. The authors in [16] tackled this problem by using an RMS model of the converter that accounts for PLL block and is used for simulating events, such as grid-topology changes and fault-ride through studies.

In the aforementioned studies, the validity of RMS models of VSCs was not evaluated with respect to the control parameters of the converters. Considering the fact that the control parameters define the time response of the converters control loops, different control parameters might lead to an increase of the impact of fast dynamics on slower modes. This can render the RMS model inappropriate even for simulating signals associated with slower dynamics. To tackle this problem, appropriate control tuning is required which allows for timescale separation of the control and physical dynamics and limits the interactions between fast and slow dynamics. To this end, the first objective of this research direction is to identify conditions under which RMS models can accurately predict the system response for a large subset of disturbances. The focus in this thesis is on grid-forming converters since they are expected to play a key role in future grids for enabling large-scale integration of RES.

The final research objective concerns the development of dynamic models that can provide fast solutions to differential-algebraic equations. Time-domain simulation analysis is a task that requires solving a system of differential-algebraic equations. Solutions to a system of differential-algebraic equations can either be calculated analytically or numerically. Analytical solutions, however, are very rare and can only be obtained for simple differential equations. To tackle this problem, numerical methods, such as Runge-Kutta, Newton-Raphson method, etc. are necessary for computing the solutions of the system of differential-algebraic equations. Machine learning techniques and in particular neural networks have been gaining momentum in predicting solutions to differential-algebraic equations [53–55]. They can provide an accurate mathematical representation of high dimensional functions and solve computational problems both in dynamics and optimization at a fraction of the time required by traditional approaches [56–60]. In [61], the authors highlight the recent developments in applying feedforward neural networks for transient stability assessment [62–64]. They argue about the credibility of neural networks approaches, since their accuracy highly depends on the quality and amount of data. Moreover, the black-box nature of neural networks offers limited interpretability, which prevents system operators from increasing their confidence on their applicability to dynamic security assessment. To this end, this thesis proposes physics-informed neural networks for power system applications which reduces the dependency of the accuracy of the neural network predictions on training data and follows the underlying physical laws of power systems.

1.3 Contributions

The main objectives of this Ph.D. thesis are to: (i) investigate frequency and converter stability issues that might occur in future power systems due to the high share of converter based resources,

(ii) develop control methods and mitigation strategies for preserving the power system stability and (iii) propose solutions to potential problems that arises when performing dynamic security assessment based on time-domain simulation analysis. The main contributions of this thesis, represented by the scientific papers [**Pub. A**] – [**Pub. G**] are listed below:

- A robust frequency control design is presented in [**Pub. A**] that accounts for the time-varying profile of system inertia. By exploiting the efficiency of H_∞ loop-shaping procedure, the control parameters of the frequency controllers are optimized. Moreover using the optimization framework presented in [**Pub. A**] we can avoid the standard time-consuming trial and error method for tuning the control parameters.

- In [**Pub. B**], we derive analytical expressions for ROCOF, frequency nadir and steady state frequency deviation of asynchronous AC systems exchanging frequency reserves through HVDC interconnectors. By linearizing the analytical expressions and incorporating them into the unit commitment formulation we can allow for the exchange of primary reserves between neighboring asynchronous systems.

- A comparative stability analysis between grid-feeding and grid-supporting converters is presented in [**Pub. C**]. Using large-disturbance analysis we identify the dynamic limit of the active power transfer capability of a VSC under different operation modes. For the analysis, it is considered that the VSC is connected to a "weak" grid, i.e. low SCR.

- In [**Pub. D**], an investigation and a comparison between two different configurations, namely zero- and low-inertia configuration is presented. Using large-disturbance analysis we evaluate the stability properties of each configuration. Furthermore, we investigate the differences in dynamic performance between a grid-forming converter and an alternative grid-forming pair comprising a synchronous condenser and a grid-following converter.

- [**Pub. E**] proposes an adaptive frequency droop control strategy for a zero-inertia offshore system, where the frequency droop gains are calculated by solving an optimization problem. The optimization problem takes into consideration the operational limits of each offshore converter and their available headroom at the pre fault-state. By optimally selecting the frequency droop values the active power is distributed in a way that the operational limits of the offshore converters are not violated in case of a contingency, i.e. loss of an offshore converter. This results in ensuring the N-1 criterion in the offshore system.

- In [**Pub. F**], we provide sufficient conditions for the control parameters of two different types of grid-forming converters (power synchronization loop, virtual synchronous machine), under which RMS modeling of the component is still valid. We evaluate the validity of these conditions for different types of disturbances, i.e. change in the active power set-point of the converter, a sudden change in grid topology and loss of a generation unit in the grid.

- [**Pub. G**] introduces for the first time a framework for physics-informed neural networks in power system applications. The contributions of the proposed framework are twofold: (i) by exploiting the underlying physical laws describing power system models, we can reduce the dependency of the physics-informed neural network on training data and (ii) we can accurately determine solutions of differential-algebraic equations at a fraction of the computational time required by conventional numerical methods.

1.4 Thesis structure

This thesis presents the key concepts and contributions of the scientific work conducted over the Ph.D study period. For brevity, comprehensive literature review is not part of this thesis and the reader should consult the scientific publications of this Ph.D project.

Chapter 2 outlines the technical challenges related to the integration of converter-based resources in the electric power system. First, the impact of low-inertia on frequency stability of a power grid is analyzed and two mitigation strategies are proposed to limit ROCOF, frequency nadir and steady state frequency deviation. Next, based on large-disturbance analysis, the impact of different operation modes of a VSC on its maximum active power transfer capability is investigated. Main findings regarding the influence of control gains as well as low SCR levels are summarized. Finally, a comparative stability analysis between two different AC configurations for an offshore system, namely zero- and low-inertia configuration, is provided. The analysis aims at assessing how secure a zero-inertia system is against large disturbances. For the analysis, the NSWPH test case is used which has been developed within the multi-DC project.

Chapter 3 deals with potential problems that arise when performing dynamic security assessment based on time-domain simulation analysis. The first part focuses on characterizing the appropriateness of RMS modeling of grid-forming converters for monitoring the power balance stability and proposing sufficient conditions for the control parameters of the grid-forming converter's outer control loops. The second part introduces physics-informed neural networks for predicting solutions to a system of differential-algebraic equations describing the power system dynamics. It is shown that physics-informed neural networks can provide numerical solutions at a fraction of the computational time required by conventional numerical solvers, which make them suitable for performing fast dynamic security assessment.

Chapter 4 provides the concluding remarks and a summary of the contributions of this thesis. Future research directions are outlined with the main focus on stability aspects, control design and dynamic security assessment of future power systems.

1.5 List of publications

The following scientific publications constitute the content of this thesis:

[**Pub. A**] G. S. Misyris, S. Chatzivasileiadis and T. Weckesser, "Robust Frequency Control for Varying Inertia Power Systems," in *2018 IEEE PES Innovative Smart Grid Technologies Conference Europe (ISGT-Europe)*, Sarajevo, 2018, pp. 1-6, doi: 10.1109/ISGTEurope.2018.8571607.

[**Pub. B**] A. Tosatto, G. Misyris, A. Junyent-Ferré, F. Teng and S. Chatzivasileiadis, "Towards Optimal Coordination between Regional Groups: HVDC Supplementary Power Control," submitted to *IEEE Transactions on Power Systems*, (under review, second round), 2021.

[**Pub. C**] G. S. Misyris, J. A. Mermet-Guyennet, S. Chatzivasileiadis and T. Weckesser, "Grid Supporting VSCs in Power Systems with Varying Inertia and Short-Circuit Capacity," in *2019 IEEE Milan PowerTech*, Milan, Italy, 2019, pp. 1-6, doi: 10.1109/PTC.2019.8810979.

[**Pub. D**] G. Misyris, T. Van Cutsem, J. G. Møller, M. Dijokas, O. Renom Estragues, B. Bastin, S. Chatzivasileiadis, A. H. Nielsen, J. T. G. Weckesser, J. Østergaard, and F. Kryezi, "North Sea Wind Power Hub: System Configurations, Grid Implementation and Techno-economic Assessment," accepted at *CIGRE (International Council on Large Electric Systems)*, 2020 .

[Pub. E] G. S. Misyris, A. Tosatto, S. Chatzivasileiadis and T. Weckesser, "Zero-inertia Offshore Grids: N-1 Security and Active Power Sharing," submitted to *IEEE Transactions on Power Systems*, (under review, first round), 2021.

[Pub. F] G. S. Misyris, S. Chatzivasileiadis and T. Weckesser, "Grid-forming Converters: Sufficient Conditions for RMS Modeling," submitted to *Electric Power Systems Research*, (under review, second round), 2021.

[Pub. G] G. S. Misyris, A. Venzke and S. Chatzivasileiadis, "Physics-Informed Neural Networks for Power Systems," in *2020 IEEE Power & Energy Society General Meeting (PESGM)*, Montreal, QC, 2020, pp. 1-5, doi: 10.1109/PESGM41954.2020.9282004.

The following publications have also been prepared during the course of the Ph.D. study, but have been omitted from this thesis because they are not directly related to the primary objective.

[Pub. H] G. S. Misyris, D. I. Doukas, T. A. Papadopoulos, D. P. Labridis and V. G. Agelidis, "State-of-Charge Estimation for Li-Ion Batteries: A More Accurate Hybrid Approach," in *IEEE Transactions on Energy Conversion*, vol. 34, no. 1, pp. 109-119, March 2019, doi: 10.1109/TEC.2018.2861994.

[Pub. I] T. Weckesser, G. Misyris, et al., "The multiDC project: Research Towards a Holistic Integration of HVDC Links into Large-Scale AC Power Systems," in *NEIS 2020; Conference on Sustainable Energy Supply and Energy Storage Systems*, Hamburg, Germany, 2020, pp. 1-7.

[Pub. J] V. Nougain, S. Mishra, G. S. Misyris, and S. Chatzivasileiadis. "Multi-Terminal DC Fault Identification for MMC-HVDC Systems based on Modal Analysis - A Localized Protection Scheme", accepted at *Journal of Emerging and Selected Topics in Power Electronics*, 2021.

[Pub. K] J. Stiasny, G. S. Misyris and S. Chatzivasileiadis, "Physics-Informed Neural Networks for Non-linear System Identification applied to Power System Dynamics,", accepted at *2021 IEEE Madrid PowerTech*, 2021

[Pub. L] G. S. Misyris, J. Stiasny and S. Chatzivasileiadis, "Capturing Power System Dynamics by Physics-Informed Neural Networks and Optimization,", submitted to *60th IEEE conference on Decision and Control*, 2021

[Pub. M] J. Stiasny, G. Misyris and S. Chatzivasileiadis, "Less Data, More Physics: How Physics-Informed Neural Networks affect the way we feed, train and evaluate our Machine Learning Models", to be submitted to *Transactions on Power Systems*, (work in progress), 2021

CHAPTER 2

Enhancing stability in low- and zero-inertia power systems

In Chapter 2.1, we analyze the impact of low-inertia on frequency stability of an electric power system and propose methods to limit Rate Of Change Of Frequency (ROCOF) and frequency nadir. We first propose a robust control design that accounts for the uncertainty on the level of system inertia due to the varying power infeed from RES. Since converter-based resources, and particularly HVDC-VSCs, are called to participate in supporting the grid during weak-grid conditions, i.e. high penetration of converter-based resources, an investigation of their impact on system stability is conducted in Chapter 2.2. In Chapter 2.3, the impact of the converter operation modes on the system dynamic performance is analyzed. For the assessment, the NSWPH test case is used which has been developed within the multi-DC project [65]. Additionally, a primary frequency droop-based control is proposed, which is applied in a decentralized manner without the need for communication and regulates the active power without violating the current limits of the converters in systems "formed" only by grid-forming converters. Last but not least, Chapter 2.4 provides concluding remarks concerning stability issues and appropriate control design in power systems with high share of RES.

2.1 Frequency stability of low-inertia systems

Frequency stability denotes the ability of the system to maintain the frequency of a power system following a severe active power imbalance, see Fig. 2.1. Several issues related to frequency stability have been analyzed and documented in [66], which concern the impact of the inertia level on the dynamic behavior of the power system. Rotational inertia is a system property that defines the total energy stored in the rotating mass of synchronous generators and adds an energy buffer to potential disturbances in the power balance. The higher the level of inertia is, the more is the kinetic energy stored in the synchronous generators rotating mass, which reduces the ROCOF and frequency nadir during a system incident. High values of ROCOF are not desirable, not only because of frequency stability issues but they can also cause: (i) stress of the prime movers of synchronous generators, (ii) large transient displacements of voltage angles, which in turn lead to network splitting, and (iii) protection devices not being able to ensure a reliable system operation. Thus, due to the decreased level of inertia, the ability of the system to withstand power unbalances deteriorates.

To counteract the problem of reduced system inertia due to large share of non-synchronous generation and ensure secure system operation, TSOs can rely on alternative power regulating resources, such as wind farms, solar photovoltaic generators and HVDC converters connecting neighboring asynchronous areas, i.e. converter-based resources. Although these resources do not inherently contribute to frequency regulation and the level of system inertia, by equipping them

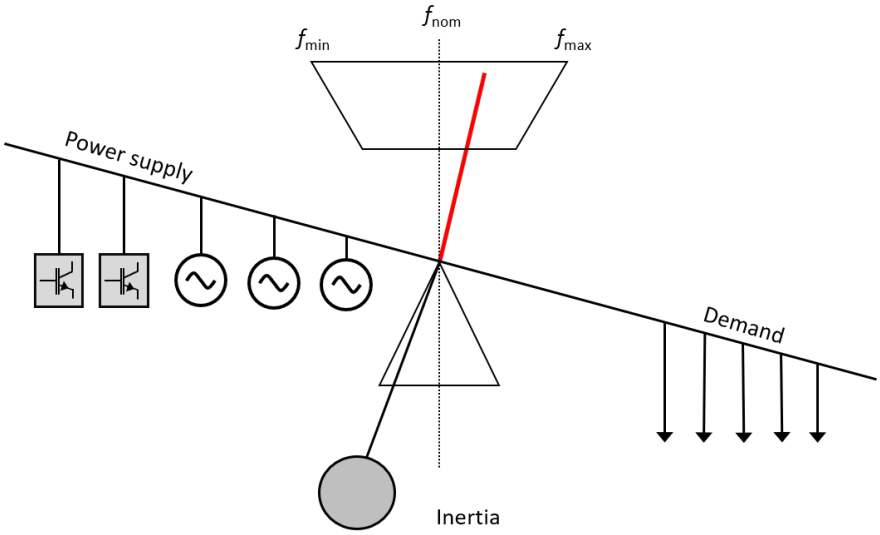

Figure 2.1: Active power balance and frequency stability.

with frequency controllers they can provide fast active power support. The frequency controllers are primarily designed around droop-based or virtual synchronous machines-based schemes, for which an appropriate control tuning is required in order to enable the converters to provide fast active power control. To enable converter-based resources to participate in frequency regulation, a framework needs to be developed that takes into consideration the frequency constraints imposed by system operators and that selects the frequency services in order to ensure the frequency stability of the system. Thus, appropriate control tuning and dispatch of fast frequency reserves are the two necessary mitigation strategies that lead to frequency restoration and minimization of the instantaneous frequency deviation. We propose two technical solutions: the first is based on publication [**Pub. A**] and proposes a robust frequency control design with the objective of limiting the ROCOF and frequency nadir, while accounting for the time-varying profile of inertia levels. The second is based on publication [**Pub. B**] and proposes frequency metrics based on current frequency controllers, e.g. power synchronization loop [45], turbine governor, etc. that can be used in a unit-commitment problem for optimally dispatching the active power regulating units needed to maintain the frequency stability of the system.

2.1.1 Robust primary frequency control

Given the varying power-infeed from RES, the system inertia exhibits a time-varying profile, which makes the tuning of frequency controllers a difficult task for TSOs [**Pub. A**]. Considering the fact that the frequency control gains are static, i.e. they are not updated regularly by the TSOs, the control parameters should be selected in order to provide robust performance and ensure the frequency stability of the system. During low-inertia periods, the devices participating in primary frequency support would ideally act adequately fast in order to limit ROCOF and frequency nadir. However, during high-inertia periods fast active power regulation leads to higher energy loss, since the controllers are more sensitive to frequency deviations [67]. Thus, the selection of the droops should be realized, so that it accounts both for limiting the frequency nadir and ROCOF in low-inertia periods, and avoids high energy loss in high-inertia periods, i.e. robust frequency control design. This thesis formulates the robust frequency control design as an optimization

problem based on H_∞ loop shaping methodology [68], which provides desirable properties, such as tracking performance and robustness against uncertainty. We consider the problem of having several power regulating resources with structured frequency controllers, such as droop-based, PID, lead-lag, etc. whose control parameters need to be tuned, in order to mitigate the impact of uncertain inertia levels on frequency stability. To this end, we propose a procedure for designing Multi-Input-Multi-Output (MIMO) frequency controllers. First, we analyze the impact of varying inertia on the frequency dynamics and then we present the optimization problem for deriving the robust controller.

Power system modeling

To assess the impact of the system inertia on the frequency dynamics, we first introduce the model that can be used to assess this type of dynamic phenomena. The swing equation is a commonly used model that describes the frequency dynamics of the system linearized around an operating point, which relates the change of rotor speed of a machine i to a power imbalance [69] and can be expressed as follows:

$$\Delta\dot{\omega}_i = \frac{1}{2H_i}[\Delta P_{m_i} - \Delta P_{e_i} + \Delta P_{p_i} - \underbrace{\left(D_i + \frac{1}{R_i}\right)}_{K_{D_i}} \Delta\omega_i], \tag{2.1}$$

$$\Delta\dot{\delta}_i = \omega_0 \Delta\omega_i, \tag{2.2}$$

where $\Delta\omega_i$ and $\Delta\delta_i$ are the speed and angle deviations of the i-th machine, respectively. H_i is the inertia constant of the generator, ω_0 is the base rotor electrical speed expressed in radians/sec, ΔP_{m_i} and ΔP_{e_i} are the deviations of the mechanical and electrical power, respectively, applied to the machine. The terms D_i and R_i are the damping and the droop coefficient of the generator, respectively. The term K_{D_i} is the aggregate damping coefficient. The variable ΔP_{p_i} is the controllable input of the power regulating components. The electrical power drained by the network at bus i is $\Delta P_{e_i} = \sum_{j\in\Omega_i} V_i V_j b_{ij} cos(\delta_{ij})$. The terms V_i and V_j are the voltage magnitudes at the i-th and j-th buses, b_{ij} is the susceptance between i and j, δ_{ij} is the angle difference between the i-th and j-th nodes. The term Ω_i is the set of all nodes adjacent to node i. The state space representation of the open-loop transfer function is:

$$\begin{bmatrix} \Delta\dot{\boldsymbol{\delta}}_N \\ \Delta\dot{\boldsymbol{\omega}}_N \end{bmatrix} = \underbrace{\begin{bmatrix} \boldsymbol{O_{n\times n}} & \boldsymbol{\omega_{0_{n\times n}}} \\ \boldsymbol{-H_N^{-1}L_N} & \boldsymbol{-H_N^{-1}K_N} \end{bmatrix}}_{A_{\text{sys}}} \begin{bmatrix} \Delta\boldsymbol{\delta}_N \\ \Delta\boldsymbol{\omega}_N \end{bmatrix} + \underbrace{\begin{bmatrix} \boldsymbol{O_{n\times n}} \\ \boldsymbol{-H_N^{-1}} \end{bmatrix}}_{B_{\text{sys}}} \Delta\boldsymbol{P}_P \tag{2.3a}$$

$$y = \underbrace{\begin{bmatrix} 0 & I \end{bmatrix}}_{C} \begin{bmatrix} \Delta\boldsymbol{\delta}_N \\ \Delta\boldsymbol{\omega}_N \end{bmatrix} \tag{2.3b}$$

with

$$\boldsymbol{H}_N = \text{diag}(2H_1, \cdots, 2H_n),\ \boldsymbol{K}_N = \text{diag}(K_{D_1}, \cdots, K_{D_n}) \tag{2.4}$$

$$\boldsymbol{\Delta\delta}_N = \begin{bmatrix}\Delta\delta_1, \cdots, \Delta\delta_n\end{bmatrix}^{\mathrm{T}},\quad \boldsymbol{\Delta\omega}_N = \begin{bmatrix}\Delta\omega_1, \cdots, \Delta\omega_n\end{bmatrix}^{\mathrm{T}}. \tag{2.5}$$

The state vectors $\boldsymbol{\Delta\delta}_N$ and $\boldsymbol{\Delta\omega}_N$ include the deviation of generators rotor angles and speeds of the system. The vector L_N is the weighted Laplacian matrix, $\Delta\boldsymbol{P}_P$ contains the deviation of electrical power of the power regulations units ΔP_{p_i}. Finally, the transfer function $G(s)$ of the open-loop

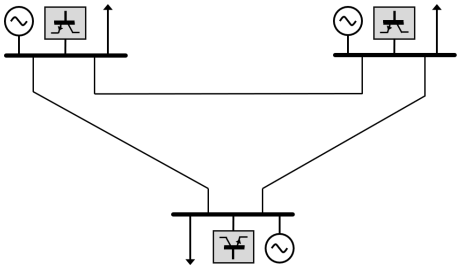

Figure 2.2: 3-Bus system. Adapted from **[Pub. A]**.

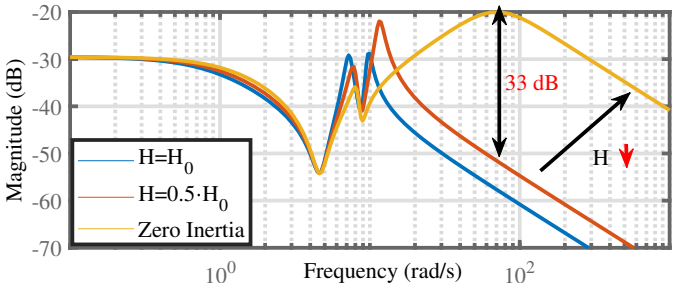

Figure 2.3: Frequency Response of $G_2(s)$ for different levels of inertia. (H: Inertia). Adapted from **[Pub. A]**.

system is:

$$G(s) = \frac{Y(s)}{U(s)} = C(sI - A_{\text{sys}})^{-1} B_{\text{sys}} \tag{2.6}$$

Sensitivity analysis for different level of inertia

To illustrate the effect of the varying level of the system inertia, we make use of Bode plot analysis using the system depicted in 2.2. We vary the inertia parameter at one of the generator buses and evaluate the effect of the system inertia on the frequency response of the system. Figure 2.3 shows the Bode plot of $G_2(s) = \frac{\Delta\omega_2(s)}{\Delta T_{m_2}(s)}$. Reducing system inertia results in gain amplification at higher frequency. Gain amplification at higher frequencies makes the system response sensitive to changes of the input signals of the system. This means that in the case of lower inertia, the frequency of an AC grid is more volatile when a power imbalance occurs.

H_∞ loop-shaping design

To mitigate the effect of the reduced-inertia constant, this thesis proposes a H_∞ loop-shaping design, which allows for shaping the frequency response system and defining a controller with desired characteristics, such as limited overshoot, slower rise-time, etc. It should be mentioned that shaping the frequency response of the system plant and controller, i.e. loop-shaping design, is a direction that was recently followed by researchers of the French transmission operator [70] in order to determine the capability of the active power regulating units to contribute to the frequency stability of the power grid. In this part of the thesis, we present the methodology for designing a robust frequency controller that mitigates the effect of the reduced level of inertia.

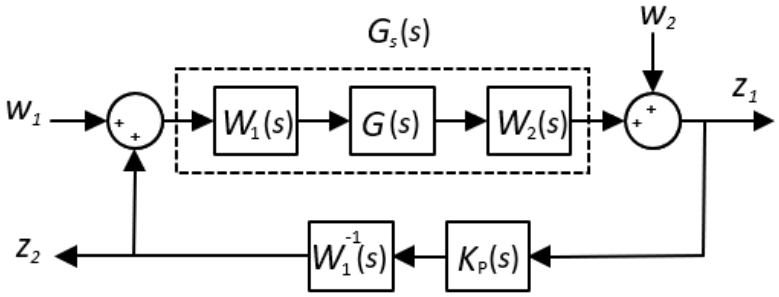

Figure 2.4: Shaped Plant and Controller [2]. Adapted from [**Pub. A**]

In Fig. 2.4, the closed-loop control system is depicted, where the input-output relationship is given by:

$$\underbrace{\begin{bmatrix} z_1 \\ z_2 \end{bmatrix}}_{\mathbf{z}} = T_{zw}(K_\mathrm{P}) \underbrace{\begin{bmatrix} w_1 \\ w_2 \end{bmatrix}}_{\mathbf{w}} \tag{2.7}$$

$$T_{zw}(K_\mathrm{P}) = \begin{bmatrix} (I + W_2 G K_\mathrm{P})^{-1} W_2 G W_1 & (I + W_2 G K_\mathrm{P})^{-1} \\ -W_1^{-1} K_\mathrm{P} (I + W_2 G K_\mathrm{P})^{-1} W_2 G W_1 & -W_1^{-1} K_\mathrm{P} (I + W_2 G K_\mathrm{P})^{-1} \end{bmatrix} = \begin{bmatrix} I \\ -W_1^{-1} K_\mathrm{P} \end{bmatrix} (I + W_2 G K_\mathrm{P})^{-1} \begin{bmatrix} W_2 G W_1 \\ I \end{bmatrix}^T \tag{2.8}$$

where $G(s)$ is the initial plant of the system. We seek to find the K controller that satisfies the following optimization problem:

$$\begin{aligned} &\text{minimize } \gamma \\ &\text{subject to } ||T_{zw}(K_\mathrm{P})||_\infty \leq \gamma \end{aligned} \tag{2.9}$$

The solution to the optimization problem (2.9) renders the final controller, which is given by:

$$K_{\text{final}}(s) = K_\mathrm{P}(s) W_2(s). \tag{2.10}$$

This corresponds to a standard P controller in cascade with the post-compensator $W_2(s)$. Finally, the transfer function of the closed loop system $CL_{\text{sys}}(s)$ is given by:

$$CL_{\text{sys}}(s) = \frac{G(s) K_{\text{final}}(s)}{1 + G(s) K_{\text{final}}(s)} \tag{2.11}$$

The selection of the pre- and post-compensators (see Fig. 2.4) is realized based on desired closed-loop design specifications and the value of γ. In case $\gamma \geq 3$, the pre- and post-compensators need to be adjusted, so that $1 \leq \gamma \leq 3$. On the on hand, $W_1(s)$ (pre-compensator) determines the characteristics of the closed loop system at low frequency range, such as disturbance rejection at both input and output of the plant, decoupling between the outputs of the system and determining the control effort. On the other hand, W_2 determines the dynamic performance of the system at higher frequencies. It is selected so that we better damp the system at higher frequencies. Considering that for low-inertia levels the magnitude of the transfer function $G(s)$ is higher at higher frequencies, we want to design a controller that mitigates this effect; by doing that, we reduce the maximum value of the ROCOF and the frequency nadir. Figure 2.5 shows the singular values of the frequency response of the controller, which indicate how the control inputs of the system are amplified based on the error between a desired reference and the output signals. As

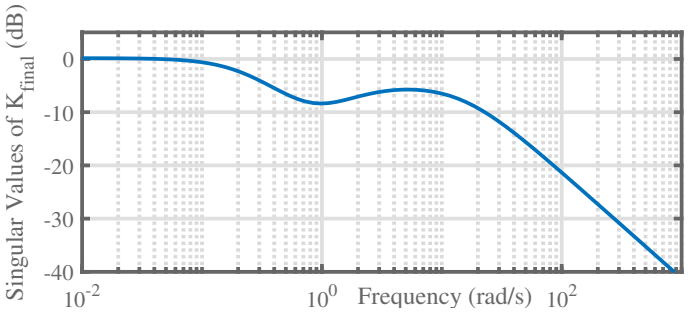

Figure 2.5: Singular Values of controller $K_{\text{final}}(s)$. Adapted from [**Pub. A**].

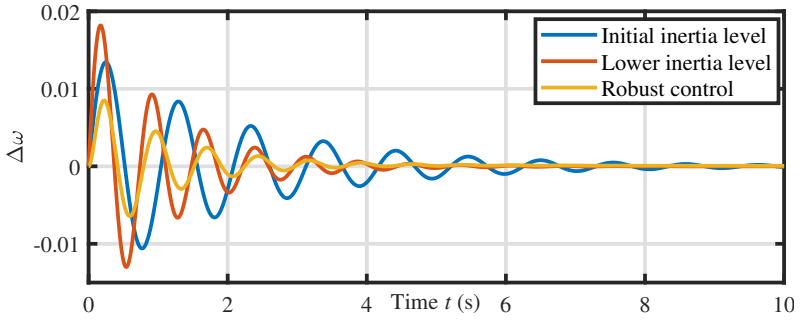

Figure 2.6: Robust control of $\Delta\omega$ & impulse response for 50% reduction of the initial inertia level.

it can be seen the controller damps well the system at higher frequencies, which implies that it reduces the effect of the low-inertia on the frequency of the AC system.

To illustrate the performance of the controller, we use as a test system the one shown in Fig. 2.2. We consider a reduction of the inertia level at bus 2 by 50%. As depicted in Fig. 2.6, with the proposed robust control design, the ROCOF and frequency nadir are reduced. This is due to the fact that the proposed controller reduces the gain of the system transfer function at high frequencies and, thus, mitigates the effect of the reduced level of inertia (see also Fig. 2.3).

2.1.2 Frequency metrics for the unit commitment problem

To mitigate the effect of low-inertia on frequency stability, dispatch of frequency reserves is required, i.e. solve the Unit Commitment Problem (UCP) while accounting for the frequency stability of the system [**Pub. B**]. Consider for example a period of low penetration of synchronous generators, i.e. a low-inertia period, if the converter-based components connected to the grid, i.e. HVDC-VSCs, are not equipped with fast frequency controllers they will not be able to maintain the frequency stability in an event of a large active power disturbance. To account for such events, we add frequency constraints to the UCP, which yields the general form:

$$\begin{aligned} \min \quad & \textit{Total system cost} \\ \text{s.t.} \quad & \textit{Generator constraints} \\ & \textit{Transmission system constraints} \\ & \textit{Power balance constraints} \\ & \textit{Frequency constraints} \\ & \textit{Reserve procurement} \end{aligned} \tag{2.12}$$

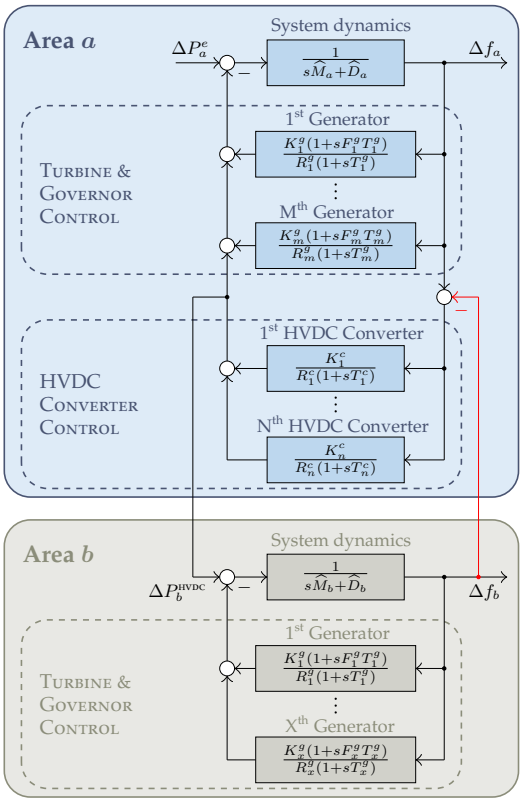

Figure 2.7: System dynamics model under unilateral and bilateral HVDC control schemes. The difference between the two schemes is highlighted in red. Adapted from [**Pub. B**].

Several several works have studied the inclusion of frequency constraints in the UCP, with researchers focusing on utilizing power regulating devices within one synchronous system, overlooking the option of exchanging frequency reserves among neighboring asynchronous systems [37–40]. In this part of the thesis, we focus on utilizing HVDC interconnectors between asynchronous areas to enable the exchange of primary frequency reserves between them. To utilize HVDC for frequency support, supplementary control loops are required. The supplementary control loops modify the active power exchanged between the HVDC and the AC systems based on the deviation of the frequency of the AC system. Various methods to control the frequency of an AC system utilizing an HVDC interconnection between asynchronous areas, can be found in the literature [71].

When HVDC interconnectors are employed for frequency support, any power flowing into and out of the HVDC links must be balanced by the frequency reserves of the interconnected AC systems, i.e. in case of a contingency in area a, area b participates in the power balancing by supplying its own frequency reserves to the area a, which results in a deviation of the frequency of the system b. This deviation is primarily affected by the value of the frequency droop, as well as the amount of the frequency reserves. It should be mentioned that the control is only activated when the frequency drops below a certain value, in this thesis this value is considered equal to 49.9 Hz. This is done, in order to avoid triggering the frequency controller in the case of small power disturbances.

This work only focuses on frequency support schemes that involves only the system frequency as an input control signal. We first present the model describing the frequency dynamics of

interconnected asynchronous areas and then provide analytical expressions for the ROCOF, the frequency nadir and steady-state frequency deviation. The schematic configurations of the supplementary frequency control loop placed in the outer control loop of the active power control of the HVDC VSCs are shown in Fig. 2.7. The configurations represent the concept of droop control schemes presented in [72].

Unilateral supplementary power control scheme

This droop control scheme only uses the frequency difference of one asynchronous area. This means that for a specific time period, frequency support can be provided only to one asynchronous area through the HVDC interconnectors. The relation between the change of the active power flow through the HVDC link and the frequency can be expressed as follows

$$\Delta P^{\text{ref}}(s) = \frac{K^c}{R^c(1+T^c s)}\left(\Delta f_a\right) \tag{2.13}$$

where $\Delta P^{\text{ref}}(s)$ is the dynamic change of the active power injected to the grid based on a frequency deviation Δf_a occurring in the AC system. The parameters K^c, R^c and T^c are the electric power gain power factor, the frequency droop gain and time constant of the active power controller, respectively. The disadvantage of the scheme, as it will be shown later (left figure in Fig. 2.8), is that it results in a higher frequency deviation in the AC system that provides the frequency support.

Bilateral supplementary power control scheme

This droop control scheme employs the frequency difference between the interconnected asynchronous areas as an input for adjusting the active power flow. With this scheme, we can consider that all the HVDC-links can provide frequency support in both areas, since the active power set point is adjusted proportionally to the frequency difference between the two AC systems. The relation between the change of the active power flow and the frequency can be expressed as follows:

$$\Delta P_{\text{ref}}(s) = \frac{K^c}{R^c(T^c s+1)}\left(\Delta f_a - \Delta f_b\right) \tag{2.14}$$

where Δf_a and Δf_b are the frequencies of the interconnected asynchronous areas.

Analytical Formulation of Frequency Metrics - Unilateral control scheme

The function describing the relation between an active power disturbance and the frequency deviation in the area a is given by:

$$G_a^U(s) = \frac{\Delta f_a(s)}{\Delta P_a^e(s)} = \left(\underbrace{(s\widehat{M}_a + \widehat{D}_a)}_{\text{swing equation}} + \underbrace{\sum_{i\in\mathcal{G}_a^S} \frac{K_i^g\,(1+sF_i^gT_i^g)}{R_i^g\,(1+sT_i^g)}}_{\text{turbine governor}} + \underbrace{\sum_{k\in\mathcal{L}_a^S} \frac{K_k^c}{R_k^c\,(1+sT_k^c)}}_{\text{HVDC converters}} \right)^{-1}, \tag{2.15}$$

where $\widehat{M}_a$ and $\widehat{D}_a$ are the total inertia and damping constants of the area a, $\mathcal{G}_a^S$ is the total number of generators that are equipped with turbine governor and $\mathcal{L}_a^S$ denotes the total number of the HVDC interconnectors that are equipped with frequency controllers. $\Delta P_a^e(s)$ is the deviation of the electrical power from its pre-fault steady state value and Δf_a is the frequency deviation in the area a. It should be noted that the subscript a denotes the AC system that experiences a contingency. Similar to [33], we consider that the turbine time constants are equal $T_i^g = T_a$ for all synchronous

machines and that the converter time constants are neglected since $T^g >> T^c$. Having made these assumptions, (2.15) takes the following generalized form:

$$G_a^{\text{U}}(s) = \frac{1}{\widehat{M}_a T_a} \frac{1 + sT_a}{s^2 + 2\zeta_a \omega_a^n s + \omega_a^{n\,2}}, \tag{2.16}$$

where the natural frequency ω_a^n and the damping ratio ζ_a are given by:

$$\omega_a^n = \sqrt{\frac{\widehat{D}_a + \widehat{R}_a}{\widehat{M}_a T_a}}, \qquad \zeta_a = \frac{\widehat{M}_a + T_a(\widehat{D}_a + \widehat{F}_a)}{2\sqrt{\widehat{M}_a T_a (\widehat{D}_a + \widehat{R}_a)}}. \tag{2.17}$$

with $\widehat{F}_a$ and $\widehat{R}_a$ being weighted model parameters, which are a function of the generators parameters, HVDC converters and system parameters of the area a. For their derivation, a detailed mathematical formulation is presented in [33]. By applying inverse Laplace transformation and assuming a stepwise disturbance of the input $\Delta P_a^e(s) = \Delta P_a/s$, we can derive a time-domain expression of the frequency deviation. This enables to extract frequency related expressions associated with the ROCOF, the frequency nadir and the steady state frequency deviation in the area a, which are defined, respectively as follows:

$$\dot{f}_a^{\max} = -\frac{\Delta P_a}{\widehat{M}_a}, \tag{2.18a}$$

$$\Delta f_a^{\max} = -\frac{\Delta P_a}{\widehat{D}_a + \widehat{R}_a} \left(1 + \sqrt{\frac{T_a(\widehat{R}_a - \widehat{F}_a)}{\widehat{M}_a}} e^{-\zeta_a \omega_a^n t_a^m}\right), \tag{2.18b}$$

$$\Delta f_a^{\text{ss}} = -\frac{\Delta P_a}{\widehat{D}_a + \widetilde{R}_a^g}, \tag{2.18c}$$

where t_a^m is the time instant that the maximum frequency deviation occurs ($\dot{f}(t_a^m = 0)$). The term $\widetilde{R}_a^g$ is a weighted parameter, which is only a function of the generators frequency droops. To ensure the frequency stability of the AC system after a contingency, we can include the expressions derived above as constraints in the UCP by bounding the absolute values of the variables $\dot{f}_a^{\max}$, $\Delta f_a^{\max}$ and Δf_a^{ss} by thresholds defined by transmission system operators. The expressions are similar to the one extracted in [38], which indicates that the HVDC acts as a generator and provides the energy that is necessary for minimizing the frequency nadir of the area a which is at fault; without accounting for the frequency deviation caused in the other area, i.e. area b.

A way to mitigate the frequency deviation in the asynchronous area b at the other end is to include additional constraints regarding the frequency nadir and rate of change of frequency of the area b. To realize that, we first derive a transfer function $G_b^{\text{U}}(s)$ which is the linear mapping of the Laplace transform of the frequency of the area a, to the Laplace transform of the frequency of the area b. Similar to the previous case, (2.16) takes the following generalized form:

$$G_b^{\text{U}}(s) = \frac{\Delta f_b(s)}{\Delta f_a(s)} = \frac{\widetilde{R}_{a,b}^c}{\widehat{M}_b T_b} \frac{1 + sT_b}{s^2 + 2\zeta_b \omega_b^n s + \omega_b^{n\,2}}, \tag{2.19}$$

where $\widetilde{R}_{a,b}^c$ denotes the contribution of the HVDC interconnectors connecting area a and b to the active power regulation. Since, area b is not receiving frequency support from area a, the parameters ω_b^n and ζ_b are functions of the system parameters and the parameters of the generators in area b only. The maximum frequency deviation that can occur in the area b is proportional to the maximum frequency variation in the area a. By considering a step-wise change of $\Delta f_a(s)$, we can

approximate the value of the frequency nadir of the area b. The magnitude of the step change is equal to $\Delta f_a^{\max}$, i.e. $\Delta f_a(s) = \Delta f_a^{\max}/s$. Although this approximation leads to wrong calculation of time nadir t_b^m, since $\Delta f_a(t)$ varies with time, it can provide an accurate approximation of frequency nadir of the area b. By applying inverse Laplace transformation and assuming a stepwise disturbance of the input $\Delta f_a = \Delta f_a^{\max}/s$, we can derive a time-domain expression of the frequency deviation of the area b. This enables to extract frequency metrics associated with the area b as follows:

$$\dot{f}_b^{\max} = -\frac{\Delta P_a \widetilde{R}_{a,b}^c}{\widehat{M}_a \widehat{M}_b}, \tag{2.20a}$$

$$\Delta f_b^{\max} = \frac{\Delta f_a^{\max} \widetilde{R}_{a,b}^c}{\widehat{D}_b + \widehat{R}_b} \left(1 + \sqrt{\frac{T_b(\widehat{R}_b - \widehat{F}_b)}{\widehat{M}_b}} e^{-\zeta_b \omega_b^n t_b^m}\right), \tag{2.20b}$$

Unlike the parameters ω_b^n and ζ_n, we can see that the frequency metrics are directly dependent on the weighted average system parameters $\widehat{M}_b$, $\widehat{D}_b$, $\widehat{R}_b$ and $\widehat{F}_b$ of area b, the HVDC converter parameters $\widetilde{R}_{a,b}^c$, as well as the system parameters $\widehat{M}_a$, $\widehat{D}_a$, $\widehat{R}_a$ and $\widehat{F}_a$ of area a. The transmission system operator of the area b can determine the amount of frequency reserves by bounding the absolute values of the variables $\dot{f}_b^{\max}$ and $\Delta f_b^{\max}$ and include them as constraints in the UCP.

Analytical Formulation of Frequency Metrics - Bilateral control scheme

The main difference between the bilateral and unilateral control schemes is that the active power flow through the HVDC-link changes proportionally to the difference of the frequency of the two interconnected AC systems, $\Delta f_a - \Delta f_b$. The function that describes the relation between an active power disturbance and the frequency deviation in the area a is given by:

$$\Delta f_a(s) = G_a^{\mathrm{U}}(s)\left(\Delta P_a^e(s) + \sum_{k \in \mathcal{C}_a^S} \frac{K_k^c}{R_k^c\left(1 + sT_k^c\right)} \Delta f_b(s)\right), \tag{2.21}$$

As it can be seen, (2.21) differs from (2.16) by the term $\sum_{k \in \mathcal{C}_a^S} \frac{K_k^c}{R_k^c\left(1+sT_k^c\right)}$. The transfer function $G_b^{\mathrm{B}}(s) = \frac{\Delta f_b(s)}{\Delta f_a(s)}$ is similar to the one in (2.19), with the main difference being the calculation of ω_b^n and ζ_b^n. The term $\sum_{k \in \mathcal{C}_a^S} \frac{K_k^c}{R_k^c\left(1+sT_k^c\right)} \Delta f_b(s)$ introduces additional complexity when deriving analytical conditions for the frequency nadir in the two asynchronous areas, since (even after the assumptions made in the previous sections) the transfer function $\frac{\Delta f_a(s)}{\Delta P_a^e(s)}$ becomes a sixth-order transfer function. To overcome this issue, similar to the previous section, we consider a step-wise change of $\Delta f_a(s) = \Delta f_a^{\max}/s$ (input of $G_b^{\mathrm{B}}(s)$), where $\Delta f_a^{\max}$ is the maximum allowable frequency deviation determined by the transmission system operator of the area a. This assumption results in an overestimation of the absolute values of the frequency nadir of both area a and area b (see Table 2.1). However, it ensures that the ROCOF and the frequency nadir stay within the operational limits that the transmission system operators set. The frequency metrics for the area b are similar to the ones described by (2.20a) and (2.20b). To derive the frequency metrics for the asynchronous area a, we consider stepwise changes of the inputs $\Delta P_a^e(s)$ and Δf_b as $\Delta P_a/s$ and $\Delta f_b^{\max}/s$, respectively. This renders similar expressions for the ROCOF and steady state frequency deviation, given by (2.18a) and (2.18c), respectively, and the following expression for the maximum frequency deviation for area a:

$$\Delta f_a^{\max} = \frac{\Delta P_a + \Delta f_b^{\max} \widetilde{R}_{a,b}^c}{\widehat{D}_b + \widehat{R}_a} \left(1 + \sqrt{\frac{T_a(\widehat{R}_a - \widehat{F}_a)}{\widehat{M}_a}} e^{-\zeta_a \omega_a^n t_a^m}\right). \tag{2.22}$$

Table 2.1: Comparison of the IFD obtained with the analytical expressions and the dynamic simulations. Adapted from [**Pub. B**].

		no lim	*no SPC*	*unilateral*	*bilateral*
Analytical expression	AREA 1	-	-	0.1550	0.1496
	AREA 2	0.7707	0.5204	0.5849	0.5007
Dynamic simulation	AREA 1	-	-	0.1261	0.1001
	AREA 2	0.7706	0.5204	0.5896	0.4875

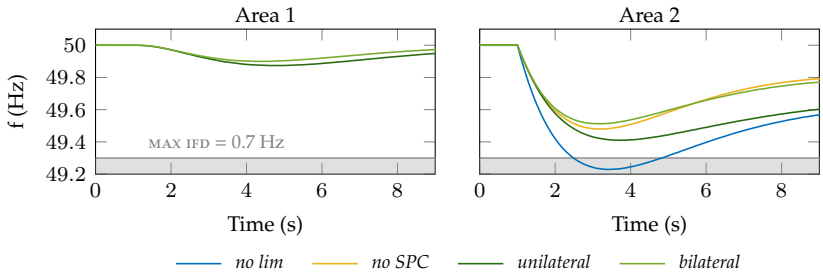

Figure 2.8: IFD following the dimensioning incident in area 2 (generation loss of 600 MW in area 2). The left graph shows the IFD in area 1 due to the activation of HVDC supplementary power control. Frequency metrics for the four simulations. Adapted from [**Pub. B**].

Because of the over estimation of the frequency deviation in area b, also the IFD in area a is slightly over estimated. However, this ensures that the limit is never exceeded.

The analytical expressions derived above are nonlinear. To determine the operation schedule of the generation units, i.e. solve the UCP, the analytical expressions need to be linearized. In [**Pub. B**], a data-driven approach is proposed to tackle this problem and these constraints are substituted by cutting hyperplanes which excludes those solutions that do not fulfill frequency requirements. By solving the UCP with frequency constraints, HVDC supplementary control and generator frequency support, we can limit the frequency nadir and ROCOF, and allow for the secure integration of RES without threatening the frequency stability of the system. To assess the benefit of the supplementary power control implementation, we perform four simulations:

- "*no lim*", where frequency constraints are not included in the UCP,
- "*no SPC*", where frequency constraints are included in the UCP, but the expressions only account for the participation of the synchronous generators in active power regulation (no HVDC contribution),
- "*unilateral*", frequency constraints account for the use of HVDC-links in exchanging primary frequency reserves between neighboring TSOs, in the case of the unilateral control scheme,
- "*bilateral*", frequency constraints account for the use of HVDC-links in exchanging primary frequency reserves between neighboring TSOs, in the case of the bilateral control scheme,

Table 2.1 compares the Instantaneous Frequency Deviation (IFD)s calculated with the analytical expressions to the ones obtained through dynamic simulations (Fig. 2.8) for a specific time instance (hour 43). The two values match in all cases, except for the "*bilateral*" case where the calculated IFD is a bit higher. This was expected due to the assumption made in order to derive the analytical expressions for the bilateral case (see Section 2.1.2). Moreover, as shown in Fig. 2.8, by incorporating frequency-related constraints the maximum frequency deviation and ROCOF stay within the

operational limits ($IFD \leq 0.7$ Hz, ROCOF ≤ 0.625 Hz/s). In the case of the bilateral control scheme, the frequency deviation in Area 1 is smaller compared to the unilateral control scheme. This was expected, since the adjustment of the active power ΔP_{ref} flowing through the HVDC interconnectors accounts for the frequency deviation in both areas (proportional to the $\Delta f_a - \Delta f_b$).

By including the frequency-related constraints in the UCP, we allow for the exchange of primary frequency reserves between asynchronous areas. Based on the market analysis presented in [**Pub. B**], by utilizing the HVDC interconnectors for exchanging primary frequency reserves the cost of reserve procurement can be reduced by up to 10%. In other words, our method shows that frequency reserves in one area can be used by other areas as well, thus reducing the costs of reserve procurement from a system point of view, while maintaining the frequency stability.

2.2 Converter stability - Weak grid

HVDC connections and particularly HVDC-VSC are expected to play a vital role in the coordination of frequency reserves and frequency support in future low-inertia grids, additional investigation needs to be performed concerning converter stability issues. Based on the grid strength, different operation modes of the converters, namely grid-following and grid-forming, present different active power transfer capabilities. This means that the maximum active power that can be delivered to the grid varies based on system strength, i.e. SCR levels. While for grid-forming converters the maximum active power that can be delivered to the grid depends on the equivalent grid-impedance between the converter and the external grid [45], for grid-following converters (grid-feeding and grid-supporting) the maximum active power also depends on the parameters of the converter controllers [16]. This part of the thesis summarizes the results presented in [**Pub. C**]. A comparison between grid-feeding and grid-supporting [41] is presented, where the maximum active power transfer capability is considered as a metric for assessing the impact of different operation modes of the converters on the system stability. Existing approaches in the literature investigate small-signal stability issues related to the operation of grid-following converters that are connected to weak grids [16–18, 42–44]. In the following, we focus on the converter and system stability under large disturbances.

2.2.1 Grid-following converters

Grid-following converters act as a controlled current source, with the current exchanged with the grid at their Point of Common Coupling (PCC). The current is adjusted by outer control loops based on the amount of active and reactive power requested by the grid. There are two types of grid-following converters, namely grid-feeding and grid-supporting converters. In the former, the converter provides constant active and reactive power, while in the latter the converter adjusts its current reference set point based on the variation of the frequency of the grid and the voltage at the PCC. Figure 2.9 and Fig. 2.10 represent the general model of a grid-feeding and a grid-supporting converter. The inner loop current control and the Phase Locked Loop (PLL) unit are the same in both cases. The main difference is found in the structure of the outer loop control unit, where in the case of grid-supporting converter Pf and QV characteristics are embedded, in order to provide grid-support to the grid.

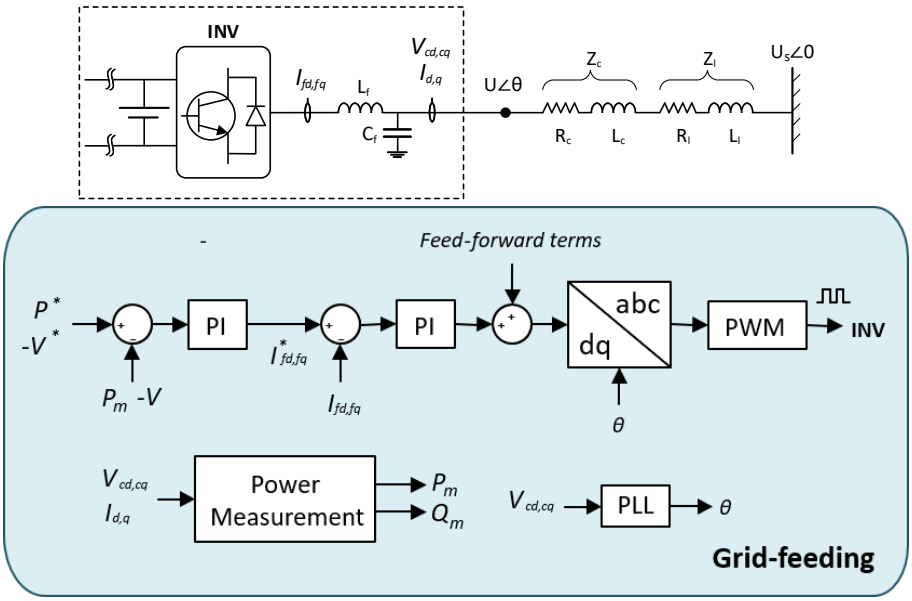

Figure 2.9: Control structure of grid feeding converter.

2.2.2 Dynamic limit of active power transfer capability

The limit of active power transfer capability of the converter can be categorized into the static and the dynamic one. The static limit is primarily determined by the voltage magnitude at the PCC of the converter V_{pcc}, the voltage magnitude E of the AC system and the grid impedance X_{eq} between the converter and the AC system. The equation describing the static limit of active power transfer capability of the converter is given by:

$$P_{\text{max}}^{\text{static}} \approx \frac{V_{\text{pcc}} E}{X_{\text{eq}}} \tag{2.23}$$

As for the dynamic limit of active power transfer capability, it corresponds to the ability of the converter to remain synchronized with the rest of the grid, when the system is subject to changes in grid-topology, i.e. sudden change of SCR or other type of large disturbances such as faults.

Following, we assess the impact of the SCR on the dynamic limit of active power transfer capability of the converter under different operation modes. We demonstrate the effect of the operating point on the converter stability. Based on the eigenvalue analysis presented in **[Pub. C]**, we can make the following remarks regarding the effect of the converter control loops on its maximum active power transfer capability:

- Very fast or very slow time response of the PLL block decreases the maximum active power transfer capability.
- Faster voltage controller than active power controller improves the active power transfer capability of the converter.
- Increase of frequency droop leads to increase of the active power transfer capability of the converter.
- Voltage control is preferable to constant reactive power control, as it allows for fast voltage recovery, which in turns increases the maximum power transfer capability of the converter.

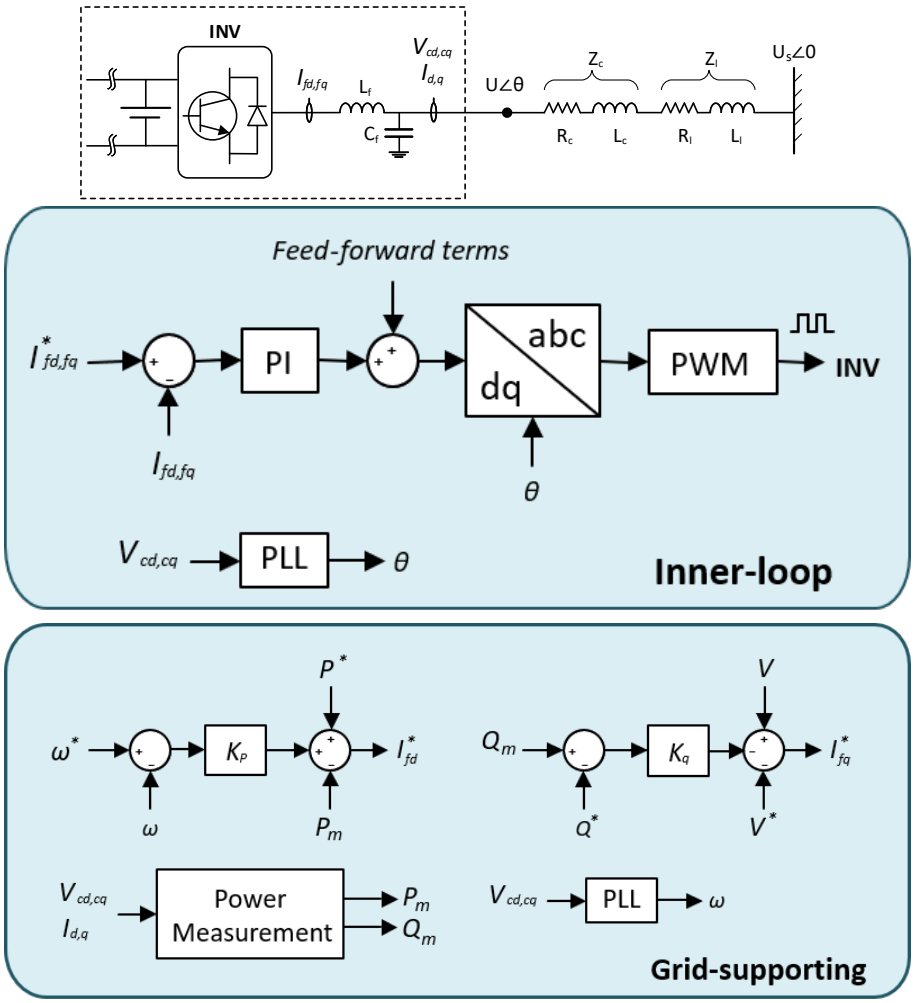

Figure 2.10: Control structure of grid supporting converter.

Fig. 2.11 shows a comparison of the active power response of the VSC for different operation modes, namely grid-supporting and grid-feeding. We consider that a sudden change of the SCR from 5 to 0.5 occurs, i.e. simulated as a line opening that leads to an increase of the equivalent grid-impedance. Based on (2.23), the static limit of active power transfer capability of the converter is around 0.5 p.u. However, when considering the dynamic limit, Fig. 2.11 shows that different operation modes of the converter have a different effect on the active power transfer capability. Particularly, the dynamic limit of the active power transfer capability for the grid-supporting and grid-feeding converter is 0.442 and 0.384 p.u., respectively. The higher transfer capability of the grid-supporting converter can be explained by the fact that the phase angle at the PCC is controlled. Due to the frequency droop characteristic, following the change of SCR, the active power injected to the grid decreases (see Fig. 2.12). This reduces the injected current to the grid, allowing the voltage to recover and thus leading to a higher dynamic limit of active power transfer capability compared to the grid-feeding converter. In the case of grid-feeding converter, where the phase angle is not controlled, the voltage depression is higher, since the converter tries to inject the pre-fault value of the active power. As a result, the dynamic limit of the active power transfer capability decreases, which in turn leads to the loss of synchronism of the grid-feeding converter (see Fig. 2.12.c). Thus, we can conclude that grid-supporting converters are preferable compared to

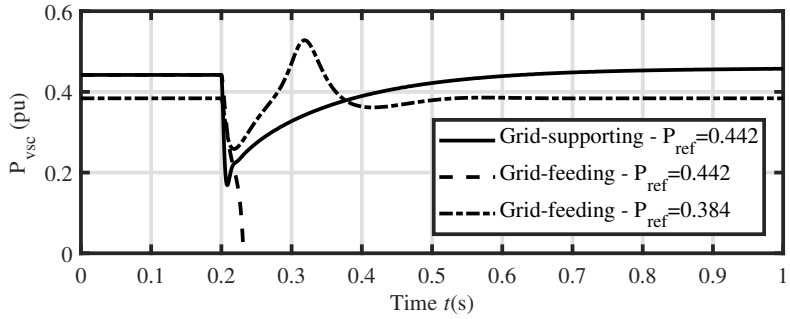

Figure 2.11: Dynamic limit of the maximum power transfer capability of grid-feeding VSC. Adapted from [**Pub. C**].

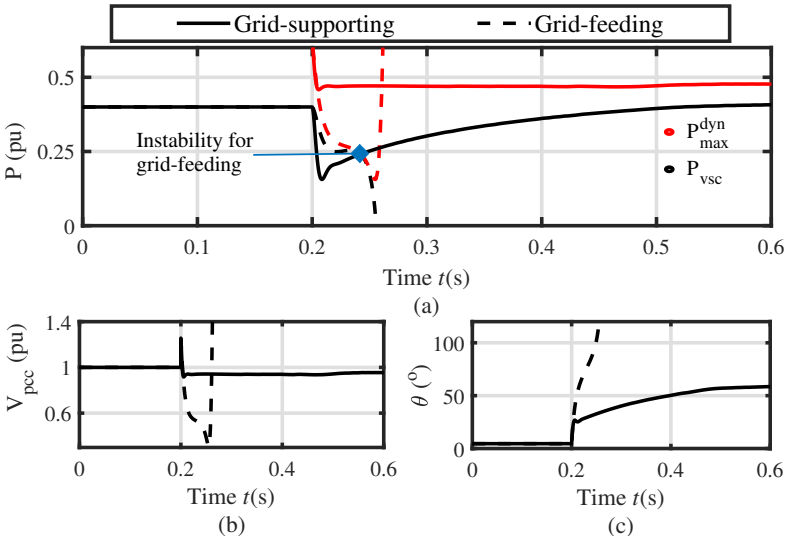

Figure 2.12: (a) Maximum power transfer capability $P_{\text{max}}^{\text{dyn}}$ (red) and VSC active power (black), (b) PCC voltage, (c) Phase angle at PCC. Adapted from [**Pub. C**].

grid-feeding converters during weak-grid conditions, since they are able to operate at lower SCRs.

2.3 The North Sea Wind Power Hub case

The North Sea Wind Power Hub (NSWPH) refers to an offshore system designed to facilitate the integration of large wind power to onshore, as well as increasing the transmission capacity for exchange power between the interconnected countries. One of the first questions that arises is whether point-to-point HVDC links or a multi-terminal HVDC grid option [73, 74] are preferable for connecting the offshore system to the shore. To answer this question, the operational reliability of a multi-terminal HVDC system needs to be taken into account, which depends on the ability of a HVDC circuit breaker to interrupt HVDC currents within several tens of milliseconds. Although, HVDC circuit breakers are available since 2012 [75], TSOs lack of experience regarding their operation (since no HVDC breakers have been installed in Europe, yet), as well as interest due to their high cost [76]. This makes the multiple point-to-point HVDC links the preferable configuration to link the offshore island to the onshore grids [21]. Hence, in this thesis multiple point-to-point HVDC connections are considered (see Fig. 2.13).

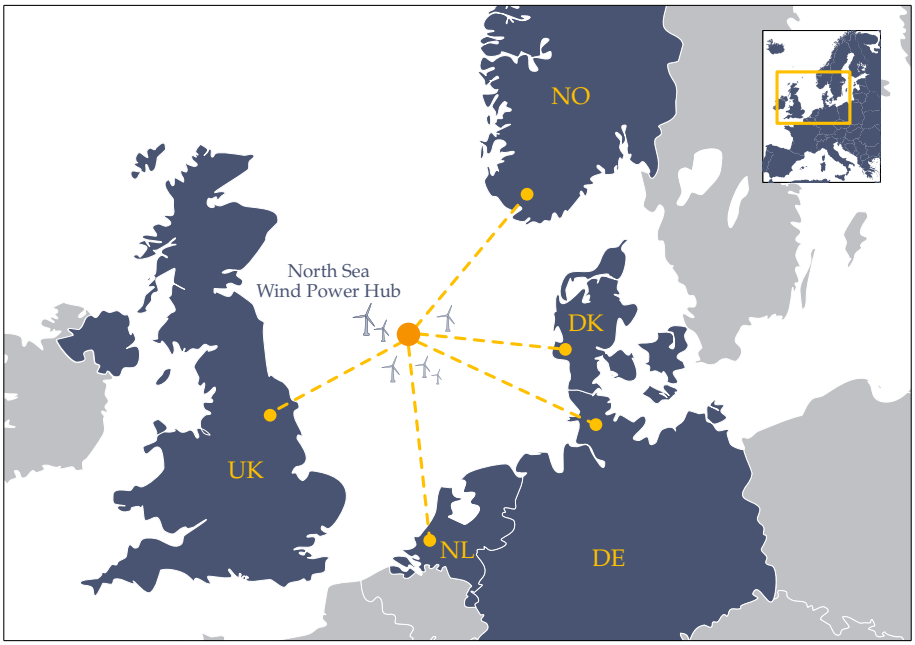

Figure 2.13: North Sea Wind Power Hub concept. Adapted from [**Pub. E**]

In this part of the thesis, we evaluate the influence of the operation mode of converters on the system dynamic performance using the NSPWH as test system. We consider two system configurations. The first one consists only of converter-based units and grid-forming converters for setting the frequency of the system, namely the zero-inertia configuration. The second configuration consists of synchronous condensers and grid-following converters for setting the system frequency, namely the low-inertia configuration. As we presented in Section 2.2, for low short circuit AC systems, grid-supporting converters are preferable as they present higher active power transfer capability compared to the grid-feeding converters. Thus, for the low-inertia configuration we consider that all the grid-following converters operate in grid-supporting mode. This part of the thesis summarizes the results presented in [**Pub. D**].

2.3.1 Low- vs zero-inertia configuration

Fig. 2.14 represents the two AC-hub configurations for the NSWPH system. They consist of multiple wind farms, AC cables connecting the wind farms with the offshore-island and multiple HVDC-links transmitting the generated wind power to the interconnected onshore grids.

Collection-grid & Wind farms

The AC collection grid and the wind farms are the same in both configurations. The wind turbines, which are in grid-following mode, operate in maximum power tracking mode and under unity power factor. Five wind farms, with a total installed capacity of 3.5 GW are connected to the island through 220 kV cables.

Onshore VSC control scheme

The control principles of the VSCs connected to the onshore AC grids are to provide constant reactive power to their corresponding PCC, and adjust the active power exchanged with the grid by controlling the DC voltage of the HVDC-link.

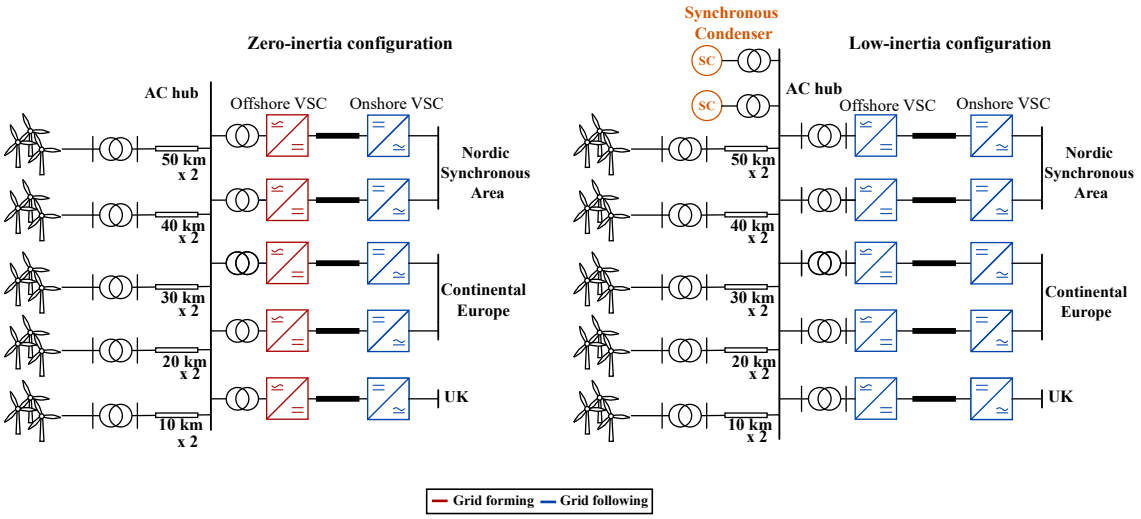

Figure 2.14: Zero-inertia (left) and low-inertia (right) configurations for NSWPH. Adapted from **[Pub. D]**.

Operating principles of low-inertia configuration

The low-inertia configuration combines the advantages of conventional generation and VSC technology, i.e. the use of synchronous-condenser and the grid-following converters respectively. The use of synchronous condenser is twofold: (i) its kinetic energy adds an energy buffer and (ii) the synchronous condenser sets the voltage at its PCC and its rotational speed sets the frequency on the island; thereby, it provides the frequency and voltage that the grid-following converters are synchronized to using their PLL device. The grid-following converters are synchronized with the imposed frequency by using a PLL device. The size of the synchronous condenser has been selected equal to 350 MVA so that the offshore system satisfies the N-1 criterion, in the event of single synchronous condenser outage **[Pub. D]**. Moreover, grid-following converters participate both in active power and reactive power regulation, i.e. grid-supporting mode, by employing a Pf and QV droop characteristics, respectively. The control structure of the offshore grid-following converter is depicted in Fig. 2.10. A secondary frequency controller with an integral action is employed, which resets the active power set-points of the grid-following converters after a disturbance and brings the steady-state frequency back to its nominal value. The full details regarding the design of the secondary frequency controller can be found in [77]. An eigenvalue analysis is provided in [77], in order to determine the control gains of the inner and outer control loops of the grid-following converters.

Operating principles of zero-inertia configuration

Unlike the low-inertia configuration, the offshore converters in the zero-inertia configuration operate in grid-forming mode [41], meaning that they impose the frequency and the AC voltage on the offshore AC grid. The basic control structure of grid-forming converter is depicted in Fig. 3.1. The main objectives is to distribute any active power imbalance among the offshore converters using a Pf droop characteristic. This operating principle is similar to the one employed by synchronous generators, except for the limited overload capability of the power electronic devices. A QV droop characteristic can also been employed for adjusting the reactive power exchanged between the offshore converters and the grid. Finally, the virtual impedance controller

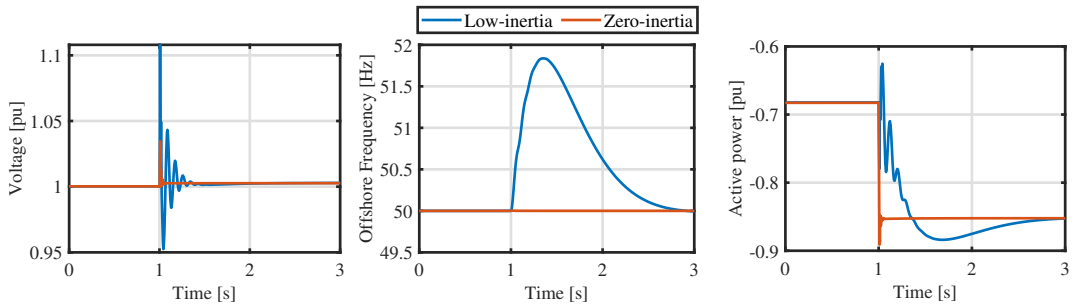

Figure 2.15: Offshore converter outage. Left figure: Voltage deviation at the AC-Hub, middle figure: Offshore frequency deviation and right figure: Active power absorbed by the offshore converters. Adapted from [**Pub. D**].

is tuned such that the eigenfrequencies in the offshore system are sufficiently damped. A secondary frequency controller with an integral action is employed, which resets the active power set-points of the grid-forming converters and brings the steady-state frequency back to its nominal value. The control parameters of the inner and outer control loops of the grid-forming converters have been taken from [78].

Time-domain simulation analysis

Following, we compare the two different configurations depicted in Fig. 2.14. We define three performance metrics, in order to evaluate the impact of the operation mode of the converters on the system performance, as well as the stability properties of the two configurations. The performance metrics are:

- How tight is the control of the voltage at the hub.
- How tight is the control of the frequency of the offshore system.
- How fast do disturbances propagate to the onshore grids.

We evaluate the performance metrics in the event of an offshore HVDC converter outage, i.e. HVDC converter trip. The aim is to illustrate their ability to maintain the voltage and power balance of the system.

Fig. 2.15 depicts the responses of the voltage (left figure), frequency (middle figure) and active power (right figure) in the event of a converter outage. Regarding the voltage trajectory, we can see that both configurations are able to control tightly the voltage with a small steady state deviation. In the case of zero-inertia configuration, it can observed that the voltage converges faster to the new equilibrium compared to the low-inertia configuration. Moreover, in both cases the voltage presents an oscillatory behavior. The frequency of these oscillations depends on the cable parameters, as well as the control parameters of the offshore converters. Regarding the frequency of oscillations, it can be seen that the frequency of oscillations is higher in the zero-inertia configuration, however the oscillations are damped out within few milliseconds. How well these oscillations are damped is primarily influenced by the damping resistor gain of the virtual impedance controller. In the low-inertia configuration, the frequency oscillations is lower and how well they are damped depends on the inner-loop control, as well as the PLL gains [79].

As for the frequency deviation, it can be seen that in the case of zero-inertia configuration, the offshore frequency can be controlled tighter, presenting an insignificant frequency nadir compared to the low-inertia configuration. This is due to the fact that small frequency droops are chosen in the active power control loop of the grid-forming converters (see Fig. 3.1), in order to ensure the small-signal stability of the system [78, 80–82]. However, due to the absence of inertia (zero-inertia configuration) the rate of change of active power is higher, which implies instantaneous disturbance propagation to the interconnected onshore grids. On the contrary, in the low-inertia configuration, due to the synchronous condenser and the kinetic energy stored in its rotating mass, the disturbance propagation is slower. This was realized by selecting a slower active power response with a small frequency droop value, which reduces the reaction of the grid-following converters to any large disturbances. Although, that increases the maximum frequency deviation in the offshore system, it allows for slower propagation of disturbances to the onshore grid. Thus we can infer that large disturbances occurring in the offshore system have less severe impact on the interconnected onshore grids.

2.3.2 Zero-inertia case: N-1 security & active power sharing

Having introduced two AC-hub configurations for the NSWPH, we now focus on the zero-inertia case and evaluate its reliability. We consider a converter outage in a system consisting only of converter-based resources and for an operation close to the limits. The objective of this part of the thesis is to develop an adaptive frequency droop-based controller that distributes the excess power based on the available headroom of the grid-forming converters. The reason why we investigate only the zero-inertia in this part of the thesis is based on the fact that grid-forming converters can experience synchronization instability during an overload period [4, 5, 50]. The authors in [5, 50] propose a localized control strategy based on dynamic virtual impedance controller in order to ensure that the grid-forming converter remains synchronized with the grid. While this approach works in a low-inertia power system, i.e. power system including a synchronous generator, it does not necessarily preserve the synchronization stability in a zero-inertia system. Thus, to tackle this problem, this thesis explores a centralized control strategy, namely an adaptive frequency droop-based controller. The proposed control strategy follows the concept of adaptive droop settings that have been previously proposed for multi-terminal DC systems [83–86], where the DC voltage droops are updated considering the available headroom of the converters and the active power is shared according to the DC voltage droops.

To this end, in [**Pub. E**], we propose a control algorithm that (i) updates the frequency droop values based on the available power headroom of the offshore converters that are equipped with frequency droop control and (ii) takes into account small-signal stability margins, the dynamic performance of the system, as well as the operational limits of the offshore converters.

Distribution of active power in case of a converter-outage

As in synchronous machines-based power systems, the relationship between the active power absorbed/injected at the PCC and the frequency imposed by an offshore grid-forming at steady-state condition can be described by the following equation:

$$P_i^* = P_i^{\text{ref}} + \frac{1}{k_{f_i}} \Delta\omega_i \tag{2.24}$$

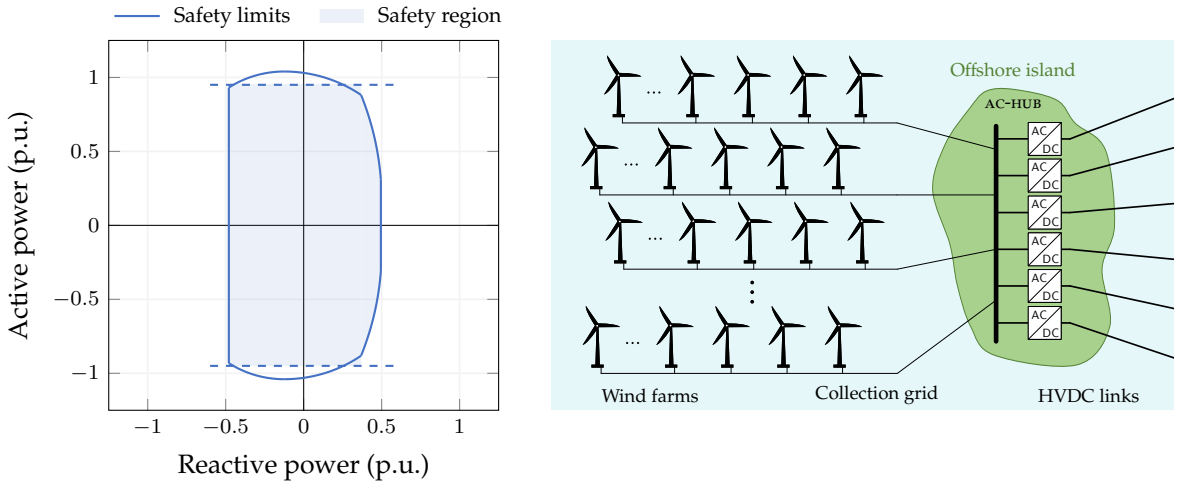

Figure 2.16: The left figure shows the PQ diagram of offshore VSCs [3]. On the y-axis, the active power output is limited based on the the maximum current the offshore converters can withstand. On the x-axis, reactive power limitations are driven by voltage constraints. To ensure that the converter can contribute to voltage control by adjusting its reactive power, the active power limit is set to 0.95 pu. The right figure depicts a representation of the zero-inertia configuration of NSWPH. Adapted from [**Pub. E**].

where the subscript i denotes the $i-th$ grid-forming offshore converter, k_{f_i} is the frequency droop gain, P_i^{ref} is the reference value of the active power and $\Delta\omega_i = \omega^{\text{ref}} - \omega_i$, with ω^{ref} the chosen reference frequency. The frequency deviation $\Delta\omega_i$ is equal to the deviation of the average frequency of the system $\Delta\omega$, i.e. $\Delta\omega_i = \Delta\omega$. The frequency deviation in case of the outage of converter k can be expressed as:

$$\Delta\omega = \frac{1}{\sum\limits_{i\neq k}\frac{1}{k_{f_i}}} P_k^{\text{ref}}. \tag{2.25}$$

where, the steady-state frequency deviation is inversely proportional to the sum of the inverse droop gains of the remaining grid-forming converters that are connected to the offshore grid. It follows that the active power injected/absorbed by the i-th grid-forming converter at the post-fault state is equal to:

$$P_i^* = P_i^{\text{ref}} + \frac{1}{k_{f_i}} \frac{1}{\sum\limits_{c\neq k}\frac{1}{k_{f_c}}} P_k^{\text{ref}}. \tag{2.26}$$

Optimization Problem - Selection of frequency droop values

To select appropriate values for the frequency droops (more precisely, their reciprocal $x_i = 1/k_{f_i}$) that ensure that the system is small-signal stable, transient stable and N-1 secure, we formulate the following optimization problem:

$$\min_x \quad \sum_{i=1}^{n-1}\sum_{c=i+1}^{n} |x_i - x_c| \tag{2.27a}$$

$$\text{s.t.} \quad \alpha = \sum_i x_i, \tag{2.27b}$$

$$x_i \geq \underline{X}_i, \qquad : \forall i \tag{2.27c}$$

$$\left| P_i + \frac{x_i}{\alpha - x_k} P_k \right| \leq \overline{P}_i^{\max}. \qquad : \forall i,\ \forall k \tag{2.27d}$$

where $x_i = \frac{1}{k_{f_i}}$. The goal of the optimization problem is to find a feasible set of droops values that guarantee that the active power remains within the operational limits of the converter. The term (2.27a) represents the sum of the distances between the droops. The aim is to find a set of droop gains that it is feasible and close to "equal droop gains". That implies that if there is no violation of the operational limits the frequency droop values will be equal. As it was presented in [**Pub. E**], equal droop values offer better dynamic system performance and reduce the maximum frequency deviation in the offshore system. The reader is referred to [**Pub. E**] for more details about the efficiency of frequency droop-based control in case of equal and different frequency droops. The term (2.27b) denotes the stiffness of the system ($\sum_i x_i$) and can be selected so that the maximum steady state deviation is kept below a certain threshold which can be determined by system operator of the offshore island. Moreover, (2.27c) ensures the small-signal stability of the system and appropriate damping of the eigenfrequencies of the offshore system. As it has been illustrated in several works [78, 80–82], too high values of frequency droops can lead the system to small-signal instability, which occurs due to the fact that higher frequency droop values increase the bandwidth of the active power controller and consequently the damping of resonances in the offshore system deteriorates. The term (2.27d) accounts for the available headroom of the converters at the pre-fault state and ensures safe post-fault operation of the system (see Fig. 2.16). In particular, when a converter operates close to its limit at a pre-fault state a higher frequency droop value (compared to the frequency droops of the other converters) has to be selected in order for the converter to participate less in the active power regulation.

The optimization problem (2.27) is nonlinear due to the constraints (2.27d). In [**Pub. E**], the (2.27) is formulated as a mixed-integer linear program, which can be solved with commercial and open-source MILP solvers (e.g. Gurobi, Mosek, etc). The formulation is omitted in this thesis for brevity and we refer the reader to the paper for more details.

Simulation and results

Following, we consider two simulation studies. In the first one, we verify the dynamic performance of the frequency droop-based controller and in the second one, we validate the N-1 criterion in case of a converter outage. For the former, we compare the system dynamic performance in terms of maximum frequency deviation with equal and different frequency droop gains, in order to highlight the improved performance with equal droops. For the latter, we highlight the need of adaptive frequency droops, in order to avoid saturation of converters and maintain the stability of the system and show that the proposed methodology is independent of the implemented current limiting strategy.

The test system considered for the validation represents an offshore power hub configuration for massive integration of offshore wind power and is depicted in Fig. 2.16. The system consists of 10 GW installed wind power, which is collected through cables to an offshore island where six point-to-point HVDC links transmit the power to the interconnected onshore grids. The rated power for the offshore converters is 1850 MVA. The dynamic simulations have been performed with DIgSILENT Powerfactory [87]. To define the operating point of the converters, a market model is used that represents the European electricity market in 2030. Figure 2.17 depicts the power flow during one day. For the dynamic simulations, we select the hour 3, which is considered as the most critical set of flows, since most of the offshore converters operate close to their limits.

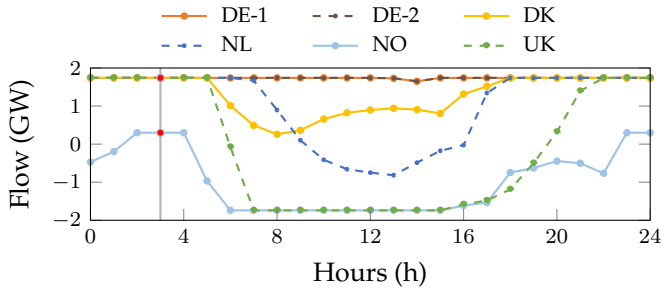

Figure 2.17: Flows over the HVDC interconnectors. Adapted from [**Pub. E**].

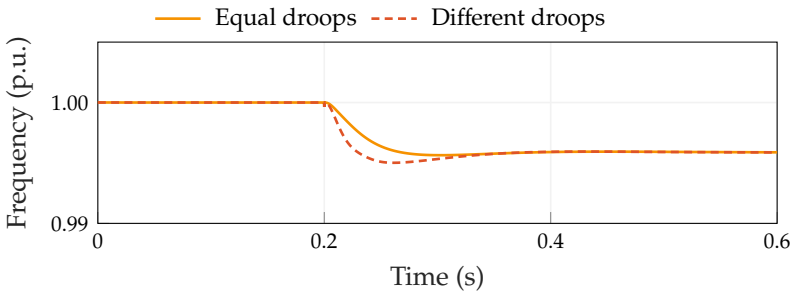

Figure 2.18: Average frequency deviation following a step decrease of wind power in case of equal and different droops. Adapted from [**Pub. E**].

In the first simulation, the effectiveness of equal droop settings is demonstrated. Figure 2.18 shows the frequency and active power deviations of the grid-forming converters occurring due to a step decrease of the wind active power by 250 MW. In both cases the stiffness of the system, defined as $\sum_i \frac{1}{k_{f_i}}$ is the same, i.e. $\alpha = 600$. We can see that in the case of different frequency droops, the maximum frequency deviation is higher compared to the case with equal droops. Thus, equal droops are preferable when the stiffness of the system is the same for both cases.

In the second simulation, the effectiveness of the proposed frequency controller is demonstrated with adaptive droop gains, updated based on the optimization problem presented in Section 2.3.2 everytime the HVDC set-points are changed. Moreover, two different current limiting controllers, presented respectively in [4] (d-axis current saturation control principle) and [5] (dynamic virtual impedance), are implemented. Figure 2.19 shows the system response to the trip of the converter connected to UK (1740 MW); for a better visualization, only the converters connected to NL and NO are displayed. During the first milliseconds after the outage, the power that was previously flowing to UK is redirected to the other converters. Once the converters are saturated, they lose synchronism and the system becomes unstable. This is due to the fact that the maximum active power transfer capability of converters decreases once the converters are saturated [4].

In the case of adaptive frequency droops, the active power initially absorbed by the converter at outage is directed towards the offshore converter with the largest available headroom at the pre-fault state. That “relieves" the offshore converters that were saturated immediately after the outage. Due to the adaptive frequency droops, there exists a stable equilibrium for every converter, since the active power at post-fault state is maintained within the operational limits of the converter and the inner current saturation is avoided. As shown in Figure 2.19, with the proposed control

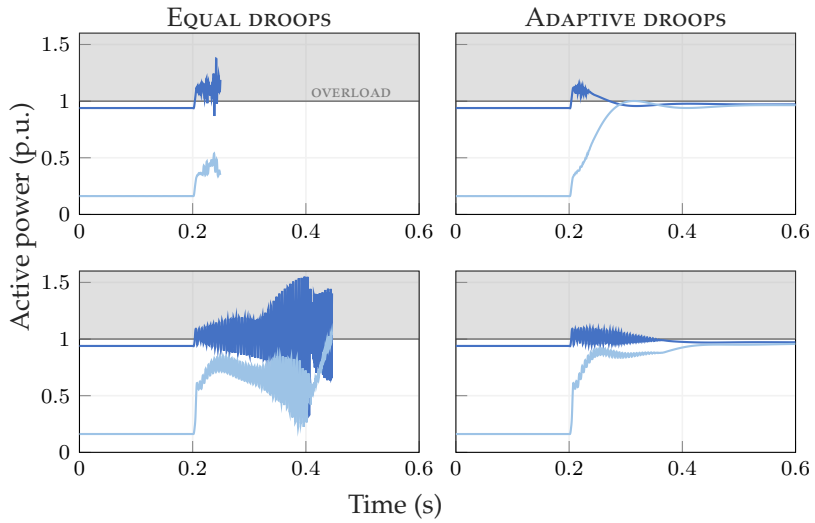

Figure 2.19: System response to an offshore converter outage. The two left figures show the power set-point of two remaining converters (NL and NO) with equal droops, while the two right figures are obtained with adaptive droops. In both cases, the two current limiting techniques in [4] (upper figures) and [5] (lower figures) are used with $I_{max} = 1.1$ pu. The overload region is represented with the gray area. Adapted from **[Pub. E]**.

methodology, we can distribute any power imbalance based on the available headroom of the converters, ensure N-1 security and preserve the stability of the system.

2.4 Remarks

The contributions presented in this chapter concern control designs and mitigation strategies that enable the secure integration of high share of RES into the power system.

Secure integration of RES begins from mitigating the impact of low-inertia inertia levels on frequency stability. To tackle this problem, we proposed two mitigation strategies. In **[Pub. A]**, we develop a robust frequency controller based on H_∞ loop-shaping procedure that optimize the control parameters of active power regulating units while taking into the time-varying profile of the system inertia. This results showed that with the proposed frequency control, the ROCOF and the frequency nadir can be reduced during low-inertia periods in the power grid. In **[Pub. B]**, we derived frequency-related constraints, namely ROCOF, frequency nadir and steady state frequency deviation from a system frequency response model describing the center of inertia frequencies of two asynchronous areas that are interconnected through HVDC links. By including the frequency-related constraints in the UCP, we allow for the exchange of primary frequency reserves between asynchronous areas, while maintaining the frequency stability in both AC systems. The contributions of this work are twofold: (i) maintain the frequency stability of neighboring AC systems at all times (during low- and high-inertia periods) and (ii) reduce the cost of reserve procurement by up to 10%.

Considering that converters are called to participate in grid-supporting services, we study in **[Pub. C]** the impact of different operation modes, namely grid-feeding and grid-supporting converters on the dynamic limit of the active power transfer capability. The results show that with grid-supporting VSCs, we can increase the maximum active power transfer capability of the VSC during low SCR periods. The is due to the inclusion of a Pf characteristic in the outer loop of the

active power controller of the grid-following converter. This allows to regulate the angle at the PCC and enhance the synchronization stability of the converter during small and large disturbances. In [**Pub. D**], we further investigate the impact of the operation modes of the converters on the system dynamic performance by comparing a grid-forming VSC with an alternative grid-forming pair, consisting of a synchronous condenser and a grid-following converter. The results suggest that the grid-forming converter can improve the frequency stability of the system by providing fast active power regulation. However, any power imbalances in the system propagate instantaneously. As for the alternative grid-forming pair, the synchronous condenser provides an energy buffer due to the kinetic energy stored in its rotating mass. This results in slower disturbance propagation in the system, but inevitably larger frequency deviations in the AC system.

Finally, since grid-forming converters are expected to play a vital role on ensuring the secure operation of future power systems, we evaluate in [**Pub. E**] the transient stability of a zero-inertia system, i.e. a system "formed" by multiple grid-forming converters. Our results show that in an overload event, the zero-inertia system is transiently unstable. The transient instability is caused due to the current-saturation of the grid-forming converters, which in turn results in a loss of synchronism. To tackle this problem, we propose a control strategy based on adaptive frequency droops. An optimization problem is set-up, which calculates the frequency droop gains based on the available headroom of the converters when there is an update on their operating point. This results in avoiding the current-saturation of the grid-forming converter in an event of a contingency and ensuring the N-1 criterion.

CHAPTER 3

Dynamic security assessment in future power systems

In this chapter, we address challenges arising when performing dynamic security assessment of power systems with high-penetration of converter-based resources. We focus on two approaches for accelerating the dynamic security assessment process while ensuring safe system operation. The first approach aims at characterizing the appropriateness of RMS modeling for monitoring the active power injection of converter-based resources. Conditions for the control gains of such devices are derived, in order to minimize the error between their RMS and EMT models. In the second approach, we propose physics-informed neural networks for predicting solutions to the set of differential equations which describe the converter dynamics. This allows to compute the power system dynamic behaviour at a fraction of the computational time compared to simulation of the full model, while maintaining high accuracy.

3.1 RMS modeling for monitoring power balance

With power systems undergoing a transformation towards carbon-free electricity generation, numerous converter-based generation units will replace synchronous generators. To ensure the secure integration of converter-based resources in the power grid, adequate simulation models are required for modeling the power injection in frequency stability analysis. There are two type of simulation models that are used by TSOs for performing time-domain simulation analysis. These are RMS and EMT models for the components. While EMT models are accurate, they are not suitable for large-scale studies due to the very small time-step ($t_s \leq 50\mu s$) required to compute the state variables of the system. On the other hand, RMS models neglect the electro-magnetic transients and capture only the slower dynamics. Consequently, RMS models make use of a larger time-step, thereby reducing computational effort and are suitable when it comes to large-scale time-domain analysis. However, that comes at the expense of reduced model accuracy for computing the evolution of the state variables.

Although the use of EMT modeling of power electronic devices looks inevitable for capturing their fast dynamics, their RMS models could still be used for a set of different type of disturbances, e.g. monitoring the power balance for frequency stability analysis. Appropriateness of RMS modeling can be thought of as answering the question whether a particular model reduction, such as neglecting the electromagnetic dynamics, can give a qualitatively good approximation of the full-detailed model, i.e. EMT model. To answer this question, we need to understand the factors that influence the mismatch between the two models and if possible to provide mathematical expressions characterizing the appropriateness of this model reduction.

Studies have been performed which demonstrate the limitation of the RMS model of a grid-forming converter to capture small-signal instability phenomena related to the tuning of the outer control

loops of the converter [27, 28]. The RMS model underestimates the coupling between the voltage and angle dynamics due to the higher resistance, which leads to an inaccurate assessment of stability boundaries. However, the studies do not present any analysis on the control parameters of grid-forming converters which can be selected, so that the RMS exactly matches the system response determined by the EMT model. Such a study is performed in [88]. However, the authors only investigate a particular type of grid-forming converter, namely dispatchable virtual oscillator control and omit the analysis for other types of grid-forming schemes. To this end in [**Pub. F**], we propose a control strategy for the two most commonly used types of grid-forming converters, namely power synchronization loop and virtual synchronous machine, that renders their RMS model appropriate for monitoring its power exchange with the grid.

3.1.1 RMS & EMT power system modeling

The system of Differential and Algebraic Equations (DAEs) for EMT modelling is described as follows:

$$\dot{\boldsymbol{x}} = \boldsymbol{f}(\boldsymbol{x}, \boldsymbol{y}, \boldsymbol{z}, \boldsymbol{u}) \tag{3.1a}$$

$$\dot{\boldsymbol{z}} = \boldsymbol{h}(\boldsymbol{x}, \boldsymbol{y}, \boldsymbol{z}) \tag{3.1b}$$

$$\boldsymbol{0} = \boldsymbol{g}(\boldsymbol{x}, \boldsymbol{y}, \boldsymbol{z}, \boldsymbol{u}) \tag{3.1c}$$

where (3.1a) is the set of the differential equations $\boldsymbol{f}$ describing the dynamics of all the components and controllers in the system except for the RLC components of the network. The network dynamics of the RLC components are described by the differential equations $\boldsymbol{h}$ in (3.1b). The algebraic equations $\boldsymbol{g}$ of the system are stated in (3.1c).

The difference between EMT modelling and RMS modeling is that in the RMS model only the slower dynamics are captured and the fast network and control dynamics are neglected [89]. Consequently, in the RMS model the differential equations $\boldsymbol{h}$ describing the dynamics of the RLC components and fast controllers are converted into algebraic equations by setting $\dot{\boldsymbol{z}}$ equal to zero. To this end, the system of DAEs for RMS modelling is as follows:

$$\dot{\boldsymbol{x}} = \boldsymbol{f}(\boldsymbol{x}, \boldsymbol{y}, \boldsymbol{z}, \boldsymbol{u}) \tag{3.1d}$$

$$\boldsymbol{0} = \boldsymbol{h}(\boldsymbol{x}, \boldsymbol{y}, \boldsymbol{z}) \tag{3.1e}$$

$$\boldsymbol{0} = \boldsymbol{g}(\boldsymbol{x}, \boldsymbol{y}, \boldsymbol{z}, \boldsymbol{u}). \tag{3.1f}$$

3.1.2 Grid-forming converters

Grid-forming converters act as a controlled voltage source, where the magnitude of the voltage and the phase angle are adjusted, in order to maintain the reactive and active power balance in the system. Figure 3.1 depicts the control structure of a grid-forming converter. The main control elements of a grid-forming converters are the outer-loop, which consists of Pf and QV droop characteristics and the inner loop which is used in order to control tightly the current and saturate the converter in the event of a large disturbance. A virtual impedance controller [81] is also included for improving the damping ratio of modes associated with electromagnetic dynamics in the system, e.g. the poorly damped resonance at nominal frequency. The inner loop is designed based on the switching frequency of the converter, so that a fast inner current and voltage control can be realized. The tuning procedure followed for selecting the control parameters of the inner

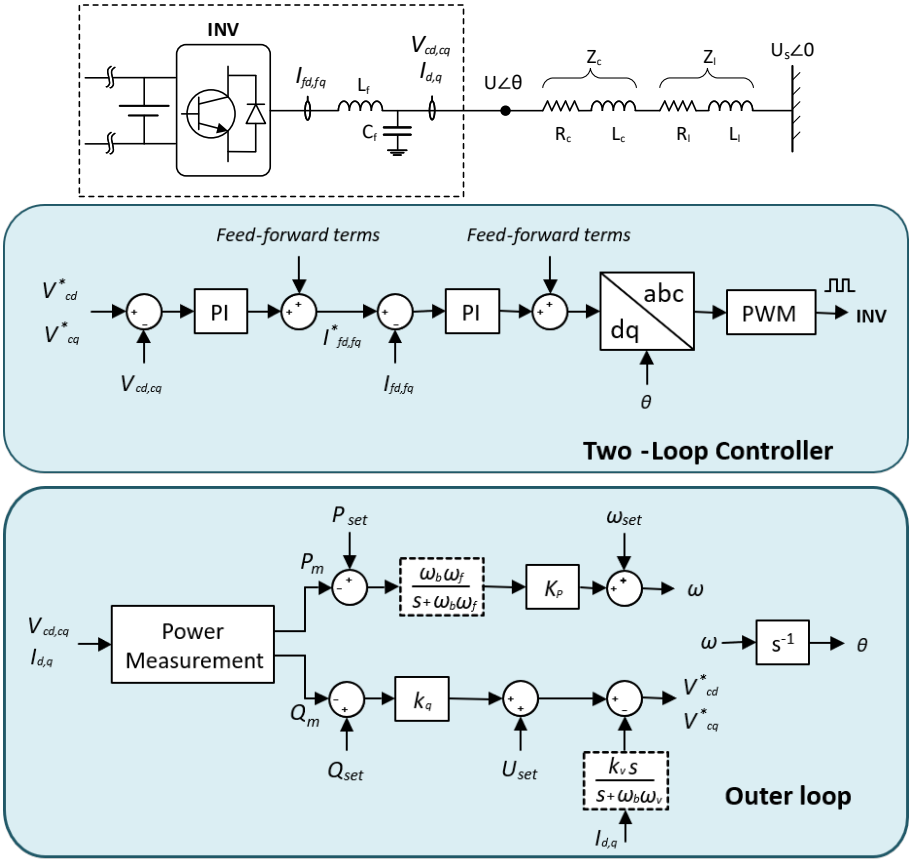

Figure 3.1: Control structure of grid forming converter. The dashed blocks in the outer control loop are either considered or disregarded. The low-pass filter on the active power is disregarded in the case of the power synchronization loop. The active damping controller $\frac{k_v s}{s+\omega_b\omega_v}$ can be disregarded in the case of the virtual synchronous generator. Adapted from [**Pub. F**].

loop is similar to the one presented in [90]. This allows for a time-scale separation between the grid-forming converter inner control and outer control loops. Similar time-scale separation has been observed with the inner gains proposed in [78, 91, 92]. This allows for independent tuning of inner and outer control gains [28]. It also enables to study only the impact of the network line dynamics on the outer loop control gains. Therefore, the control dynamics presented in this section only concern the outer control loops. Another reason for only investigating the outer control loops of the converters is that TSOs can usually only determine the converters control gains that are associated with the active and reactive power control; and they do not have information about the inner control loop design procedure followed by the vendors.

Based on the outer control loop modulation, we can define two different grid-forming schemes, namely the Power Synchronization Loop (PSL) [45] and the Virtual Synchronous Generator (VSG) [92], which are the two very commonly used grid-forming schemes. Each of these schemes requires different control tuning in order for the system to be stable and to limit the mismatch between the RMS and EMT models. Figure 3.2 and Fig. 3.3 show a comparison between the RMS and EMT models of the PSL and VSG control schemes, respectively. The left figures show the eigenvalues of the system and the right figures the active power exchanged between the converter and the grid. Each row of the figures correspond to different control gains (increase of the bandwidth of the active power controller from top to bottom). As it can be seen, based on the selected control

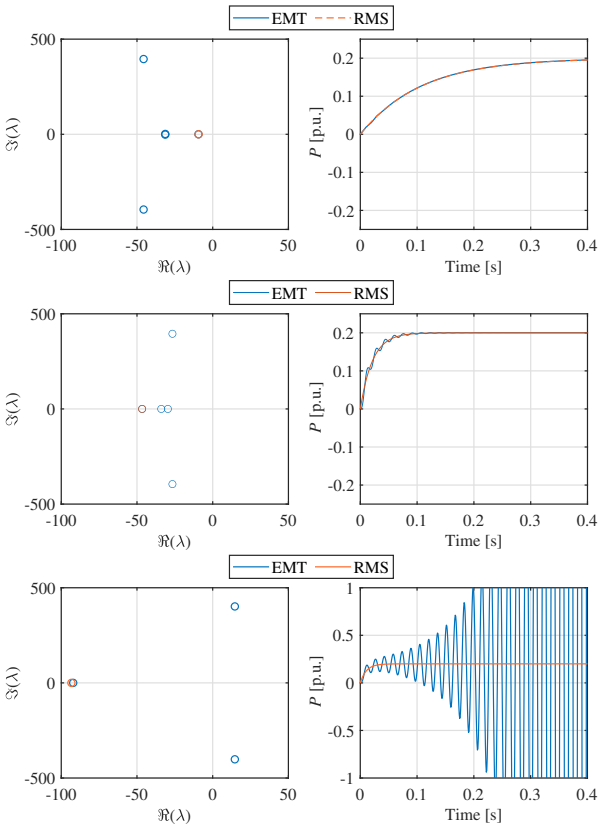

Figure 3.2: Power synchronization loop - Comparison between RMS and EMT models. Left figure: Eigenvalue analysis. Right figure: Trajectory of active power response. In the bottom right figure, the RMS model predicts that the system is stable whereas the EMT model shows that the system is unstable. Each row of the figures correspond to different control gains (increase of the bandwidth of the active power controller from top to bottom). High bandwidth of the active power controller deteriorates the converter stability and increases the mismatch between the RMS and EMT model.

gains, the mismatch between the RMS and EMT models of the grid-forming converters can either increase or decrease. In the worst case (bottom figures in Fig. 3.2 and Fig. 3.3), the RMS model can show that the system is stable, when in fact it is not (see also bottom left figures in Fig. 3.2 and Fig. 3.3 - the eigenvalues of the system lies in the right half plane). The instability is caused due to the increased bandwidth of the active power controller and not utilizing the active damping controller ($k_v = 0$, see Fig. 3.1). Thus, the mismatch between the two models depends on: (i) how well damped are the unobserved modes (modes that cannot be observed by the RMS model) and (ii) how well the common modes of the RMS and EMT models match.

3.1.3 Control tuning of grid-forming converters

Considering the significant influence of the control parameters on the appropriateness of RMS modeling of grid-forming converters, we present a control strategy that renders the use of the RMS model of a grid-forming converter appropriate. Figure 3.4 shows an illustrative example for the stability regions determined by the RMS and EMT models of the grid-forming converters. R_1 is a stable region of the system. Selecting the control parameters of the converter within this region will limit the error between the RMS and EMT models, i.e. the two models provide almost the same numerical solutions for slow state variables of the converter. R_2 represents a stable

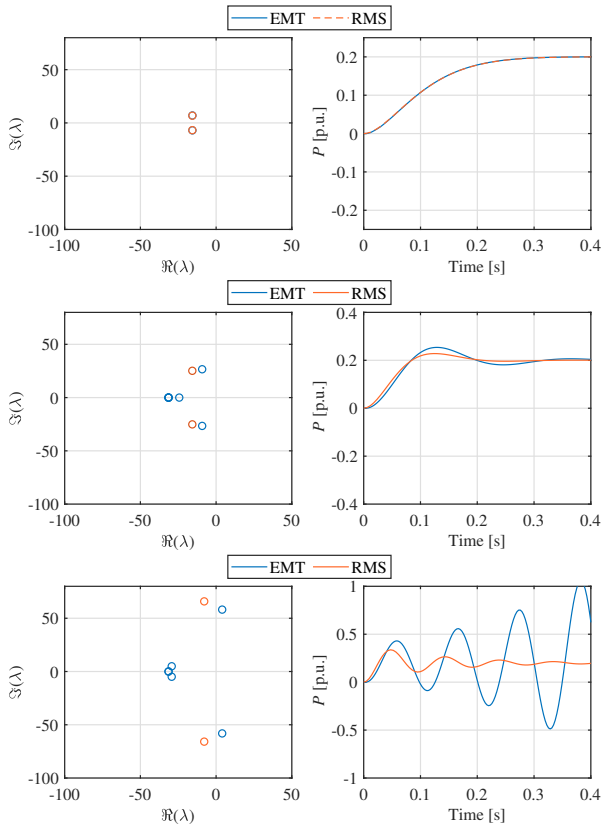

Figure 3.3: Virtual synchronous generator - Comparison between RMS and EMT models. Left figure: Eigenvalue analysis. Right figure: Trajectory of active power response. In the bottom right figure, the RMS model predicts that the system is stable whereas the EMT model shows that the system is unstable. Each row of the figures correspond to different control gains (increase of the bandwidth of the active power controller from top to bottom). High bandwidth of the active power controller deteriorates the converter stability and increases the mismatch between the RMS and EMT model.

region of the system. If the control parameters are inside this region, then both models show that the system is stable, however the mismatch between the RMS and EMT models increases. Finally, R_3 represents a region, in which the system is unstable. The instability can be observed in time-domain simulations only when the EMT model of the converter is used (see bottom right figures in Fig. 3.2 and Fig. 3.3).

The aim is to derive sufficient conditions for selecting the control parameters of the converters within the stable region R_1. The conditions have to account for the different X/R ratio of the transmission line and the SCR. Moreover, they need to ensure that the predicted response provided by the RMS and EMT models matches and the impact of the fast dynamics on slower dynamics of the system is limited (acceptable accuracy of the reduced order model, i.e. RMS model). There are two key-points to consider, so that the mismatch between the RMS and EMT models is minimized:

- The stability of the grid-forming converters, as well as the appropriateness of RMS modeling are highly affected by how well-damped the line resonance is. The higher is the bandwidth of the active power loop, the smaller becomes the damping of the mode associated with the line resonance [81].

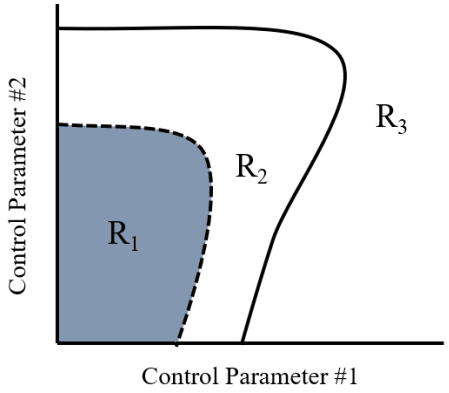

Figure 3.4: R_1 represents a region for the control parameters of the converters, in which the error between the RMS and EMT models is limited. R_2 represents a region for the control parameters in which the error between the RMS and EMT increases. R_3 represents the unstable region of the system determined by the EMT model. The goal is to select control parameters from the blue area. The region R_1 is defined based on the following remarks: (i) the gain crossover frequency is 10 times less than the nominal frequency and (ii) the gain margin of the open loop system of the active power controller is higher than 10. Based on the remarks the parameters of the outer control loop are tuned accordingly.

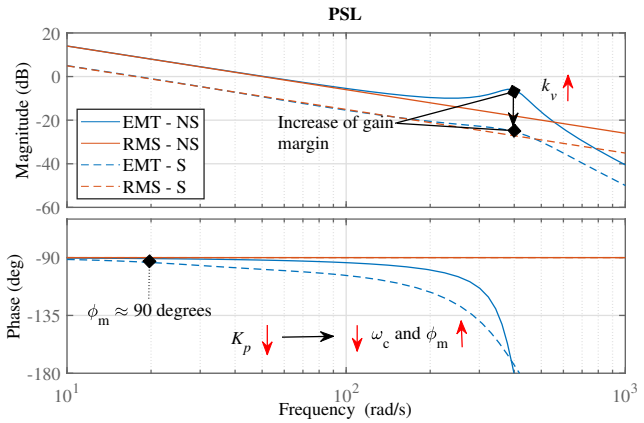

Figure 3.5: PSL: Bodeplot of the open loop system of the active power controller. The solid line corresponds to the case, where the control parameters are within the region R_2 (see Fig. 3.4), while the dashed lines corresponds to the case, where the control parameters are selected so that the mismatch between the RMS and EMT modes is minimized. NS implies that the control parameters are outside the region R_1 and S are selected from the blue area.

- The virtual impedance controller improves the damping of the mode associated with the line resonance. However, it has a negative effect on the phase margin of the open loop system that needs to be taken into account when tuning the frequency droop. The virtual impedance controller acts as an additive resistance to the line, which leads to a decrease of the X/R ratio. A decrease of the X/R ratio results in higher coupling between the angle and voltage dynamics, which in turn deteriorates the stability margins of the system [28].

In **[Pub. F]**, we provide sufficient conditions for the control parameters of grid-forming converters, using a loop-shaping design procedure [68] for the active power controller of the two grid-

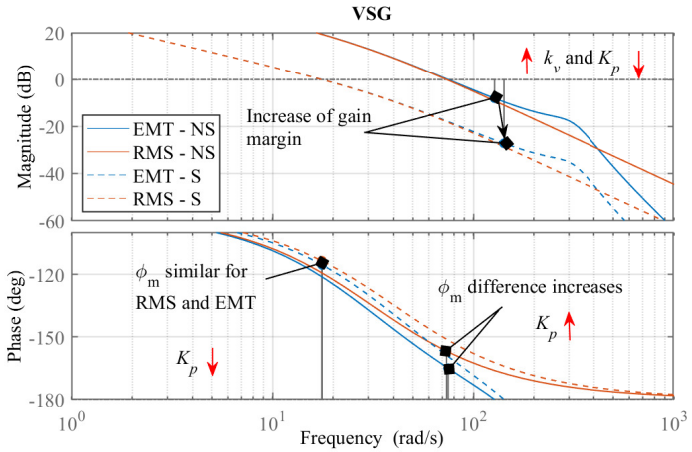

Figure 3.6: VSG: Bodeplot of the open loop system of the active power controller. The solid line corresponds to the case, where the control parameters are within the region R_2 (see Fig. 3.4), while the dashed lines corresponds to the case, where the control parameters are selected so that the mismatch between the RMS and EMT modes is minimized. NS implies that the control parameters are outside the region R_1 and S are selected from the blue area.

forming schemes. Figure 3.5 shows the bode plot of the open loop system in the case of the power synchronization control scheme. The solid line corresponds to the case, where the control parameters are arbitrarily selected, while the dashed lines correspond to the case, where the control parameters are selected so that the mismatch between the RMS and EMT modes is minimized. The figure shows that by increasing the damping resistor gain k_v (see Fig. 3.1) and decreasing the frequency droop K_p, we can increase the damping at higher frequencies and decrease the value of the gain crossover frequency ω_c, respectively. An increase of the damping at higher frequencies limits the impact of eigenfrequencies on the active power signal. A decrease of the gain crossover frequency results in an increase of the phase margin of the open loop system. Considering that the phase of the open loop system of the RMS model is constant and equal to 90^o degrees, we want the phase margin of the open loop system of the EMT model to be as close to 90^o degrees as possible. This allows for the common eigenvalues of the two models to be the same. Figure 3.6 shows the bode plot of the open loop system in the case of the virtual synchronous generator control scheme. Compared to the power synchronization loop, the main difference is in the phase margin. Particularly, the higher is the gain crossover frequency, i.e. higher bandwidth of the active power controller, the higher is the difference in the phase margin of the open loop system of the two models (see also Fig. 3.3). By reducing the frequency droop value, the gain crossover frequency becomes smaller and the phase margin of the open loop system of the models more similar. This also allows for the common eigenvalues of the two models to be the same. By taking into consideration the following, the sufficient conditions presented in [**Pub. F**], allows for limited mismatch between the RMS and EMT models.

- limiting the gain crossover frequency [68] so that it is ten time less than the nominal frequency of the power system, i.e. limit the bandwidth of the active power controller. This can be achieved by enforcing an upper bound on the control parameters of the outer control loops,

- ensuring that the phase margin of the RMS and EMT models is similar. This renders that the common modes/eigenvalues of the two models are the same,

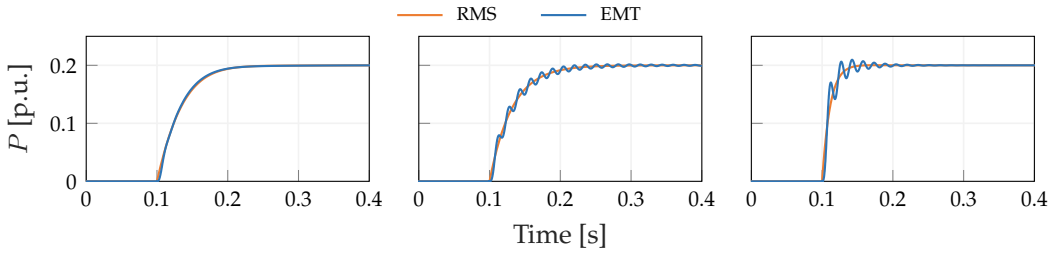

Figure 3.7: Active power response of power synchronization loop. Left figure: Case 1, Middle figure: Case 2, Right figure: Case 3. Adapted from [**Pub. F**].

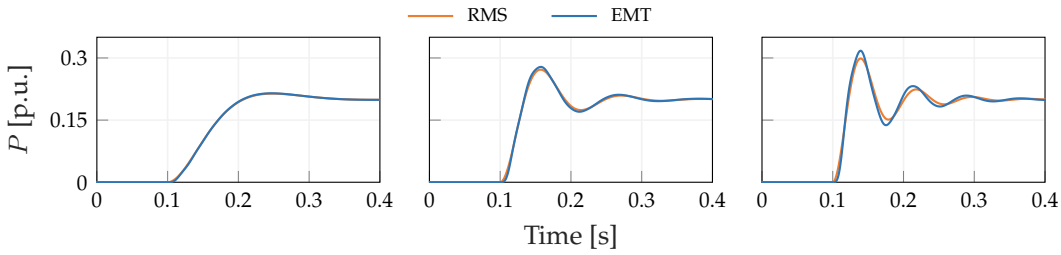

Figure 3.8: Active power response of virtual synchronous generator. Left figure: Case 1, Middle figure: Case 2, Right figure: Case 3. Adapted from [**Pub. F**].

- tuning the virtual impedance controller and the damping resistor gain k_v (see Fig. 3.1), in order to increase the damping of the line resonance, i.e. increase the gain margin of the open loop system,

Finally, considering that the grid-forming converter is subject to different X/R ratios and SCR, a gain scheduling of the control parameters can be realized. This means that the control parameters can be updated based on the available information about the equivalent grid impedance, i.e. equivalent impedance between the converter and the grid.

3.1.4 Simulation & Results

We evaluate the validity of the derived conditions both for the power synchronization loop and virtual synchronous generator control schemes. For the analysis two system topologies were considered, in which we simulate the following events:

- Step change of the active power set-point of the grid-forming converter.

- Line trip, i.e. change of SCR, where we evaluate the ability of the converter to operate in low short circuit systems.

- Generation outage, where we evaluate the inertia and frequency support provided by the converter.

Change of active power set-point

Fig. 3.7 and Fig. 3.8 show the evolution of the active power signal for a step change of the active power set-point in the case of PSL and VSG schemes, respectively. For the PSL, we consider the following three cases:

- Control parameters have been selected based on the sufficient conditions presented in [**Pub. F**] (control parameters lie in R_1, see Fig. 3.4).
- No virtual impedance control is considered. However the bandwidth of the active power controller is limited so that the gain crossover frequency is 10 times less the nominal frequency (control parameters lie in R_2, see Fig. 3.4).
- The bandwidth of the active power controller approaches the nominal frequency of the power system (control parameters lie in R_2, see Fig. 3.4).

For the VSG, we consider the following three cases:

- Control parameters have been selected based on the sufficient conditions presented in [**Pub. F**] (control parameters lie in R_1, see Fig. 3.4).
- Increase of the active power controller's bandwidth, while keeping the inertia effect constant (control parameters lie in R_2, see Fig. 3.4).
- Further increase of the active power controller's bandwidth, by means of increasing the frequency droop (control parameters lie in R_2, see Fig. 3.4).

As it can be seen in Fig. 3.7 and Fig. 3.8 (left figures), when the control parameters are selected based on the sufficient conditions presented in [**Pub. F**], the mismatch between the RMS and EMT models decreases. By increasing the bandwidth of the active power controller or decreasing the damping resistor gain k_v, we can see that the mismatch between the RMS and EMT models increases. In particular, for the PSL we can see that higher frequency oscillations appear on the active power signal. The frequency of these oscillations is around 50 Hz, which indicates that a higher bandwidth of the active power controller or a lower damping resistor gain result in a lower damping ratio of the mode associated with the line resonance. As for the VSG, by increasing the active power controller's bandwidth, it can be seen that the phase difference between the active power signal predicted by the RMS and EMT models increases. Finally, it can be seen that when the control parameters lie in region R_2, the RMS model underestimates the oscillation behavior (in the case of the power synchronization loop) and the maximum deviation of the active power (in the case of the virtual synchronous generator) given a change of the active power set-point.

Line-trip

To further validate the sufficiency of the control design proposed in [**Pub. F**], we consider an event of a line trip, simulated as a sudden drop of the SCR from 3 to 1, i.e. increase of the equivalent grid impedance. We want to show the effect of the active damping controller on the appropriateness of the RMS model. Figure 3.10 and Fig. 3.11 depict the trajectory of the active power exchanged with the grid, in the case of the PSL and VSG, respectively. In the left figure, the simulation is performed with a small value of k_v, while in the right figure a higher value of k_v is considered. As described

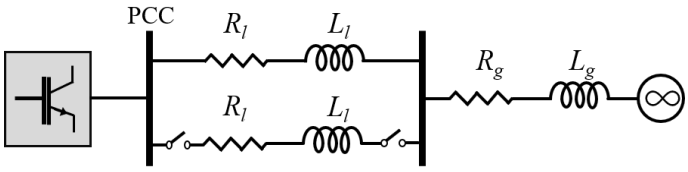

Figure 3.9: Test system containing a single-line diagram of a converter connected to an infinite bus via two parallel transmission lines. Adapted from [**Pub. F**].

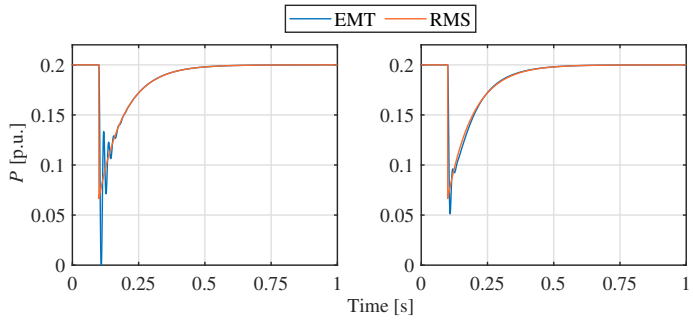

Figure 3.10: Trajectory of the active power signal for a sudden drop of the SCR from 3 to 1 - Power synchronization loop. In the left figure the value of k_v = 0.1333 and in the right k_v=0.4. Adapted from [**Pub. F**].

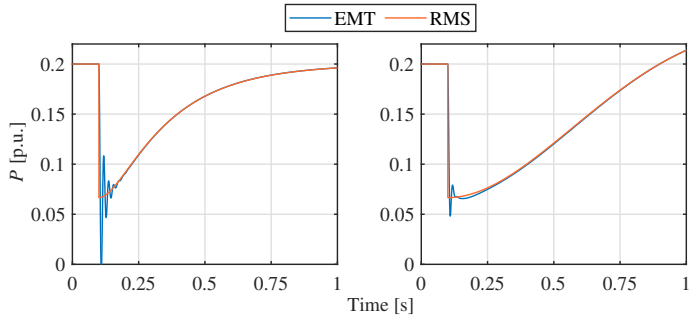

Figure 3.11: Trajectory of the active power signal for a sudden drop of the SCR from 3 to 1 - Virtual synchronous generator. In the left figure the value of k_v = 0.1333 and in the right k_v=0.4. Adapted from [**Pub. F**].

in [**Pub. F**], a small value of k_v results in a worse damping ratio of the mode associated with the line resonance. This results in the appearance of high frequency oscillations on the active power signal. By increasing the value of k_v, we virtually increase the resistance of the line, which in turns improves the damping ratio of the mode associated with the line resonance. As it can be seen in both Fig. 3.10 and Fig. 3.11, this results in smaller mismatch between the RMS and EMT models, rendering the RMS appropriate for simulating changes in grid topology.

Multi-converter topology

To validate the sufficiency of the derived conditions presented in [**Pub. F**] in case of nearby connections of grid-forming converters, we consider the test system shown in Fig. 3.12. We consider the occurrence of two events. The first one is a line outage happening at $t = 0.1s$ and the

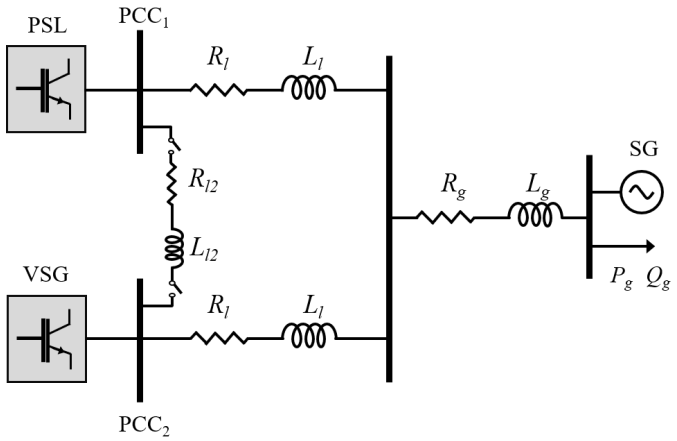

Figure 3.12: Test system containing a single-line diagram of two grid-forming converters, one using Power Synchronization Loop (PSL) active power control and the other the Virtual Synchronous Generator (VSG). The grid-forming converters are connected to an equivalent variable frequency AC grid and a load. Adapted from **[Pub. F]**.

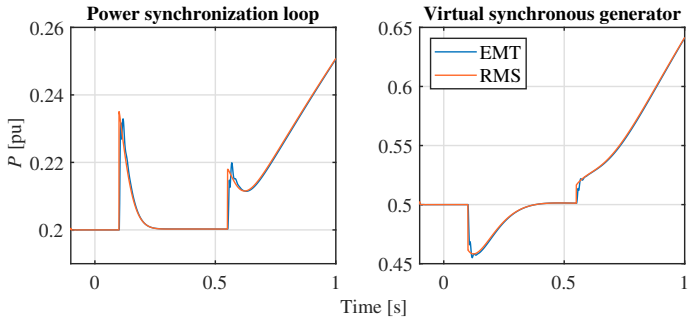

Figure 3.13: Trajectory of the active power signal of the two converters. Adapted from **[Pub. F]**.

second one a generation loss equal to 1000 MW happening at $t = 0.55s$. As it can be seen from the Fig 3.13, the RMS and EMT models provide almost identical results for the active power exchanged between the converters and the grid. This comes to show that with the proposed control tuning, there are no interactions occurring between the grid-forming converters, which would be related to poorly damped modes associated with fast dynamics, i.e. modes that cannot be captured when using the RMS model. This is due to: (i) the bandwidth of the active power controller is limited, which results in not exciting eigenfrequencies of the grid and (ii) the virtual impedance controller that acts as an additive resistance and results in better damping of high frequency oscillations.

To summarize the results of this section, we show that by appropriate tuning of the control parameters, we can limit the excitation of eigenfrequencies in the network and provide better damping of high frequency oscillations. This renders the RMS model appropriate for simulating the power balance in the system in events such as: (i) change of active power set-point of the converter, (ii) change of the grid topology and (iii) loss of generation, i.e. large active power disturbances.

3.2 Physics-informed neural networks

In the previous section, we evaluated the appropriateness of RMS modeling of grid-forming converters, as they are expected to play a vital role in the power balance stability of future power

systems. This was done, in order to allow the use of simulation tools of low computational complexity when performing dynamic security assessment of a power system. In this section, by making use of research advancements in machine learning, we explore an alternative approach that will enable system operators to perform fast dynamic security assessment of power systems based on time-domain simulation analysis.

Existing approaches in the literature focus on using neural networks as a mathematical model for predicting solutions to a system of differential equations [53–55]. After appropriate training they can solve computational problems at a fraction of the time required by traditional approaches. However, their main limitations are that their accuracy is highly influenced by the quality and amount of data and they offer limited interpretability. Despite the effort of researchers to efficiently generate data that improve the accuracy of these methods [93, 94], the main drawback of being agnostic to the underlying physical model still remains.

Taking that into consideration, in **[Pub. G]** we propose physics-informed neural networks, which reduce the dependency on training data by exploiting during the training process the underlying physical laws described by power system models.

3.2.1 Neural networks for predicting solutions to differential equations

To understand physics-informed neural networks, we first provide the general concept of using feed-forward neural networks for predicting solutions to a system of differential equations, which was first introduced in [95]. Consider the following system of differential equations

$$\dot{\boldsymbol{x}} = \boldsymbol{f}(\boldsymbol{x}, \boldsymbol{y}, \boldsymbol{u}), \tag{3.2}$$

$$\boldsymbol{0} = \boldsymbol{g}(\boldsymbol{x}, \boldsymbol{y}, \boldsymbol{u}), \tag{3.3}$$

where $\boldsymbol{x}$, $\boldsymbol{y}$ and $\boldsymbol{u}$ are the state, algebraic and input variables, respectively. A solution of this system of differential equations is a function of the initial conditions of the state $\boldsymbol{x}_0$ and algebraic $\boldsymbol{y}_0$ variables, the input variables $\boldsymbol{u}$ and the time t, and be expressed as follows:

$$\boldsymbol{x} = \boldsymbol{h}(t, \boldsymbol{u}, \boldsymbol{x}_0, \boldsymbol{y}_0) \approx \mathrm{NN}(t, \boldsymbol{u}, \boldsymbol{x}_0, \boldsymbol{y}_0) \tag{3.4}$$

where NN denotes the function describing the relation between the inputs and the outputs of the neural network. It should be mentioned that NN is an approximation of the function $\boldsymbol{h}$. Given the fact that neural networks are universal approximators, they can be used to approximate the solution of $\hat{\boldsymbol{x}}$ (3.4) and directly learn the mapping between the inputs and the outputs of the dynamical system (3.2). Thus we seek a function that can predict the state evolution of the system (3.2). Fig. 3.14 illustrates the general architecture of a NN, where the input-output relationship can be expressed as follows:

$$z_k^i = \sigma(\hat{z}_k^i) \qquad \forall k = 1, ..., K \qquad \forall i = 1, ..., N_k \tag{3.5}$$

$$\hat{\boldsymbol{z}}_{k+1} = \mathbf{W}_{k+1}\boldsymbol{z}_k + \mathbf{b}_{k+1} \qquad \forall k = 0, 1, ..., K-1 \tag{3.6}$$

$$[t, \boldsymbol{u}^\top, \boldsymbol{x}_0^\top, \boldsymbol{y}_0^\top]^\top = \boldsymbol{z}_0 \tag{3.7}$$

$$[\hat{\boldsymbol{x}}^\top, \hat{\boldsymbol{y}}^\top]^\top = \mathbf{W}_{k+1}\boldsymbol{z}_K + \mathbf{b}_{k+1}. \tag{3.8}$$

where the neural network consists of a number of K of fully connected hidden layers, where each of this layer contains a number of N_k neurons. The input vector of the neural network $\boldsymbol{z}_0$ contains the time t, the input variables $\boldsymbol{u}$, the state variables at the initial condition and the algebraic variables at

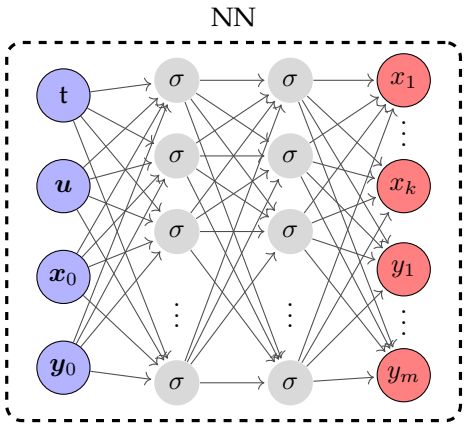

Figure 3.14: Neural network architecture. The variable t is the time, u is a vector containing the input variables of the dynamical system, σ is a non-linear activation function, x_i is the *i-th* state variable and y_j is the *j-th* algebraic variable of the dynamical system. Adapted from **??**.

the initial condition. The output vector of the neural network comprises the state $\hat{\boldsymbol{x}}$ and algebraic variables $\hat{\boldsymbol{y}}$. $\mathbf{z}_k$ denotes the output of each layer (except the last one), while $\hat{z}_k^i$ denotes the input to each neuron in the hidden layers. The function σ is a nonlinear activation function and is applied to $\hat{z}_k^i$. In this thesis, as an activation function we use the hyperbolic tangent. Finally, $\mathbf{W}_{k+1}$ and $\mathbf{b}_{k+1}$ are the weight matrices and bias vector, respectively. Using a training dataset, that provides a mapping between the input and output of the neural network, the weights and biases of the neural network are optimized. This is realized by minimizing a loss function over the training dataset. As a loss function, we select the Mean Squared Error (MSE) between the neural network prediction and the training dataset labels. This yields:

$$MSE_u = \frac{1}{N_u}\sum_{j=1}^{N_u}(\boldsymbol{x}_j - \hat{\boldsymbol{x}}_j)^2 + \frac{1}{N_u}\sum_{j=1}^{N_u}(\boldsymbol{y}_j - \hat{\boldsymbol{y}}_j)^2 \tag{3.9}$$

where N_u is the number of data points which are used for optimizing the weights and biases of the neural network. The more data points are provided for the mapping between the inputs and the outputs of the dynamical model the higher is the accuracy. However, the following problem arises, when it comes to interpolating between data. As shown in Fig. 3.15, even if the neural network is able to predict the function value at the two black dots, there are infinitely many ways the underlying function (3.4) can look like between these points. This means that for a dynamical system with an oscillatory behavior, many simulated data-points are required in order for the neural network to improve the accuracy of the neural network predictions.

Thus, the accuracy of the solutions of the neural networks is highly influenced by the amount and quality of the training data. As long as large training databases are available or efficiently generated [93, 94], neural networks can be trained and provide accurate solutions of a system of differential algebraic equations. However, generating the required training database size still requires excessive computational effort. In this thesis, inspired by [96, 97], we attempt to reduce the need for training data during the training process of the NN, by exploiting: (i) advances in automatic differentiation [6] that are implemented in Tensorflow [98] and (ii) the underlying physical laws governing power systems.

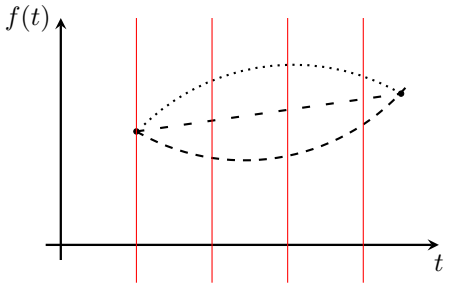

Figure 3.15: Multiple trajectories that could be correct. Additional evaluation at intermediate points (red lines) helps increasing the confidence. Adapted from [**Pub. M**].

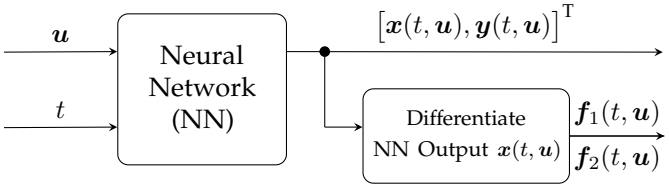

Figure 3.16: General structure of a physics-informed neural network: it predicts the outputs $\boldsymbol{x}(t,\boldsymbol{u})$ and $\boldsymbol{y}(t,\boldsymbol{u})$ given inputs $\boldsymbol{u}$ and t. Then, using automatic differentiation [6] of the same neural network, the derivatives of $\boldsymbol{x}(t,\boldsymbol{u})$ are computed, and $\boldsymbol{f}_1(t,\boldsymbol{u})$ and $\boldsymbol{f}_2(t,\boldsymbol{u})$ are evaluated. Adapted from [**Pub. G**]

3.2.2 General architecture of physics-informed neural networks

Having introduced the general architecture of neural networks, we now introduce the framework for physics-informed neural networks. The general structure of a physics-informed neural network is shown in Fig. 3.16. The main difference between a physics-informed and a classical feedforward neural network is found in the training process and particularly in the loss function. As mentioned above for the training of a classical neural network, the weights and biases are optimized by minimizing the loss function (3.9), i.e. minimizing the mean squared error between the neural network prediction and the true value. For training the physics informed neural network, however, the loss function contains additional terms which enforce the physical laws describing the dynamical system (3.2). The loss function that we seek to minimize in order to optimize the weights and biases of the physics-informed neural network is described as follows:

$$MSE = \underbrace{\frac{1}{N_u}\sum_{j=1}^{N_u}(\boldsymbol{x}_j - \hat{\boldsymbol{x}}_j^i)^2 + \frac{1}{N_u}\sum_{j=1}^{N_u}(\boldsymbol{y}_j - \hat{\boldsymbol{y}}_j^i)^2}_{MSE_u} + \underbrace{\frac{1}{N_f}\sum_{i}^{N_f}|\boldsymbol{f}_1(t_f^i, u_f^i)|^2 + \frac{1}{N_f}\sum_{i}^{N_f}|\boldsymbol{f}_2(t_f^i, u_f^i)|^2}_{MSE_f} \tag{3.10}$$

where MSE_f is an additional term in the loss function that penalizes how much the neural network predictions violate the physical laws of the dynamical system imposed by $\boldsymbol{f}_1$ and $\boldsymbol{f}_2$ at a finite set of collocation points, i.e. points spread across the input domain, without having an input-output mapping. N_f is the number of collocation points. The functions $\boldsymbol{f}_1$ and $\boldsymbol{f}_2$ enforce the physical laws of the dynamical system (3.2) and are defined as:

$$\boldsymbol{f}_1 = \dot{\hat{\boldsymbol{x}}} - \boldsymbol{f}(\hat{\boldsymbol{x}}, \hat{\boldsymbol{y}}, \boldsymbol{u}), \tag{3.11}$$

$$\boldsymbol{f}_2 = \boldsymbol{g}(\hat{\boldsymbol{x}}, \hat{\boldsymbol{y}}, \boldsymbol{u}), \tag{3.12}$$

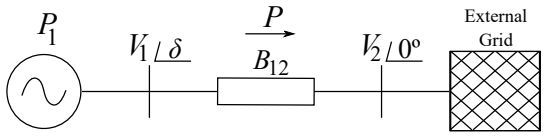

Figure 3.17: Single machine infinite bus system. Adapted from [**Pub. G**].

To determine the derivatives of the estimated by the neural network state variables $\hat{\dot{\boldsymbol{x}}}$ with respect to time t, we make use of the automatic differentiation [6] that is implemented in TensorFlow [98]. The main advantage of physics-informed neural networks over classical neural networks is that they can optimize the weights and biases with a reduced requirement of simulated data-points, while providing accurate solutions. This is possible through the use of a finite set of collocation points and the additional term in the loss function that penalizes the violation of the physical laws governing the dynamical system.

According to Picard-Lindelöf theorem, to make sure that the solution of a system of differential equations is unique and the neural network is able to predict the trajectory of the state variables at a specified time-interval, we need to specify a point on the solution trajectory. Otherwise, given a certain input, there might be multiple solutions for the outputs of the neural network that minimize MSE_f, given the fact that the optimization problem is non-convex. To this end, we additionally provide an initial condition at $t = 0$ and $\boldsymbol{u} = \boldsymbol{u}_0$ as a second loss term MSE_u. Effectively, we have transformed the previously supervised learning task into an unsupervised one with the single exception of the initial condition. That is because the loss function now does not contain a loss term for data points (points for which you have an input-output mapping), except for the initial condition. Hence we can completely omit the need to provide input-output mappings, i.e. data points, for the training process and make the neural network's accuracy independent of the data points and dependent on the collocation points.

3.2.3 Simulation & Results

To evaluate the physics-informed neural network performance, we use two test systems.

Single machine infinite bus system

In their simplest form, the system of ordinary differential equations describing the frequency dynamics of the system depicted in Fig. 3.17 are given by:

$$x(t,u) := [\delta(t,P_1), \omega(t,P_1)] \tag{3.13}$$

$$f_{t,P_1} = m_1\ddot{\delta} + d_1\dot{\delta} + B_{12}V_1V_2\sin(\delta) - P_1,$$
$$P_1 \in [P_{\text{min}}, P_{\text{max}}], \qquad t \in [0,T], \tag{3.14}$$

where $[0,\ T]$ is a time interval which is defined based on the time period of interest for the dynamic simulation, $\omega(t,P_1) = \dot{\delta}(t,P_1)$ and $[P_{\text{min}}, P_{\text{max}}]$ is the minimum and maximum values of the mechanical power of the generator of the system. The inputs of the neural network are (t, P_1) and the outputs of the neural network are the generator angle and speed $[\delta(t,P_1), \omega(t,P_1)]$.

For this case study, we consider that the system that the system is initially at a perturbed state, i.e. the system is not at an equilibrium at $t = 0$ s. The initial values for δ and ω are 0.1 rad and 0.1 rad/s,

respectively. The voltage magnitudes V_1 and V_2 are considered constant and equal to 1 p.u. The intervals $[0,\ T]$ and $[P_{\text{min}}, P_{\text{max}}]$ are equal to [0, 20] and [0.08, 0.18], respectively. The susceptance B_{12} is equal to 0.2 p.u. We want to show the capability of the physics-informed neural network to accurately predict the evolution of the trajectory of the generator angle and speed, using a limited amount of data points. We remind the reader that the main advantage of the physics-informed neural network is that it relies also on collocation points (points spread across the input space, used for evaluating how much the physical laws describing the dynamical system are violated) and not only on data points for optimizing the weights and biases of the neural network. To this end, we generate a training and test set that consists of 20'100 samples. We choose 8000 collocation points, i.e. the true values of δ and ω are unknown, and 40 data points, i.e. the true values of δ and ω are known. We also consider a 5-layer neural network with 10 neurons per hidden layer. Finally, we use a gradient-based optimization algorithm to optimize the function $MSE = MSE_f + MSE_u$ (3.10). The MSE_f term of the loss function is evaluated at the 8000 collocation points, where MSE_u is evaluated at the 40 data points.

Fig. 3.18 shows a comparison of the physics-informed neural network predicted and true solution for the angle $\delta(t)$ and the frequency $\omega(t)$. The left figures show the most accurate estimation, while the right figures show the least accurate estimation of the generator angle and speed. It can be observed that the physics-informed neural network is able to accurately predict the trajectories of the system state variables. However, the most important takeaway from this simulation is the time that it takes for the physics-informed neural network to predict the solutions of the state variables. Particularly, comparing the computation time of the physics-informed neural networks with MATLAB's numerical solver $ode45$ to solve the system of ordinary differential equations, we observed the following:

- $ode45$ numerical solver takes on average 0.45 s to solve the system of differential equations,

- physics-informed neural network solves the system of differential equations in 0.016 s.

This results in a speed-up of factor 28 for predicting the trajectories of the state variables of the system. Last but not least, another important aspect of using physics-informed neural networks is that we can directly determine the values of the system state variables at any time instant. Let us consider that we want to calculate the values of the state variables at a time instant t_1. While numerical solvers require to integrate from t_0 until t_1 in order to determine the values of the state variables, the neural network can directly determine the value, by specifying $t = t_1$ (t is an input to the neural network). This illustrates that physics-informed neural networks can predict the solutions of a system of differential equations with high accuracy and low computational cost, offering significant advantages when performing time-domain simulation analysis.

Two-area Kundur system

Similar to the previous case study, we first introduce the system of differential equations describing the dynamical system depicted in Fig. 3.19. The governing equations describing the frequency

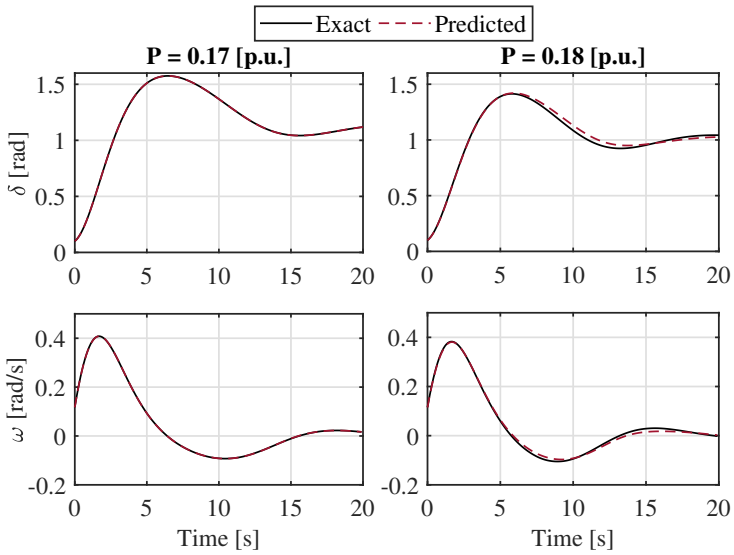

Figure 3.18: Comparison of the predicted and exact solution for the angle $\delta(t)$ and frequency $\omega(t)$ with the physics-informed neural network NN_δ. In the left figures, we show the most accurate estimation of the trajectory of $\delta(t)$ and $\omega(t)$, with a relative L_2 error of $2.55 \cdot 10^{-4}$. In the right figures, we show the least accurate estimation of the trajectory of $\delta(t)$ and $\omega(t)$, with a relative L_2 error of $2.37 \cdot 10^{-2}$. Adapted from **[Pub. G]**.

dynamics of the power system are given by:

$$\boldsymbol{x}(t,u) := [\boldsymbol{\delta_g}(t,\boldsymbol{P}), \boldsymbol{\omega}_g(t,\boldsymbol{P}), \boldsymbol{\delta_L}(t,\boldsymbol{P})] \tag{3.15}$$

$$f^{\delta_{g,i}}_{t,P_i^{\text{set}},P_i^{\text{dist}}} = \dot{\delta}_i - (\omega_i - \omega_0) \tag{3.16}$$

$$f^{\omega_{g,i}}_{t,P_i^{\text{set}},P_i^{\text{dist}}} = \dot{\omega}_i - \left(\frac{\omega_0}{2H_i} \left(P_i^{\text{set}} + P_i^{\text{dist}} - \sum_j \frac{V_i V_j}{X_{ij}} \sin(\delta_i - \delta_j) \right) \right) \tag{3.17}$$

and a load respectively

$$f^{\delta_{L,i}}_{t,P_i^{\text{set}},P_i^{\text{dist}}} = \dot{\delta}_i - \left(\frac{1}{D_i} \left(P_i^{set} + P_i^{dist} - \sum_j \frac{V_i V_j}{X_{ij}} \sin(\delta_i - \delta_j) \right) \right) \tag{3.18}$$

where the state variables and outputs of the neural networks are the rotor angles and speeds, as well as the load angles (angles at buses with no generators). The inputs of the neural networks are the time t, the mechanical power P_i^{set} and the load disturbance P_i^{dist}. The functions $f^{\delta_{g,i}}_{t,P_i^{\text{set}},P_i^{\text{dist}}}$, $f^{\omega_{g,i}}_{t,P_i^{\text{set}},P_i^{\text{dist}}}$ and $f^{\delta_{L,i}}_{t,P_i^{\text{set}},P_i^{\text{dist}}}$ are the ones that are evaluated for a number of collocation points N_f, in order to penalize the violation of the physical laws of the dynamical system, i.e. their values should be equal to zero. The system parameters and the voltage magnitudes are given in [9]. With this simulation set-up, we want to evaluate the advantage of the physics-informed neural network over a classical neural network in predicting the solutions of a system of differential equations, using a limited amount of simulated data-points. For the analysis, we consider that the number of data-points N_u used in the training process of both the physics-informed and the classical neural network are the same. While the classical neural network optimizes its parameters by minimizing the loss function MSE_u, the physics-informed neural network by the use of collocation points optimizes its parameters by minimizing $MSE = MSE_u + MSE_f$.

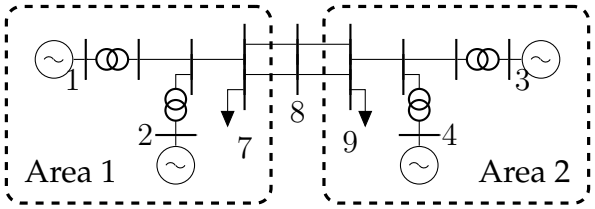

Figure 3.19: Kundur 2 area system. Adapted from [**Pub. M**].

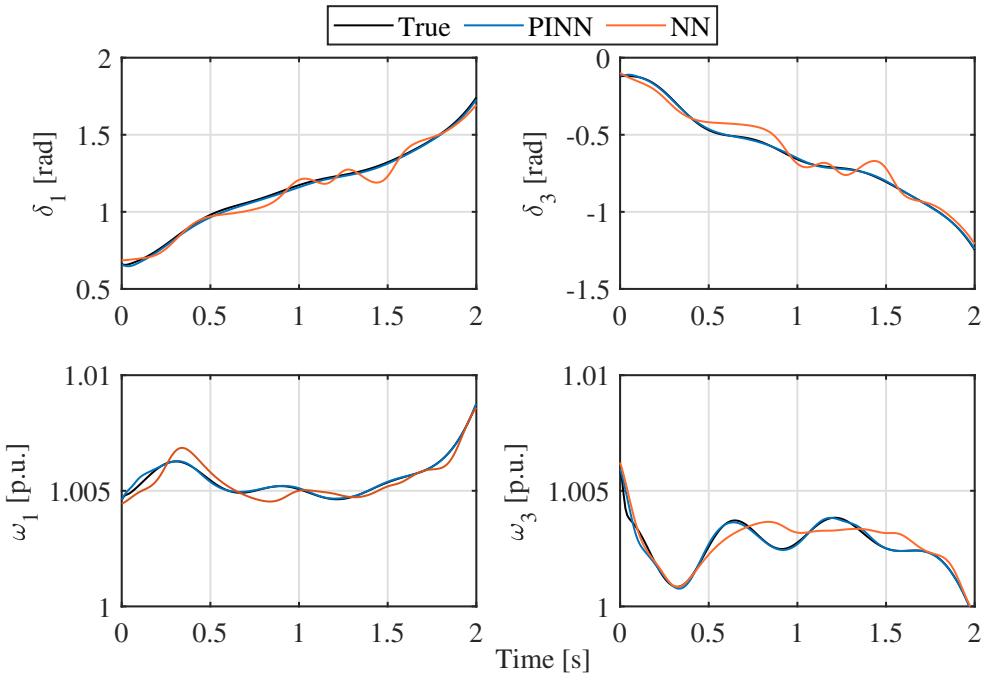

Figure 3.20: Comparison of the predicted and exact solution (black solid line) for the rotor angles $\delta(t)$ at buses 1 (left figure) and 3 (right figure) and speeds $\omega(t)$ at bus 1 (left figure) and 3 (right figure), with the physics-informed neural network (PINN) (blue solid line) and the classical neural network (NN).

.

Fig. 3.20 shows a comparison between a physics-informed and a classical neural network in predicting the trajectories of the rotor speeds and angles at the buses 1 and 3, considering a short-circuit at bus-9 and a system split occurring at $t = 0$. As shown in the figure, the physics-informed neural network outperforms the classical one in terms of accuracy. This comes to show that by utilizing the collocation points and minimizing the violation of the physical laws describing the dynamical system, we are able to improve the accuracy of the physics-informed neural network to predict the trajectory of the system state variables.

3.3 Remarks

The contributions presented in this chapter concern the need for fast dynamic security assessment of future power systems based on time-domain simulations.

In [**Pub. F**], we validate the appropriateness of an existing reduced complexity model, i.e. RMS model, for two different types of grid-forming converters, namely power synchronization loop and virtual synchronous generator. We propose sufficient conditions for the control parameters of the

converters and show that by utilizing active damping controllers and restricting the bandwidth of the outer control loops of the grid-forming converters, the excitation of eigenfrequencies in the network can be limited. This results in a reduced and in some cases negligible mismatch between the RMS and EMT model. It should be mentioned that the validity of the sufficient conditions were verified using time-domain analysis, where we consider the following events: (i) change of active power set-point of the converter, (ii) change of the grid topology and (iii) loss of generation, i.e. large active power disturbances. To conclude, by properly selecting the control parameters of the converters, we can limit the impact of fast dynamics on slow dynamics and make the RMS appropriate for simulating grid-forming converters.

In [**Pub. G**], we demonstrate for the first time successful application of physics-informed neural network to solve systems of differential equations describing fundamental power system dynamics. The fundamental difference between classical neural networks and physics-informed ones is that the latter can exploit the knowledge of the underlying physics of a dynamical model. This can be achieved by adjusting the loss function for training the neural network, i.e. the inclusion of an additional term indicating the violation of the physical laws describing the dynamical system. To verify the precision of the physics-informed neural network we use a single machine infinite bus system. The results show that they can accurately determine the solutions of a system of differential equations at a fraction of the time required by conventional numerical methods. Furthermore, we demonstrate the efficiency of a physics-informed neural network in simulating larger systems and unstable events. Furthermore, we compare it to a classical feed-forward neural network in order to highlight its ability to accurately determine the solutions of a system of differential equations, while requiring substantially less training data compared to the classical neural network approach. To conclude, physics-inform neural networks unlock a series of opportunities for fast dynamic security assessment of future power systems, given their good accuracy and high computational speed.

CHAPTER 4

Conclusion and future work

This last chapter summarizes the main contributions of this thesis, and provides future research directions that could contribute to enabling a seamless integration of a high share of renewable energy sources into the power grid.

4.1 Conclusion

The transition towards a carbon-free power system entails multiple technical challenges, related to power system stability and simulation tools for time-domain analysis. This thesis addresses these challenges by following two research directions. The first investigates the impact of high shares of converter-based resources on the system stability and then proposes control designs and metrics to enable the secure integration of renewable energy sources. The second investigates analysis tools for time-domain simulations by evaluating the appropriateness of existing reduced complexity models for converters and by proposing the use of physics-informed neural networks which provide accurate and fast solutions.

High shares of renewable energy sources reduce the level of rotational inertia in the system, which deteriorates the system frequency stability. This thesis proposed two mitigation strategies that help preserve the frequency stability of the system. In **[Pub. A]** a frequency controller based on an H_∞ loop-shaping design procedure was proposed, that optimizes the control parameters of frequency controllers placed in active power regulating units. The key insights obtained are that by accounting for the lowest level of the system inertia, robust performance can be achieved in the presence of time-varying system inertia. This results in limiting the ROCOF and frequency nadir and allowing for high penetration of renewable energy sources without deteriorating the frequency stability of the system. In **[Pub. B]**, we take advantage of the advanced control functionalities of HVDC lines and introduce methods that support the frequency stability of low-inertia systems. More specifically, we propose the inclusion of supplementary control function of HVDC in an optimization framework for the exchange of primary frequency reserves between asynchronous areas. By deriving analytical expressions for the ROCOF, the frequency nadir, and the steady state frequency deviation and linearizing them, we can incorporate frequency-related constraints into the unit commitment problem, which determines the primary frequency reserves so that the frequency stability of the system is preserved.

Considering that HVDC-VSC are expected to play a vital role in supporting the power-grid, additional investigations need to be performed concerning converter stability issues. In **[Pub. C]**, the active power transfer capability of grid-following converters subject to low SCR was investigated. The main findings suggest that by equipping grid-following converters with a frequency droop characteristic, we can increase the dynamic active power transfer capability of the converter during large disturbances, as well as improve the small-signal stability of the system. In **[Pub. D]**, we investigate the differences in the system dynamic performance between a grid-forming converter

and an alternative grid-forming pair comprising a synchronous condenser and a grid-following converter. For the analysis, an offshore AC system, representing the North Sea wind power hub, was used that consists of 100% converter-based resources and is interconnected with multiple asynchronous areas. The key insight is that by pairing a grid-following VSC with a synchronous condenser (i.e. equivalent of a grid-forming converter), we can make use of the kinetic energy stored in the rotating mass of the synchronous condenser to slow down the disturbance propagation to interconnected AC systems. Moreover, grid-forming converters, due to their fast reaction can improve the frequency stability of the offshore AC system. At the same time, however, any type of disturbance in the offshore system propagates instantly to the interconnected AC systems. This can cause synchronous instability and violation of the N-1 criterion in the case of an overload incident in the offshore AC system, due to the saturation of grid-forming converters. To tackle this problem in [**Pub. E**], a preventive control strategy was proposed that determines the frequency droop values of the grid-forming converters. By optimally selecting the frequency droop values the active power is distributed in a way that the operational limits of the offshore converters are not violated in case of a contingency, i.e. loss of an offshore converter. This results in ensuring the N-1 criterion in the offshore system.

To ensure the secure integration of renewable energy sources in the power grid, fast dynamic security assessment based on time-domain simulation analysis is necessary. To tackle this problem, this thesis took two approaches. In the first approach, the appropriateness of existing simulation tools of low computational complexity was assessed, i.e. RMS modeling, when monitoring systems with high penetration of grid-forming VSCs. In [**Pub. F**], the influence of control parameters on neglecting the fast dynamics of the system was investigated. The main findings are that by deriving analytical conditions that limit the bandwidth of the outer loops of the grid-forming converters we can minimize the impact of fast dynamics on slower ones. This leads to an appropriate model reduction, where the fast dynamics of the system are neglected and, consequently, to a reduction of the mismatch between the RMS and EMT models of the system. In the second approach, new simulation tools for performing time-domain analysis were explored. In [**Pub. G**], a framework for physics-informed neural networks in power system applications was proposed. Physics-informed neural networks combine the advancements in machine learning with the knowledge of underlying physical laws governing power systems and provide solutions for a system of differential algebraic or ordinary differential equations at a fraction of the time required for conventional numerical approaches, while maintaining high accuracy and requiring less data.

4.2 Perspectives for future research

The insights gained in this thesis concern strategies for ensuring secure system operation with high share of converter-based resources and simulation tools for performing fast dynamic security assessment of future power systems. Following, we provide several perspective for future research.

Current practices for solving the unit commitment problem do not account for frequency-related constraints. In [**Pub. B**], we presented a framework where we extracted frequency metrics and incorporate them into the unit commitment problem to investigate the benefits of sharing reserves over HVDC to the system costs. However, the model describing the frequency dynamics did not account for hydropower in the system. Considering that AC systems, such as the Nordic system, rely on hydro-units in order to maintain the frequency stability, a promising future direction would be to extract frequency-related constraints that also account for the dynamics of hydropower.

As an outcome, we would obtain an optimal solution for the unit-commitment problem, while maintaining the frequency stability and reducing the cost of reserve procurement in AC systems with large shares of hydropower.

This thesis has introduced a model of an asynchronous offshore system, namely the North Sea Wind Power Hub. The system consists of 100% converter-based resources, which collects all the power produced by wind turbines and transmits this power through several HVDC links to different asynchronous AC systems. The study performed in [**Pub. D**] investigates the impact of two different AC configurations, namely zero- and low-inertia configuration, on the system stability. For both configurations we considered that the offshore converters are responsible for maintaining the power balance. However, this results in the propagation of any type of disturbance to the onshore grids, putting their operation at risk. To tackle this problem, two alternatives could be considered as a future research direction. The first one concerns the placement of alternative storage infrastructure components, such as battery energy storage, electrolyzer etc. (instead of a synchronous condenser), for maintaining the power balance of the system. A techno-economic assessment could answer the question whether a synchronous condenser is necessary or not. The second path forward concerns the operation mode of the wind turbines. In [**Pub. D**] we considered that the wind turbines operate in a grid-feeding mode. By utilizing the ability of VSCs to control the active and reactive power independently, wind turbines could also be used for maintaining the power balance of the system. A system dynamic performance analysis (similar to the one presented in [**Pub. D**]) could provide insights on the degree to which offshore systems should participate in the power balance.

Furthermore, in [**Pub. E**] the proposed optimization problem updates the frequency droops to ensure the N-1 criterion of the offshore system (taking into account the available headroom of the offshore converters). This work could be extended so that the optimization problem would also account for the system strength of the onshore grids that are interconnected to the offshore system. Considering that each onshore AC grid is subjected to different inertia levels, the frequency droops can be selected to direct disturbances to areas with higher inertia, while ensuring the N-1 criterion of the offshore system. As an outcome, we would reduce the impact of any contingency occurring in the offshore system on the frequency stability of the interconnected onshore AC systems.

Exploring machine learning as an alternative to conventional time domain simulations, in [**Pub. G**], we used physics-informed neural networks for simulating phenomena related to the frequency dynamics of the system. However, to increase their reliability as an appropriate simulation tool for performing fast dynamic security assessment, the next step would be to extend their application to different types of dynamic phenomena related to voltage and converter stability studies. Moreover, linking machine learning and power system optimization, we can use physics-informed neural networks to model a system dynamic response. By reformulating the neural equations to a mixed intenger linear program [99], we can incorporate the system response into optimization problems. This then allows to include previously intractable dynamic security constraints (e.g. constraints associated with small-signal and transient stability) into AC/DC-OPF. Leveraging an exact mixed-integer reformulation of these physics-informed neural networks, solutions to mixed-integer linear programs accurately approximate solutions to the originally intractable optimization problems, while ensuring the stability and secure operation of the system.

Bibliography

[1] Uros Markovic, Ognjen Stanojev, Petros Aristidou, Evangelos Vrettos, Duncan S Callaway, and Gabriela Hug. Understanding small-signal stability of low-inertia systems. *IEEE Transactions on Power Systems*, 2021.

[2] Rosario Toscano. *H_2 and Mixed H_2/H_∞ Design of Structured Controllers*, pages 199–231. Springer London, London, 2013.

[3] ABB. HVDC Light - It's time to connect. Technical report, 2017. Available at https://library.e.abb.com/public/285c256c03cd4e168eaae9834ad05c90/PRINTPOW0038%20R7%20HR.pdf.

[4] H. Xin, L. Huang, L. Zhang, Z. Wang, and J. Hu. Synchronous instability mechanism of p-f droop-controlled voltage source converter caused by current saturation. *IEEE Transactions on Power Systems*, 31(6):5206–5207, 2016.

[5] A. D. Paquette, M. J. Reno, R. G. Harley, and D. M. Divan. Sharing transient loads : Causes of unequal transient load sharing in islanded microgrid operation. *IEEE Industry Applications Magazine*, 20(2):23–34, 2014.

[6] Atilim Gunes Baydin, Barak A Pearlmutter, Alexey Andreyevich Radul, and Jeffrey Mark Siskind. Automatic differentiation in machine learning: a survey. *Journal of machine learning research*, 18(153), 2018.

[7] United Nations. Paris Agreement. Technical report, Dec. 2015. Available at https://unfccc.int/process-and-meetings/the-paris-agreement/the-paris-agreement.

[8] ENTSO-E. Powerfacts europe 2019, 2019. Available at https://eepublicdownloads.entsoe.eu/clean-documents/Publications/ENTSO-E%20general%20publications/ENTSO-E_PowerFacts_2019.pdf?Web=1.

[9] Prabha Kundur, Neal J Balu, and Mark G Lauby. *Power system stability and control*, volume 7. McGraw-hill New York, 1994.

[10] Nordic Transmission System Operators. Report: Challenges and opportunities for the nordic power system, 2016. Available at https://www.fingrid.fi/en/pages/news/news/2016/report-challenges-and-opportunities-for-the-nordic-power-system/.

[11] Federico Milano, Florian Dörfler, Gabriela Hug, David J. Hill, and Gregor Verbič. Foundations and challenges of low-inertia systems (invited paper). In *2018 Power Systems Computation Conference (PSCC)*, pages 1–25, Jun. 2018.

[12] Nordic Transmission System Operators. Report: Fast frequency reserve - solution to the nordic inertia challenge, 2019. Available at https://www.fingrid.fi/en/pages/news/news/2019/report-fast-frequency-reserve--solution-to-the-nordic-inertia-challenge/.

[13] European Commission. Commission regulation (eu) 2016/1447 establishing a network code on requirements for grid connection of high voltage direct current systems and direct current-connected power park modules, 2016. Available at https://eur-lex.europa.eu/eli/reg/2016/1447/oj.

[14] ENTSO-E. FCR-D design of requirements-phase 2, 2019. Available at https://www.statnett.no/globalassets/for-aktorer-i-kraftsystemet/utvikling-av-kraftsystemet/nordisk-frekvensstabilitet/fcr-d-design-of-requirements--phase-2.pdf.

[15] ENTSO-E. ENTSO-E transmission system map, 2019. Available at https://www.entsoe.eu/data/map/.

[16] L. Papangelis, M. Debry, T. Prevost, P. Panciatici, and T. Van Cutsem. Stability of a voltage source converter subject to decrease of short-circuit capacity: A case study. In *2018 Power Systems Computation Conference (PSCC)*, pages 1–7, 2018.

[17] J. Z. Zhou, H. Ding, S. Fan, Y. Zhang, and A. M. Gole. Impact of short-circuit ratio and phase-locked-loop parameters on the small-signal behavior of a vsc-hvdc converter. *IEEE Transactions on Power Delivery*, 29(5):2287–2296, 2014.

[18] D. L. H. Aik and G. Andersson. Fundamental analysis of voltage and power stability of single-infeed voltage-source converter hvdc systems. *IEEE Transactions on Power Delivery*, 34(1):365–375, 2019.

[19] European Commision. Political Declaration on energy cooperation between the North Seas Countries. Technical report, Jun. 2016.

[20] North Sea Wind Power Hub - Consortium Partners. Power hub as an island, 2017. Available at https://northseawindpowerhub.eu/wp-content/uploads/2017/11/Concept-Paper-3-Hub-as-an-Island.pdf.

[21] North Sea Wind Power Hub Consortium. Cost evaluation of north sea offshore wind post 2030, 2019. Available at https://northseawindpowerhub.eu/wp-content/uploads/2019/07/Cost-Evaluation-of-North-Sea-Offshore-Wind-1.pdf.

[22] Mario Paolone, Trevor Gaunt, Xavier Guillaud, Marco Liserre, Sakis Meliopoulos, Antonello Monti, Thierry Van Cutsem, Vijay Vittal, and Costas Vournas. Fundamentals of power systems modelling in the presence of converter-interfaced generation. *Electric Power Systems Research*, 189:106811, 2020.

[23] Nikos Hatziargyriou, Jovica Milanović, Claudia Rahmann, Venkataramana Ajjarapu, Claudio Cañizares, Istvan Erlich, David Hill, Ian Hiskens, Innocent Kamwa, Bikash Pal, et al. Stability definitions and characterization of dynamic behavior in systems with high penetration of power electronic interfaced technologies. 2020.

[24] J.H. Chow, J.R. Winkelman, M.A. Pai, and P.W. Sauer. Singular perturbation analysis of large-scale power systems. *International Journal of Electrical Power & Energy Systems*, 12(2):117–126, 1990.

[25] Petros Aristidou, Simon Lebeau, and Thierry Van Cutsem. Power system dynamic simulations using a parallel two-level schur-complement decomposition. *IEEE Transactions on Power Systems*, 31, 09 2016.

[26] Babak Badrzadeh - Australian Energy Market Operator. Electromagnetic transient simulation models for large-scale system impact studies in power systems having a high penetration of inverter-based resources, 2019.

[27] Ivo Caduff, Uros Markovic, Ciaran Roberts, Gabriela Hug, and Evangelos Vrettos. Reduced-order modeling of inverter-based generation using hybrid singular perturbation. 05 2020.

[28] P. Vorobev, P. Huang, M. Al Hosani, J. L. Kirtley, and K. Turitsyn. High-fidelity model order reduction for microgrids stability assessment. *IEEE Transactions on Power Systems*, 33(1):874–887, 2018.

[29] Qoria Taoufik, Quentin Cossart, Chuanyue Li, François Gruson, Frédéric Colas, Xavier Kestelyn, and Xavier Guillaud. D3.2 - local control and simulation tools for large transmission systems. 12 2018.

[30] Guillaume Denis and Thibault Prevost. Migrate d3.6: Requirement guidelines for operating a grid with 100power electronic devices. 12 2019.

[31] P. Kundur et al. Definition and classification of power system stability ieee/cigre joint task force on stability terms and definitions. *IEEE Transactions on Power Systems*, 19(3):1387–1401, 2004.

[32] M. Farrokhabadi et al. Microgrid stability definitions, analysis, and examples. *IEEE Transactions on Power Systems*, 35(1):13–29, 2020.

[33] U. Markovic, Z. Chu, P. Aristidou, and G. Hug. Lqr-based adaptive virtual synchronous machine for power systems with high inverter penetration. *IEEE Transactions on Sustainable Energy*, 10(3):1501–1512, 2019.

[34] U. Markovic, Z. Chu, P. Aristidou, and G. Hug. Fast frequency control scheme through adaptive virtual inertia emulation. In *2018 IEEE Innovative Smart Grid Technologies - Asia (ISGT Asia)*, pages 787–792, 2018.

[35] Ognjen Stanojev, Uros Markovic, Petros Aristidou, Gabriela Hug, Duncan S Callaway, and Evangelos Vrettos. Mpc-based fast frequency control of voltage source converters in low-inertia power systems. *IEEE Transactions on Power Systems*, 2020.

[36] Dominic Groß, Saverio Bolognani, Bala K Poolla, and Florian Dörfler. Increasing the resilience of low-inertia power systems by virtual inertia and damping. In *Proceedings of IREP'2017 Symposium*, page 64. International Institute of Research and Education in Power System Dynamics, 2017.

[37] H. Ahmadi and H. Ghasemi. Security-Constrained Unit Commitment With Linearized System Frequency Limit Constraints. *IEEE Trans. Power Syst.*, 29(4):1536–1545, July 2014.

[38] M. Paturet, U. Markovic, S. Delikaraoglou, E. Vrettos, P. Aristidou, and G. Hug. Stochastic Unit Commitment in Low-Inertia Grids. *IEEE Trans. Power Syst.*, 35:3448–3458, 2020.

[39] Luis Badesa, Fei Teng, and Goran Strbac. Optimal Portfolio of Distinct Frequency Response Services in Low-Inertia Systems. *IEEE Trans. Power Syst.*, 2020.

[40] Z. Chu, U. Markovic, G. Hug, and F. Teng. Towards Optimal System Scheduling With Synthetic Inertia Provision From Wind Turbines. *IEEE Trans. Power Syst.*, 35(5):4056–4066, 2020.

[41] J. Rocabert, A. Luna, F. Blaabjerg, and P. Rodríguez. Control of power converters in ac microgrids. *IEEE Transactions on Power Electronics*, 27(11):4734–4749, 2012.

[42] J. A. Suul, S. D'Arco, P. Rodríguez, and M. Molinas. Impedance-compensated grid synchronisation for extending the stability range of weak grids with voltage source converters. *IET Gener., Transm. Dis.*, 10(6):1315–1326, 2016.

[43] L. Harnefors, M. Bongiorno, and S. Lundberg. Input-admittance calculation and shaping for controlled voltage-source converters. *IEEE Transactions on Industrial Electronics*, 54(6):3323–3334, 2007.

[44] L. Harnefors, X. Wang, A. G. Yepes, and F. Blaabjerg. Passivity-based stability assessment of grid-connected vscs-an overview. *IEEE Journal of Emerging and Selected Topics in Power Electronics*, 4(1):116–125, 2016.

[45] L. Zhang, L. Harnefors, and H. Nee. Power-synchronization control of grid-connected voltage-source converters. *IEEE Transactions on Power Systems*, 25(2):809–820, 2010.

[46] S. D'Arco, J. A. Suul, and O. B. Fosso. A virtual synchronous machine implementation for distributed control of power converters in smartgrids. *Electric Power Systems Research*, 122:180–197, 2015.

[47] K. Wallace, H. Anderson, T. Jin, K. Benjamin, and H. Bri-Mathias. Grid-following inverters and synchronous condensers: A grid- forming pair? 03 2020.

[48] T. Qoria, F. Gruson, F. Colas, G. Denis, T. Prevost, and X. Guillaud. Critical clearing time determination and enhancement of grid-forming converters embedding virtual impedance as current limitation algorithm. *IEEE Journal of Emerging and Selected Topics in Power Electronics*, pages 1–1, 2019.

[49] A. Tayyebi, D. Groß, A. Anta, F. Kupzog, and F. Dörfler. Frequency stability of synchronous machines and grid-forming power converters. *IEEE Journal of Emerging and Selected Topics in Power Electronics*, 8(2):1004–1018, 2020.

[50] A. D. Paquette and D. M. Divan. Virtual impedance current limiting for inverters in microgrids with synchronous generators. *IEEE Transactions on Industry Applications*, 51(2):1630–1638, 2015.

[51] D. Ramasubramanian, Z. Yu, R. Ayyanar, V. Vittal, and J. Undrill. Converter model for representing converter interfaced generation in large scale grid simulations. *IEEE Transactions on Power Systems*, 32(1):765–773, 2017.

[52] W. Wang, G. M. Huang, P. Kansal, L. E. Anderson, R. J. O'Keefe, D. Ramasubramanian, P. Mitra, and E. Farantatos. Instability of pll-synchronized converter-based generators in low short-circuit systems and the limitations of positive sequence modeling. In *2018 North American Power Symposium (NAPS)*, pages 1–6, 2018.

[53] Cedric Flamant, Pavlos Protopapas, and David Sondak. Solving differential equations using neural network solution bundles. *arXiv preprint arXiv:2006.14372*, 2020.

[54] Martin Magill, Faisal Qureshi, and Hendrick W de Haan. Neural networks trained to solve differential equations learn general representations. *arXiv preprint arXiv:1807.00042*, 2018.

[55] Craig Michoski, Miloš Milosavljević, Todd Oliver, and David R Hatch. Solving differential equations using deep neural networks. *Neurocomputing*, 399:193–212, 2020.

[56] Louis A Wehenkel. *Automatic learning techniques in power systems*. Springer Science & Business Media, 2012.

[57] Benjamin Donnot, Isabelle Guyon, Marc Schoenauer, Patrick Panciatici, and Antoine Marot. Introducing machine learning for power system operation support. *CoRR, arXiv preprint arXiv:1709.09527*, 2017.

[58] M. Sun, I. Konstantelos, and G. Strbac. A deep learning-based feature extraction framework for system security assessment. *IEEE Transactions on Smart Grid*, 10(5):5007–5020, Sep. 2019.

[59] J. H. Arteaga, F. Hancharou, F. Thams, and S. Chatzivasileiadis. Deep learning for power system security assessment. In *2019 IEEE Milan PowerTech*, pages 1–6, June 2019.

[60] Ferdinando Fioretto, Terrence W. K. Mak, and Pascal Van Hentenryck. Predicting ac optimal power flows: Combining deep learning and lagrangian dual methods. *arXiv preprint arXiv:1909.10461*, 2019.

[61] L. Duchesne, E. Karangelos, and L. Wehenkel. Recent developments in machine learning for energy systems reliability management. *Proceedings of the IEEE*, 108(9):1656–1676, 2020.

[62] S. A. Siddiqui, K. Verma, K. R. Niazi, and M. Fozdar. Artificial neural network based early detection of real-time transient instability for initiation of emergency control through wide-area synchrophasor measurements. In *2015 International Conference on Computer, Communication and Control (IC4)*, pages 1–6, 2015.

[63] Yang Liu, Liu Youbo, Ji Liu, Maozhen Li, Tingjian Liu, Gareth Taylor, and Kunyu Zuo. A mapreduce based high performance neural network in enabling fast stability assessment of power systems. *Mathematical Problems in Engineering*, 2017:1–12, 02 2017.

[64] B. P. Soni, V. Gupta, R. Kumar, A. Saxena, and S. L. Surana. Application of ann for stability assessment of large power system by post-fault rotor angle measurements. In *2018 IEEMA Engineer Infinite Conference (eTechNxT)*, pages 1–6, 2018.

[65] THE MULTI-DC PROJECT. http://www.multi-dc.eu/.

[66] ENTSO-E Technical Group. Frequency stability evaluation criteria for the synchronous zone of continental europe, 2016. Available at https://eepublicdownloads.entsoe.eu/clean-documents/SOC%20documents/RGCE_SPD_frequency_stability_criteria_v10.pdf.

[67] B. K. Poolla, D. Groß, and F. Dörfler. Placement and implementation of grid-forming and grid-following virtual inertia and fast frequency response. *IEEE Transactions on Power Systems*, 34(4):3035–3046, 2019.

[68] Sigurd Skogestad and Ian Postlethwaite. *Multivariable Feedback Control: Analysis and Design*. John Wiley & Sons, 2005.

[69] T. S. Borsche, T. Liu, and D. J. Hill. Effects of rotational inertia on power system damping and frequency transients. In *2015 54th IEEE Conference on Decision and Control (CDC)*, pages 5940–5946, 2015.

[70] M. Debry, G. Denis, and T. Prevost. Characterization of the grid-forming function of a power source based on its external frequency smoothing capability. In *2019 IEEE Milan PowerTech*, pages 1–6, 2019.

[71] J. Fradley, R. Preece, and M. Barnes. VSC-HVDC for frequency support (a review). In *2017 13th IET Int. Conf. ACDC Power Transmiss.*, pages 1–6, 2017.

[72] J. Huang and R. Preece. HVDC-based fast frequency support for low inertia power systems. In *2017 13th IET Int. Conf. ACDC Power Transmiss.*, pages 1–6, 2017.

[73] F. Thams, R. Eriksson, and M. Molinas. Interaction of droop control structures and its inherent effect on the power transfer limits in multiterminal vsc-hvdc. *IEEE Trans. Power Del.*, 32(1):182–192, Feb 2017.

[74] Dirk Van Hertem, Oriol Gomis-Bellmunt, and Jun Liang. *HVDC grids: for offshore and supergrid of the future*. John Wiley & Sons, 2016.

[75] M. Callavik, A. Blomberg, J. Häfner, and B. Jacobson. The hybrid hvdc breaker: An innovation breakthrough enabling reliable hvdc grids. Technical report, ABB, 2012.

[76] M. Raza, E. Prieto-Araujo, and O. Gomis-Bellmunt. Small-signal stability analysis of offshore ac network having multiple vsc-hvdc systems. *IEEE Trans. Power Del.*, 33(2):830–839, April 2018.

[77] B. Bastin. Master thesis : Dynamics and control of a future off-shore wind power hub. 2019.

[78] S. D'Arco, J. A. Suul, and O. B. Fosso. A Virtual Synchronous Machine implementation for distributed control of power converters in SmartGrids. *Electric Power Systems Research*, 122:180 – 197, 2015.

[79] L. Harnefors, X. Wang, A. G. Yepes, and F. Blaabjerg. Passivity-based stability assessment of grid-connected vscs-an overview. *IEEE Journal of Emerging and Selected Topics in Power Electronics*, 4(1):116–125, 2016.

[80] N. Pogaku, M. Prodanovic, and T. C. Green. Modeling, Analysis and Testing of Autonomous Operation of an Inverter-Based Microgrid. *IEEE Trans. Power Electron.*, 22(2):613–625, March 2007.

[81] L. Harnefors, M. Hinkkanen, U. Riaz, F. M. M. Rahman, and L. Zhang. Robust Analytic Design of Power-Synchronization Control. *IEEE Trans. Ind. Electron.*, 66(8):5810–5819, Aug 2019.

[82] E. Barklund, N. Pogaku, M. Prodanovic, C. Hernandez-Aramburo, and T. C. Green. Energy management in autonomous microgrid using stability-constrained droop control of inverters. *IEEE Transactions on Power Electronics*, 23(5):2346–2352, Sep. 2008.

[83] R. Eriksson. Current Sharing in Multiterminal DC Grids-The Analytical Approach. *IEEE Trans. Power Syst.*, 33(6):6278–6288, Nov 2018.

[84] N. R. Chaudhuri and B. Chaudhuri. Adaptive droop control for effective power sharing in multi-terminal dc (mtdc) grids. *IEEE Transactions on Power Systems*, 28(1):21–29, 2013.

[85] J. Beerten and R. Belmans. Analysis of Power Sharing and Voltage Deviations in Droop-Controlled DC Grids. *IEEE Trans. Power Syst.*, 28(4):4588–4597, Nov 2013.

[86] J. Beerten, R. Eriksson, and D. Van Hertem. A new approach to hvdc grid voltage control based on generalized state feedback. In *2014 IEEE PES General Meeting | Conference Exposition*, pages 1–5, July 2014.

[87] DIgSILENT. PowerFactory 2021 - Integrate Power System Analysis Software. Nov. 2020.

[88] I. Subotic, D. Gross, M. Colombino, and F. Dorfler. A lyapunov framework for nested dynamical systems on multiple time scales with application to converter-based power systems. *IEEE Transactions on Automatic Control*, pages 1–1, 2020.

[89] Turhan Demiray. *Simulation of Power System Dynamics using Dynamic Phasor Models*. PhD thesis, ETH Zurich, 2008.

[90] S. D'Arco, J. A. Suul, and O. B. Fosso. Automatic tuning of cascaded controllers for power converters using eigenvalue parametric sensitivities. *IEEE Transactions on Industry Applications*, 51(2):1743–1753, 2015.

[91] L. Luo and S. V. Dhople. Spatiotemporal model reduction of inverter-based islanded microgrids. *IEEE Transactions on Energy Conversion*, 29(4):823–832, 2014.

[92] J. Chen and T. O'Donnell. Parameter constraints for virtual synchronous generator considering stability. *IEEE Transactions on Power Systems*, 34(3):2479–2481, 2019.

[93] F. Thams, A. Venzke, R. Eriksson, and S. Chatzivasileiadis. Efficient database generation for data-driven security assessment of power systems. *IEEE Transactions on Power Systems*, pages 1–1, 2019.

[94] Andreas Venzke, Daniel K Molzahn, and Spyros Chatzivasileiadis. Efficient creation of datasets for data-driven power system applications. *Electric Power Systems Research*, 190:106614, 2021.

[95] MWMG Dissanayake and Nhan Phan-Thien. Neural-network-based approximations for solving partial differential equations. *communications in Numerical Methods in Engineering*, 10(3):195–201, 1994.

[96] Tian Qi Chen, Yulia Rubanova, Jesse Bettencourt, and David K Duvenaud. Neural ordinary differential equations. In *Advances in neural information processing systems*, pages 6571–6583, 2018.

[97] M. Raissi, P. Perdikaris, and G.E. Karniadakis. Physics-informed neural networks: A deep learning framework for solving forward and inverse problems involving nonlinear partial differential equations. *Journal of Computational Physics*, 378:686 – 707, 2019.

[98] Martín Abadi et al. Tensorflow: Large-scale machine learning on heterogeneous distributed systems. *arXiv preprint arXiv:1603.04467*, 2016.

[99] Andreas Venzke, Guannan Qu, Steven Low, and Spyros Chatzivasileiadis. Learning optimal power flow: Worst-case guarantees for neural networks. In *2020 IEEE International Conference on Communications, Control, and Computing Technologies for Smart Grids (SmartGridComm)*, pages 1–7. IEEE, 2020.

Collection of relevant publications

[**Pub. A**] G. S. Misyris, S. Chatzivasileiadis and T. Weckesser, "Robust Frequency Control for Varying Inertia Power Systems," in *2018 IEEE PES Innovative Smart Grid Technologies Conference Europe (ISGT-Europe)*, Sarajevo, 2018, pp. 1-6, doi: 10.1109/ISGTEurope.2018.8571607.

[**Pub. B**] A. Tosatto, G. Misyris, A. Junyent-Ferré, F. Teng and S. Chatzivasileiadis, "Towards Optimal Coordination between Regional Groups: HVDC Supplementary Power Control," submitted to *IEEE Transactions on Power Systems*, (under review, second round), 2021.

[**Pub. C**] G. S. Misyris, J. A. Mermet-Guyennet, S. Chatzivasileiadis and T. Weckesser, "Grid Supporting VSCs in Power Systems with Varying Inertia and Short-Circuit Capacity," in *2019 IEEE Milan PowerTech*, Milan, Italy, 2019, pp. 1-6, doi: 10.1109/PTC.2019.8810979.

[**Pub. D**] G. Misyris, T. Van Cutsem, J. G. Møller, M. Dijokas, O. Renom Estragues, B. Bastin, S. Chatzivasileiadis, A. H. Nielsen, J. T. G. Weckesser, J. Østergaard, and F. Kryezi, "North Sea Wind Power Hub: System Configurations, Grid Implementation and Techno-economic Assessment," accepted at *CIGRE (International Council on Large Electric Systems)*, 2020 .

[**Pub. E**] G. S. Misyris, A. Tosatto, S. Chatzivasileiadis and T. Weckesser, "Zero-inertia Offshore Grids: N-1 Security and Active Power Sharing," submitted to *IEEE Transactions on Power Systems*, (under review, first round), 2021.

[**Pub. F**] G. S. Misyris, S. Chatzivasileiadis and T. Weckesser, "Grid-forming Converters: Sufficient Conditions for RMS Modeling," submitted to *Electric Power Systems Research*, (under review, second round), 2021.

[**Pub. G**] G. S. Misyris, A. Venzke and S. Chatzivasileiadis, "Physics-Informed Neural Networks for Power Systems," in *2020 IEEE Power & Energy Society General Meeting (PESGM)*, Montreal, QC, 2020, pp. 1-5, doi: 10.1109/PESGM41954.2020.9282004.

[Pub. A] Robust Frequency Control for Varying Inertia Power Systems

Authors:
G. S. Misyris, S. Chatzivasileiadis and T. Weckesser

Published in:
2018 IEEE PES Innovative Smart Grid Technologies Conference Europe (ISGT-Europe)

DOI:
10.1109/ISGTEurope.2018.8571607

Robust Frequency Control for Varying Inertia Power Systems

George S. Misyris, *Student Member, IEEE,* Spyros Chatzivasileiadis, *Senior Member, IEEE,* and Tilman Weckesser, *Member, IEEE,*

***Abstract*—Increased penetration of fluctuating Renewable Energy Sources (RES) adds a significant uncertainty in the dynamic behavior of the power system. Varying power infeed from RES significantly affects the number of conventional generators to be dispatched at any time instant. As a result, system parameters, such as inertia and damping can no longer be considered constants, but instead they obtain a time-varying profile. In this paper, a robust frequency control scheme is introduced to account for the time-varying system inertia and damping under increased RES penetration. The proposed method is based on an H_∞ loop-shaping design procedure, and it guarantees good frequency response for varying levels of inertia and damping. After presenting the impact of varying system parameters to the system dynamic behavior, the design method for the proposed controller is presented, and its performance is demonstrated in case studies.**

***Index Terms*—frequency dynamics analysis, H_∞ loop-shaping design, robust control.**

I. Introduction

Increased penetration from Renewable Energy Sources (RES) impacts the dynamic behavior of the power system and may jeopardize its stability. In the absence of conventional generators, the Rate Of Change Of Frequency (ROCOF) becomes higher due to the lower inertia and the frequency nadir deteriorates [1]. Furthermore, conventional generators can assist towards the damping of electromechanical oscillations, and can provide services such as automatic voltage regulation and frequency control [2]. Consequently, transmission system operators face increasing challenges to maintain the security and stability of the electricity network [3].

Generally, RESs do not inherently contribute to frequency control, since they are usually operated in a maximum power point tracking mode [4]. Moreover, varying weather conditions affect RES generation levels and, hence, the number of committed conventional generators is changing over time. Consequently, total inertia level, provided by rotating mass, and the damping of the system, provided by e.g. Power System Stabilizers (PSS) and damper windings, are varying in time. To ensure stable grid operation, the frequency control needs to be designed to perform well for a range of system conditions, where the system inertia and damping levels are uncertain. In control theory, an approach for designing controllers, explicitly dealing with uncertainty, is robust control.

Several methods have been developed for enhancing stability under consideration of low system inertia and damping. The authors of [5]–[7] address the problem by proposing an optimization that informs system operators how to choose optimal levels of inertia with respect to damping of power system oscillations, while ensuring admissible transient behavior after a large disturbance. In [8], the authors propose an explicit model predictive control, which allows to directly incorporate operational constraints of power system units (ramp-rate, power rating, energy constraints) to achieve real-time tractability while keeping the online computation effort low. In [9], the authors propose an extended control loop based on the generator emulation control concept to provide inertia by using the stored energy in the dc-link capacitors of VSC-HVDC links. Moreover, researchers have been seeking different ways to control power electronic converters in power systems to enhance system stability [10]. One approach is to embed the dynamics and behavior of conventional synchronous machines into power electronic converters as Virtual Synchronous Machines (VSMs) [11], [12].

To implement this approach structured controllers are added to the control circuits of the converters. Structured controllers, such as PID, lead-lag controllers, etc. are preferred due to their properties, since they are easy to implement and re-tune whenever performance or system properties change. However, the uncertain RES power infeed makes the tuning procedure of the controllers challenging. Several methods have been proposed to increase robustness of structured controllers [13]. Among those methods, the H_∞ loop shaping methodology introduced in [14] is a good technique for combining desirable properties such as tracking performance, disturbance rejection, robustness to model uncertainty.

This paper first investigates the impact of time-varying inertia and damping on the frequency dynamics of the system. An analysis is conducted using tools from control system theory on how the uncertainty of those parameters affect frequency dynamics. Then, a structured robust control design is proposed to increase the security of the system operation under uncertainty. Reducing ROCOF and maximum frequency deviation is associated with inertia response and primary frequency control [8]. Most existing converter and generation systems use proportional control – in the form of droop control – to stabilize frequency right after a disturbance. Therefore, in this paper the focus is on proportional control for the robust control design. In the analysis, the frequency dynamics are represented by a second order model.

Accounting for the uncertainty of system dynamics due to the fluctuation of system inertia, the contribution of this

G. S. Misyris, S. Chatzivasileiadis and T. Weckesser are with the Department of Electrical Engineering, Technical University of Denmark, 2800 Kgs. Lyngby, Denmark (e-mail: {gmisy, spchatz, jtgw}@elektro.dtu.dk).

paper is to propose a procedure for designing Multi-Input-Multi-Output (MIMO) controllers by exploiting the efficiency of the H_∞ loop-shaping in synthesizing optimal and robust structured controllers. The outcome of the proposed design will be a state feedback controller that improves the power oscillation damping and decreases the ROCOF and the frequency overshoot for a wide range of system inertia and damping levels.

This paper is organized as follows: Section II describes the power system model considered in the control design procedure. Section III presents an analysis of the impact of varying inertia on the frequency dynamics of the power system. Section IV presents the procedure for deriving the robust controller. Section V demonstrates robust performance of the implemented controller. Conclusions are drawn in Section VI.

II. Power System Modeling

A. Dynamic generator model

A commonly used model to assess dynamic phenomena in power systems is the swing equation, see Eq. (1). It relates the change of rotor speed of a machine i to a torque imbalance.

$$\Delta\dot{\omega}_i = \frac{1}{2H_i}[\Delta T_{m_i} - \Delta T_{e_i}], \tag{1}$$

$$\Delta\dot{\delta}_i = \omega_0 \Delta\omega_{\mathrm{i}}, \tag{2}$$

where i refers to the number of the bus, $\Delta\omega_i$ is the per unit speed deviation, H_i is the inertia constant of the machine [s], ΔT_{e_i} is the electrical torque deviation [p.u.] and ΔT_{m_i} is the deviation of the mechanical torque applied to the machine [p.u.]. $\Delta\delta_i$ is the rotor angle deviation in electrical radians and ω_0 is the base rotor electrical speed in radians per second. (1) and (2) formulate the equations of motion linearized around an operating point.

The change in electrical torque (ΔT_{e_i}) following a disturbance can be resolved into two components, the synchronizing torque component (ΔT_{S_i}) and the damping component (ΔT_{D_i}). (3) describes this change [2]:

$$\Delta T_{e_i} = \Delta T_{S_i} + \Delta T_{D_i} = K_{S_i}\Delta\delta_i + K_{D_i}\Delta\omega_i, \tag{3}$$

where ΔT_{S_i} is in phase with $\Delta\delta_i$, and K_{S_i} is the synchronizing torque coefficient; and ΔT_{D_i} is in phase with $\Delta\omega_i$, and K_{D_i} is the damping torque coefficient. Synchronizing torque depicts the non-linear nature of dynamics of interconnected generators. Insufficient synchronizing torque can lead to transient instability. On the other hand, lack of sufficient damping torque leads to oscillatory instability.

Although the swing equation is a simplified representation of power system dynamics, it can model adequately well first swing instability [2], [15]. Since the goal of this paper is to limit the maximum ROCOF and maximum frequency deviation, which usually appear during the first swing, the swing equation can represent sufficiently well the generator dynamics. Beside that, this modeling approach has been widely used in literature as a first step to gain insights and develop control approaches for a large number of power system stability problems [1], [5].

In a "conventional" grid, synchronous generators ensure system stability, supported by Automatic Voltage Regulators (AVR) and PSS, which affect the magnitude of K_{S_i} and K_{D_i}. However, with high penetration of fluctuating RES, the number of committed synchronous generators vary, and with them the number of AVR and PSS, operating at each time instant. As a result, K_{S_i} and K_{D_i} vary with time. To counter the varying nature of K_{S_i} and K_{D_i}, new robust control approaches need to be developed.

B. State Space Model

Taking into consideration (1)-(3), the state space representation of the dynamics at each generator or aggregated generator unit is given by (4). This state space representation is of the form $\dot{x} = Ax + Bu$:

$$\underbrace{\begin{bmatrix}\Delta\dot{\omega}_{\mathrm{i}}\\ \Delta\dot{\delta}_{\mathrm{i}}\end{bmatrix}}_{\dot{x}_i} = \underbrace{\begin{bmatrix}-\frac{K_{D_i}}{2H_i} & -\frac{K_{S_i}}{2H_i}\\ \omega_0 & 0\end{bmatrix}}_{\mathrm{A_i}} \underbrace{\begin{bmatrix}\Delta\omega_{\mathrm{i}}\\ \Delta\delta_{\mathrm{i}}\end{bmatrix}}_{x_i} + \underbrace{\begin{bmatrix}\frac{1}{2H_i}\\ 0\end{bmatrix}}_{\mathrm{B_i}} \underbrace{\Delta T_{m_i}}_{u_i} \tag{4}$$

where x_i is a vector containing the system state variables, A_i is a matrix termed as the state matrix of the system, B_i is the input matrix and u_i contains the system input variables. The order of A_i matrix determines the number of modes of the system and the system eigenvalue properties.

The elements of the state matrix A_i are dependent on the system parameters K_{D_i}, K_{S_i}, H_i and the initial operating condition. The coefficients K_{S_i} and K_{D_i} can be calculated given an initial operating point based on (5) and (6), respectively.

$$K_{S_i} = \sum_{j\in\Omega_i} V_i V_j b_{ij} cos(\delta_{ij}) \tag{5}$$

$$K_{D_i} = \mathrm{c_{d_i}} \tag{6}$$

where V_i is the bus voltage magnitude, b_{ij} is the susceptance between i and j, δ_{ij} is the angle difference between i and j nodes, $\mathrm{c_{d_i}}$ is a constant value that represents the magnitude of the damping torque coefficient at each generator bus and Ω_{p} the set of all nodes adjacent to node p. Power losses are neglected.

C. Multi-machine system

In (4), $\Delta\omega_i$ represents the rotor speed. In a multi-machine system, the frequency measured at a particular bus is a function of the rotor speeds of all generators. In the following, it is assumed that larger regions of a power system are aggregated and represented by an equivalent machine. The dynamics of this equivalent machine can be described by (4) and the model parameters are determined through aggregation of the individual generators in the region. Consequently, the parameters H_i, K_{D_i} and K_{S_i} of the equivalent machine vary depending on the generation dispatch and power infeed of RES in the region. In the proposed modeling approach, the rotor speed dynamic response of the equivalent machine corresponds to the frequency dynamic response in the region. The overall aim is to develop a robust controller which improves the rotor speed dynamic response of that equivalent machine, and, hence, the frequency response of the aggregated region. Therefore, in

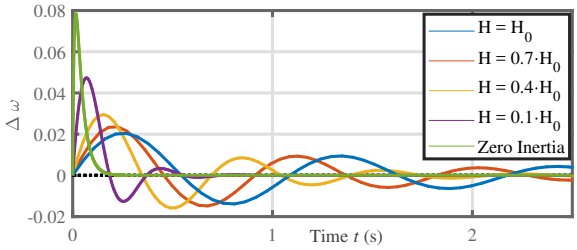

Fig. 1. $\Delta\omega$ impulse response at different inertia levels

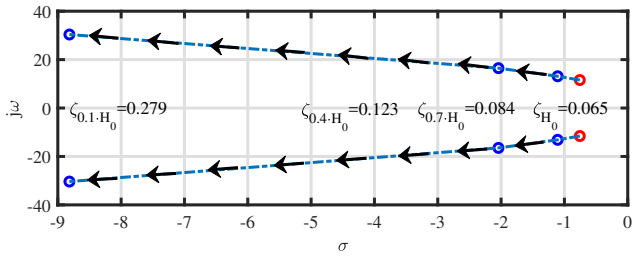

Fig. 2. Eigenvalues trajectory concerning the oscillatory mode of generator 3 (3-bus system, Section V), while reducing inertia level at bus 2 (ζ: Damping Ratio)

the rest of this paper, the terms rotor speed of the equivalent machine and frequency are used interchangeably.

For the observation of the frequency dynamics in multi-machine systems, the focus is on electromechanical oscillatory modes, which indicate how the generators oscillate against each other [2]. The second order model, defined by (4)-(6), can be used to describe the electromechanical oscillations of each generator. The multi-machine system is linearized over an equilibrium x_0, using Taylor approximation [2]. The connectivity between two buses i and j at an equilibrium, and the LaPlacian of the network, are given by:

$$P_{ij} = V_i V_j b_{ij} cos(\delta_{ij}), \qquad L_{ij} = \begin{cases} -P_{ij}, & i \neq j \\ K_{S_i}, & i = j \end{cases} \tag{7}$$

where K_{S_i} and P_{ij} are given by (5) and (7), respectively. Assuming a system with n buses, $\boldsymbol{L_N} \in R^{n\times n}$. The parameters of the system, such as inertia and damping, are collected in matrix form and the states in vectors.

$$\boldsymbol{H}_{\mathrm{N}} = \mathrm{diag}(2H_1, \cdots, 2H_{\mathrm{n}}),\ \boldsymbol{K}_{\mathrm{N}} = \mathrm{diag}(K_{D_1}, \cdots, K_{D_{\mathrm{n}}}) \tag{8}$$

$$\boldsymbol{\Delta\delta}_{\mathrm{N}} = \left[\Delta\delta_1, \cdots, \Delta\delta_n\right]^{\mathrm{T}},\quad \boldsymbol{\Delta\omega}_{\mathrm{N}} = \left[\Delta\omega_1, \cdots, \Delta\omega_{\mathrm{n}}\right]^{\mathrm{T}} \tag{9}$$

where H_i is the inertia at each bus and K_{D_i} is given by (6), with $\boldsymbol{H}_{\mathrm{N}} \in R^{\mathrm{n}\times\mathrm{n}}$ and $\boldsymbol{K}_{\mathrm{N}} \in R^{\mathrm{n}\times\mathrm{n}}$. The state vectors $\boldsymbol{\Delta\delta}_{\mathrm{N}}$ and $\boldsymbol{\Delta\omega}_{\mathrm{N}}$ include the deviation of generators' rotor angles and speeds of the system, with $\boldsymbol{\Delta\delta}_{\mathrm{N}} \in R^{\mathrm{n}\times\mathrm{n}}$ and $\boldsymbol{\Delta\omega}_{\mathrm{N}} \in R^{\mathrm{n}\times\mathrm{n}}$.

The input for the multi-machine system is the vector containing the deviation of mechanical torque of each generator and the output is a vector containing the angular velocity deviation of each generator. The state space representation of the open-loop transfer function is:

$$\begin{cases} \dot{x} = \boldsymbol{A_{sys}} x + \boldsymbol{B_{sys}} u \\ y = \boldsymbol{C} x \end{cases} \tag{10}$$

$$\boldsymbol{A_{sys}} = \begin{bmatrix} \boldsymbol{O_{n\times n}} & \boldsymbol{\omega_{0_{n\times n}}} \\ -\boldsymbol{H_N^{-1}} \boldsymbol{L_N} & -\boldsymbol{H_N^{-1}} \boldsymbol{K_N} \end{bmatrix},\ \boldsymbol{B_{sys}} = \begin{bmatrix} \boldsymbol{O_{n\times n}} \\ -\boldsymbol{H_N^{-1}} \end{bmatrix} \tag{11}$$

$$x = \begin{bmatrix} \boldsymbol{\Delta\delta_N} & \boldsymbol{\Delta\omega_N} \end{bmatrix}^{\mathrm{T}},\qquad u = \begin{bmatrix} \Delta T_{m_1}, \cdots, \Delta T_{m_n} \end{bmatrix} \tag{12}$$

where x, A_{sys}, B_{sys} and u are given by (11) and (12). $\boldsymbol{O_{n\times n}}$ and $\boldsymbol{\omega_{0_{n\times n}}}$ are diagonal matrices, containing zero and ω_0 in their diagonal entries, respectively. C is a matrix mapping the speed deviation of each generator ($\Delta\omega_{\mathrm{i}}$). The transfer function $G(s)$ of the open-loop system is:

$$G(\mathrm{s}) = \frac{Y(\mathrm{s})}{U(\mathrm{s})} = C(\mathrm{s}I - A_{sys})^{-1} B_{sys} \tag{13}$$

III. Analysis of Impact of Varying Inertia and Damping on Frequency Dynamics

A. Modal analysis

To quantify the effect of the varying system inertia and damping, modal analysis, Bode gain and eigenvalue plots are used to visualize the response of the examined system. For the presented case study the following assumptions are made:

1) The voltage dynamics and the dynamics for reactive power compensation are not included.
2) Under varying penetration of RES, the decrease rate of system inertia (H_{sys}) is higher than the one of system damping ($K_{D_{\mathrm{sys}}}$).

B. Sensitivity Analysis - Time varying parameters

For the sensitivity analysis, the 3-bus system introduced in Section V.A is used (see also Fig. 8) and the inertia as well as the damping parameter at generator bus 2 are varied. Similar results can be extracted by varying the parameters at other generator buses. It is worth mentioning that, in the examined system, there are two oscillatory modes, one associated with generators 1 and 3 and the other with generators 2 and 3.

Fig. 1 presents the impulse response of the frequency deviation at a system node, where an equivalent machine is connected. As it can be observed, the frequency overshoot and ROCOF greatly depends on inertia levels: the lower the inertia is, the higher the frequency deviation and ROCOF become. This could also be explained by (1), where decreasing system inertia results to higher rate of frequency deviation for the same magnitude of torque imbalance. Moreover, decrease of inertia levels leads to increased damping ratio. This can be seen both in Fig. 1 and 2, where the trajectory of the eigenvalues of electromechanical mode associated with generators 2 and 3 for a 90% reduction of inertia level are presented. As seen in Fig. 2, at the initial level of inertia the eigenvalues indicate low damping ratio (red circles). While decreasing the inertia level, the eigenvalues move further to the left, which results to higher damping ratio.

In Fig. 3 the Bode plot of $G_2(s) = \frac{\Delta\omega_2(s)}{\Delta T_{m_2}(s)}$ is illustrated. To evaluate the system response, the rise-time, the overshoot and the settling time parameters are used [16]. Considering $G_2(s)$, the system rise-time is associated with the ROCOF and the system overshoot with the maximum frequency deviation. As shown in the figure, reducing system inertia leads to gain amplification at higher frequencies and an increase of the system

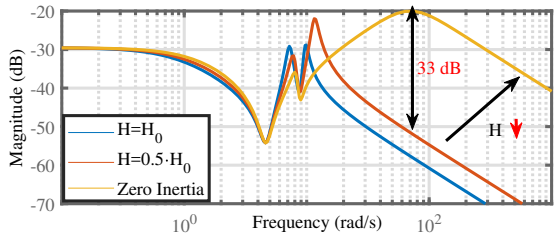

Fig. 3. Frequency Response of $G_2(s)$ for different levels of inertia. (H:Inertia)

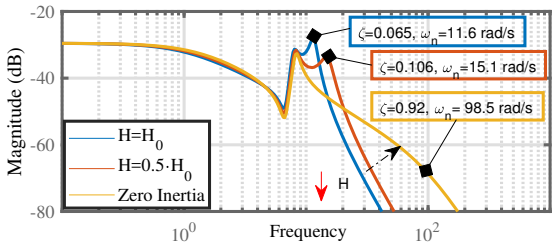

Fig. 4. Frequency Response of $G_{32}(s)$ for different levels of inertia. (H: Inertia, ζ: Damping ratio of the electromechanical modes, ω_n: Natural Frequency of the mode)

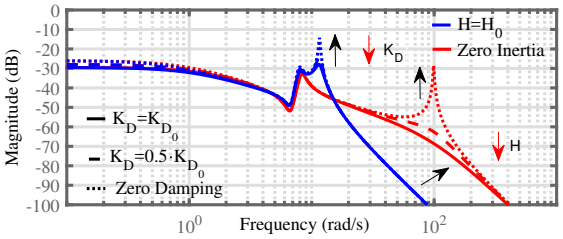

Fig. 5. Frequency response of $G_{32}(s)$ for different levels of damping and inertia. (K_D: Damping Torque Coefficient, H: Inertia)

bandwidth (also illustrated in Fig. 4), which results to shorter rise-time and higher overshoot [16] (also illustrated in Fig. 1). In Fig. 4 the Bode plot of $G_{32}(s) = \frac{\Delta\omega_3(s)}{\Delta T_{m_2}(s)}$ is illustrated. As the inertia level decreases at bus 2, the magnitude becomes smaller around the frequency of electromechanical modes (3.5-12 rad/s), which results to better damping of the oscillatory mode associated with generators 2 and 3. As for the oscillatory mode of generators 1 and 3, its damping ratio and frequency are insignificantly different.

Fig. 5 presents the frequency response for different levels of damping and inertia varied at bus 2. Blue lines represent the case with high inertia and red lines the case with low inertia. As the damping decreases, the gain becomes larger at the frequencies of oscillatory modes and the system becomes undamped [16]. Moreover, it can be seen that the varying inertia affects the frequency of the oscillatory modes. In particular, as inertia level becomes lower, the frequency of the oscillatory modes become higher. It is worth mentioning, however, that the steady state gain (below 1 rad/s) remains almost constant despite the varying inertia and damping.

Based on these observations, the goal in this paper is to derive a robust control approach to compensate the impact of damping and inertia (varying penetration of RES), while not altering the steady-state behavior of the system.

IV. Structured Robust Controller

A. H_∞ loop-shaping design

In [14] the authors proposed an H_∞ design procedure, in which the desired performance of the controller can be specified by shaping the singular values of the nominal system system $G(s)$ using pre- and post-compensators $W_1(s)$ and $W_2(s)$. The H_∞ design procedure is applied for a PID controller in [17], [18]. Since the focus is on tuning the gains of a structured proportional controller (P-controller), the above design procedure is adjusted. In this framework, the controller $K(s)$, see Fig. 6, is structured as:

$$K(s) = -W_1(s)^{-1} K_{\mathrm{P}}(s) \tag{14}$$

where W_1 is stable transfer matrix and K_{P} is the transfer matrix of the P-controller. The transfer matrix K_{P} is a diagonal matrix with the proportional gains as elements, which correspond to the gains of each P controller of every bus ($K_{\mathrm{P}} = \mathrm{diag}(k_{p_1}, k_{p_2} \cdots k_{p_n})$, where n is the number of buses considered in the system). This particular structure of Fig. 6 ensures that the final controller has the desired P-structure since K_{final}=$W_1 {W_1}^{-1} K_{\mathrm{P}} W_2 = K_{\mathrm{P}} W_2$ [17].

The input-output relationship of the closed-loop system, see Fig. 6 is given by:

$$\underbrace{\begin{bmatrix} z_1 \\ z_2 \end{bmatrix}}_{\mathbf{z}} = T_{zw}(K_{\mathrm{P}}) \underbrace{\begin{bmatrix} w_1 \\ w_2 \end{bmatrix}}_{\mathbf{w}} \tag{15}$$

$$T_{zw}(K_{\mathrm{P}}) = \begin{bmatrix} (I + W_2 G K_{\mathrm{P}})^{-1} W_2 G W_1 & (I + W_2 G K_{\mathrm{P}})^{-1} \\ -W_1^{-1} K_{\mathrm{P}} (I + W_2 G K_{\mathrm{P}})^{-1} W_2 G W_1 & -W_1^{-1} K_{\mathrm{P}} (I + W_2 G K_{\mathrm{P}})^{-1} \end{bmatrix}$$
$$= \begin{bmatrix} I \\ -W_1^{-1} K_{\mathrm{P}} \end{bmatrix} (I + W_2 G K_{\mathrm{P}})^{-1} \begin{bmatrix} W_2 G W_1 & I \end{bmatrix} \tag{16}$$

where $G(s)$ is the initial plant of the system. After determining $T_{zw}(K_{\mathrm{P}})$ the objective is to find the K controller that satisfies the following optimization problem:

$$\begin{aligned} &\text{minimize } \gamma \\ &\text{subject to } ||T_{zw}(K_{\mathrm{P}})||_\infty \leq \gamma \end{aligned} \tag{17}$$

After solving the optimization problem, described in (17), the final controller is given by:

$$K_{\mathrm{final}}(s) = K_{\mathrm{P}}(s) W_2(s) \tag{18}$$

which corresponds to a standard P controller in cascade with the post-compensator $W_2(s)$.

In the following subsection the procedure of deriving the weighting functions is presented. The minimal achievable value of $||T_{zw}(K_{\mathrm{P}})||_\infty$ indicates that the closed-loop system is bounded by a value of γ at all frequencies, which indicates the robust performance of the closed loop system (Fig. 6) against uncertainty. The values for the parameter γ range between 1 and 3 [13]. The closer to 1 is the value of γ the more robust is the performance of the closed loop system. In case $\gamma \geq 3$ the W_1 and W_2 have to be adjusted until the condition ($1 \leq \gamma \leq 3$) is satisfied [13].

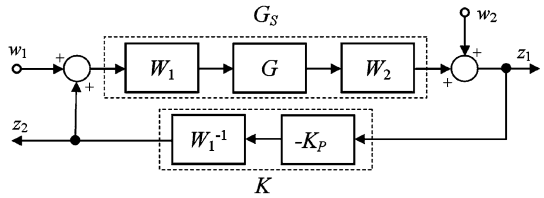

Fig. 6. Shaped Plant and Controller [19]

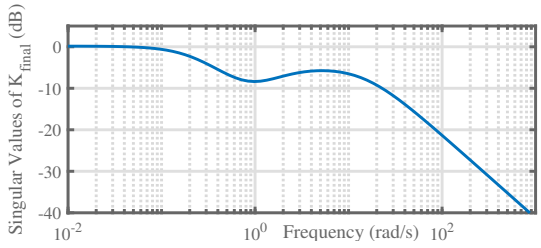

Fig. 7. Singular Values of controller K_{final}

B. Weighting Functions

According to [13] and Fig. 6, W_2 reflects the relative importance of the outputs to be controlled being fed back to controller and W_1 contains the dynamic shaping such as an integral action for low frequency performance and disturbance attenuation. By this means W_1 determines the gain at low and W_2 the gain at high frequencies.

The objective of the controller is determined based on the results presented in Section III. As mentioned above and depicted in Fig. 5, varying inertia affects the gain in the higher frequencies and varying damping the gain at the frequencies of electromechanical modes. Therefore, concerning the varying inertia, it is desirable that the robust controller exposes the characteristics of a low pass filter with a cut-off frequency in the range of 15-20 rad/s. As for the varying damping, to increase resilience to damping uncertainty, a bandstop filter is required at the frequencies of oscillatory modes (2-15 rad/s). Considering the above and the H_∞ design procedure [17], pre- and post-compensators are chosen accordingly.

The desired loop shape of the controller $K_{\text{final}}(s)$ is depicted in Fig. 7. The singular values [20] of the frequency response of the controller is depicted. The maximum singular value indicates the maximum amplification of the corresponding inputs by the system seen from a specific output. As it is illustrated, the controller has zero gain at low frequencies, which indicates the system is not affected within that range by the controller. At mid-range and higher frequencies, it can be seen that the controller results to a negative gain and consequently will increase the damping ratio and decrease ROCOF and maximum frequency deviation.

V. Results

A. 3-Bus System

To evaluate the robust control, the 3-Bus System presented in Fig. 8 is used. The state variables of the 3-Bus System are collected in vectors and in the form $\dot{\mathrm{x}} = \mathrm{A_{sys}x} + \mathrm{B_{sys}}u$,

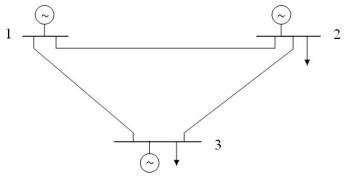

Fig. 8. 3-Bus System.

TABLE I
Bus voltages, Mechanical inputs, Static loads

Node	Voltage [p.u.]	Power [p.u.]	Damping K_{D_i}	Inertia H_i
1	1.0526	-1.5	10	5.5
2	1.0502	1.05	10	2.75
3	1.017	0.45	10	5.5

see (10). The system characteristics are given in Table I. The susceptances of the transmission lines are: $b_{12} = 0.739$, $b_{13} = 1.0958$ and $b_{23} = 1.245$. At the operating point, the synchronizing torque coefficients of the state space model can be calculated by (5). The values of the damping torque coefficients at each generator bus are given in Table I.

Having derived the state space model of the 3-Bus system and the transfer function for the actual plant $G(s)$ using (13), the robust control design technique, presented in Section IV, is implemented. Once the proportional controller is tuned and the state feedback gain is defined, then it is added to each bus of the 3-Bus system. There are 3 additional state variables in the second order model describing the frequency dynamics of each bus. Considering the two cases mentioned above, the results for the frequency deviation at bus 2 of the 3-Bus system are presented. The transfer function of the closed loop system $CL_{\text{sys}}(s)$, with $\mathrm{K_{final}(s)}$ as a controller and a negative feedback gain is:

$$CL_{\text{sys}}(s) = \frac{G(s)K_{\text{final}}(s)}{1 + G(s)K_{\text{final}}(s)} \tag{19}$$

B. Case 1 - low inertia

In case 1 the performance and the response of the system after 50% reduction of the inertia level at bus 2 is evaluated. As illustrated in Fig. 9, low inertia results to higher frequency deviation and overshoot compared to the initial levels. The effect of the controller, applied during operation of the system with low inertia, results to smaller maximum frequency deviation and lower ROCOF. This can be explained by seeing Fig. 7, where it is depicted that the controller decreases the gain of the system transfer function at high frequencies. Overall, the results and the impact of the controller on system response are summarized in Table II, where the values of ROCOF, maximum frequency deviation and settling time are presented for this particular case.

C. Case 2 - low damping

In case 2 the performance and the response of the system after 60% reduction of the damping torque coefficient at

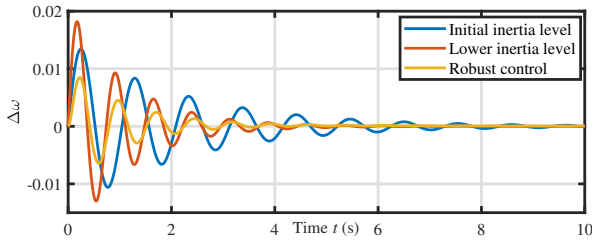

Fig. 9. Robust control of $\Delta\omega$ & impulse response for 50% reduction of the initial inertia level.

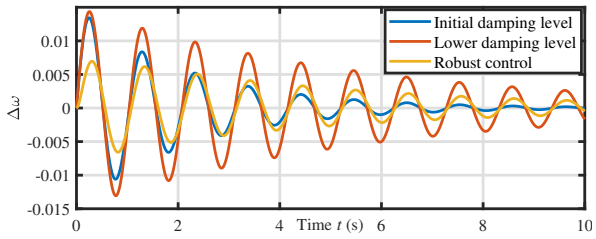

Fig. 10. Robust control of $\Delta\omega$ & impulse response for 60% reduction of the initial damping level.

bus 2 is evaluated. As shown in Fig. 10, lower K_D results to shorter settling time and damping of the oscillations, and has no impact on frequency overshoot. The effect of the controller, applied during operation of the system with lower K_D, results to lower frequency deviation and ROCOF, and has a positive effect on damping of oscillations. However, it does not compensate for the 60% reduction of K_D, as it has longer settling time, see Fig. 10, compared to initial operation of the system. Thus, it does not increase the damping ratio significantly. The impact of the controller on system response for 60% reduction of the initial damping level is depicted in Table III.

VI. Conclusions & Future Work

In this paper, the impact of the time-varying inertia and damping on grid operation has been addressed using frequency domain analysis. The results showed that the varying inertia increases ROCOF and maximum frequency deviation, but improves damping. To compensate for the increased uncertainty caused by these time-varying parameters, a robust controller is implemented. The proposed controller deals with the negative effect of the varying inertia and damping on the frequency dynamics. Concluding, through the use of an H_∞ loop-shaping design procedure, the developed controller increases the resilience of the system to imminent disturbances in the case of high penetration of RES.

Future work intends to extend the proposed methodology to higher order power system models and evaluate the robust control on large power system models.

VII. Acknowledgement

This work is supported by the multiDC project funded by Innovation Fund Denmark, Grant Agreement No. 6154-00020B.

TABLE II
Case 1 - low inertia

	ROCOF ($\frac{\text{pu}}{\text{s}}$)	Overshoot (pu)	Settling t (s)
Initial Inertia	0.0909	0.013	8.66
Lower Inertia	0.1817	0.018	4.31
Robust Control	0.0031	0.008	5.51

TABLE III
Case 2 - low damping

	ROCOF ($\frac{\text{pu}}{\text{s}}$)	Overshoot (pu)	Settling t (s)
Initial Damping	0.0909	0.013	8.66
Lower Damping	0.0909	0.013	21.60
Robust control	0.0016	0.006	17.52

References

[1] A. Ulbig, T. S. Borsche, and G. Andersson, "Impact of low rotational inertia on power system stability and operation," *IFAC Proc. Vol.*, vol. 47, no. 3, pp. 7290 – 7297, 2014, 19th IFAC World Congress.

[2] P. Kundur, N. Balu, and M. Lauby, *Power system stability and control*, ser. EPRI power system engineering series. McGraw-Hill, 1994.

[3] P. Tielens and D. Van Hertem, "The relevance of inertia in power systems," *Renew. Sust. Energ. Rev.*, vol. 55, pp. 999 – 1009, 2016.

[4] F. Wilches-Bernal, J. H. Chow, and J. J. Sanchez-Gasca, "A fundamental study of applying wind turbines for power system frequency control," *IEEE Trans. Power Syst.*, vol. 31, no. 2, pp. 1496–1505, Mar. 2016.

[5] T. S. Borsche, T. Liu, and D. J. Hill, "Effects of rotational inertia on power system damping and frequency transients," in *2015 54th IEEE Conference on Decision and Control (CDC)*, Dec. 2015, pp. 5940–5946.

[6] B. K. Poolla, S. Bolognani, and F. Dörfler, "Optimal placement of virtual inertia in power grids," *IEEE Trans. Autom. Control*, vol. 62, no. 12, pp. 6209–6220, Dec. 2017.

[7] D. Gross, S. Bolognani, B. Poolla, and F. Dörfler, "Increasing the Resilience of Low-inertia Power Systems by Virtual Inertia and Damping," in *IREP Bulk Power System Dynamics & Control Symposium*, Sep. 2017.

[8] A. Ulbig, T. Rinke, S. Chatzivasileiadis, and G. Andersson, "Predictive control for real-time frequency regulation and rotational inertia provision in power systems," in *52nd IEEE Conference on Decision and Control*, Dec. 2013, pp. 2946–2953.

[9] X. Liu and A. Lindemann, "Control of VSC-HVDC connected offshore windfarms for providing synthetic inertia," *IEEE Trans. Emerg. Sel. Topics Power Electron.*, vol. PP, no. 99, pp. 1–1, Sep. 2017.

[10] Q. C. Zhong, "Virtual synchronous machines: A unified interface for grid integration," *IEEE Power Electron. Mag.*, vol. 3, no. 4, pp. 18–27, Dec. 2016.

[11] H. P. Beck and R. Hesse, "Virtual synchronous machine," in *2007 9th International Conference on Electrical Power Quality and Utilisation*, Oct. 2007, pp. 1–6.

[12] Q. C. Zhong and G. Weiss, "Synchronverters: Inverters that mimic synchronous generators," *IEEE Trans. Ind. Electron.*, vol. 58, no. 4, pp. 1259–1267, Apr. 2011.

[13] S. Skogestad and I. Postlethwaite, *Multivariable Feedback Control: Analysis and Design*. John Wiley & Sons, 2005.

[14] D. McFarlane and K. Glover, "A loop-shaping design procedure using H_∞ synthesis," *IEEE Trans. Autom. Control*, vol. 37, no. 6, pp. 759–769, Jun. 1992.

[15] T. Weckesser and T. Van Cutsem, "Equivalent to represent inertial and primary frequency control effects of an external system," *IET Gener., Transm. & Dis.*, vol. 11, pp. 3467–3474(7), September 2017.

[16] G. C. Goodwin, S. F. Graebe, and M. E. Salgado, *Control System Design*. Prentice Hall, 2001.

[17] A. U. Genç and S. T. Impram, "A state-space algorithm for designing H_∞ loop shaping PID controllers," *IFAC Proc. Vol.*, vol. 36, no. 11, pp. 281 – 286, 2003, 4th IFAC Symposium on Robust Control Design 2003, Milan, Italy, 25-27 Jun. 2003.

[18] P. Apkarian, V. Bompart, and D. Noll, "Non-smooth structured control design with application to PID loop-shaping of a process," *Int. J. Robust Nonlin. Control*, vol. 17, no. 14, pp. 1320–1342, Jan. 2007.

[19] R. Toscano, *H_2 and Mixed H_2/H_∞ Design of Structured Controllers*. London: Springer London, 2013, pp. 199–231.

[20] K. Zhou and J. Doyle, *Essentials of Robust Control*, ser. Prentice Hall Modular Series for Eng. Prentice Hall, 1998.

[Pub. B] Towards Optimal Coordination between Regional Groups: HVDC Supplementary Power Control

Authors:
A. Tosatto, G. Misyris, A. Junyent-Ferré, F. Teng and S. Chatzivasileiadis

Submitted to:
IEEE Transactions on Power Systems (under review, second round)

Towards Optimal Coordination between Regional Groups: HVDC Supplementary Power Control

Andrea Tosatto, *Student Member, IEEE*, Georgios S. Misyris, *Student Member, IEEE*, Adrià Junyent-Ferré, *Senior Member, IEEE*, Fei Teng, *Member, IEEE*, Spyros Chatzivasileiadis, *Senior Member, IEEE*

***Abstract*—With Europe dedicated to limiting climate change and greenhouse gas emissions, large shares of Renewable Energy Sources (RES) are being integrated in the national grids, phasing out conventional generation. The new challenges arising from the energy transition will require a better coordination between neighboring system operators to maintain system security. To this end, this paper studies the benefit of exchanging primary frequency reserves between asynchronous areas using the Supplementary Power Control (SPC) functionality of High-Voltage Direct-Current (HVDC) lines. First, we focus on the derivation of frequency metrics for asynchronous AC systems coupled by HVDC interconnectors. We compare two different control schemes for HVDC converters, which allow for unilateral or bilateral exchanges of reserves between neighboring systems. Second, we formulate frequency constraints and include them in a unit commitment problem to ensure the N-1 security criterion. A data-driven approach is proposed to better represent the frequency nadir constraint by means of cutting hyperplanes. Our results suggest that the exchange of primary reserves through HVDC can reduce up to 10% the cost of reserve procurement while maintaining the system N-1 secure.**

***Index Terms*—Asynchronous areas, droop frequency control, frequency balancing, HVDC transmission, optimization, Supplementary Power Control, unit commitment.**

I. Introduction

AFTER the Paris Agreement, the European Union has taken a leading role in the energy transition, with ambitious targets for energy efficiency (32.5%) and RES penetration (32%). With the high intermittence of RES and their location far from load centers, electricity flows are expected to increase and become more variable, requiring more efficient network development. In this regard, ENTSO-e has identified the need of more than 90 GW of new installed transmission capacity by 2030. Among the different projects, more than 60 GW are new High-Voltage Direct-Current (HVDC) lines [1].

Additionally, large integration of inverter-based generation will result in decreasing kinetic energy (or inertia) in the system. With lower kinetic energy, Transmission System Operators (TSOs) could face difficulties in operating the system in a stable and reliable way [2]. These new challenges will require better coordination between regional entities, spanning from new enhanced operational processes to the prevention and management of common threats [3].

A. Tosatto, G. S. Misyris and S. Chatzivasileiadis are with the Technical University of Denmark, Department of Electrical Engineering, Kgs. Lyngby, Denmark (emails: {antosat,gmisy,spchatz}@elektro.dtu.dk).

A. Junyent-Ferré and F. Teng are with the Department of Electrical and Electronic Engineering, Imperial College London, London SW7 2AZ, U.K. (email: {adria.junyent-ferre,f.teng}@imperial.ac.uk).

This work is supported by Innovation Fund Denmark through the multiDC project (grant no. 6154-00020B).

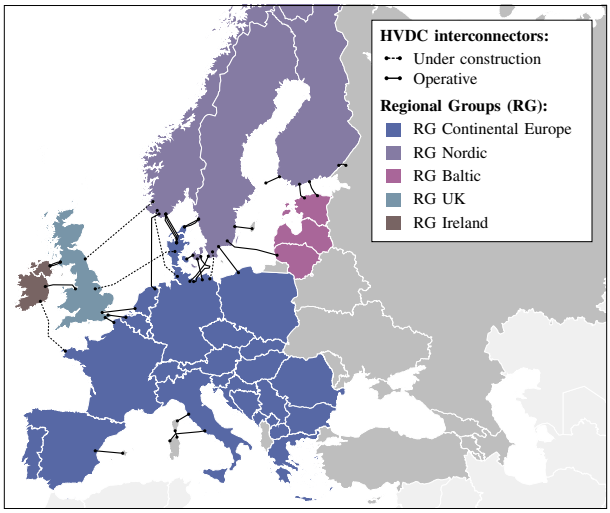

Fig. 1. Regional groups in Europe and HVDC connections.

Decrease of system inertia is classified as one of the biggest future challenges by system operators around the world. The problem is particularly pronounced in small systems, e.g. Ireland or Australia [4], [5], but it is progressively growing to comprise also larger interconnected systems such as the Nordic countries (Denmark, Sweden, Norway and Finland) or the UK [6], [7]. As more and more system operators are facing these challenges, many technical and regulatory solutions have been proposed in the literature [8]–[10], ranging from new balancing products and control methods to market measures. However, most of these solutions require a substantial change of paradigm, e.g. new grid codes and/or market rules, or expensive remedial actions, e.g. down-regulation of critical units, RES curtailment and load shedding. Recent studies have shown how HVDC converters, equipped with droop frequency controllers, could adjust their power set-points based on frequency measurements and support the system in the event of power disturbances. Given the large number of HVDC lines connecting asynchronous areas (also called regional groups) in Europe (see Fig. 1), this method, referred to as Emergency Power Control (EPC) of HVDC links, is considered by ENTSO-e as one of the most promising among all the possible options [8]. The dynamic performance of HVDC EPC is largely discussed in [11] and its cost-efficiency in [12]. However, HVDC frequency support has been studied only for critical situations, while it could be utilized by

TSOs for sharing primary frequency reserves also during normal operation (HVDC Supplementary Power Control - SPC). Moreover, this functionality has never been analyzed in an optimization framework, where the benefit of sharing primary frequency reserves between asynchronous areas could be effectively determined.

The aim of HVDC SPC is to improve the frequency stability of the system while reducing the costs of reserve procurement. In order to have an optimization model responsive to the frequency behaviour of the system, frequency metrics, such as Rate of Change of Frequency (RoCoF), Instantaneous Frequency Deviation (IFD) and Steady-State Frequency Deviation (SSFD), must be included in the problem formulation. In this regard, two main challenges can be identified: (i) the analytical derivation of frequency metrics and (ii) the tractability of frequency constraints. Several works have already studied how to include frequency constraints in a Unit Commitment Problem (UCP) for systems with high RES penetration [13]–[16]. In [13], the authors derive analytical frequency metrics for RoCoF, IFD and SSFD and include them in a UCP by means of piecewise linear approximations. The authors in [14] and [15], extended the work of [13] by including converter control schemes and fast frequency response services, such as frequency droop and virtual synchronous machine controls provided by inverter-based generation units. The authors in [16], instead, present a UCP formulation which accounts for frequency support from variable speed wind turbines. Compared to [13], [14] presents also a less computational intense method to limit the IFD, introducing safe bounds for the single variables. This method increases the tractability of the IFD constraint but disproportionately reduces the feasible space, calling for more efficient methods. Moreover, in all the aforementioned works the authors considered only one synchronous system, overlooking the option of exchanging primary frequency reserves among neighboring asynchronous systems via HVDC.

To this end, this paper aims at deriving frequency metrics for asynchronous AC systems whose frequency dynamics are coupled by HVDC links, and to include the corresponding frequency constraints in an optimization framework to assess what the benefit of the HVDC SPC implementation is. To improve the accuracy and the computational efficiency of the proposed formulation, the IFD constraint is implicitly included in the optimization problem by limiting the feasible space with cutting hyperplanes. In detail, the contributions of this paper are:

- The derivation of analytical expressions for the frequency metrics of asynchronous AC systems exchanging primary frequency services through HVDC links.
- An improved unit commitment formulation with frequency constraints, which considers the dynamic response of generators and converters based on their droop coefficients;
- A data-driven approach to better represent the frequency nadir constraint by means of cutting hyperplanes;
- The inclusion of the SPC functionality of HVDC lines in an optimization framework for the exchange of primary reserves between neighboring asynchronous systems.

The remainder of this paper is structured as follows. Section II outlines two different control schemes for the implementation of HVDC SPC, and Section III describes the derivation of frequency metrics for asynchronous AC systems interconnected by HVDC links. Section IV presents the optimization framework for the exchange of primary frequency services between asynchronous areas. A dedicated test case and simulation results are then described in Section V. Finally, Section VI gathers conclusions and perspectives regarding further works.

II. HVDC Supplementary Power Control Schemes

Frequency controllers have been developed with the aim of balancing the active power in the system in the event of load disconnection or generator tripping. Among the different control techniques, droop-based frequency controllers adjust the active power set-point proportionally to the frequency deviation in the system. When implemented on HVDC converters, such controllers modify the active power exchanged between the DC and AC systems in response to a frequency deviation. This is obtained by including supplementary control loops in the converter control scheme [17], using either frequency or RoCoF measurement as input signal. Since accurate local measurements of the RoCoF are difficult to obtain, TSOs usually do not trust such inputs. For this reason, this work considers control schemes with frequency only as an input.

In addition, depending on where the frequency is measured, HVDC converters can be set to react to the frequency deviation in only one area, or in both [18]. Thus, it is possible to distinguish between unilateral and bilateral control schemes. In the following, these two schemes are presented.

A. Unilateral SPC Scheme

In the unilateral control scheme (UCS), the frequency is measured only in one of the two interconnected AC systems. In the event of a disturbance in the monitored area, the active power exchange between the two areas is increased (or decreased) to balance the power mismatch. This means that part of the disturbance is propagated in the supporting area and some frequency reserves are activated to preserve the frequency in this area, which is equivalent to saying that some frequency reserves in the supporting area are exchanged with the area under contingency. A schematic representation of this control scheme is provided in Fig. 2.

The relation between the change in the active power flow and the frequency can be expressed as follows:

$$\Delta P^{\mathrm{ref}}(s) = \frac{K^c}{R^c(1+sT^c)}\Delta f_a \tag{1}$$

with P^{ref} the active power reference, K^c, R^c and T^c respectively the electric power gain factor, the frequency droop value and the time constant of the active power controller of the converters, s the Laplace operator and Δf_a the frequency deviation in the monitored area (area a).

The advantage of this scheme is that it reduces the IFD which follows a contingency in the supported area. However, the resulting frequency deviation in the supporting area is not monitored by the HVDC converter and only depends on the

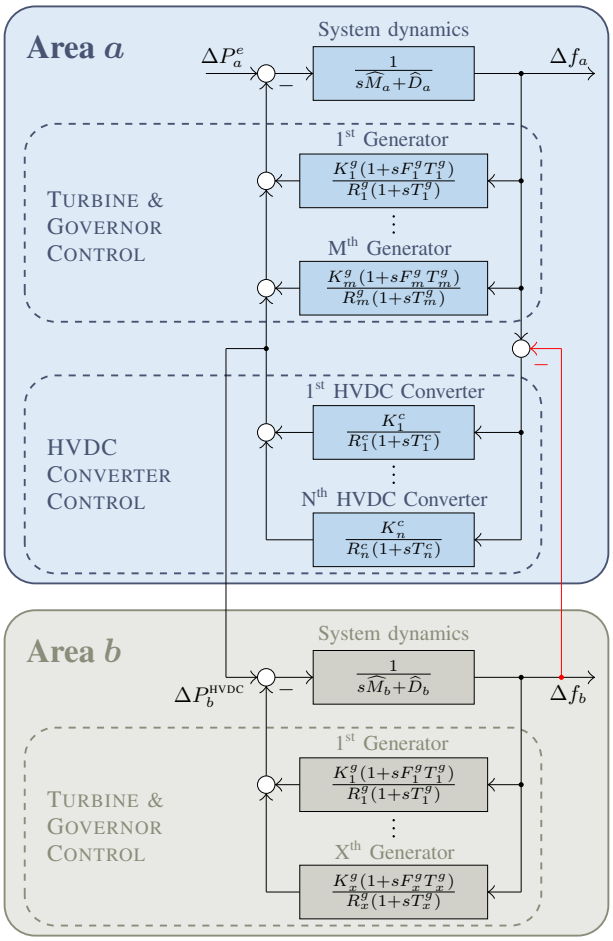

Fig. 2. System dynamics model under unilateral and bilateral HVDC EPC schemes. The difference between the two schemes is highlighted in red.

stiffness of the supporting AC system. In case a weak AC system provides frequency support to another asynchronous area, this could result in unacceptable large frequency excursions which in turn might force system operators in the supporting area to procure more frequency reserves.

B. Bilateral SPC Scheme

The bilateral control scheme (BCS) follows the same principles of the unilateral scheme, with the only difference that the frequency is measured in both the interconnected areas. The converter, thus, reacts to the frequency difference between the two areas and adjusts the active power flow accordingly. The active power change is then defined as:

$$\Delta P^{\text{ref}}(s) = \frac{K^c}{R^c(1+sT^c)}\left(\Delta f_a - \Delta f_b\right) \tag{2}$$

with f_b the frequency of the supporting area (area b). Being responsive to the frequency deviations in both areas, the HVDC link can be used for supporting both areas. A schematic representation of this control scheme is also provided in Fig. 2, with the differences between the two schemes marked in red.

Compared to the unilateral scheme, the main advantage of this scheme is that the exchange of frequency reserves is not limited to one direction. However, a change in the active power flow will cause a frequency deviation also in the second area, and thus the improvement of the IFD in the area under contingency is smaller.

III. Frequency Dynamic Model

In order to account for frequency stability issues in power systems and optimally dispatch synchronous generators, additional constraints must be included in the unit commitment problem to limit RoCoF, IFD and SSFD. Thus, in this section, we derive a simplified frequency response model of AC systems with multiple synchronous generators and HVDC interconnectors, as shown in Fig. 2, which will be used for obtaining the frequency metrics. For the analytic formulation of the frequency metrics, we consider that a contingency cannot occur simultaneously in the interconnected AC systems. For the notation, generators are referred to with the index i, converters with the index k. When a parameter or variable refers to a specific area, e.g. the total inertia constant, the subscript refers to that area (a, b and so on).

The dynamics that need to be taken into account for an accurate extraction of the center of inertia frequency of an AC system are: (i) the generator dynamics, (ii) governor droop and turbine dynamics and (iii) HVDC converter dynamics. The generator dynamics can be described by the swing equation (see Fig. 2), where $\widehat{M}_a$ and $\widehat{D}_a$ represent the total inertia and damping constants of the generators in area a. A low-order model, proposed in [19] and evaluated in [20], is used to model the governor droops and turbine dynamics, with R_i^g and K_i^g respectively the frequency droop and mechanical power gain factor, F_i^g the fraction of total power generated by the turbines of the synchronous generators and T_i^g the turbine time constant. For the HVDC converters, the frequency droop controllers described by (1) and (2) are used to provide support during the containment phase, while frequency restoration is assumed to rely only on local reserves.

A. Frequency Metrics - Unilateral Scheme

The relation between an active power disturbance ΔP_a^e and the frequency deviation Δf_a in the supported area (area a from now on) is given by:

$$G_a^{\text{U}}(s) = \frac{\Delta f_a(s)}{\Delta P_a^e(s)} = \Bigg(\left(s\widehat{M}_a + \widehat{D}_a\right) + \sum_{i\in\mathcal{G}_a^S} \frac{K_i^g\left(1+sF_i^gT_i^g\right)}{R_i^g\left(1+sT_i^g\right)} + \sum_{k\in\mathcal{L}_a^S} \frac{K_k^c}{R_k^c\left(1+sT_k^c\right)}\Bigg)^{-1}, \tag{3}$$

with $\mathcal{G}_a^S$ and $\mathcal{L}_a^S$ respectively the set of generators and HVDC interconnectors providing frequency support in area a. Similar to [21], we consider that the turbine time constants are equal, i.e. $T_i^g = T_a$, for all the synchronous machines within the same synchronous area and that the converter time constants are neglected ($T^g \gg T^c$). With these assumptions, (3) takes the following generalized form:

$$G_a^{\text{U}}(s) = \frac{1}{\widehat{M}_a T_a}\frac{1+sT_a}{s^2+2\zeta_a\omega_a^n s+\omega_a^{n\,2}}, \tag{4}$$

where the natural frequency ω_a^n and the damping ratio ζ_a are given by:

$$\omega_a^n = \sqrt{\frac{\widehat{D}_a + \widehat{R}_a}{\widehat{M}_a T_a}}, \qquad \zeta_a = \frac{\widehat{M}_a + T_a(\widehat{D}_a + \widehat{F}_a)}{2\sqrt{\widehat{M}_a T_a (\widehat{D}_a + \widehat{R}_a)}}. \tag{5}$$

$\widehat{M}_a$, $\widehat{D}_a$, $\widehat{F}_a$ and $\widehat{R}_a$ are weighted model parameters, functions of system parameters and parameters of generators and HVDC converters in area a. For their derivation, a detailed mathematical formulation is presented in [21]. Similar to [11], the damping constant $\widehat{D}_a$ is considered a fixed parameter. By applying the inverse Laplace transformation and assuming a step-wise disturbance ΔP_a, we can derive a time-domain expression of the frequency deviation. This enables to extract the RoCoF, the IFD and the SSFD in area a, respectively:

$$\dot{f}_a^{\max} = -\frac{\Delta P_a}{\widehat{M}_a}, \tag{6a}$$

$$\Delta f_a^{\max} = -\frac{\Delta P_a}{\widehat{D}_a + \widehat{R}_a}\left(1 + \sqrt{\frac{T_a(\widehat{R}_a - \widehat{F}_a)}{\widehat{M}_a}} e^{-\zeta_a \omega_a^n t_a^m}\right), \tag{6b}$$

$$\Delta f_a^{\mathrm{ss}} = -\frac{\Delta P_a}{\widehat{D}_a + \widetilde{R}_a^g}, \tag{6c}$$

where t_a^m is the time instant when the maximum frequency deviation occurs, i.e. $\Delta \dot{f}_a(t_a^m) = 0$. The obtained expressions are similar to the ones derived in [14], meaning that HVDC converters act as generators and provide the necessary power to contain the frequency in area a. After the frequency containment phase, instead, only generators provide frequency support, thus only the term $\widetilde{R}_a^g$ (which considers only the contribution of generators in area a) appears in (6c).

In case the supporting TSOs want to limit the frequency deviation in their areas, additional constraints could be included. In the supporting area (area b from now on), the change in the converters set-point $\Delta P_b^{\mathrm{HVDC}}$ corresponds to the frequency deviation $\Delta f_b(s)$. The transfer function of area b, which is the mapping of the Laplace transform of $\Delta f_a(s)$ to the Laplace transform of $\Delta f_b(s)$, can be derived in a similar way to 4, resulting in:

$$G_b^{\mathrm{U}}(s) = \frac{\Delta f_b(s)}{\Delta f_a(s)} = \frac{\widetilde{R}_{a,b}^c}{\widehat{M}_b T_b} \frac{1 + sT_b}{s^2 + 2\zeta_b \omega_b^n s + \omega_b^{n\,2}}, \tag{7}$$

Since this area is not receiving support from area a through HVDC, ω_b^n and ζ_b^n are calculated by replacing $\widehat{R}_b$ and $\widehat{F}_b$ respectively with $\widetilde{R}_b^g$ and $\widetilde{F}_b^g$, meaning that only the generators in area b provide frequency support. The term $\widetilde{R}_{a,b}^c$, instead, refers only to the contribution of the HVDC links connecting area a and b. By applying the inverse Laplace transformation and assuming a step-wise disturbance $\Delta f_a(s) = \Delta f_a^{\max}/s$, we can derive a time-domain expression of the frequency deviation in area b. This enables to extract frequency metrics for the supporting area as well:

$$\dot{f}_b^{\max} = -\frac{\Delta P_a \widetilde{R}_{a,b}^c}{\widehat{M}_a \widehat{M}_b}, \tag{8a}$$

$$\Delta f_b^{\max} = \frac{\Delta f_a^{\max} \widetilde{R}_{a,b}^c}{\widehat{D}_b + \widehat{R}_b}\left(1 + \sqrt{\frac{T_b(\widehat{R}_b - \widehat{F}_b)}{\widehat{M}_b}} e^{-\zeta_b \omega_b^n t_b^m}\right), \tag{8b}$$

It should be noted that, by considering $\Delta f_a(s)$ as a step-wise disturbance, it is not possible to calculate the exact solution for $\Delta f_b(t)$ since its trajectory varies based on the generator, turbine governor and HVDC converters parameters. Although this results in the wrong calculation of the time to nadir, t_b^m, $\Delta f_b^{\max}(s)$ is accurately represented. Moreover, the SSFD in the supporting area is equal to zero as there is no contribution of HVDC to frequency restoration in area a.

B. Frequency Metrics - Bilateral Scheme

The main difference between the bilateral and the unilateral schemes is that, in the bilateral scheme, the active power set-points of the HVDC converters change proportionally to the difference between the frequencies of the interconnected AC systems. In the event of a power disturbance ΔP_a, the corresponding frequency deviation is given by:

$$\Delta f_a(s) = G_a^{\mathrm{U}}(s)\left(\Delta P_a^e(s) + \sum_{k \in \mathcal{C}_a^S} \frac{K_k^c}{R_k^c\left(1 + sT_k^c\right)} \Delta f_b(s)\right), \tag{9}$$

showing that the frequency deviation in the area under contingency depends also on the frequency deviation in the supporting area. To derive expressions of the frequency metrics, first we need to analyze the frequency deviation in area b. The transfer function $G_b^{\mathrm{B}}(s)$, which models the relation between $\Delta f_b(s)$ and $\Delta f_a(s)$, is similar to (7), where ω_b^n and ζ_b can be calculated using $\widehat{R}_b$ and $\widehat{F}_b$, meaning that both generators and HVDC converters participate in frequency support in area b.

Plugging $G_b^{\mathrm{B}}(s)$ into (9) introduces additional complexity to the derivation of the analytical expressions, since (even after the assumptions made in the previous sections) the transfer function $\Delta f_b(s)/\Delta P_a^e(s)$ becomes a fourth-order transfer function and, in turn, $\Delta f_a(s)/\Delta P_a^e(s)$ becomes a six-order transfer function. To overcome this issue, similarly to the previous section, we first consider a step-wise change of $\Delta f_a(s) = \Delta f_a^{\max}/s$, where $\Delta f_a^{\max}$ is the maximum allowable frequency deviation determined by the transmission system operator in area a. This assumption results in an overestimation of the absolute value of the frequency nadir in both areas. However, this guarantees that the RoCoF and the IFD stay within the operational limits. The frequency metrics for area b are similar to the ones described by (8a) and (8b), where $\widehat{R}_b$ and $\widehat{F}_b$ consider both generators and HVDC converters participating in the frequency support of area b.

Similar to the UCS case, we consider that there is no contribution of HVDC to the SSFD of the AC network that faces the contingency. To derive the frequency metrics for area a, we consider stepwise changes $\Delta P_a^e(s)$ and Δf_b as $-\Delta P_a/s$ and $\Delta f_b^{max}/s$, respectively. This leads to similar expressions for the RoCoF and steady state frequency deviation as in (6a) and (6c) and the following expression for the frequency nadir:

$$\Delta f_a^{\max} = \frac{\Delta P_a + \Delta f_b^{\max} \widetilde{R}_{a,b}^c}{\widehat{D}_b + \widehat{R}_a}\left(1 + \sqrt{\frac{T_a(\widehat{R}_a - \widehat{F}_a)}{\widehat{M}_a}} e^{-\zeta_a \omega_a^n t_a^m}\right). \tag{10}$$

We remind again the reader that (10) overestimates the value of the frequency nadir. However, it still ensures that the frequency of the area a will remain within the limits set by the transmission system operators.

IV. Optimization Framework

The calculation of the weighted model parameters depends on which synchronous generators are online and able to provide frequency support. Thus, in order to include frequency constraints in an optimization problem, specific variables associated with the status of the units must be defined. In a Unit Commitment Problem (UCP), the status of generators is modelled by means of binary variables. This allows to include ramping limits, minimum and maximum generation limits, minimum online and offline duration and start-up and shut-down costs. The frequency metrics derived in the previous section can thus be directly included in a UCP without modifying its basic structure. In this section, we present the UCP formulation, augmented with frequency constraints and reserve sharing through HVDC.

A. Basic Structure

The basic structure of the Unit Commitment problem is the minimization of the total system cost subject to generator, transmission system and power balance constraints. In this section, the objective function and these constraints will be quickly explained. For the complete formulation, the reader is referred to [22].

The objective function of a UCP is the sum of all the costs associated with power generation $g_{i,t}$ and reserve procurement $g^s_{i,t}$. In addition, load shedding $d^s_{j,t}$ and wind curtailment $w^c_{r,t}$ can be included.

Generator constraints include the minimum and maximum power output ($\underline{P}_i$ and $\overline{P}_i$), the upward and downward ramping limits ($\overline{R}_i$ and $\underline{R}_i$), and the minimum online and offline duration periods (T^{on}_i and T^{off}_i). A binary variable $u_{i,t}$ defines the online or offline status of unit i at the time instance t; additional constraints are included to model the start-up and shut-down variables $y_{i,t}$ and $z_{i,t}$. If load shedding and wind curtailment are included, additional variables are required to bound these variables between zero and the actual consumption (for loads) or production (for wind/solar producers).

For the transmission system, power flows of AC lines can be modelled using voltage angle differences ($\theta_{n,t} - \theta_{m,t}$) or power transfer distribution factor matrices ("DC" power flow approximation); power flows on HVDC lines are free variables ($f^{\text{DC}}_{k,t}$). To ensure safe operation, AC and HVDC thermal limits are enforced ($\overline{F}^{\text{AC}}_{n,m}$ and $\overline{F}^{\text{DC}}_{k}$). Finally, power balance constraints are introduced to ensure that generation and consumption are matched.

B. Weighted Model Parameters

The participation of generators and HVDC converters to frequency support is decided by means of additional binary variables: $v^g_{i,t}$ defines the participation of generators while $v^c_{a,b,t}$ the areas that are supported (index a) or support (index b). Since only online generators can offer frequency support, the following constraint is enforced:

$$v^g_{i,t} \leq u_{i,t} \qquad \forall i, \forall t \tag{11}$$

For the HVDC converters, depending on the SPC scheme applied, two different constraints are introduced. For the unilateral scheme:

$$v^c_{a,b,t} + v^c_{b,a,t} \leq 1 \qquad \forall a, \forall b \in \mathcal{A} \setminus \{a\}, \forall t \tag{12}$$

with $\mathcal{A}$ the set of asynchronous areas. Eq. (12) enforces that if area a is supported by area b, area a cannot support area b. For the bilateral scheme, instead, the following constraint is introduced:

$$v^c_{a,b,t} = v^c_{b,a,t} \qquad \forall a, \forall b \in \mathcal{A} \setminus \{a\}, \forall t \tag{13}$$

meaning that if area a is supported by area b, also area b is supported by area a.

With the new variables, the weighted model parameters are calculated as follows:

$$\widetilde{R}^g_{a,t} = \textstyle\sum_{i \in \mathcal{G}_a} \frac{K^g_i}{R^g_i} \overline{P}_i v^g_{i,t} \qquad \forall a, \forall t \tag{14a}$$

$$\widetilde{R}^c_{a,t} = \textstyle\sum_{k \in \mathcal{L}^{\text{DC}}_a} \frac{K^c_k}{R^c_k} \overline{F}_k v^c_{a,\sim,t} \qquad \forall a, \forall t \tag{14b}$$

$$\widetilde{F}^g_{a,t} = \textstyle\sum_{i \in \mathcal{G}_a} \frac{K^g_i F^g_i}{R^g_i} \overline{P}_i v^g_{i,t} \qquad \forall a, \forall t \tag{14c}$$

$$\widehat{R}_{a,t} = \widetilde{R}^g_{a,t} + \widetilde{R}^c_{a,t} \qquad \forall a, \forall t \tag{14d}$$

$$\widehat{F}_{a,t} = \widetilde{F}^g_{a,t} + \widetilde{R}^c_{a,t} \qquad \forall a, \forall t \tag{14e}$$

$$\widehat{M}_{a,t} = \textstyle\sum_{i \in \mathcal{G}_a} 2H^g_i \overline{P}_i u^g_{i,t} \qquad \forall a, \forall t \tag{14f}$$

with H^g_i the inertia constant of the synchronous unit i. Note that the subscript $\sim$ in (14b) means whatever area is connected to area a through the HVDC line k.

C. Frequency Constraints

The weighted model parameters are calculated to include frequency constraints in the optimization problem. This is done in order to limit the RoCoF, the IFD and the SSFD in the event of the worst contingency (N-1 security criterion), i.e. the loss of the biggest generating unit. For this, we consider a fixed power deviation $\Delta P^e_a = \max\{\overline{P}_i\}$, with $i \in \mathcal{G}_a$. This assumption is justified by the fact that the biggest generating units are usually nuclear power plants (mostly) contracted in the long term market to always produce at full capacity. Moreover, we do not consider these events to happen simultaneously in more than one area.

From (6a), it is possible to observe a linear dependence of the RoCoF on the inertia level of the AC system. Similarly, (6c) shows a linear dependence between the total sum of droop coefficients and the SSFD. Thus, these two frequency metrics can be bounded by bounding the corresponding weighted model parameters:

$$\widehat{M}_{a,t} \geq \frac{f^{\text{base}}_a}{\dot{f}^{\max}_a} \Delta P^e_a \qquad \forall a, \forall t \tag{15a}$$

$$\widetilde{R}^g_{a,t} \geq \frac{f^{\text{base}}_a}{\Delta f^{\text{ss,max}}_a} \Delta P^e_a - \widehat{D}_{a,t} \qquad \forall a, \forall t \tag{15b}$$

Being $\widehat{R}_{a,t}$ a linear combination of $\widetilde{R}^g_{a,t}$ and $\widetilde{R}^c_{a,t}$, by bounding $\widetilde{R}^g_{a,t}$ also $\widehat{R}_{a,t}$ is automatically bounded.

Regarding the IFD, it is not possible to directly include (6b) and (10) in the optimization problem as they are non-linear and non-convex. The authors in [13] introduce a piecewise linearization of the frequency nadir which consists of a set of

hyperplanes, activated by binary variables, that are included as equality constraints. The authors in [14], instead, introduce bounds on the single variables to avoid excursions of the frequency beyond the limits. However, the first approach requires many hyperplanes to accurately represent the nadir function, making the problem computationally intense to solve, while the second significantly reduces the feasible space. Within reasonable bounds (determined by realistic values of the weighted model parameters), (6b) is monotonically decreasing in all the considered variables, meaning that the higher is $\widehat{R}_{a,t}$, $\widehat{F}_{a,t}$ or $\widehat{M}_{a,t}$, the smaller is the IFD (see Fig. 3). Thus, the points on the boundary (i.e. close to the IFD limit) can be approximated with a hyperplane. This hyperplane, which is a linear combination of the weighted model parameters, divides the feasible space into two regions, one with the triplets ($\widehat{R}_{a,t}$,$\widehat{F}_{a,t}$,$\widehat{M}_{a,t}$) that violate the IFD requirements and one with the ones that do not. Thus in order to discard the triplets that violate the IFD constraints, the following inequality constraint is included in the optimization problem (for the UCS case):

$$\widehat{F}_{a,t} \geq A^{\mathrm{R}}_a \widehat{R}_{a,t} + A^{\mathrm{M}}_a \widehat{M}_{a,t} + A^{0}_a \qquad \forall a,\, \forall t \tag{16}$$

with A^{R}_a, A^{M}_a and A^{0}_a the coefficients of the hyperplane.

In the case of BCS, the maximum IFD depends on the weighted model parameters of the system that experiences the contingency and the supporting systems. Thus the 3D hyperplane becomes a 7D hyperplane (or more), and the IFD constraint is included as follows:

$$\begin{aligned}\widetilde{F}_{a,t} \geq \sum_{b\in\mathcal{A}_a} \left(A^{\mathrm{R}^g}_{a,b}\widetilde{R}^g_{b,t} + A^{\mathrm{M}}_{a,b}\widehat{M}_{b,t} + A^{\mathrm{F}}_{a,b}\widetilde{F}^g_{b,t} + A^{\mathrm{R}^c}_{a,b}\widetilde{R}^c_{a,b,t}\right) \\ + A^{\mathrm{R}}_a\widetilde{R}^g_{a,t} + A^{\mathrm{M}}_a\widehat{M}_{a,t} + A^{0}_a \qquad \forall a,\, \forall t\end{aligned} \tag{17}$$

with $\mathcal{A}_a$ the set of asynchronous areas connected to area a, and $A^{\mathrm{R}^g}_{a,b}$, $A^{\mathrm{M}}_{a,b}$, $A^{\mathrm{F}}_{a,b}$ and $A^{\mathrm{R}^c}_{a,b}$ the corresponding coefficients of the hyperplane.

This data-driven approach, which consists in (i) calculating the IFD for a large number of possible combinations of system parameters and in (ii) finding the points on the boundary to be approximated by the hyperplane, significantly increases the computational speed of the problem while keeping the relative error small (average relative error 0.04).

D. Post-contingency Constraints

With droop frequency controllers, the response of generators and HVDC converters is proportional to the ratio between their droop coefficient and the total droop in the system. To ensure that generators committed to provide frequency services and HVDC converters with SPC have enough capacity to support the system, some capacity must be reserved. The following constraints model the response of generator and HVDC converters and ensure enough capacity reservation:

$$g^s_{i,t} = v^g_{i,t}\frac{K^g_i\overline{P}_i}{R^g_i\widehat{R}_{(a|i\in\mathcal{G}_a),t}}\Delta P^e_{(a|i\in\mathcal{G}_a)} \qquad \forall i,\, \forall t \tag{18a}$$

$$g_{i,t} + g^s_{i,t} \leq u_{i,t}\overline{P}_i \qquad \forall i,\, \forall t \tag{18b}$$

$$f^s_{k,t} = v^c_{(a|k\in\mathcal{L}^{\mathrm{DC}}_a),\sim,t}\frac{K^c_k\overline{F}^{\mathrm{DC}}_k}{R^c_k\widehat{R}_{(a|k\in\mathcal{L}^{\mathrm{DC}}_a),t}}\Delta P^e_{(a|k\in\mathcal{L}^{\mathrm{DC}}_a)} \qquad \forall k,\, \forall t \tag{18c}$$

$$-\overline{F}^{\mathrm{DC}}_k \leq f^{\mathrm{DC}}_{k,t} + f^s_{k,t} \leq \overline{F}^{\mathrm{DC}}_k \qquad \forall k, \forall t \tag{18d}$$

with $g^s_{i,t}$ the response of generator i (equal to the reserved capacity), and $f^s_{k,t}$ the response of the HVDC converter k (and the reserved capacity). Constraints (18a) and (18c) are non-linear because $\widehat{R}_{a,t}$ appears in the denominator and the fraction is then multiplied by $v^g_{i,t}$ or $v^c_{a,\sim,t}$. In the following, two techniques to linearize these expressions are presented.

E. Relaxation techniques

In order to linearize contraints (18a) and (18c), the first step is to introduce a new variable $\widehat{S}_{a,t}$ such that:

$$\widehat{R}_{a,t}\widehat{S}_{a,t} = 1 \qquad \forall a,\, \forall t \tag{19}$$

This constraint is bilinear and, in order to linearize it, the McCormick relaxation is applied [23]. Unless the bounds of the variables are quite small, this relaxation is not tight. To improve it, a piecewise version of the relaxation is applied, as suggested in [24]. Constraint (19) is then substituted by:

$$\textstyle\sum_{x,y}\left(\underline{S}^a_y R^a_{x,y,t} + \underline{R}^a_x S^a_{x,y,t} - \underline{S}^a_y\underline{R}^a_x w^a_{x,y,t}\right) \leq 1 \qquad \forall a,\, \forall t \tag{20a}$$

$$\textstyle\sum_{x,y}\left(\overline{S}^a_y R^a_{x,y,t} + \overline{R}^a_x S^a_{x,y,t} - \overline{S}^a_y\overline{R}^a_x w^a_{x,y,t}\right) \leq 1 \qquad \forall a,\, \forall t \tag{20b}$$

$$\textstyle\sum_{x,y}\left(\overline{S}^a_y R^a_{x,y,t} + \underline{R}^a_x S^a_{x,y,t} - \overline{S}^a_y\underline{R}^a_x w^a_{x,y,t}\right) \geq 1 \qquad \forall a,\, \forall t \tag{20c}$$

$$\textstyle\sum_{x,y}\left(\underline{S}^a_y R^a_{x,y,t} + \overline{R}^a_x S^a_{x,y,t} - \underline{S}^a_y\overline{R}^a_x w^a_{x,y,t}\right) \geq 1 \qquad \forall a,\, \forall t \tag{20d}$$

$$\widehat{R}_{a,t} = \textstyle\sum_{x,y} R^a_{x,y,t}, \quad \widehat{S}_{a,t} = \textstyle\sum_{x,y} S^a_{x,y,t} \qquad \forall a,\, \forall t \tag{20e}$$

$$w^a_{x,y,t}\underline{R}^a_x \leq R^a_{x,y,t} \leq w^a_{x,y,t}\overline{R}^a_x \qquad \forall x,\, \forall y,\ \forall a,\, \forall t \tag{20f}$$

$$w^a_{x,y,t}\underline{S}^a_y \leq S^a_{x,y,t} \leq w^a_{x,y,t}\overline{S}^a_y \qquad \forall x,\, \forall y,\ \forall a,\, \forall t \tag{20g}$$

$$\textstyle\sum_{x,y} w^a_{x,y,t} = 1 \qquad \forall a,\, \forall t \tag{20h}$$

where $R^a_{x,y,t}$ and $R^a_{x,y,t}$ are new continuous variables (for the sake of space the index a is written as superscript), $w^a_{x,y,t}$ new binary variables and $\underline{R}^a_x$, $\overline{R}^a_x$, $\underline{S}^a_y$ and $\overline{S}^a_y$ the lower and upper bounds defining the segments in which $\widehat{R}_{a,t}$ and $\widehat{S}_{a,t}$ are divided. The subscript x refers to the x-th segment of

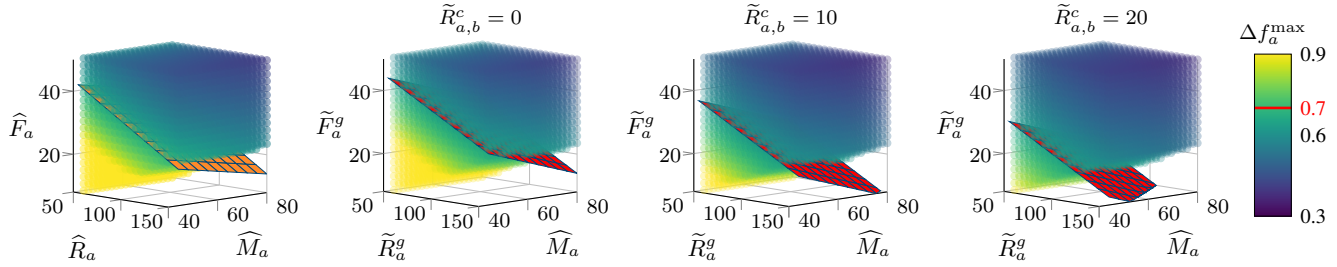

Fig. 3. Spatial representation of the frequency nadir function with the related hyperplanes. The orange plane is the 3D plane for the UCS, which divides the space into two regions, one with feasible and one with infeasible points. The red plane is the 7D plane for the BCS. The visualization of the 7D space is obtained by fixing $\widetilde{R}^g_b = 71$, $\widetilde{F}^g_b = 19$ and $\widehat{M}_b = 53$; three values of $\widetilde{R}^c_{a,b}$ are considered for the three plots. $\Delta f^{\max}_a$ is set to 0.7 Hz.

$\widehat{R}_{a,t}$ and y to the y-th segment of $\widehat{S}_{a,t}$. Given that $\widehat{S}_{a,t}$ is the reciprocal of $\widehat{R}_{a,t}$, the division of $\widehat{S}_{a,t}$ in segments is linked to the division of $\widehat{R}_{a,t}$, meaning that high accuracy can be obtained with few segments.

Similar to (19), the terms $v^g_{i,t}\widehat{S}_{a,t}$ and $v^c_{a,\sim,t}\widehat{S}_{a,t}$, which appear in constraints (18a) and (18c) after the introduction of the new variable, must be linearized. In this case, these terms are the product of a binary and a continuous variable, thus the *bigM* method can be applied [25]. Constraints (18a) and (18c) are then replaced by:

$$g^s_{i,t} = \frac{K^g_i \overline{P}_i}{R^g_i} \widehat{VS}^g_{i,(a|i\in\mathcal{G}_a),t} \Delta P^e_{(a|i\in\mathcal{G}_a)} \quad \forall i, \forall t \quad (21a)$$

$$f^s_{k,t} = \frac{K^c_k \overline{F}^{\text{DC}}_k}{R^c_k} \widehat{VS}^c_{k,(a|k\in\mathcal{L}^{\text{DC}}_a),\sim,t} \Delta P^e_{(a|i\in\mathcal{G}_a)} \quad \forall k, \forall t \quad (21b)$$

$$0 \le \widehat{VS}^g_{i,(a|i\in\mathcal{G}_a),t} \le v^g_{i,t} M \quad \forall i, \forall t \quad (21c)$$

$$\widehat{S}_{a,t} - (1 - v^g_{i,t})M \le \widehat{VS}^g_{i,(a|i\in\mathcal{G}_a),t} \le \widehat{S}_{a,t} \quad \forall i, \forall t \quad (21d)$$

$$0 \le \widehat{VS}^c_{k,(a|k\in\mathcal{L}^{\text{DC}}_a),\sim,t} \le v^c_{a,\sim,t} M \quad \forall i, \forall t \quad (21e)$$

$$\widehat{S}_{a,t} - (1 - v^c_{a,\sim,t})M \le \widehat{VS}^c_{k,(a|k\in\mathcal{L}^{\text{DC}}_a),\sim,t} \le \widehat{S}_{a,t} \quad \forall i, \forall t \quad (21f)$$

with $\widehat{VS}^g_{i,(a|i\in\mathcal{G}_a),t}$ and $\widehat{VS}^c_{k,(a|k\in\mathcal{L}^{\text{DC}}_a),\sim,t}$ the new continuous variables. As pointed out in [26], the selection of the right M is a delicate process: with too small values, constraint (21c) might be binding even when $v^g_{i,t}$ is equal to one. On the other hand, too large values might cause numerical inaccuracies when solving the problem. In this case, since $\widehat{S}_{a,t}$ is the reciprocal of $\widehat{R}_{a,t}$, and $\widehat{R}_{a,t} \ge 1$, it is possible to set $M = 10$ without incurring in any of these problems.

F. Optimization Problem

The UCP with frequency constraints, HVDC SPC and generator frequency support is formulated as:

$$\begin{aligned} &\min \quad \textit{Total system cost} \\ &\text{s.t.} \quad \textit{Generator constraints} \\ &\qquad \textit{Transmission system constraints} \\ &\qquad \textit{Power balance constraints} \\ &\qquad (11),\ (14a)-(14f),\ (15a),\ (15b) \\ &\qquad (12),\ (16) \text{ or } (13),\ (17) \\ &\qquad (20a)-(20h),\ (21a)-(21f),\ (18b),\ (18d) \end{aligned} \quad (22)$$

Constraints (12) and (16) are enforced in case of unilateral exchange of reserves; for the bilateral exchange, instead, constraints (13) and (17) are introduced. In case of different control schemes applied between different zones, a combination of these constraints is included.

The energy prices can be calculated as suggested in [27]: first the solution of the MILP problem is calculated, then the integer variables are relaxed to continuous variables and fixed to the obtained solution, and the problem (now a LP problem) is solved again. In this way, Lagrangian multipliers can be obtained. Energy prices are then calculated as the derivative of the Lagrangian function of the relaxed problem ($\mathcal{L}^*$) with respect to a marginal increase δ in the demand:

$$\text{EP}_n = \frac{\partial \mathcal{L}^*}{\partial \delta} = \lambda_n - \textstyle\sum_{d\in\mathcal{D}_n} \rho_d \quad (23)$$

with λ_n the Lagrangian multiplier associated with the nodal balance equation (bus n) and ρ_d the multiplier associated with the upper bound on load shedding (load d).

For the numerical example in the next section, the reserve are procured on a daily basis and the energy market is cleared for a 24-hour time period. This means that, if a generator (or HVDC converter) commits to provide frequency support, the capacity is reserved for the whole day. The reasoning behind this is that, in Europe, most of the TSOs procure reserves in D-2 or D-1 for the entire day of operation, and the energy market is cleared once for every hour of the following day. However, the presented formulation is general and it also allows for hourly procurement if required. Also, the unit commitment problem could be solved for longer time windows. In case the size of the UCP would make it intractable, decomposition techniques such as the one in [28] could be applied to decompose the problem by time instances. These techniques could also be used for spatial decomposition of the problem, e.g. to solve it for each area. Finally, the problem formulation is presented in a deterministic setup; however, the problem formulation could also be solved in a probabilistic fashion.

V. Numerical Results

The presented formulation has been tested on a system with two asynchronous areas connected by two HVDC links. Since the focus of the study is on the center of inertia frequency, the intra-zonal network configuration does not have any impact on the results. Thus, the AC systems in the two areas have been omitted to enhance the readability of the results. Note that the inclusion of the AC systems would not increase the complexity or the computation time of the problem.

The two areas are approx. of the same size: the installed generating capacity is 13 and 11 GW respectively (35 and 30 generating units), with a peak demand of 9 and 6 GW. The synchronous generation mix includes nuclear, natural gas, oil, hard coal, lignite and biomass steam units; the maximum RES penetration in the two areas is 47% and 55%. Two nuclear power plants are the dimensioning incidents in the two areas, respectively 600 MW and 550 MW. The total transfer capacity of the HVDC links is 500 MW. The demand, wind and solar time series correspond to the actual profiles of East and West Denmark during July 2019. The dynamic parameters of generators are based on [14], while the economic parameters are taken from [29]. The system data is available in [30].

To assess the benefit of the SPC implementation, four simulations are executed: i) "*no lim*", the frequency constraints are omitted in the model and the reserve procurement is done by enforcing a minimum reserve requirement, ii) "*no SPC*", the reserve procurement is done in accordance to the frequency constraints, iii) "*unilateral*" and iv) "*bilateral*", HVDC lines are involved in the exchange of frequency services, first with the unilateral scheme and then with the bilateral. All the simulations are run using YALMIP [31] and Gurobi [32].

By looking at Fig. 4, it is clear that frequency constraints are violated if they are not included in the model (blue lines). This does not happen in the other simulations, showing that procuring reserves only on a cost basis without considering the response of the system is not enough to ensure its stability.

[1]Used as a reference for the other simulation, the unit is million Euros.

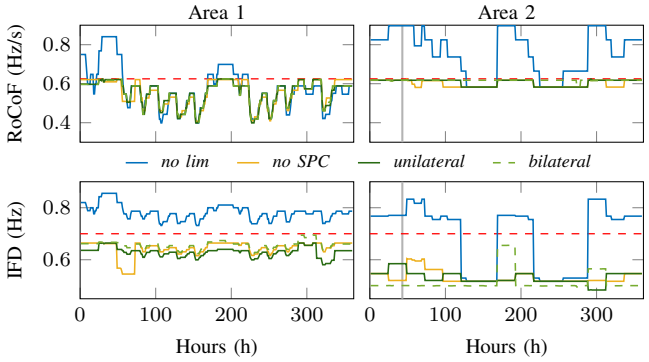

Fig. 4. Frequency metrics for the four simulations. The red dashed lines are the limits (0.625 Hz/s for the RoCoF and 0.7 Hz for the IFD), while the gray vertical ones highlight the time instance used for validation.

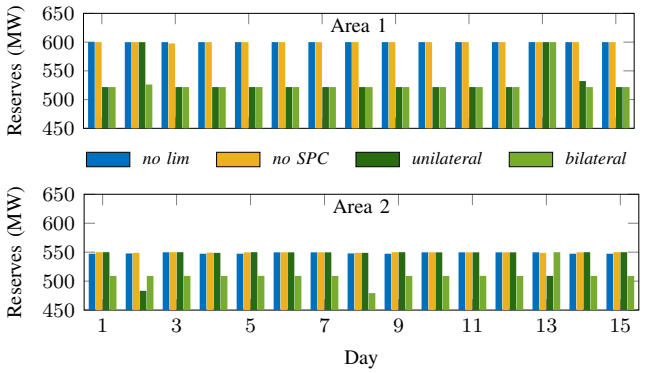

Fig. 5. Generation capacity reserved during each day of the simulations.

Moreover, from Fig. 5, it is clear that the exchange of frequency reserves through HVDC can help reducing the costs of reserve procurement while maintaining the system N-1 secure. In terms of system costs, the total costs decrease by 1% in the "*unilateral*" case and by 1.4% in the "*bilateral*". The comparison is made with respect to "*no SPC*" (total system cost 69.95 M€), as in the "*no lim*" case (total system cost 68.16 M€) frequency constraints are not included (and are also violated) and thus the comparison would not be fair. The cost reduction is more pronounced if we only look at the reserve procurement costs, which decrease by 8.5% in the "*unilateral*" case and by 10.8% in the "*bilateral*" (in the "*no SPC*" case the cost is 3.9 M€).

The impact of the activation of HVDC SPC on the market outcome is provided in Table I. The amount of generator

TABLE I
IMPACT OF HVDC EPC ON THE MARKET OUTCOME.

		no lim	*no SPC*[1]	*unilateral*	*bilateral*
Reserve Cost	AREA 1	-2.2%	(1.77)	-12.3%	-14.21%
	AREA 2	-11.6%	(2.15)	-5.3%	-7.9%
Energy Cost	AREA 1	+2.6%	(35.86)	+1.5%	+1.6%
	AREA 2	-8.1%	(30.17)	-3.1%	-3.8%
Total Cost	AREA 1	+2.3%	(37.63)	+0.9%	+0.8%
	AREA 2	-8.3%	(32.33)	-3.2%	-4.1%
Gen. Rev.	AREA 1	+13.1%	(28.89)	+5.7%	+5.9%
	AREA 2	+27.1%	(15.67)	-3.4%	+0.2%
Load Pymt.	AREA 1	-5.0%	(71.16)	-1.5%	-1.7%
	AREA 2	-7.5%	(42.85)	+0.8%	-
HVDC Rev.	-	-54.0%	(0.23)	+21.0%	+9.0%

TABLE II
COMPARISON OF THE IFD OBTAINED WITH THE ANALYTICAL EXPRESSIONS AND THE DYNAMIC SIMULATIONS.

		no lim	*no SPC*	*unilateral*	*bilateral*
Analytical expression	AREA 1	-	-	0.1550	0.1496
	AREA 2	0.7707	0.5204	0.5849	0.5007
Dynamic simulation	AREA 1	-	-	0.1261	0.1001
	AREA 2	0.7706	0.5204	0.5896	0.4875

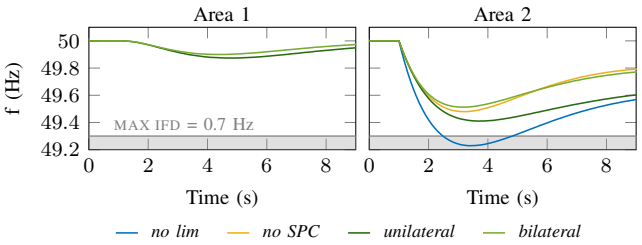

Fig. 6. IFD following the dimensioning incident in area 2. The left graph shows the IFD in area 1 due to the activation of HVDC EPC.

capacity that is not reserved (because of SPC), results in more capacity available in the energy market. Since generators must be dispatched to provide support, this means that local production increases in the importing area (without affecting the energy price), while exports decrease in the other area. This means more revenues for the generators in the importing area and less revenues for the ones in the exporting area. At the same time, the increased generation results in higher energy production and lower reserve procurement costs in area 1.

Looking at load payments, these increase in area 2 while decreasing in area 1. The explanation for this is that the hours with congestion decrease (respectively 283, 222, 163 and 188 hours in the four simulations) meaning that consumers in the two areas are subject to the same price for more hours. Given that area 1 is the "high price" area and area 2 the "low price" one, the result is lower payments from the loads in area 1 and higher payments from the loads in area 2.

Concerning the HVDC line owner, one could expect lower congestion rents due to the reservation of a portion of the capacity. However, the lower capacity results in higher price differences (respectively 0.58, 1.28, 2.04 and 1.81 €/MWh in average) and in turns in higher congestion rent.

Finally, Table II compares the IFDs calculated with the analytical expressions to the ones obtained through dynamic simulation (Fig. 6) for a specific time instance (hour 43). The two values match in all the cases, only in the "*bilateral*" case the calculated IFD is a bit higher (this was expected due to the assumptions in Section II), meaning that the UC solution is more conservative.

VI. CONCLUSION

While RES are being integrated into electrical networks around the world, transmission system operators are facing serious challenges in operating the system with low inertia levels. With the ambitious climate targets set by the European Commission, coordination between system operators will be key to secure the operation of power systems during the energy transition. In this regard, the goal of this paper is to highlight the benefits of sharing reserves through HVDC interconnectors

using their Supplementary Power Control (SPC) functionality. First, we have derived analytical expressions for the frequency metrics of asynchronous AC systems connected by HVDC lines. We have then introduced these metrics as constraints into a unit commitment problem. Two different control schemes for HVDC converters have been analyzed: the unilateral scheme, which allows to share reserves only in one direction, and the bilateral scheme, which allows it in both directions. The results of the optimization problem show how procurement costs can be reduced up to 10% if the SPC functionality of HVDC lines is activated. Moreover, we have analyzed how generators and loads are impacted by these modifications, showing that the unilateral scheme might results in one-side benefits, while with a bilateral scheme the benefits are more distributed.

REFERENCES

[1] ENTSO-E, "Completing the map - Power system needs in 2030 and 2040," Tech. Rep., Aug. 2020.

[2] G. S. Misyris, S. Chatzivasileiadis, and T. Weckesser, "Robust Frequency Control for Varying Inertia Power Systems," in *2018 IEEE PES ISGT Conf. Europe*, Oct. 2018, pp. 1–6.

[3] ENTSO-E, "Vision on Market Design and System Operation towards 2030," Tech. Rep., Aug. 2020.

[4] EirGrid and SONI, "RoCoF Alternative & Complementary Solutions Project," Tech. Rep., Mar. 2016.

[5] AEMO, "Future Power System Security Program (FPSSP) - Progress report," Tech. Rep., Mar. 2017.

[6] Nordic TSOs, "Challenges and Opportunities for the Nordic Power System," Tech. Rep., Aug. 2016.

[7] National Grid, "Operating a Low Inertia System - A System Operability Framework document," Tech. Rep., Feb. 2020.

[8] E. Ørum, L. Haarla *et al.*, "Future System Inertia 2," ENTSO-E, Tech. Rep., Aug. 2018.

[9] B. Hartmann, I. Vokony, and I. Táczi, "Effects of decreasing synchronous inertia on power system dynamics - Overview of recent experiences and marketisation of services," *Int. Trans. Electr. Energy Syst.*, vol. 29, no. 12, June 2019.

[10] O. Dudurych and M. Conlon, "Impact of Reduced System Inertia as a Result of Higher Penetration Levels of Wind Generation," in *2014 49th Int. UPEC*, 2014, pp. 1–6.

[11] D. Obradovic, *Coordinated Frequency Control Between Interconnected AC/DC Systems*. Licentiate dissertation, KTH Royal Institute of Technology, Oct. 2020.

[12] A. Tosatto, M. Dijokas *et al.*, "Sharing Reserves through HVDC: Potential Cost Savings in the Nordic Countries," *IET Gener. Transm. Distrib.*, Sept. 2020.

[13] H. Ahmadi and H. Ghasemi, "Security-Constrained Unit Commitment With Linearized System Frequency Limit Constraints," *IEEE Trans. Power Syst.*, vol. 29, no. 4, pp. 1536–1545, July 2014.

[14] M. Paturet, U. Markovic *et al.*, "Stochastic Unit Commitment in Low-Inertia Grids," *IEEE Trans. Power Syst.*, vol. 35, pp. 3448–3458, 2020.

[15] L. Badesa, F. Teng, and G. Strbac, "Optimal Portfolio of Distinct Frequency Response Services in Low-Inertia Systems," *IEEE Trans. Power Syst.*, p. 1–1, 2020.

[16] Z. Chu, U. Markovic *et al.*, "Towards Optimal System Scheduling With Synthetic Inertia Provision From Wind Turbines," *IEEE Trans. Power Syst.*, vol. 35, no. 5, pp. 4056–4066, 2020.

[17] J. Fradley, R. Preece, and M. Barnes, "VSC-HVDC for frequency support (a review)," in *2017 13th IET Int. Conf. ACDC Power Transmiss.*, 2017, pp. 1–6.

[18] J. Huang and R. Preece, "HVDC-based fast frequency support for low inertia power systems," in *2017 13th IET Int. Conf. ACDC Power Transmiss.*, 2017, pp. 1–6.

[19] P. M. Anderson and M. Mirheydar, "A low-order system frequency response model," *IEEE Trans. Power Syst.*, vol. 5, pp. 720–729, 1990.

[20] Q. Shi, F. Li, and H. Cui, "Analytical Method to Aggregate Multi-Machine SFR Model With Applications in Power System Dynamic Studies," *IEEE Trans. Power Syst.*, vol. 33, no. 6, pp. 6355–6367, 2018.

[21] U. Markovic, Z. Chu *et al.*, "LQR-Based Adaptive Virtual Synchronous Machine for Power Systems With High Inverter Penetration," *IEEE Trans. Sustain. Energy*, vol. 10, no. 3, pp. 1501–1512, 2019.

[22] G. W. Chang, Y. D. Tsai *et al.*, "A Practical Mixed Integer Linear Programming Based Approach for Unit Commitment," in *2004 IEEE PES General Meeting*, vol. 1, Aug. 2004, pp. 221–225.

[23] G. P. McCormick, "Computability of global solutions to factorable nonconvex programs: Part I — Convex underestimating problems," *Math. Program.*, vol. 10, no. 1, pp. 147–175, Dec. 1976.

[24] P. M. Castro, "Tightening piecewise McCormick relaxations for bilinear problems," *Comput. Chem. Eng.*, vol. 72, pp. 300–311, Jan. 2015.

[25] J. Fortuny-Amat and B. McCarl, "A Representation and Economic Interpretation of a Two-Level Programming Problem," *J. Oper. Res. Soc.*, vol. 32, no. 9, pp. 783–792, Sept. 1981.

[26] S. Pineda and J. M. Morales, "Solving Linear Bilevel Problems Using Big-Ms: Not All That Glitters Is Gold," *IEEE Trans. Power Syst.*, vol. 34, no. 3, pp. 2469–2471, Jan. 2019.

[27] R. P. O'Neill, P. M. Sotkiewicz *et al.*, "Efficient market-clearing prices in markets with nonconvexities," *Eur. J. Oper. Res.*, vol. 164, no. 1, pp. 269–285, July 2005.

[28] B. Hua, R. Baldick, and J. Wang, "Representing Operational Flexibility in Generation Expansion Planning Through Convex Relaxation of Unit Commitment," *IEEE Trans. Power Syst.*, vol. 33, pp. 2272–2281, 2018.

[29] A. Tosatto and S. Chatzivasileiadis, "HVDC Loss Factors in the Nordic Power Market," *Electr. Power Syst. Res.*, vol. 190, p. 106710, Jan. 2021.

[30] A. Tosatto, "SCUCP HVDC EPC," GitHub repository, 2020. Available: https://github.com/antosat/SCUCP_HVDC_EPC.

[31] J. Löfberg, "YALMIP : A Toolbox for Modeling and Optimization in MATLAB," in *Proc. CACSD Conference*, Taipei, Taiwan, 2004.

[32] Gurobi Optimization, LLC, "Gurobi optimizer reference manual," 2020. [Online]. Available: http://www.gurobi.com

[Pub. C] Grid Supporting VSCs in Power Systems with Varying Inertia and Short-Circuit Capacity

Authors:
G. S. Misyris, J. A. Mermet-Guyennet, S. Chatzivasileiadis and T. Weckesser

Published in:
2019 IEEE Milan PowerTech

DOI:
10.1109/PTC.2019.8810979

Grid Supporting VSCs in Power Systems with Varying Inertia and Short-Circuit Capacity

George S. Misyris, *Student Member, IEEE,* Jeanne A. Mermet-Guyennet, *Student Member, IEEE,* Spyros Chatzivasileiadis, *Senior Member, IEEE,* and Tilman Weckesser, *Member, IEEE*

***Abstract*—Voltage Source Converters (VSCs) can offer various control strategies to enable realization of the vision of a "Global Grid". With the increasing penetration of renewable energy sources, it is becoming more frequent for VSCs to be required to provide active and reactive power regulation. In this paper, a model of a grid-supporting VSC connected to a weak AC grid with low Short Circuit Capacity (SCC) and low inertia is presented. The impact of SCC and inertia is then illustrated by means of small-signal stability, H_2 norm and large-disturbance analysis.**

***Index Terms*—High Voltage Direct Current (HVDC), stability analysis, Grid-Supporting Voltage Source Converter, weak AC grid, varying inertia.**

I. INTRODUCTION

Due to national and global climate targets aiming at reducing the emission of greenhouse gases [1], Renewable Energy Sources (RES) progressively replace conventional generation based on fossil fuels. Increased penetration of RES adds significant uncertainty to the dynamic behaviour of power systems. This originates from the fluctuating nature of resources such as wind and solar as well as from the fact that RES are often connected through power electronics to the grid. As a result, system parameters such as inertia and Short-Circuit Capacity (SCC) will vary greatly over time, which will affect the strength and stability of (Alternating Current) AC [2].

Additionally, High Voltage Direct Current (HVDC) connections make their way against installation of new AC lines [3]. These HVDC connections are based either on Line Commutated Converters (LCCs) or Voltage Source Converters (VSCs) [4]. However, VSCs have been gaining momentum, because of their flexibility and control capabilities [5]. Consequently, they are ideally suited to integrate the growing capacity of RES being installed.

To ensure stable grid operation in the absence of conventional generators, grid-connected VSCs should participate in the regulation of the AC grid voltage and frequency, by controlling the active and reactive power delivered to the grid. These VSCs are classified as grid-supporting converters and their outer controllers are commonly equipped with droop control algorithms (P/f and Q/V droop characteristic) to avoid communication-based solutions [6].

By taking advantage of the ability of power electronics to respond fast using a P-f droop characteristic for HVDC-VSC interconnections becomes a feasible solution to provide frequency support in AC systems with low inertia. It has been demonstrated that this is an efficient approach for reducing the maximum frequency deviation in such systems [7], [8]. In [7], a review of supplementary local control strategies for VSC-HVDC for low-inertia and islanded systems is presented. In [9], In [8], a frequency control scheme for VSCs, which are part of an HVDC grid connecting asynchronous AC systems, is proposed. In these studies, time domain simulations were used to verify the impact of the $P-f$ droop characteristic of the VSC on frequency stability. However, by time domain simulation analysis, it does not become analytically evident, how the VSC control gains contribute to AC frequency regulation. As indicated in [10], H_2 system norm can be incorporated to provide a measure of the magnitude of the system output in response to a disturbance. Therefore, in this work the H_2-norm is considered as a performance metric to validate the impact of the VSC control parameters on inertial and primary frequency response.

Apart from low inertia, the system can be subject to low SCC, which is dependent on the system strength. In [11], the small-signal stability of a VSC connected to weak AC system is studied, where the results show that the maximum power transfer capability of the VSC-HVDC converter is affected by the PLL gains. In [12], the authors propose a grid synchronization mechanism by introducing an impedance-conditioning term in the Phase Locked Loop (PLL), to increase the range of stable power transfer of VSCs, which operate in weak grids. Furthermore, in [5], an investigation of the stability of VSC connected subject to low SCC is performed, where the impact of the various control parameters on system stability and maximum stable power transfer of VSC are studied. In the aforementioned work, VSCs operate in a grid-feeding mode, where the active and reactive power injected to the grid are kept constant.

However as mentioned above, it is envisioned that in a future grid with high penetration from inverter-based generation and transmission, it will be necessary that VSCs actively support the grid and, hence, are operated in a grid-supporting mode. This could be realized by adding $P-f$ and $Q-V$ droop characteristics, which can affect the stability of the system and the dynamic limit of the maximum power transfer capability. An investigation of this is carried out in this work.

The contribution of this paper is to provide a groundwork for understanding the nonlinear behavior of grid-supporting VSCs, connected to weak AC grids. The system model, used in this paper, is an extension of the one presented in [5]. Moreover, constraints on the magnitudes of VSC control gains

G. S. Misyris, J. A. Mermet-Guyennet, S. Chatzivasileiadis and T. Weckesser are with the Department of Electrical Engineering, Technical University of Denmark, 2800 Kgs. Lyngby, Denmark (e-mail: {gmisy, jamg, spchatz, jtgw}@elektro.dtu.dk).

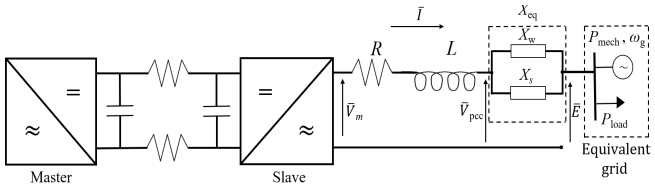

Fig. 1. Test system: VSC and equivalent grid

are defined based on eigenvalue and H_2 norm analysis. An investigation on the dynamic limit for a sudden drop of the SCC is carried out. At last, the influence of the VSC on the inertial and primary frequency response is analyzed using H_2 norm and time-domain simulations.

This paper is organized as follows: Section II describes the system state space model of the system. In section III, a stability analysis of a VSC connected to weak AC system is performed. Section IV demonstrates the system response to large disturbances. Conclusions are drawn in Section VI.

II. System Modeling

In this section, the VSC control structure is presented, as well as the equations forming the state space model of the overall system. The state space representation relates the state variables, x, and the inputs of the system, u to their derivatives, $\dot{x}$ and outputs of the system, y in the form:

$$\dot{x} = f(x, u) \tag{1}$$

$$y = g(x, u) \tag{2}$$

where $f(x, u)$ corresponds to the first order non-linear differential equations of the system, and $g(x, u)$ to the algebraic equations relating the outputs of the system to its state variables and inputs.

Fig. 1 shows the study system, i.e. two VSCs in a master-slave configuration. With this configuration, the DC link voltage $V_{\rm dc}$ is assumed to remain constant as it is controlled by the master VSC. The slave VSC controls the current flowing through the phase reactor by adjusting the voltage $V_{\rm m}$. Fig. 2 demonstrates the inner and outer control loops of the VSC.

The VSC and its components are represented in the dq frame, whose d-axis is shifted of an angle $\theta_{\rm pll}$ with the x-axis of the xy frame, rotating at the speed of the Center Of Inertia (COI) $\omega_{\rm coi}$ obtained from angular speed of the generator equivalent. $X_{\rm eq}$ represents the Thevenin equivalent reactance of the AC grid. The equivalent reactance $X_{\rm eq}$ can be defined as a function of SCC [11]:

$$X_{\rm eq} = \frac{V_{\rm rated}^2}{SCC \cdot P_{\rm rated}} \tag{3}$$

where $V_{\rm rated}$ and $P_{\rm rated}$ are the rated AC voltage and power of the VSCs, respectively.

The AC grid is represented by a generator and a load. The bus corresponding to equivalent grid is considered as an angle reference. The corresponding equations are summarized below, all quantities being expressed in per unit, except for the angular frequencies, in rad/s. It is assumed that the magnitude of E is equal to 1 p.u. and it is kept constant during the disturbances.

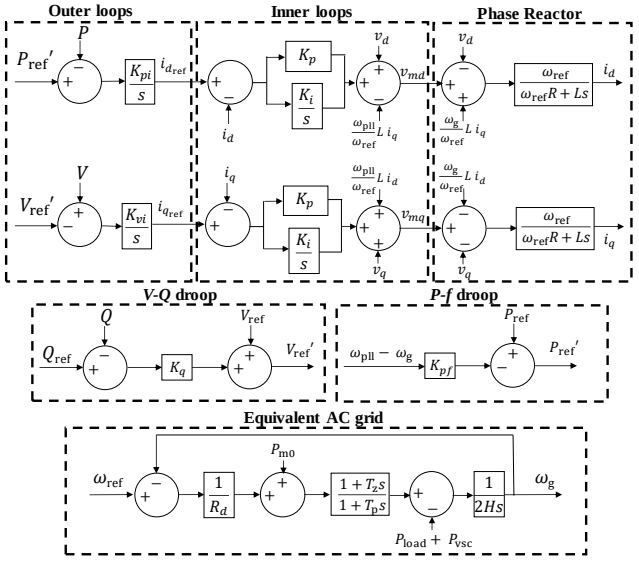

Fig. 2. Test system: VSC control

A. Electromechanical dynamics of AC system

In this section, an equivalent to represent the inertial and primary frequency response of AC system is implemented according to [13]. The purpose of the equivalent is to capture the COI frequency deviation after a power disturbance, with which the PLL is aligned. Since, a single machine equivalent is considered, $\omega_{\rm coi}$=$\omega_{\rm g}$, where $\omega_{\rm g}$ corresponds to the frequency of the equivalent grid. As mentioned in [13], the current model represents primary frequency control, where power is dominantly provided by steam turbines. The nominal rotor speed is $\omega_{\rm ref} = 2\pi \cdot 50$ rad/s. The phase angle $\theta_{\rm g}$ of the voltage of the equivalent grid's generator is such as:

$$\frac{d\theta_{\rm g}}{dt} = \omega_{\rm ref}\Delta\omega_{\rm g} \tag{4}$$

where $\Delta\omega_{\rm g} = \omega_{\rm g} - \omega_{\rm ref}$. The dynamics of the frequency deviation in response of a change in electric active power seen from the equivalent grid are derived from the swing equation:

$$\frac{d\Delta\omega_{\rm g}}{dt} = \frac{1}{M}\left(P_{\rm mech} + P_{\rm vsc} - P_{\rm load}\right) \tag{5}$$

where $P_{\rm mech}$ corresponds to the mechanical power input of the generator and $P_{\rm vsc}$ is the electrical power of the VSC received by the generator. The real part of the equivalent grid impedance is neglected, thus $P_{\rm vsc} = v_d i_d + v_q i_q = E_d i_d + E_q i_q$, where v_d, E_d and v_q, E_q are the d and q components of $\bar{V}_{\rm pcc}$ and $\bar{E}$, respectively. The i_d and i_q variables correspond to d and q components of the current flowing through the phase reactor and the equivalent grid impedance. The parameter H is the system inertia constant given in seconds.

With a speed droop $R_{\rm d}$, and a primary frequency control similar to the one provided by steam turbines characterized by time constants $T_{\rm z}$ and $T_{\rm p}$ as described in [13], the equivalent grid mechanical power dynamics can be written as:

$$\begin{aligned}\frac{dP_{\rm mech}}{dt} = &-\frac{1}{T_{\rm p}}(P_{\rm mech} - P_{m0}) - \frac{1}{R_{\rm d}T_{\rm p}}\Delta\omega_{\rm g} \\ &- \frac{T_{\rm z}}{2HR_{\rm d}T_{\rm p}}(P_{\rm mech} - P_{\rm load} - P_{\rm vsc})\end{aligned} \tag{6}$$

B. Phase-Locked Loop (PLL)

The VSC is synchronized with the corresponding AC grid through a PLL and aligned with the COI frequency. The PLL provides an estimation of the phase angle $\theta_{\rm pll}$ of the voltage $V_{\rm pcc}$ at the Point of Common Coupling (PCC). By adjusting v_q with a PI controller, it aims at aligning the voltage phasor $\bar{V}_{\rm pcc}$ with the d-axis of the dq rotating frame, so that in the steady-state $\omega_{\rm pll} = \omega_{\rm g}$, $v_d = V_{\rm ref}$ and $v_q = 0$. It can hence be represented by the following equations:

$$\frac{d\theta_{\rm pll}}{dt} = \omega_{\rm pll} - \omega_{\rm g} \tag{7}$$

$$\frac{dM_\omega}{dt} = K_{\rm i\omega} v_q \tag{8}$$

$$\omega_{\rm pll} = K_{p\omega} v_q + M_\omega \tag{9}$$

with $K_{\rm i\omega}$ and $K_{p\omega}$ the integral and proportional gains of the PI controller. M_ω is the integrator internal state of the PLL control system.

C. Phase reactor

The relations between the current I, the voltage output of the VSC V_m and the voltage at the PCC $V_{\rm pcc}$ in the dq frame are as follows:

$$L\frac{di_d}{dt} = \omega_{\rm ref}\left(\frac{\omega_{\rm g}}{\omega_{\rm ref}} L i_q - R i_d + v_{md} - v_d\right) \tag{10}$$

$$L\frac{di_q}{dt} = \omega_{\rm ref}\left(-\frac{\omega_{\rm g}}{\omega_{\rm ref}} L i_d - R i_q + v_{mq} - v_q\right) \tag{11}$$

where L is the inductance and R the resistance of the phase reactor. The variables v_{md} and v_{mq} correspond to the d and q components of voltage $\bar{V}_m$.

D. Inner current control loops

The current controller keeps the currents i_d and i_q to their references values, $i_d^{\rm ref}$ and $i_q^{\rm ref}$ by adjusting the components of the voltage of the VSC, v_{md} and v_{mq} (see Fig. 2):

$$v_{md} = v_d - \frac{\omega_{\rm pll}}{\omega_{\rm ref}} L i_q + K_{\rm p}(i_d^{\rm ref} - i_d) + M_d \tag{12}$$

$$v_{mq} = v_q + \frac{\omega_{\rm pll}}{\omega_{\rm ref}} L i_d + K_{\rm p}(i_q^{\rm ref} - i_q) + M_q \tag{13}$$

$$\frac{dM_d}{dt} = K_{\rm i}(i_d^{\rm ref} - i_d), \quad \frac{dM_q}{dt} = K_{\rm i}(i_q^{\rm ref} - i_q) \tag{14}$$

where $K_{\rm p}$ and $K_{\rm i}$ are the proportional and integral gains of the PI controllers, and M_d and M_q are the internal states of the integrators.

E. Outer control loops

The outer control is used to calculate the d- and q-axis current references, $i_d^{\rm ref}$ and $i_q^{\rm ref}$. In this current control configuration of the VSC, the active current reference $i_d^{\rm ref}$ is adjusted to control the active power P injected by the VSC to its reference $P_{\rm ref}$. Due to the $P - f$ droop characteristic, the active power reference is adjusted in response to a deviation of the PLL frequency $\omega_{\rm pll}$ with respect to the grid frequency, $\omega_{\rm g} = \omega_{\rm ref} + \Delta\omega_{\rm g}$, with $K_{\rm pf}$ the corresponding frequency droop gain. It should be noted that a deadband is considered in the range of [49.9, 50.1] Hz, to avoid continuous changes in the AC frequencies of the interconnected areas.

The reactive current reference $i_q^{\rm ref}$ aims at keeping the voltage $V_{\rm pcc}$ at the PCC to its reference $V_{\rm ref}$, which is also adjusted by a $V - Q$ droop control characteristic of gain $K_{\rm q}$. The two control loops are implemented with integral controllers of gains K_{id} and K_{iq} (both positive).

$$\frac{di_d^{\rm ref}}{dt} = K_{id}\left(P_{\rm ref} - K_{\rm pf}(\omega_{\rm pll} - \omega_{\rm g}) - P_{\rm vsc}\right) \tag{15}$$

$$\frac{di_q^{\rm ref}}{dt} = K_{iq}\left(V_{\rm pcc} - V_{\rm ref} + K_{\rm q}(Q_{\rm vsc} - Q_{\rm ref})\right) \tag{16}$$

where $Q_{\rm vsc} = v_q i_d - v_d i_q$ and $V_{\rm pcc} = \sqrt{v_d^2 + v_q^2}$

F. Final state-space model

Based on the grid equations, the d and q component of the voltage at the PCC can be written as:

$$v_d = -X_{\rm eq} i_q + E\cos(\theta_{\rm g} - \theta_{\rm pll}) \tag{17}$$

$$v_q = X_{\rm eq} i_d + E\sin(\theta_{\rm g} - \theta_{\rm pll}) \tag{18}$$

where $X_{\rm eq}$=$X_{\rm w}||X_{\rm s}$. After elimination of the algebraic equations describing $\omega_{\rm pll}$, v_{md}, v_{mq}, v_d and v_q in the above equations, we obtain a set of 11 differential equations corresponding to the vector of 11 state variables (19).

$$x = [\theta_{\rm pll}, M_\omega, i_d, i_q, M_d, M_q, i_d^{\rm ref}, i_q^{\rm ref}, \Delta\omega_{\rm g}, \theta_{\rm g}, P_{\rm mech}] \tag{19}$$

These differential equations form the state-space representation and can be expressed in the following way:

$$\frac{dx}{dt} = Ax + B_u u + B_w w \tag{20}$$

$$z = C_z x \tag{21}$$

where x is the state vector, w the disturbance vector, u the input vector and z the output vector. The matrices A, B_u, B_w are defined based on the differential and algebraic equations (7)-(18).

Moreover, the input vector u contains the variables that can be used to control the system. The disturbance vector w consists of the variables that can not be used for controlling the system. At last, the vector z includes the variables that can be observed and be used by the controller. The vectors u, w and z are given by:

$$u = [P_{\rm ref}, V_{\rm ref}, P_{\rm m0}, Q_{\rm ref}],\ \ w = [P_{\rm load}],\ \ z = [\Delta\omega_{\rm g}] \tag{22}$$

III. Small-signal stability analysis of VSC connected to weak AC system

The system shown in Fig. 1 was used for the stability analysis and validation. A linearization of the system of differential-algebraic equations is performed. The control parameters used for model validation are tuned according to [5] and shown in Table I. For the stability analysis the equivalent grid impedance is equal to $X_{\rm eq}$ = $X_{\rm w}$ = 2 p.u..

TABLE I
CONTROL AND SYSTEM PARAMETERS

Parameter	Value	Parameter	Value	Parameter	Value
R	0.01	L	0.2	M	8
K_{p}	0.2574	K_{i}	57.3	R_{d}	0.08
K_{pi}	20	K_{vi}	15	T_{z}	1.2
$K_{p\omega}$	200	$K_{\mathrm{i}\omega}$	10000	T_{p}	6.8
K_{pf}	10	K_{q}	0.2	P_{load}	20
P_{m0}	23.51	P_{ref}	0.49	Q_{ref}	0.4005
V_{ref}	1	X_{w}	2	X_{s}	0.222

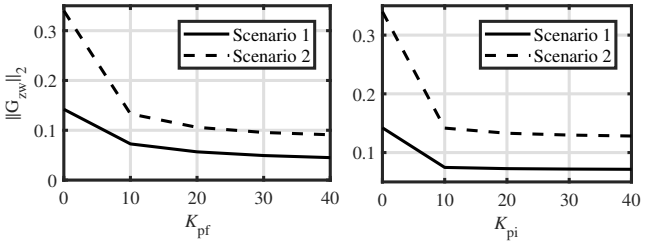

Fig. 3. Impact of gains on the H_2 norm of $G_{zw}(\mathrm{s})$

A. Impact of VSC control gains on inertial and primary frequency response

To investigate the impact of VSC control gains on inertial and primary frequency response, the transfer function $G_{zw}(\mathrm{s})$ is considered, which is relating a mismatch in active power to speed deviation $\Delta_{\omega_{\mathrm{g}}}$.

$$G_{zw}(\mathrm{s}) = \frac{\Delta\omega_{\mathrm{g}}}{\Delta P_{\mathrm{load}}} = C_z(sI - A)^{-1}B_w \tag{23}$$

where C_z is a matrix mapping the speed deviation of the generator equivalent. The matrices A and B_w (see (20)) are extracted by linearizing the system around an equilibrium. As defined in [10], the H_2 system norm is used as a performance metric, to measure the impact of the control gains on the AC frequency deviation. H_2 system norm takes the form of an input-output gain, which gives a measure of the total energy of the output after an instantaneous change of the input. Considering $G_{zw}(\mathrm{s})$, the H_2 norm shows how much the rotor speed deviates from its reference value after a load disturbance ΔP_{load}. Among the control gains, the frequency droop gain K_{pf} and the control gain of active power loop K_{pi} are the ones that determine the speed response of the VSC to a power imbalance [8]. To evaluate the impact of the gains, two scenarios are considered:

- Scenario 1, $H = 4$ s, $R_{\mathrm{d}} = 0.08$
- Scenario 2, $H = 1.5$ s, $R_{\mathrm{d}} = 0.16$

As shown in Fig. 3, both the active power loop and frequency droop gain (K_{pi} and K_{pf}) affect the energy of the frequency signal to a load disturbance. Increase of the frequency droop gain, decreases the H_2 norm significantly. As a result, for larger values of the frequency droop, the maximum frequency deviation will be smaller after a change of the load. However, large values of K_{pf} can cause frequency instability for different primary frequency control schemes (hydro) [14], create large frequency dip in the other AC-system and lead to undesired dip of the DC voltage. Thus, large values for K_{pf} gain should be avoided.

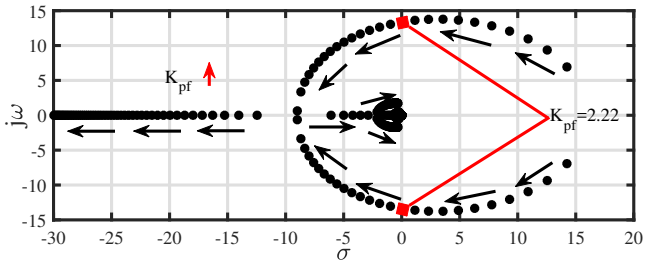

Fig. 4. Effect on system eigenvalues when varying K_{pf}

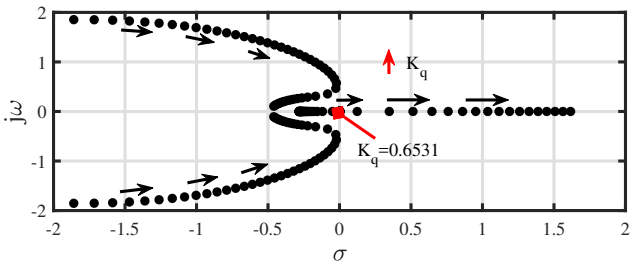

Fig. 5. Effect on dominant system eigenvalues when varying K_{q}

Regarding the active power loop gain K_{pi}, it is shown in Fig. 3, that for $K_{\mathrm{pi}} > 20$, its impact on the frequency stability is only slightly improved. Considering the results derived in [5], accelerating the active power control deteriorates the small-signal stability of the system. Therefore, an intermediate value could be considered for the active power loop gain K_{pi}, given that the impact on H_2 norm is insignificant for higher values of it. Based on the analysis, a $K_{\mathrm{pi}} = 20$ is used in the rest of the paper.

B. Effect of frequency droop

The trajectory of the system eigenvalues when varying the frequency droop gain is shown in Fig. 4. For this case, the power operating point is equal to P_{ref} = 0.49 p.u. The value of K_{pf} varies in the range of [0, 20]. Increasing the droop gain improves the small signal stability by moving the system eigenvalues further to the left half plane. This can be explained as follows. Following a small disturbance, a change in PCC angle occurs. The angle starts oscillating, until it reaches a new equilibrium. By adding frequency droop, the active current i_d is quickly adjusted, the oscillations are damped out within a short time (see also Fig. 6) and the VSC reaches its new equilibrium. Based on these findings, a $K_{\mathrm{pf}} = 10$ is used in the rest of the paper.

C. Effect of Q-V droop characteristic

The root locus of the system eigenvalues, when the voltage droop gain increases, is depicted in Fig. 5. The value of K_{q} varies in the range of [0, 1]. Unlike the effect of frequency droop on small-signal stability, when the voltage droop gain increases, the small-signal stability deteriorates. For $K_{\mathrm{q}} > 0.6531$, the system eigenvalues become positive, thus the system becomes unstable. A large value of K_{q} results in prioritization of Q-control after a contingency. The higher the value of K_{q}, the larger the voltage depression at post-fault state becomes. Thus, the maximum power transfer capability decreases significantly (24). Based on the analysis, an adequate value for the $Q - V$ droop is K_{q} = 0.2.

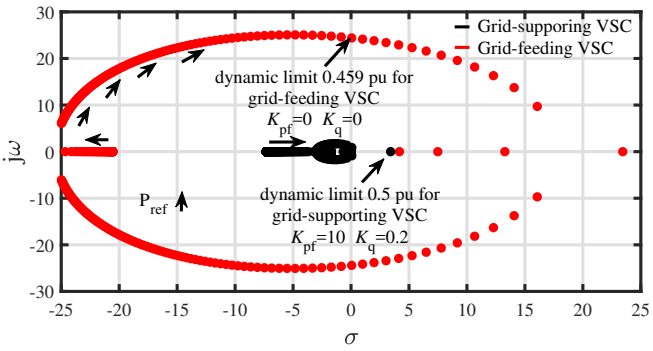

Fig. 6. Effect on dominant system eigenvalues when P_{ref} increases

D. Effect of operating point

For low SCC, the operating point of the VSC is bounded by the static stability limit defined by:

$$P_{\max}^{\text{static}} = \frac{V_{\text{pcc}} E}{X_{\text{eq}}} \tag{24}$$

where V_{pcc} is the voltage at the PCC, E is the voltage magnitude of the AC system. The impact of increasing the P_{ref} of the VSC on the system eigenvalues is depicted in Fig. 6. It can be seen, that as P_{ref} of the VSC increases the system eigenvalues move towards the right half plane. The real part of the eigenvalues is negative, when P_{ref} is smaller than $P_{\max}^{\text{static}}$ and become positive for $P_{\text{ref}} \geq 0.5$ p.u., which results in the VSC becoming unstable. As shown in Fig. 6, the dynamic limit of grid-supporting VSC is higher than the one of grid-feeding. It will be seen later in the paper, that this happens, because of the additional frequency droop gain.

IV. Large Disturbance: Case Studies

A. Case 1 - Tripping of short reactance without fault

The considered disturbance is a line opening without a fault and occuring at t = 0.2 s. This increases the grid impedance from $X_{\text{eq}} = X_{\text{w}} || X_{\text{s}}$ = 0.2 p.u. to $X_{\text{eq}} = X_{\text{w}}$ = 2 p.u.. As a result, the SCC is reduced to 0.5. Depending on the operating mode of the VSC, the $P-f$ and $Q-V$ droop gains are:

- Grid-supporting: K_{pf} = 10 and K_{q} = 0.2
- Grid-feeding: K_{pf} = 0 and K_{q} = 0

The VSC, in grid-supporting mode, participates in the regulation of the AC voltage and frequency by controlling the active and reactive power delivered to the grid. On the other hand, the VSC, in grid-feeding mode, delivers constant power equal to P_{ref} to the grid and regulates the reactive power to keep the terminal voltage equal to V_{ref}.

1) Dynamic limit of maximum power transfer capability of grid-supporting VSC: The evolution of the VSC active power can be seen in Fig. 7. As shown in Fig. 6 and mentioned above, the maximum transfer capability of the VSC, in steady-state condition, is approximately equal to the steady-state stability limit ($P_{\text{ref}} \approx 0.5$ p.u.) defined by (24). However, in case of a sudden SCC, the maximum transfer capability of the VSC is determined by the dynamic limit [5]. That implies that if the pre-fault power operating point is higher than the dynamic limit, VSC will lose its synchronism and

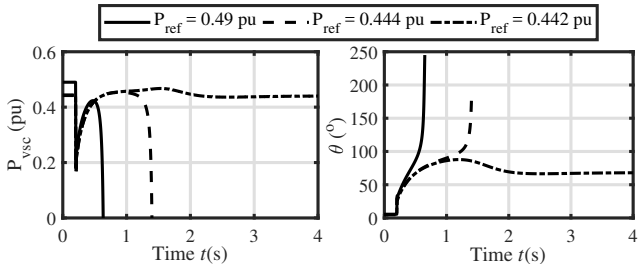

Fig. 7. Case 1 - Dynamic limit of maximum power transfer capability of grid-supporting VSC for K_{pf}=10

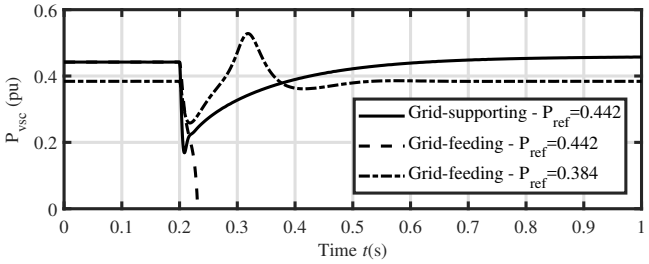

Fig. 8. Case 1 - Dynamic limit of the maximum power transfer capability of grid-feeding VSC

becomes unstable. This can be explained by the fact that, VSC prioritizes the active power and tries to restore it to its pre-fault value. However, due to the voltage dip, the maximum transfer capability temporarily decreases and instability occurs, due to the VSC trying to restore active power injection faster than the voltage is being restored.

As it can be seen in Fig. 7, VSC loses syncrhronism after tripping the short reactance, when the pre-fault power operating point is equal to the steady-state stability limit determined by (24). To identify the dynamic limit, the pre-fault power operating point is gradually decreased. As it is shown in Fig. 7, the first stable operating point was found to be $P_{\text{ref}} = 0.442$ p.u..

2) Dynamic limit of maximum power transfer capability of grid-feeding VSC: The evolution of the VSC active power can be seen in Fig. 8. As before, to identify the dynamic limit for the grid-feeding converter, the P_{ref} is gradually decreased. It can be seen in Fig. 8, that the dynamic limit for the grid-feeding converter is $P_{\text{ref}} = 0.384$ p.u.. Thus, the dynamic limit of the grid-feeding VSC is lower.

3) Comparison between grid-supporting and grid-feeding VSC: Fig. 9 demonstrates a comparison between the grid-feeding and the grid-supporting scheme, where the initial operating point is equal to P_{ref} = 0.4 p.u.. The dashed lines correspond to the grid feeding and the solid to the grid-supporting.

As shown in Fig. 9a, due to the frequency droop characteristic of the grid-supporting VSC, the power is reduced to 0.2 p.u. right after the disturbance. That leads to smaller voltage depression, so that $P_{\max}^{\text{dyn}} > 0.5$ p.u., even after the disturbance.

In the case of the grid-feeding VSC, the voltage depression is higher (see Fig. 9b), since the VSC tries to inject the initial P_{ref} to the AC system. As a result, the $P_{\max}^{\text{dyn}}$ decreases and

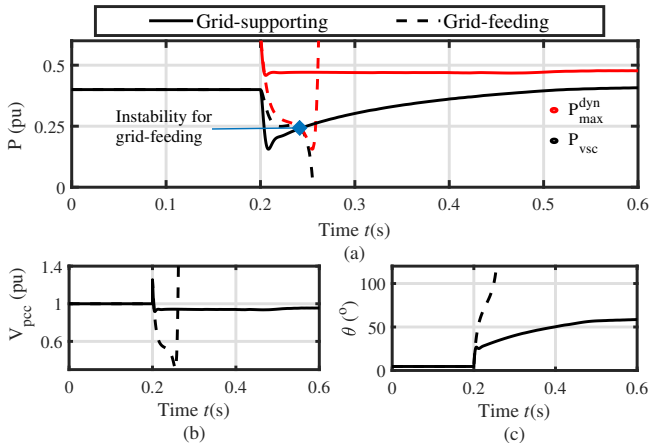

Fig. 9. Case 1 - (a) Maximum power transfer capability $P_{\max}^{\text{dyn}}$ (red) and VSC active power (black), (b) PCC voltage, (c) Angle difference $\theta_{\text{pll}} - \theta_{\text{g}}$

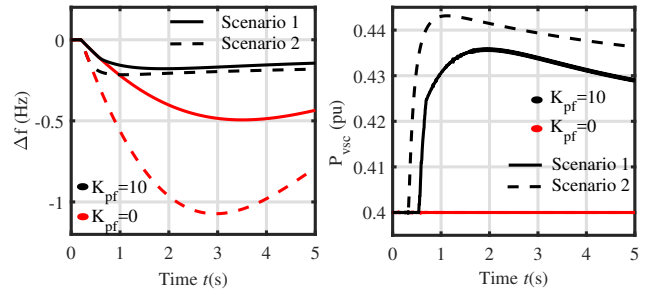

Fig. 10. Case 2 - Frequency deviation & VSC active power, Comparison of frequency response with and without the frequency droop

becomes equal to P_{vsc} at $t = 0.24$s, which leads to the grid-feeding VSC losing synchronism (see Fig. 9c).

B. Case 2 - Power imbalance for lower inertia

The frequency deviation to a power imbalance is investigated for different levels of inertia. In this case, the grid impedance is considered equal to $X_{\text{eq}} = 0.2$ p.u.. An increase of the load occurs at $t = 0.2$ s. The considered disturbance is equal to $\Delta P_{\text{load}} = 0.05$ p.u..

The evolution of the frequency is shown in Fig. 10, where the two presented scenarios in Section III.A were considered with and without the droop. The values for K_{pi} and K_{pf} are given in Table I. As it is depicted in Fig. 10, the impact of the frequency droop is mostly on the maximum frequency deviation, where it is significantly smaller compared to the case where the frequency droop is not considered. Although, the fast reaction of the VSC leads to reduced maximum frequency deviation, there is no direct contribution to the rate of change of frequency. As it was expected from Fig. 3, the frequency droop characteristic of the VSC contributes to the frequency stability and reduces the frequency deviation.

V. Conclusions & Future Work

This paper has investigated the stability of a grid-supporting VSC connected to a weak AC grid. By means of eigenvalue analysis, the impact of $P-f$ and $Q-V$ droop characteristics of the VSC on the system stability is analyzed. Moreover, H_2 norm is utilized to demonstrate how the outer loop parameters affect the AC frequency response. To gain further insight into the system properties, time domain simulations were performed for a sudden drop of SCC and a load disturbance.

The main findings are as follows:

1) In case of a grid-supporting VSC, due to the $P-f$ droop characteristic, the system synchronization can be preserved for larger disturbances of SCC.
2) The fast reaction of the VSC leads to reduced maximum frequency deviation. However, there is no direct contribution to the rate of change of frequency.
3) Unlike the effect of $P-f$ droop, the $Q-V$ droop characteristic reduces the dynamic limit of maximum power transfer capability of the VSC.

Future work is intended to investigate the interaction between the different parameters, characterizing the inertial and primary frequency control of the AC equivalent, for optimal tuning of K_{pf} and K_{pi}, as well as, the influence of varying inertia levels on the dynamic limit of the VSCs.

Acknowledgment

This work is supported by the multiDC project funded by Innovation Fund Denmark, Grant Agreement No. 6154-00020B.

References

[1] United Nations, "Paris Agreement," Tech. Rep., Dec. 2015.
[2] G. S. Misyris, S. Chatzivasileiadis, and T. Weckesser, "Robust frequency control for varying inertia power systems," in *2018 IEEE PES Innovative Smart Grid Technol. Conf. Europe (ISGT-Europe)*, Oct 2018, pp. 1–6.
[3] S. Chatzivasileiadis, D. Ernst, and G. Andersson, "The global grid," *Ren. Energy*, vol. 57, pp. 372 – 383, 2013.
[4] N. Flourentzou, V. G. Agelidis, and G. D. Demetriades, "VSC-based HVDC power transmission systems: An overview," *IEEE Trans. Power Electron.*, vol. 24, no. 3, pp. 592–602, Mar. 2009.
[5] L. Papangelis, M. Debry, T. Prevost, P. Panciatici, and T. Van Cutsem, "Stability of a voltage source converter subject to decrease of short-circuit capacity: A case study," in *2018 Power Systems Computation Conference (PSCC)*, Jun. 2018, pp. 1–7.
[6] J. Rocabert, A. Luna, F. Blaabjerg, and P. Rodríguez, "Control of power converters in AC microgrids," *IEEE Trans. Power Electron.*, vol. 27, no. 11, pp. 4734–4749, Nov. 2012.
[7] J. Fradley, R. Preece, and M. Barnes, "VSC-HVDC for frequency support (a review)," *IET Conf. Proc.*, pp. 1–6, Jan. 2017.
[8] L. Papangelis, X. Guillaud, and T. Van Cutsem, "Frequency support among asynchronous AC systems through VSCs emulating power plants," in *11th IET Int. Conf. on AC and DC Power Transmission*, Feb. 2015, pp. 1–9.
[9] J. Huang and R. Preece, "HVDC-based fast frequency support for low inertia power systems," *IET Conf. Proc.*, pp. 1–6, Jan. 2017.
[10] D. Gross, S. Bolognani, B. K. Poolla, and F. Dörfler, "Increasing the resilience of low-inertia power systems by virtual inertia and damping," in *Proc. of IREP'2017 Symposium*. Int. Institute of Research and Education in Power System Dynamics (IREP), 2017-08-31, p. 64.
[11] J. Z. Zhou, H. Ding, S. Fan, Y. Zhang, and A. M. Gole, "Impact of short-circuit ratio and phase-locked-loop parameters on the small-signal behavior of a VSC-HVDC converter," *IEEE Trans. Power Del.*, vol. 29, no. 5, pp. 2287–2296, Oct. 2014.
[12] J. A. Suul, S. D'Arco, P. Rodríguez, and M. Molinas, "Impedance-compensated grid synchronisation for extending the stability range of weak grids with voltage source converters," *IET Gener., Transm. Dis.*, vol. 10, no. 6, pp. 1315–1326, 2016.
[13] T. Weckesser and T. Van Cutsem, "Equivalent to represent inertial and primary frequency control effects of an external system," *IET Gener., Transm. Dis.*, vol. 11, no. 14, pp. 3467–3474, 2017.
[14] L. Shen, M. Barnes, R. Preece, and J. Milanović, "Frequency stabilisation using VSC-HVDC," in *2016 IEEE Power and Energy Society General Meeting*, Jul. 2016, pp. 1–5.

[Pub. D] North Sea Wind Power Hub: System Configurations, Grid Implementation and Techno-economic Assessment

Authors:
G. Misyris, T. Van Cutsem, J. G. Møller, M. Dijokas, O. Renom Estragues, B. Bastin, S. Chatzivasileiadis, A. H. Nielsen, J. T. G. Weckesser, J. Østergaard, and F. Kryezi

Accepted at:
CIGRE (International Council on Large Electric Systems)

North Sea Wind Power Hub:
System Configurations, Grid Implementation and Techno-economic Assessment

G. MISYRIS[1]*, T. VAN CUTSEM[2], J. G. MØLLER[1], M. DIJOKAS[1], O. RENOM ESTRAGUÉS[1], B. BASTIN[2], S. CHATZIVASILEIADIS[1], A. H. NIELSEN[1], T. WECKESSER[3], J. ØSTERGAARD[1], F. KRYEZI[4]

[1]Technical University of Denmark (DTU), [2]University of Liège, [3]Dansk Energi, [4]Energinet Denmark, Belgium

SUMMARY

In 2017, Energinet and TenneT, the Danish and Dutch Transmission System Operators (TSOs), have announced the North Sea Wind Power Hub (NSWPH) project. The project aims at increasing by 36 GW the North Sea offshore wind capacity, with an artificial island collecting all the power produced by wind turbines and several HVDC links transmitting this power to the onshore grids. This project brings together new opportunities and new challenges, both from a technical and economic point of view. In this regard, this paper presents three analyses regarding the design and operation of such an offshore system.

First, we perform a techno-economic assessment of different grid configurations for the collection of the power produced by wind farms and its transmission to the hub. In this analysis, two frequencies and two voltage levels for the operation of the offshore grid are investigated. Our findings show that the nominal-frequency high-voltage option is the more suitable, as low-frequency does not bring any advantage and low-voltage would results in higher costs.

The second analysis is related to the differences in operating the system with low- or zero-inertia; different dynamic studies are performed for each configuration to identify proper control actions and their stability properties. Comparing the outcomes of the simulations, we observed that voltage and frequency oscillations are better damped in the zero-inertia system; however, the risk of propagating offshore faults in the connected onshore grids is mitigated with the inclusion of the synchronous condensers.

Lastly, a comparison of ElectroMagnetic Transient (EMT) and phasor-mode (also known as RMS) models is presented, in order to understand their appropriateness of simulating low- and zero-inertia systems. The results show that phasor approximation modelling can be used, as long as eigen-frequencies in power network are well damped.

KEYWORDS

High – Voltage – DC, Voltage – Source – Converter, North – Sea – Wind – Power – Hub, Low – and Zero – Inertia – Systems, EMT – Models, Phasor – Mode – Simulation – Tools.

***gmisy@elektro.dtu.dk**

I. INTRODUCTION

National and international ambitions of reducing greenhouse gas emissions result in Renewable Energy Sources (RES) progressively replacing conventional generation based on fossil fuels [1]. In 2017, representatives of the Dutch, Danish and German Transmission System Operators (TSOs) established a consortium to explore the possibility of developing a North Sea Wind Power Hub (NSWPH). This project aims at increasing the North Sea offshore wind capacity by integrating additional 36 GW of wind power, with an artificial island collecting all the power produced by wind turbines and several High Voltage Direct Current (HVDC) links transmitting this power to Denmark, the Netherlands, Norway, Germany and the UK [2].

Due to the length of the submarine power cables, the HVDC technology is the only solution to build a cost-effective transmission infrastructure. Moreover, Voltage-Source Converters (VSC) allow for high flexibility and improved control capabilities. Thus, the connections between the offshore island and the onshore grids will be formed by multiple point-to-point VSC-HVDC links; although considered at the beginning, the option of a multi-terminal HVDC grid [3] was discarded due to the lack of experience with HVDC breakers. The function of a NSWPH would be twofold: (i) increase the shares of renewable generation in the involved countries, and (ii) allow for power exchanges between partner TSOs by means of additional transmission capacity.

Such a project brings together a series of new opportunities and new challenges, both from a technical and economic point of view. Starting from the economic aspects, the main question is whether the NSWPH shall operate at nominal AC frequency (50 Hz) or at Lower Frequency AC (LFAC), e.g. 16.67 Hz. Considering that the maximum net power of NSWPH could go up to 36 GW, several medium- and high-voltage AC cables will be deployed for the connection of wind turbines to the hub. Hence, reactive power compensation is necessary to improve power quality and voltage profiles in proximity of the island. At lower frequency, series reactances and shunt susceptances of power cables are lower compared to their values at nominal frequency (50 Hz). On the one hand, the distance between the island and the wind farms can be extended without the need of additional compensation. On the other hand, transformers and inductors increase in size when designed to operate at lower frequencies, which imposes an additional constraint in terms of footprint on the artificial island.

The technical aspect of this study concerns the growing use of non-synchronous converter-based resources. Integrating these resources affects the reliability of the power system and changes the nature of grid dynamics and control. Indeed, the replacement of synchronous generators with inverter-based resources is followed by a decrease of system inertia. When the replacement is only partial, the system is referred to as low-inertia power system. In case of complete absence of synchronous generation, it becomes a zero-inertia system. This poses the challenge of faster active power sharing between the converters of the HVDC links.

Another challenge concerns voltage control in the proximity of those converters. Indeed, the control systems of Power Electronic (PE) devices usually rely on measurements of voltage magnitudes and phase angles at their terminals. In high-inertia systems, voltage and frequency are stiff, therefore voltage magnitudes and angles at the terminals are not largely affected. Onshore grids usually host multiple synchronous generating units, that inherently provide a stiff voltage and frequency [4]; this does not happen in offshore grids, which usually consist only of multiple PE devices. Particularly, active power will be generated by (Type IV) wind turbines, then gathered through submarine cables in various offshore converter platforms and lastly transferred through HVDC links to the interconnected onshore grids [5]. Consequently, in such zero-inertia offshore systems, voltage magnitudes and phase angles are relatively sensitive to current injections from the wind turbines.

Furthermore, harmonic instability challenges [6] arise when connecting PE resources to grids without synchronous generators because of the interaction between converter control actuation

and eigen-frequencies in power networks. Converters are commonly equipped with multiple time-scale control systems for regulating current flows at their terminal and power exchanges with the grid. To analyse the stability of a zero-inertia system and consider harmonic instability phenomena, both voltage and signal processing dynamics need to be included in the model. On the one hand, detailed modelling of the system dynamics increases the reliability of stability analyses; on the other hand, it increases the computational time required to solve the differential algebraic system of equations describing grid dynamics. Large computing times make security assessment more difficult, e.g. it takes more time to perform an analysis of post-disturbance system conditions in order to verify that power ratings and voltage constraints are violated.

To decrease computing times, system operators could resort to phasor-mode simulation, widely used in AC systems without large PE devices. In the latter, network lines, converters' inner controllers and signal processing dynamics are neglected. On the one hand, by neglecting these dynamics, models under phasor approximation are unable to capture harmonic instability phenomena; on the other hand, they are suitable for capturing slower phenomena associated with the dynamics of converters' outer controllers (as far as there is a distinct time separation between converters' outer controllers and voltage dynamics). The need for fast, accurate and representative models for performing time-domain simulation analysis in grids with high penetration of PE devices calls for the evaluation under which conditions the phasor approximation is still able to predict the system response after a disturbance. Identifying those conditions will allow performing online security assessment with faster phasor-mode simulation tools for a (hopefully large) subset of disturbances, while keeping the computationally demanding EMT for the other, more severe disturbances.

The aim of this paper is to provide the groundwork for understanding the non-linear behaviour of offshore AC networks, as well as novel insights in their fundamental stability and control properties. More specifically:

- We perform a techno-economic analysis to identify the economic benefit of offshore grids operated at low and normal frequency; this includes both the costs for the components as well as the maximum power transfer capability of the cables.
- We investigate and compare a zero- (100% inverter-based grid) and a low-inertia (synchronous condensers on the island) configuration, where the stability properties of each system and their responses to large disturbances are investigated.
- We assess the limitations of simulation software techniques for low- and zero- inertia systems, to examine when EMT simulations become crucial in capturing phenomena that the phasor-mode approximation cannot.

The rest of the paper is organized as follows. Section 2 presents the concept of NSWPH and the study case considered in this paper. In Section 3, first, a techno-economic analysis is carried out to identify the preferable frequency and voltage level for the offshore AC grid. Then, two different configurations of the offshore system are presented. Section 4 presents a comparison between the two considered configurations, with reference to their respective stability properties. Section 5 presents a comparison of EMT and phasor-mode (also known as RMS) models. Conclusions are drawn in Section 6.

II. NORTH SEA WIND POWER HUB (NSWPH): GRID TOPOLOGY

The NSWPH will follow a modular Hub-and-Spoke concept, according to NSWPH consortium, which is the common practice for large-scale offshore wind deployment. This concept relies on the progressive construction of modular hubs in the North Sea which are connected to the countries in Northern Europe by means of HVDC lines.

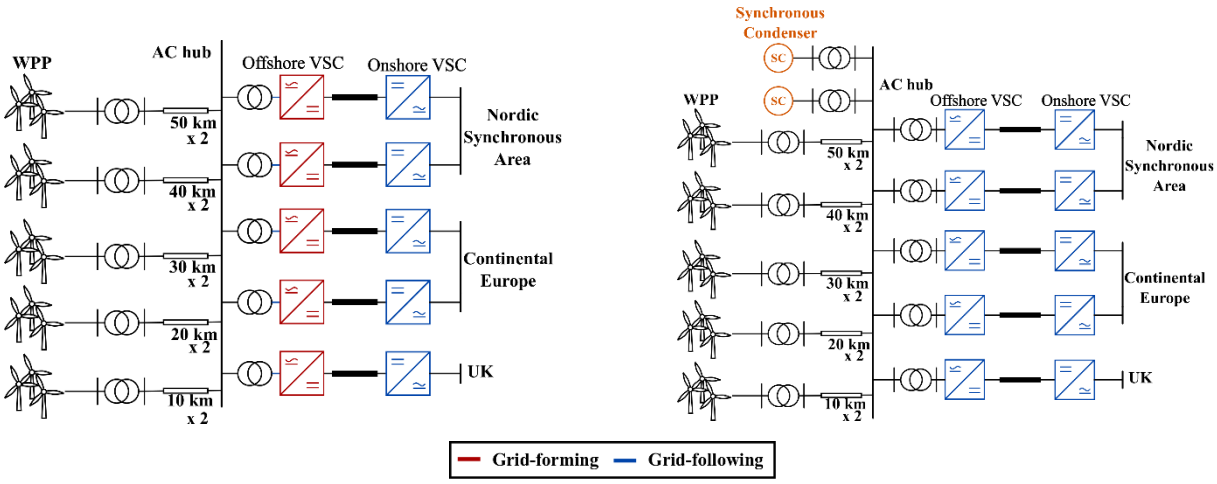

Figure 1: Zero-inertia (left) and low-inertia (right) topologies for NSWPH.

The grid layout used for the analyses of this paper is depicted in Figure 1. This grid configuration is based on the topology that the TSOs involved in the project are considering at the moment. In this layout, the wind power generated by the wind farms is transferred through High-Voltage-Alternating-Current (HVAC) cables (220 kV, with 400 MVA nominal power) to the hub. The cable parameters are taken from manufacturer data sheets [7]. Five HVDC links are used to transfer onshore the amount of power. The onshore grid is represented by a grid equivalent with inertial and primary response [8], [9]. The converters on the offshore side operate in grid-forming (zero-inertia) or grid-following (low-inertia) mode. As base power, we consider S_b = 1000 MVA. We assume the rated power of offshore converters is 1100 MVA, while the rated power of wind farms is 700 MVA. In the low-inertia configuration, the rated power of each of the two synchronous condensers is 350 MVA. This model represents a small system compared to the maximum total power capacity envisioned for the NSWPH, but it equally captures all relevant dynamic phenomena and provides a good overview of the instability mechanisms.

III. TECHNO-ECONOMIC ANALYSIS OF OFFSHORE AC COLLECTION GRID OPTIONS

One of the major technical limitations of long-distance AC submarine transmission is the charging current, caused by the shunt capacitance of the cables, which results in a huge amount of reactive power produced. For this reason, conventional 50/60 Hz AC transmission cables connecting remote offshore wind farms to onshore grids require reactive compensation in such proportions that HVDC is often the preferred option [10].

As an alternative, authors in [11], [12], [13] have proposed to operate wind farms at lower frequencies to reduce effects of line charging and permit longer transmission distances. However, the design of grid components depends on the operating frequency of the system. In this chapter, we present a techno-economic assessment of operating collection grids and transmission systems at different frequencies and voltage levels.

III.i. Design Considerations

For the techno-economic assessment of the collection grids and transmission cables, two voltage levels (66 and 220 kV) and two system frequencies (16.67 and 50 Hz) are considered. In order to evaluate the different options, a selection of power cables and power transformers has been made.

The power cables are three-core cables with copper conductors: to make calculation easier, each of them is assumed to be a solid cylinder with cross-section of 630 mm^2 and diameter of 28.3 mm. The nominal current of the cables is 1.05 kA, while the power rating varies with the voltage level, respectively 120 and 400 MVA (for 66 and 220 kV). The model proposed in [14] is adopted for

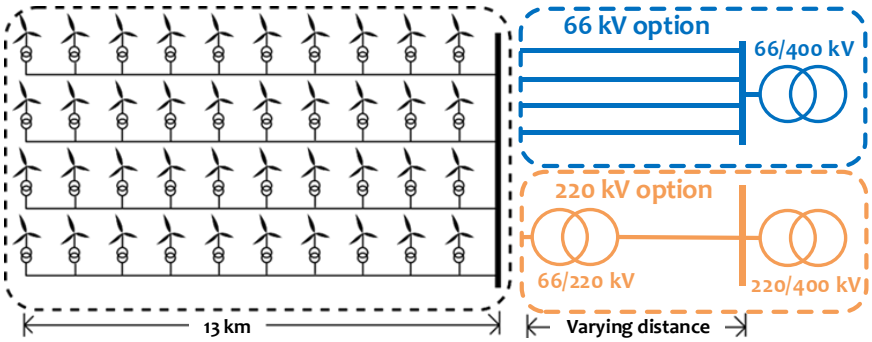

Figure 2: Wind farm layout and options of transmission voltage

assessing the cost of the cables, which are shown in Table 4. Cable installation costs have been chosen equal to 0.345 Mill. Euros per kilometer as suggested in [15].

The transformers are core-type transformers with different power and voltage ratings. For the 66-kV option, each turbine is connected to the transmission system through a 0.67/66-kV transformer, which has a power rating of 10 MVA. A 66/400-kV transformer is then located at the hub, in the proximity of the HVDC converter station; its power rating is 400 MVA. For the 220-kV option, the voltage is stepped up by a 66/220-kV transformer with power rating of 400 MVA and then again in proximity of the hub, with a 220/400-kV 400-MVA transformer. The two configurations are depicted in Figure 2. In the following part, the pros and cons of each grid layout are discussed.

As mentioned above, the transmission of active power through long-distance AC cables is limited by the reactive power produced by their shunt capacitance. Figure 3 shows the maximum power transfer for the four transmission options assuming a charging capacitance of 0.2 µF/km. The reactive power produced by shunt capacitances is proportional to the system frequency [16]. Operating a transmission cable at one third of the frequency would lead to a one-third reduction of the shunt reactance. However, the shunt inductance is the main component of the cost of reactive compensation [17]. At 16.67 Hz, the inductance would be exactly equal to the inductance at 50 Hz. This relation is valid for short distances, where reactive compensation is performed at the two terminals of the cable. For transmission distances far beyond 50 km, 50-Hz operation would require compensation equally distributed along the length of the cable. This would significantly increase the cost of the 50-Hz alternative.

Transmission losses are also impacted by the frequency, as the skin-effect of the current increases at higher frequencies. The skin-depth, that is the depth at which the current density drops significantly, is proportional to the reciprocal of the square root of the frequency [18]. The smaller is the skin-dept of a cylindrical conductor, the greater is its AC resistance [18]. Thus, lowering the operating frequency will reduce joule losses in transmission cables. Annual losses and the resulting costs for the two frequency options are shown in Table 2. For the calculation of annual losses, a utilization factor of 0.5 is assumed, resulting in 4380 full-load hours per year. For the cost of losses,

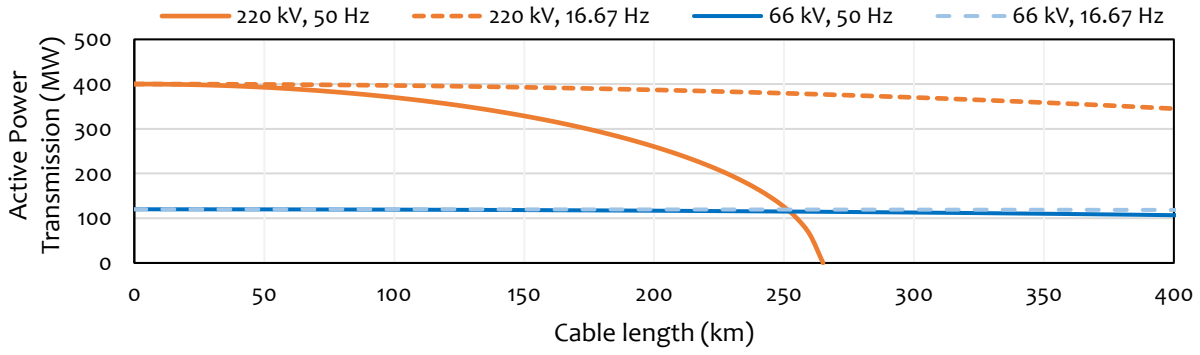

Figure 3: Maximum active power transfer depending on the length of the transmission cable.

the price of electricity is assumed to be 30 Euro/MWh, similar to the five-year average of Denmark. An estimation of the total losses can be obtained by multiplying the average distance between the wind farms and the hub by the losses per km at 50 or 16.67-Hz.

It must be said that, in order to reduce the skin-effect, it is common practice to use stranded wires instead of solid conductors. In this analysis, we consider solid conductors to make the calculations easier; the presented costs are most probably an overestimation of the actual costs but represent a plausible basis for comparison of the two frequency options.

Concerning power transformers, their cost and size depend on the operating frequency. Indeed, the core cross-sectional area of a transformer is inversely proportional to the system frequency [19]. It follows that, by reducing the system frequency to 16.67-Hz, the core cross-section increases threefold. Moreover, also the length of the windings increases because of the greater circumference of transformer legs. The cost and the required mass of active materials for the different transformers are displayed in Table 1. In the table, B_{max} is the saturation flux density of the core material, J_{max} is the maximum winding current density, used to compute winding cross-sections, and dV_{max} is the maximum voltage drop per turn, used for computing the minimum number of turns. The price of copper and steel is assumed to be respectively 7 and 3 Euros per kilogram. Additional cost of casing, civil engineering, transport and installation must be assumed to scale in proportion with the mass.

The cost of a 500-MW 220-kV AC platform is provided in [15]. This is used as basis for estimation of the cost of the 400-MW platform to be used in the 50-Hz 220-kV alternative. For the 16.67-Hz option, the cost has been scaled by a factor of 3, as it is assumed to be proportional to the load of the platform. A detailed structural design would be required to obtain the true cost for the low-

Voltage level (kV)	Power rating (MVA)	Cost (mill. Euros / km)
66	120	**0.72**
220	400	**1.31**

Table 4: Cost of power cables.

	16.67 Hz	50 Hz
Jacket	27,6	9,2
Topside	66	22
Installation	22,08	7,36
Total	**115,68**	**38,56**

Table 3: Cost of offshore AC platform (mill. Euros).

	DC	16.67Hz	50.0Hz
Resistance (mΩ/km)	29.5	29.7	34.9
Full load losses, $3I_n^2R$ (W/m)	97.6	98.2	115.4
Annual losses (MWh/km)	**427**	**430**	**506**
Cost of 20-year losses (mill. Euro/km)	**0.256**	**0.258**	**0.303**

Table 2: Cable resistances, annual losses and related costs.

Transformer design parameters					Mass (T)			Cost (Mill. Euro)		
Voltage rating (kV)	Power rating (MVA)	B_{max} (T)	J_{max} (A/mm²)	dV_{max} (V)	16.67 Hz	50.0 Hz	Diff.	16.67 Hz	50.0 Hz	Diff.
0.67/66	10	1	7	22	27	9	**18**	0,10	0,04	**0,06**
66/220	400	1	3	220	1075	371	**704**	3,75	1,49	**2,27**
220/400	400	1	3	220	1387	489	**897**	4,78	1,93	**2,85**
66/400	400	1	3	220	1207	417	**791**	4,16	1,64	**2,52**

Table 1: Mass and cost of active material (core and windings) for a range of medium and high voltage transformers.

frequency option; however, this is out of the scope of this study. The costs of offshore AC platform are shown in Table 3. On the one hand, 66-kV transmission could avoid certain costs, e.g. for the offshore transformer platforms, as it is expected that wind turbines will be able to operate at this voltage in near future [10]. On the other hand, increasing the voltage to 220-kV would significantly reduce transmission losses and the number of cables required to collect the power produced by wind turbines.

III.ii. Economic Assessment

A cost estimation model is developed for comparing the Total Cost of Ownership (TCO) of the different option for a time window of 20 years. The capital costs included in model comprise the cost of active materials of transformers and their platforms (if present), the cost of the cables and their installation and the 20-year amortization of all investments at 2% interest. Cost components which are invariant of design frequency and transmission voltage, such as cost of array cables and turbines, are excluded from the study. Moreover, the cost of losses is included in the model, considering losses in the transmission cables and in the collection grids. The losses are calculated for a time period of 20 years. The TCO of the four grid options are shown in Figure 4.

For the NSWPH project, the power collected by the hub will probably be in the range of 10-15 GW [20], although alternatives up to 36 GW are also under consideration [21]. The amount of power collected by the hub has an impact on the length of power cables. Indeed, the area covered by the turbines, and thus the maximum transmission distance between these and the hub, increases with the amount of power produced. From Figure 4, it is evident that the transmission distance plays an important role on the decision of the type of transmission technology.

The test system used in the remainder of this paper is a 4 GW hub surrounded by 5 wind farms (WF) with 800 MW of installed capacity. Assuming a maximum wind power production of 6W/m2 [22], the resulting area covered by the wind farms is, at least, 667 km2. This corresponds to a circular area with a radius of 14.5 km. If the same calculation is done for a hub collecting 36 GW of wind power, the corresponding radius would be in the range of 40-50 km. These distances seem far too small for low frequency AC transmission to be a relevant option for the offshore grid. Below 50 km, the line charging of both the 220kV and the 66kV cables is simply too small to justify a change of standards.

Figure 4 compares the magnitude of those cost components which depend on either design frequency or transmission system voltage. It can be noted that for the 66-kV option, there is a very small difference between TCO of the low- and normal frequency alternatives. At short transmission distances, the 50-Hz alternative is more convenient due to smaller investments in transformers, while the 16.67-Hz alternative is more convenient for longer transmission distances (above 30km) due to smaller losses. It is worth mentioning that for the 66-kV option and short transmission distances, the 16.67-Hz alternative is slightly more convenient than the 220-kV option and 50-Hz

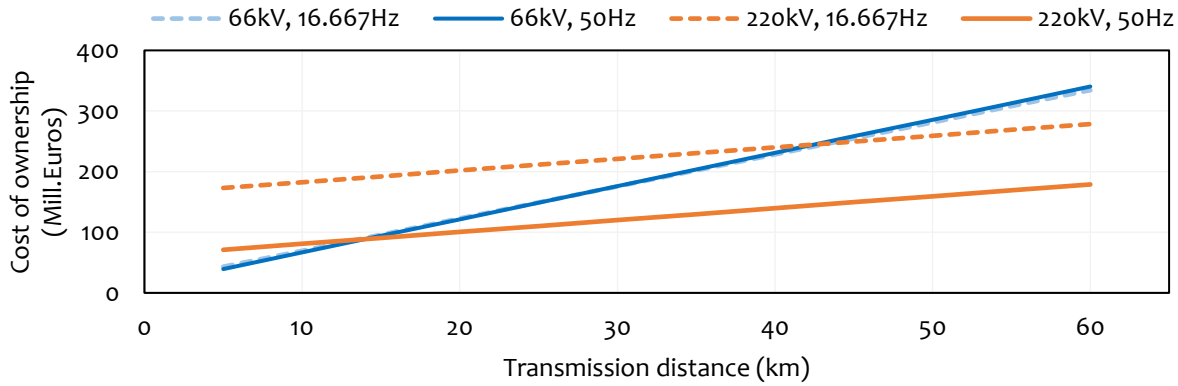

Figure 4: Comparison of cost of ownership between transmission system options for a 400 MW wind farm.

alternative. However, normal design frequency and 220-kV transmission is the preferred option for transmission distances of about 15 km due to the excessive cost of cables in the 66-kV option. The combination of high voltage and low frequency transmission is not a cost-effective alternative for transmission distances below 60 km.

Based on the findings of this economic analysis, in the following section it is assumed that the AC offshore grid is operated at 50 Hz and 220 kV.

IV. TECHNICAL ANALYSIS OF OFFSHORE AC GRID CONFIGURATION

In case of an AC grid on the island and between the wind farms, there are two possible configurations, namely a zero- and a low-inertia solution. The zero-inertia solution corresponds to a 100% converter-based system (see Figure 1 - left) while the low-inertia solution corresponds to a system dominated by PE devices, but with at least one synchronous condenser connected (see Figure 1 - right). The purpose of the latter is to provide: (i) a voltage source to which the VSCs synchronise in grid following mode, and (ii) a buffer of kinetic energy, stored in the rotating masses (rotor, possibly complemented by a flywheel). The speed of rotation of the synchronous condenser sets the frequency of the offshore AC grid. On the onshore side, each converter operates in grid-following mode [3], where it provides constant reactive power and regulates the voltage of the HVDC-link. A generic wind farm model is used, based on the dynamic equivalent presented in [23]. No special control is required from the wind generators (grid-following control), which operate in maximum power tracking mode, and under unity power factor.

The main difference between the two configurations lies in the control of the offshore VSCs and the components placed on the island (see Figure 5 left and Figure 5 right, respectively).

IV.i. Zero-inertia configuration

The zero-inertia configuration includes multiple grid-forming converters [24] operating in parallel, controlling the voltage at their terminals. Figure 5 (left) depicts the basic control structure of a grid-forming converter, which consists of the active power controller and the virtual impedance controller. Their main principles are to impose the frequency and the AC voltage on the offshore AC grid.

Multiple grid-forming VSCs operating in parallel be equipped each with a frequency droop control scheme [5], which is automatically activated to adjust the active power injected or absorbed by the VSCs after a disturbance. The objective is to distribute the change in power among the converters in the zero-inertia systems based on pre-defined participations. In that process, the system frequency is used as a communication signal between the converters. We can infer that the operating principle of a grid-forming converters is similar to the one of synchronous generators, apart from the hard-current limits of the converters. However, due to the lack of an energy buffer, a sudden power imbalance requires an almost immediate reaction of the VSCs. As a result, fast control actions are necessary to stabilize the system, considering though the current limits of the converters.

Moreover, a voltage set-point is used to control the output voltage of the offshore converter. The reactive power injected/absorbed by the offshore converter reacts to voltage deviations on the Point of Common Coupling (PCC) caused by reactive power imbalances in the system. Lastly, the virtual impedance controller is also employed for damping the grid-frequency resonant poles and electromagnetic transients caused by the multiple cables of the offshore grid [25].

IV.ii. Low-inertia configuration

The low-inertia configuration combines the advantages of conventional generation and VSC technology [26]. It consists of synchronous condensers connected to the offshore grid and multiple

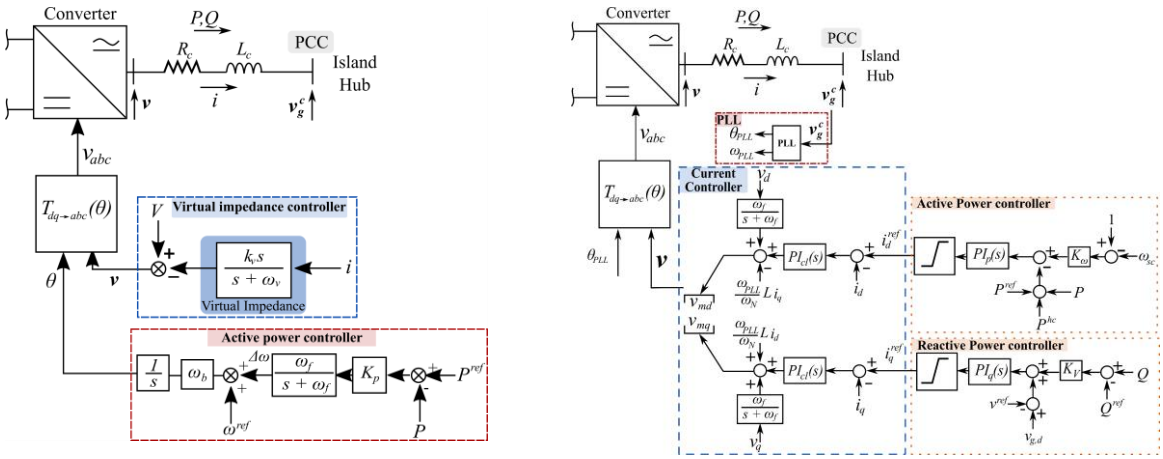

Figure 5: Control principles of grid forming offshore converters for the zero-inertia case (left) and grid-following converter for the low-inertia case (right).

grid-following converters [26]. The synchronous condensers set the frequency and the voltage at the PCC. Any mismatch in active power on the island is reflected on a change of rotor speed of the synchronous condensers. The grid-following converters closely track the frequency set by the synchronous condensers, collect the wind power and transfer it through the HVDC links to the onshore grids. As aforementioned, the synchronous condensers act as an energy buffer in the case of a power imbalance. This buys some time to re-dispatch power to the grid-following converters. Dynamic simulations have shown that the system can stand the outage of one of the two synchronous condensers, i.e. it operates in a stable manner with a single 350-MVA machine [26].

To restore the active power balance and the stored kinetic energy of the synchronous condenser, the offshore converters must be able to adjust the power extracted from the offshore grid. This adjustment has to be performed with specific time response; not too slow, in order to avoid excessively large frequency deviations but not too fast either, in order to avoid large DC-voltage deviations of the HVDC-link, as well as fast disturbance propagations to the onshore grids. Thus, additional frequency droops (see Figure 5 - right) are added to their outer controllers to enable their participation to frequency regulation of the grid. A reactive power-voltage droop control is used for the participation of the VSC converters in the hub voltage control (also controlled by the AVRs of the synchronous condensers). The resulting offshore converter control is depicted in Figure 5 (right) and is similar to the one presented in [26]. The main components of the control unit are the PLL, the outer active and reactive controllers and the inner controllers.

Additionally, a centralized frequency controller for active power regulation is considered to return to nominal frequency after a disturbance [26]. Its principle is to provide an active power correction for each of the offshore VSC based on the deviation of the synchronous condenser's rotor speed. It should be noted that no time-delay is considered on the frequency (rotor speed) measurement, since the distance between the offshore converters and the synchronous condenser is very short, and the centralized controller is rather slow. Another advantage of the centralized frequency controller is the additional degree of freedom for sharing the active power among the converters (in the zero-inertia case the active power sharing depends only on the frequency droop values of the converters).

IV.iii. Comparison between low- and zero- inertia configurations

In this section, a comparison between the two configurations is performed, in order to show their stability properties and illustrate their ability to restore the voltage and the frequency of the offshore system for different type of disturbances. For comparison purposes, we define the following criteria for secure operation of the offshore system:

1. Maintain nearly constant voltage at the AC hub,

2. Regulate the frequency of the offshore system,
3. Avoid fast disturbance propagation to the onshore grids.

Moreover, we evaluate them based on three different scenarios:

1. A 200 MW power request from one of the onshore grids interconnected to the island, where active power is transferred from the rest of the interconnected onshore grids. The active power sharing depends on the frequency droops. For our studies, the offshore converters are tuned homogeneously. Hence, the frequency droops have the same values, and the requested active power is distributed equally among the converters.
2. Offshore HVDC converter outage, i.e. HVDC converter trip, where one of the offshore converters is disconnected without considering a DC fault. With this scenario, we validate how fast a disturbance is propagated to the interconnected onshore grids. Considering that future onshore grids will operate with lower inertia, fast disturbance propagation may cause large frequency deviations.
3. Wind power loss corresponding to the disconnection of the furthest wind farm. With this scenario we validate the ability of both configurations to stabilize and restore the Hub-voltage and how fast the disturbance propagates to the onshore grids.

The performance of the zero- and low-inertia configuration are assessed based on EMT simulations for all 3 scenarios.

Figure 6 presents voltage evolution at the AC-Hub bus in the aforementioned scenarios. As it can be seen, both configurations are able to maintain voltage after all three disturbances. It can also be noted that the disconnection of the furthest wind farm causes the largest voltage deviation compared to the other scenarios. This was expected since both cables were fully loaded at pre-fault state, causing a large change of the reactive power at the AC-Hub bus. Moreover, the voltage presents an oscillatory behavior. The frequency of these oscillations depends on the cable parameters and the damping ratio of these oscillations depends on the tuning of the virtual impedance controller. Lastly, for the considered scenarios, we can conclude that in the zero-inertia configuration the voltage responses are better damped and a new steady state is reached faster than in the low-inertia configuration.

In the zero-inertia configuration, due to the absence of energy storage, a disturbance propagates almost instantaneously to the interconnected onshore grids. Considering scenario 2 and the system response depicted in Figure 7 (middle plot), where an offshore converter outage occurs, the active powers absorbed by the remaining offshore converters change to a new steady state (post-fault equilibrium) within a few milliseconds. In the low inertia case, due to the kinetic energy stored in

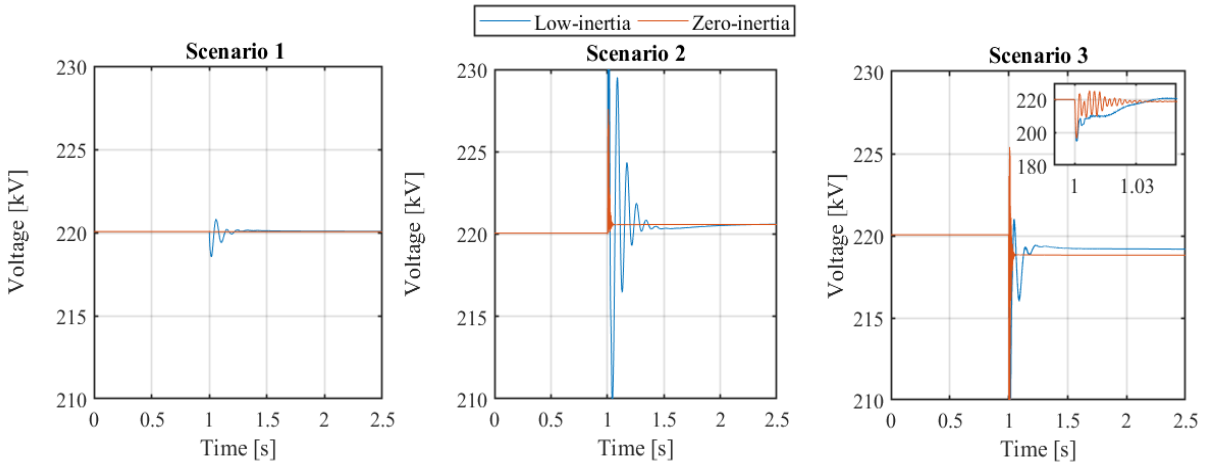

Figure 6: Voltage deviation at the AC-Hub. Scenario 1: 200 MW power request from a partner TSO. Scenario 2: DC-link outage. Scenario 3: Wind power loss with AC cable disconnection.

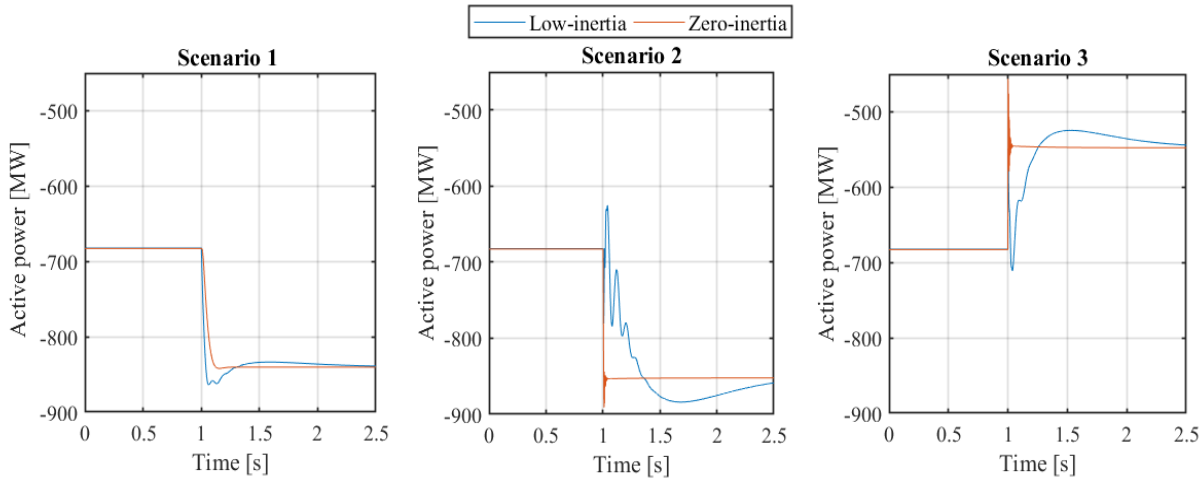

Figure 7: Active power absorbed by the offshore converters. Scenario 1: 200 MW power request from a partner TSO. Scenario 2: DC-link outage. Scenario 3: Wind power loss with AC cable disconnection.

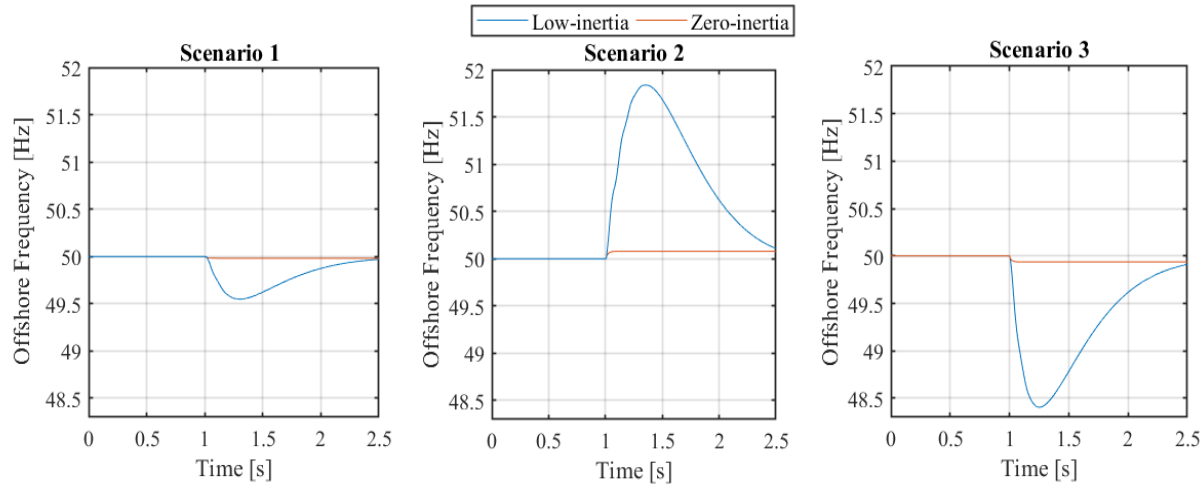

Figure 8: Offshore frequency deviation. Scenario 1: 200 MW power request from a partner TSO. Scenario 2: DC-link outage. Scenario 3: Wind power loss with AC cable disconnection.

the rotating mass of the synchronous condenser, the disturbance in scenario 2 and 3 propagate slower to the interconnected onshore grids. As can be seen in Figure 7, the rate of change of active power delivered to the interconnected onshore grids is much lower compared to the zero-inertia case. Thus, we can infer that large disturbances taking place in the offshore grid have less severe impact on the frequencies of the interconnected onshore grids. Lastly, considering scenario 1 and the results depicted in Figure 7 (left plot), we can infer that both configurations can fast provide active power to a connected onshore grid. In the zero-inertia system a fast response with short settling time can be observed, while in the low-inertia configuration the power request resulted in an overshoot.

Regarding the frequency of the offshore system (see Figure 8), in the zero-inertia case the system frequency varies almost instantaneously. However, due to the small values of frequency droops the maximum frequency deviation is small (less than 0.07 Hz). In the low-inertia case, the maximum frequency deviation is higher compared to the zero-inertia case. This is due to the larger values of the frequency droops of the grid-following converters. In the investigated large disturbances, this result in significant frequency deviations (up to 1.6 Hz). Such variations, unacceptable in conventional AC grids, can be tolerated on the isolated offshore island with no load (except for auxiliaries of course). The wind park controllers should be tuned to accept such frequency deviations. Furthermore, the frequency deviation is corrected by the centralized controller, which is updating the power reference set points of the offshore converters.

V. TOOLS FOR SIMULATION OF A FUTURE NORTH SEA WIND POWER HUB

In this section, we assess the accuracy of the phasor-approximation models for the simulation of offshore systems, such as the NSWPH. The objective is to investigate to what extent those simplified models can be used, and when EMT models are mandatory. The motivation is that system operators of the interconnected AC/DC grids could continue using the phasor approximation for security assessment of their systems including the NSWPH (which is computationally more efficient), as long as the mismatch between the phasor-approximation and the EMT models are within acceptable limits.

As already mentioned, EMT models can capture high frequency modes that phasor-approximation models cannot. Therefore, the appropriateness of the phasor- approximation will depend on the damping ratio of those high frequency modes. The control units that affect the damping ratio of high frequency modes are the virtual impedance controller of the grid-forming converters and the active damping controller of the grid-following converters.

As in Section 4, we are interested in the Hub-voltage and the power exchanged between the offshore converters and the grid. For both configurations, we are interested in evaluating the accuracy of the phasor-approximation for power exchanges between countries, as well as loss of a single element in the NSWPH (N-1 criterion). To this end, we perform the analysis using two scenarios: (i) A 200 MW power request from one of the onshore grids interconnected to the island, and (ii) an offshore HVDC converter outage (N-1 criterion).

Figure 9.a depicts the AC hub voltage (left) and the active power absorbed by an offshore converter (right) following the outage of another offshore converter. During the transients, high frequency oscillations are experienced in both the voltage and the active power. These oscillations are not detected by the phasor-approximation model. However, regarding the active power the mismatch

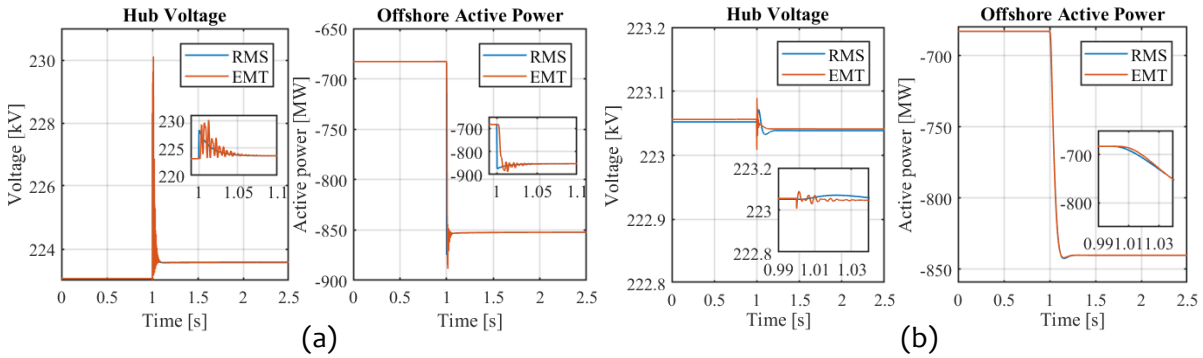

Figure 9: Accuracy of phasor-approximation model for the zero-inertia configuration: (a) response to an offshore converter outage; (b) response to a power exchange between partner TSOs. Left figures: voltage at the hub. Right figures active power in offshore converter.

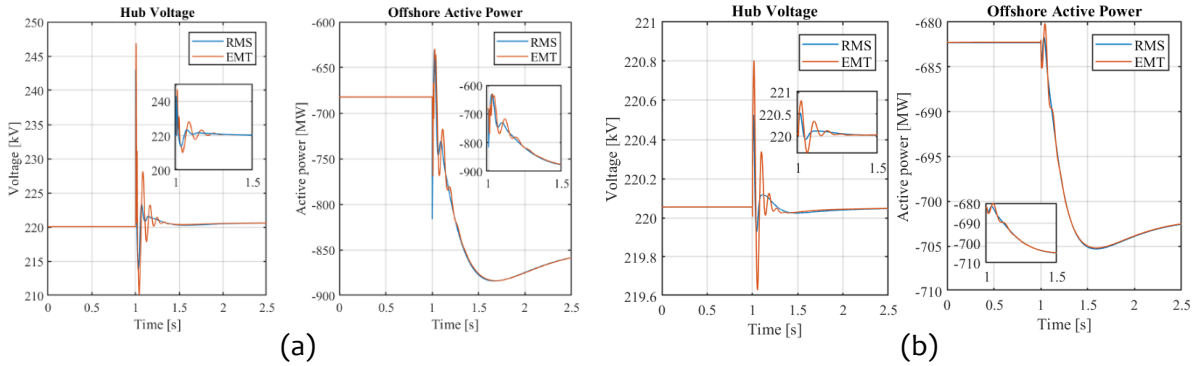

Figure 10: Accuracy of phasor-approximation model for the low-inertia configuration (a) response to an offshore converter outage; (b) response to a power exchange between partner TSOs. Left figures: voltage at the hub. Right figures: active power in offshore converter

between the phasor-approximation and the EMT models becomes negligible in less than 5 cycles (0.1 s). Similar conclusions can be drawn for the voltage of the AC hub, although the phasor-approximation model is not able to capture the maximum voltage deviation during the disturbance. Such voltage deviations must be checked with the EMT model.

Similar conclusions can be drawn for the low-inertia case. Figure 10.a depicts the hub voltage (left) and the active power absorbed by an offshore converter (right) following an offshore converter outage. Compared to zero-inertia case, the oscillations are of lower frequency and damp out slower. The mismatch between the phasor-approximation and the EMT models becomes negligible after approximately 10 cycles (0.2 s), which is twice as much compared to the zero-inertia case.

Figure 9.b and Figure 10.b depict the system response during a power exchange between partner TSOs for zero- and low-inertia configurations, respectively. In both cases the mismatch between the phasor-approximation and the EMT models is negligible for the active power absorbed by the offshore converters. As regards the hub voltage a larger mismatch can be observed, due to less-damped eigen-frequencies associated with the cables connected to the AC-Hub bus (these are eigen-frequencies that cannot be controlled by the active damping controllers of the converters). In both cases the phasor- approximation model cannot restitute the reference evolution provided by the EMT model. However, the response of the offshore system, seen from the onshore grids, is accurate enough for evaluating the system response during a power exchange between countries.

Summarizing the results from this section, we can make the following observations:

- Active power disturbances, such as power exchanges between partner TSOs, through the hub, can be accurately simulated using the phasor approximation modelling, in both the zero- and low-inertia configurations.
- As far as the hub voltage is concerned, after large disturbances, the phasor approximation model is much less satisfactory in terms of maximum voltage deviation. Expectedly, it cannot reproduce the oscillations with a period significantly smaller than its time step size. However, the average evolution is rendered satisfactorily.
- During large disturbances, the active power signal is well captured by the phasor-approximation model. Notably, in the zero-inertia case the mismatch between the EMT and the phasor-approximation models becomes negligible in less than five cycles of the alternating current.
- Grid-forming converters can control more tightly the voltage at their point of common coupling, compared to grid-following converters. With proper tuning, they control voltage and active power very well during large disturbances, by providing better damping to high frequency modes, which correspond to state variables associated with the offshore converters. This results in a small mismatch between the phasor-approximation and EMT model, since the dominant dynamics are the ones corresponding to the low frequency modes. The latter are of interest in dynamic security assessment.

VI. CONCLUSION

To realize the Paris Agreement's target in time, an accelerated deployment of large offshore wind farms is required. To that end, transmission system operators from the North Sea region agreed on exploring the possible development of a North Sea Wind Power Hub (NSWPH). In this paper, first, an economic assessment has been presented, which investigates different system frequencies and voltages for the offshore AC grid. The results show that for a NSWPH the distances between wind farms and the hub are below 50 km. For such short distances, there is no advantage in using low frequency AC systems. Based on a preliminary economic analysis, it is shown that a nominal voltage of 220 kV is preferable for long distances. Only for distances below 20 km, 66 kV is a better option. Beyond this distance, the costs of cables and cable laying dominate the total cost and render the

lower voltage option unattractive. These findings suggest that a voltage of 220 kV and a frequency of 50 Hz are the preferred solution for the offshore AC collection grid.

In the technical analysis, this paper explored two configurations for the NSWPH and provided a comparison regarding the dynamic behaviour of such a system. For comparison purposes, performance criteria regarding the voltage and the frequency of the offshore system have been considered, as well as the impact of large disturbances on the active power delivered to the interconnected onshore systems. The following observations were made:

- In the zero-inertia configuration the voltage and the frequency oscillations are better damped for the considered scenarios. Moreover, the active power is transmitted faster between partner TSOs.
- In the zero-inertia configuration, large disturbances, which result in active power imbalance of the offshore system, propagate instantaneously to the interconnected onshore grids and can lead to high frequency deviations in those grids.
- In the low-inertia configuration, such fast propagations of large disturbances are avoided, due to kinetic energy stored in the synchronous condenser. This reduces the impact of offshore incidents on the interconnected onshore grids.

Finally, this paper highlighted that the phasor approximation modelling can be used, as long as eigen-frequencies in power network are well damped. In the zero-inertia case, due to the ability of the grid-forming converter to damp high frequency oscillations, the difference between the phasor approximation and EMT models is negligible. In regard to the low inertia configuration, there is a mismatch between the two models for a slightly higher duration (namely, within 200 ms after the disturbance inception), due to some less-damped eigen-frequencies (depending on the tuning of the inner-current controllers). Our findings suggest that system operators could keep on using the phasor-approximation model in the presence of the NSWPH system for performing dynamic security assessment.

VII. ACKNOWLEDGMENT

This work was supported by the multiDC project, funded by Innovation Fund Denmark under Grant 6154-00020B.

BIBLIOGRAPHY

[1] United Nations, "Paris Agreement," Dec. 2015.

[2] European Commision, "Political Declaration on energy cooperation between the North Seas Countries," Jun. 2016.

[3] F. Thams, R. Eriksson and M. Molinas, "Interaction of Droop Control Structures and its Inherent Effect on the Power Transfer Limits in Multi-terminal VSC-HVDC," IEEE Transactions on Power Delivery, vol. 32, no. 1, pp. 182 - 192, 2016.

[4] P. Kundur, J. Paserba, V. Ajjarapu, G. Andersson, A. Bose, C. Canizares, N. Hatziargyriou, D. Hill, A. Stankovic, C. Taylor, T. Van Cutsem and V. Vittal, "Definition and classification of power system stability IEEE/CIGRE joint task force on stability terms and definitions," IEEE Trans. on Power Syst., vol. 19, no. 3, pp. 1387-1401, 2004.

[5] M. Raza, E. Prieto-Araujo and O. Gomis-Bellmunt, "Small-Signal Stability Analysis of Offshore AC Network Having Multiple VSC-HVDC Systems," IEEE Trans. on Power Del., vol. 33, no. 2, pp. 830-839, 2018.

[6] X. Wang and F. Blaabjerg, "Harmonic Stability in Power Electronic-Based Power Systems: Concept, Modeling, and Analysis," IEEE Transactions on Smart Grid, 2018.

[7] ABB, "XLPE submarince cable systems: Attachment to XLPE land cable systems," 2010.

[8] T. Weckesser and T. Van Cutsem, "Equivalent to represent inertial and primary frequency control effects of an external system," IET Generation, Transmission & Distribution, vol. 11, no. 14, pp. 3467-3474, 2017.

[9] G. Misyris, J. Mermet-Guyennet, S. Chatzivasileiadis and T. Weckesser, "Grid Supporting VSCs in Power Systems with Varying Inertia and Short-Circuit Capacity," in IEEE Powertech 2019, Milan, Italy, 2019.

[10] A. Madariaga, J. L. Martín, I. Zamora, I. Martínez De Alegría and S. Ceballos, "Technological trends in electric topologies for offshore wind power plants," Renewable and Sustainable Energy Reviews, pp. 32--44, 2013, (24).

[11] H. Chen, M. H. Johnson and D. C. Aliprantis, "Low-frequency ac transmission for offshore wind power," IEEE Transactions on Power Delivery, pp. 2236--2244, 2013 (28).

[12] X. Wang, Y. Teng, L. Ning, Y. Meng and Z. Xu, "Feasibility of Integrating Large Wind Farm via Fractional Frequency Transmission System Case Study," INTERNATIONAL TRANSACTIONS ON ELECTRICAL ENERGY SYSTEMS, 2014 (24).

[13] S. Liu, X. Wang, L. Ning, B. Wang, M. Lu and C. Shao, "Integrating Offshore Wind Power Via Fractional Frequency Transmission System," IEEE Transactions on Power Delivery, vol. 32, pp. 1253--1261, 2017.

[14] S. Lundberg, "Performance comparison of wind park configurations," Chalmers University of Technology, 2003.

[15] ENTSO-E, "Offshore Transmission Technology," 2011.

[16] Z. Hanzelka, W. Szpyra, A. Cziker and K. Piatek, "Reactive Power Compensation," in Electrical Energy Efficiency: Technologies and Applications, John Wiley & Sons, 2012, pp. 371-398.

[17] G. Guidi and O. B. Fosso, "Investment cost of HVAC cable reactive power compensation off-shore," in 2012 IEEE International Energy Conference and Exhibition (ENERGYCON), Florence, 2012.

[18] F. Mitschke, "Skin Effect," in Fiber Optics, Berlin, Springer, 2016, pp. 317-318.

[19] S. D. Sudhoff, "Transformer Design," in Power Magnetic Devices, Wiley - IEEE Press, 2014.

[20] North Sea Wind Power Hub Consortium, "Concept Paper 3: Modular Hub-and-Spoke: Specific solution options," June, 2019.

[21] S. Krishna, S. Novita and S. P. Warnaar, "Benefit study for potential locations of an offshore hub-island," TNO, Petten, July, 2019.

[22] M. Müller, E. Haesen, L. Ramaekers and N. Verkaik, "Translate COP212045 outlook and implications for offshore wind in the North Seas," ECOFYS, 2017.

[23] G. Chaspierre, P. Panciatici and T. Van Cutsem, "Dynamic Equivalent of a Distribution Grid Hosting Dispersed Photovoltaic Units," in IREP, Espinho, Portugal, 2017.

[24] J. Rocabert, A. Luna, F. Blaabjerg and P. Rodriguez, "Control of Power Converters in {AC} Microgrids," IEEE Trans. Power Electron., vol. 27, no. 11, pp. 4734-4739, 2012.

[25] L. Zhang, L. Harnefors and H.-P. Nee, "Power-Synchronization Control of Grid-Connected Voltage-Source Converters," IEEE Transactions on Power Systems, vol. 25, no. 2, pp. 809-820, 2010.

[26] B. Bastin, "Dynamics and control of a future off-shore wind power hub," M.Sc. thesis, University of Liège, June 2019. [Online]. Available: http://hdl.handle.net/2268.2/6802.

[Pub. E] Zero-inertia Offshore Grids: N-1 Security and Active Power Sharing

Authors:
G. S. Misyris, A. Tosatto, S. Chatzivasileiadis and T. Weckesser

Submitted to:
IEEE Transactions on Power Systems

Zero-inertia Offshore Grids: N-1 Security and Active Power Sharing

Georgios S. Misyris, *Student Member, IEEE*, Andrea Tosatto, *Student Member, IEEE*, Spyros Chatzivasileiadis, *Senior Member, IEEE,* and Tilman Weckesser, *Member, IEEE*

***Abstract*—With Denmark dedicated to maintaining its leading position in the integration of massive shares of wind energy, the construction of new offshore energy islands has been recently approved by the Danish government. These new islands will be zero-inertia systems, meaning that no synchronous generation will be installed in the island and that power imbalances will be shared only among converters. To this end, this paper proposes a methodology to calculate and update the frequency droops gains of the offshore converters in compliance with the N-1 security criterion in case of converter outage. The frequency droop gains are calculated solving an optimization problem which takes into consideration the power limitations of the converters as well as the stability of the system. As a consequence, the proposed controller ensures safe operation of off-shore systems in the event of any power imbalance and allows for greater loadability at pre-fault state, as confirmed by the simulation results.**

***Index Terms*—Electricity markets, frequency droop control, High-Voltage Direct-Current (HVDC), N-1 security, power sharing, zero-inertia off-shore grids.**

I. Introduction

SINCE the 1990s, Denmark has taken a leading role in the wind energy industry, in particular in the offshore sector. With the new Global Climate Action Strategy aiming at mitigating climate change, investments on Renewable Energy Sources (RES) will further increase. As part of this strategy, the Danish Government has approved the plans for the world's first two energy islands: Bornholm and the North Sea Wind Power Hub (NSWPH). The latter is the result of the international collaboration between the Dutch, German and Danish Transmission System Operators (TSOs) with the aim of installing more than 30 GW of wind power in the North Sea [1]. An artificial island will be built to collect the wind power produced, while several *point-to-point* High-Voltage Direct-Current (HVDC) links will connect the island to the onshore grids [2], forming a zero-inertia offshore AC system [3].

Being a first-of-a-kind project, TSOs face a series of new technical challenges related to reliability of power systems with only converter-based resources. Indeed, in the event of any power outage (N-1), the system must be able to restore the power balance fast enough to preserve the transient stability of the system [4]. Due to the complete absence of synchronous generators, the system will need either additional devices, such as DC choppers or crowbars, or a coordinated control strategy for active power sharing among converters, such as slack bus or frequency droop control [5]. In case of slack bus control, one converter absorbs the complete deviation, while the others do not take part in the active power regulation. The main disadvantage of this approach is that the converter acting as slack bus must be significantly oversized to satisfy the N-1 security criterion. On the contrary, frequency droop control allows the converters to share the power imbalance according to their droop gains, mimicking the behavior of synchronous generators. As for now, the latter appears as the preferable option for maintaining the power balance in the system.

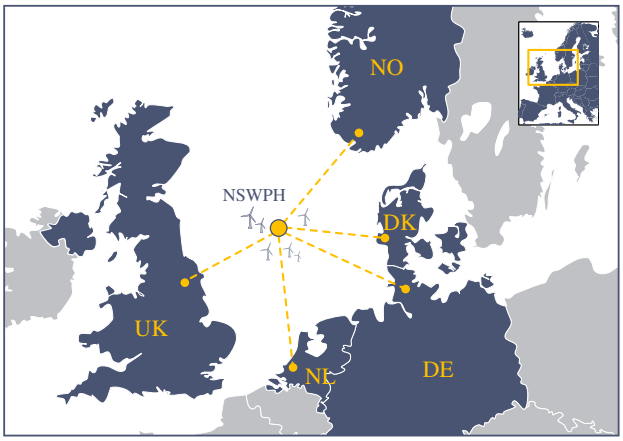

Fig. 1. North Sea Wind Power Hub concept.

The selection of frequency droop gains is mainly determined based on small-signal stability and dynamic performance of the system [6]–[11]. In addition to this, other limitations must be taken into consideration when tuning the frequency droops of converters in zero-inertia systems. With the main components of power converters being semiconductor switches, current limits represent a strict constraint for operation. To ensure that converters operate within their safety region, researchers have focused on developing various current limiting control strategies. However, these strategies can result in overload-induced instabilities if the active power set point of the converter is not adjusted, as presented in [10] and [12]. Although the schemes proposed by the authors improve the transient stability of grid-forming converters using only local measurements, they have only been evaluated in systems containing synchronous generators or an infinite bus, while the offshore system will consist of only grid-forming converters.

Moreover, the active power set-point of the HVDC convert-

G. S. Misyris, A. Tosatto and S. Chatzivasileiadis are with the Technical University of Denmark, Department of Electrical Engineering, Kgs. Lyngby, Denmark (emails: {gmisy, antosat, spchatz}@elektro.dtu.dk). T. Weckesser is with Dansk Energi, Frederiksberg C, Denmark (email: twe@danskenergi.dk).

This work is supported by the multiDC project, funded by Innovation Fund Denmark, Grant Agreement No. 6154-00020B.

Submitted to "IEEE Transactions on Power Systems" on February 19, 2021.

ers will be determined by the market and will vary significantly based on the total wind power produced and the resulting exchanges between NSWPH-connected countries. The question that arises is: will it be possible to define an unique set of gains that never violates the operating limits of the converters in case of contingency? Given that TSOs will want to guarantee the N-1 security criterion without relying on current limiting control techniques, the only possibility in case of fixed gains is to increase the Transmission Reliability Margin (TRM) and decrease the capacity available for market operation. This could lead to wind curtailment and market inefficiencies, calling for a new centralized approach to update the frequency droop values and adjust the active power set-points in case of contingency, ensuring reliable system operation in the island.

Centralized control strategies have already been deployed by TSOs, an example is the MIO controller of the back-to-back converter installed in Kriegers Flak CGS [13]. In addition, the concept of adaptive droop settings has been previously proposed for multi-terminal DC systems [14]–[17], where the DC voltage droops are updated considering the available headroom of the converters. In this context, this paper combines both approaches and proposes a centralized method for updating the frequency droop values of HVDC converters in offshore systems, with the goal of distributing the active power in a way that does not violate the operational limits of the converters in case of contingency. The calculation of frequency droop gains is performed solving an optimization problem which takes into consideration the available headroom of each converter and guarantees N-1 security. Dynamic and market simulations are performed to show the benefits of the proposed approach both in terms of dynamic response of the system and market operation. In detail, the contributions of this paper can be summarized as follows:

- a methodology to determine the frequency droop values and distribute any power imbalance without violating the operational limits of the remaining converters at the post-fault state.
- an analysis of the dynamic performance of the proposed methodology using the H_2 norm of the system as a performance metric.
- a cost benefit analysis which compares the proposed methodology to the common paradigm (static equal droops) in terms of market operation, highlighting the benefits of increased transmission capacity.

The rest of this paper is organized as follows. Section II introduces the operating principles of offshore and onshore converters. In section III, the optimization problem for selecting the droop gains of the converters is presented. The results of the dynamic and market simulations are discussed in Section IV. Section V concludes the paper.

II. Offshore Systems - Operating Principles

An offshore system consists of multiple offshore wind farms, a collection grid that transfers the produced power to a single or multiple offshore substations, and several HVDC links which transfer the collected wind power to the onshore systems, as depicted in Fig. 2. In the specific case of the NSWPH, the project consortium is considering to build one or multiple artificial islands instead of having floating substations. Multiple grid-forming converters are placed on these islands and are used to set the frequency of the offshore system.

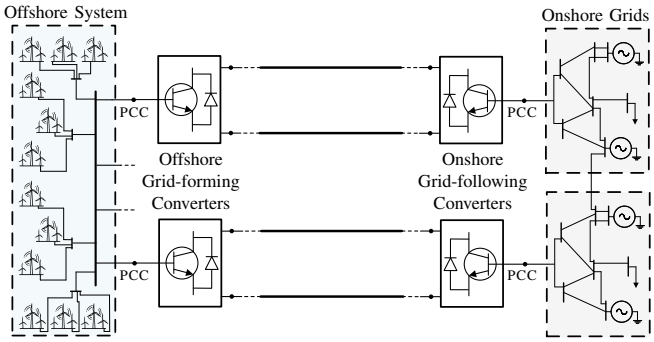

Fig. 2. Offshore energy islands with point-to-point HVDC connections to the onshore grids.

In zero-inertia systems, offshore converters share any power mismatch using a frequency droop control scheme: the active power exchanged with the AC system after a contingency depends on the frequency droop gain of each converter. However, when multiple grid-forming converters are connected to the same AC system, it becomes difficult to define the exact amount of power that each converter should handle after a contingency (wind farm loss, converter outage, etc.), which makes the system unreliable. Reliability of electricity supply is a fundamental requirement of power system operation, such that TSOs enforce different security criteria to limit the impact of disturbances. Among others, the N-1 criterion establishes that the system must be capable of withstanding the loss of a single component without violating operational security limits. Using fixed frequency droops might require additional control actions to be in compliance with the N-1 security criterion, such as blocking multiple offshore converters, or curtail wind in order not to exceed the current limits of the offshore converters. As a result, there is a need of adaptive frequency-droop based controller that accounts for the headroom of the converters and the varying profile of wind power generation. Similarly to [14], in our studies, we consider a converter station outage as a critical contingency that the system should withstand (N-1 security).

In the following, the control principle of the converters connected to the offshore and onshore systems are presented. In this work, we consider that the wind farms connected to the hub operate at unity power factor ($Q = 0$) at pre-fault state and do not participate in the primary frequency control.

A. Onshore VSC Control Scheme

VSCs connected to the onshore AC grids operate in grid-following mode [18]. In such operating mode, the main goal of the active power controller is to balance the voltage on the DC side. For point-to-point HVDC connections, PI controllers are deployed to control the DC voltage of the link and the reactive power exchanged with the onshore AC grid to their reference values, respectively.

B. Offhore VSC Control Scheme

VSCs connected to the offshore AC network operate in grid-forming mode [18]. The basic control structure of grid-forming converter consists of an active power controller, a voltage controller and a current limiter controller that saturates the converter in case it exceeds its nominal current value. More details on the grid-forming control structure can be found in [8] and [19]. In case of power imbalance, the main objective of a grid-forming converter is to remain synchronized with the rest of the grid without violating its operational limits, i.e. the converter will not share the burden of the converter loss if it operates close to its limits. To ensure this, we propose an adaptive primary frequency droop-based controller that considers the dynamic performance of the system and complies with the N-1 security criterion in case of converter outage. A frequency droop gain is assigned to each converter, and the post-contingency steady-state power output of each converter will then depend on the combined effect of the droops of the grid-forming converters.

III. Proposed Methodology

The scope of this work is to develop a methodology for calculating frequency droop gains of offshore converters in zero-inertia offshore grids which enable current distribution among the HVDC links without exceeding the converter limits. In this section, we present the optimization problem used to determine the set of droop gains with these properties.

A. Frequency Control in Zero-Inertia Offshore Systems

Similar to synchronous machine-based systems, the frequencies imposed by grid forming VSCs must converge to a common value ω at steady-state. The relationship between the active power absorbed/injected by the i-*th* offshore converter, P_i^*, and the imposed frequency, ω_i, is given by:

$$P_i^* = P_i^{\text{ref}} + \frac{1}{k_{f_i}} \Delta\omega_i \tag{1}$$

where k_{f_i} is the frequency droop gain, P_i^{ref} is the reference value of the active power and $\Delta\omega_i = \omega^{\text{ref}} - \omega_i$, with ω^{ref} the chosen reference frequency. At steady state $\Delta\omega_i = \Delta\omega$, with $\Delta\omega$ being the deviation of the average frequency of the offshore system.

To preserve the stability of the offshore system, the sum of the active power injected/withdrawn by the converters must be equal to the wind power produced. In case of converter (k) outage, the mismatch between the power produced by the wind farms and the power absorbed by the converters results in a frequency deviation equal to:

$$\Delta\omega = \frac{1}{\sum\limits_{i \neq k} \frac{1}{k_{f_i}}} P_k^{\text{ref}}. \tag{2}$$

where P_k^{ref} is the reference set-point of the k-*th* converter at pre-fault state. In case of converter outage, thus, the steady-state frequency deviation is inversely proportional to the sum of the inverse droop gains of the remaining converters connected to the offshore grid. It follows that the post-fault power flowing through the i-*th* converter, P_i^*, is given by:

$$P_i^* = P_i^{\text{ref}} + \frac{1}{k_{f_i}} \frac{1}{\sum\limits_{c \neq k} \frac{1}{k_{f_c}}} P_k^{\text{ref}}. \tag{3}$$

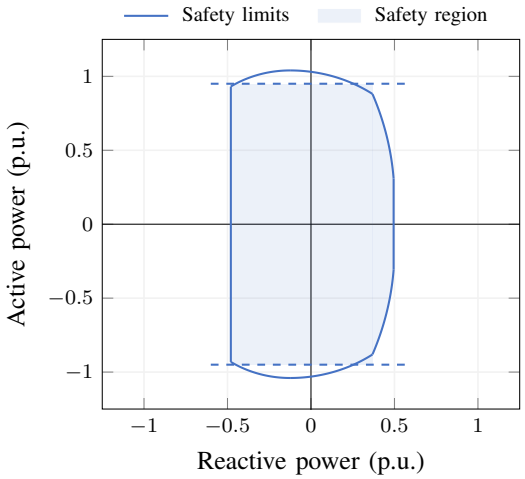

Fig. 3. PQ diagram of offshore VSCs [21].

In the following, the proposed methodology for calculating the droop gains of offshore converters is presented.

B. Optimization Problem

The selection of the frequency droop gains of converters plays a key role in ensuring small-signal stability and reliable operation of zero-inertia offshore systems [20].

The safe operating region of VSC converters is depicted in Fig. 3. On the y-axis, the active power output is limited by the maximum current the power electronic components can withstand: as the heating is proportional to the square of the current magnitude, the active power output slightly decrease with increasing reactive power output. On the x-axis, reactive power limitations are driven by voltage constraints. To ensure that the converter can contribute to voltage control by adjusting its reactive power, the active power limit is set to 0.95 pu.

On the one hand, too small values of frequency droop gains can lead to operating the converter outside its safety region; on the other hand, too high values of frequency droops make the system small-signal unstable due to the high influence of eigenfrequencies on the angle dynamics of the converter. This has already been illustrated in numerous works [6]–[8], [19], [22], [23] and, thus, the analysis for identifying the stability margins is omitted in this paper. To ensure small-signal stability while achieving a sufficient level of damping to avoid power oscillations, we consider a maximum value of the frequency droop equal to 0.1, similar to [4] and [23].

The selection of adequate droop gains can be performed by solving an optimization problem where the conditions to ensure small-signal stability of the system and N-1 security are enforced as constraints. Such an optimization problem, where

frequency droop gains (more precisely, their reciprocal x) are the decision variables, can be formulated as:

$$\min_{x} \sum_{i=1}^{n-1} \sum_{c=i+1}^{n} |x_i - x_c| \tag{4a}$$

$$\text{s.t. } \alpha = \sum_{i} x_i, \tag{4b}$$

$$x_i \geq \underline{X}_i, \qquad : \forall i \tag{4c}$$

$$\left| P_i + \frac{x_i}{\alpha - x_k} P_k \right| \leq \overline{P}_i^{\max}. \qquad : \forall i, \forall k \tag{4d}$$

For simplicity, droop coefficients k_f have been replaced by their reciprocal $x = 1/k_f$.

The objective function (4a) represents the sum of the distances between the droop gains. The goal of the optimization problem is, thus, to find a feasible set of droop gains close to "equal droop gains". This is done in order to have an equal distribution of the post-fault extra power in case constraints (4d) are not binding. As it will be shown later in section III-C, this control objective helps avoid power oscillations between the offshore converters and improve the dynamic performance of the frequency droop controllers [24].

The maximum Steady-State Frequency Deviation (SSFD) after the occurrence of an active power disturbance in the offshore network is a function of the sum of the droop gains (α), which is also a measure of the stiffness of the system. Thus, constraint (4b) makes sure that the selected droop gains sum up to the desired value (in this work, α is considered equal to 600, which is equivalent to a maximum steady state deviation of 0.0833 Hz after a step change of 2000 MW). Constraints (4c), instead, ensure small-signal stability, representing the upper bound on the droop gains. Finally, constraints (4d) are derived from equation (3) and limit the selection of the droop gains to those value which guarantee safe post-fault operation.

Problem (4) is non-linear, as constraints (4d) contain variables both in the numerator and denominator. By defining:

$$\alpha_k = \alpha - x_k, \tag{5a}$$

$$\sigma_k = \frac{1}{\alpha_k}, \tag{5b}$$

$$z_{k,i} = \sigma_k x_i, \tag{5c}$$

constraint (4d) can be rewritten as:

$$|P_i + z_{k,i} P_k| \leq \overline{P}_i^{\max}. \qquad : \forall i, \forall k \tag{6}$$

Although Eq. (6) is now linear, Eq. (5b) and (5c) are bilinear. In order to linearize them, the multi-parametric disaggregation technique presented in [25] is used. Eq. (5b) and (5c) are thus recast into:

$$1 = \sum_{b} \sum_{a} \hat{\sigma}^{\alpha}_{k,a,b} \cdot a \cdot 10^b, \tag{7a}$$

$$z_{k,i} = \sum_{d} \sum_{a} \hat{\sigma}^{x}_{k,i,a,d} \cdot a \cdot 10^d, \tag{7b}$$

In order to keep consistency with Eq. (5b), the following set of equalities and inequalities should be included together with Eq. (7a):

$$\alpha_k = \sum_{b} \sum_{a} a \cdot 10^b \cdot y^{\alpha}_{k,a,b}, \tag{8a}$$

$$\sigma_k = \sum_{a} \hat{\sigma}^{\alpha}_{k,a,b}, \qquad : \forall b \tag{8b}$$

$$0 \leq \hat{\sigma}^{\alpha}_{k,a,b} \leq \overline{S}_k \cdot y^{\alpha}_{k,a,b} \qquad : \forall a, \forall b \tag{8c}$$

$$\sum_{b} y^{\alpha}_{k,a,b} = 1, \qquad : \forall b \tag{8d}$$

$$y^{\alpha}_{k,a,b} \in \{0, 1\}. \qquad : \forall a, \forall b \tag{8e}$$

with $a \in \{0, 1, ..., 9\}$ and $b \in \{\psi_b, ..., \eta_b\}$. In Eq. (8a), α_k is expressed as a multi-parametric sum of active decimal powers determined by the binary variables $y^{\alpha}_{k,a,b}$, while σ_k is disaggregated into a set of continuous non-negative variables, represented by $\hat{\sigma}^{\alpha}_{k,a,b}$, in Eq. (8b). The two parameters ψ_b and η_b denotes the powers of ten used for the parameterization of α_k. Eq. (8c) enforces the limits on $\hat{\sigma}^{\alpha}_{k,a,b}$, which must be non-negative and equal to the upper bound $\overline{S}_k$ at most. From Eq. (5b), $\overline{S}_k = \frac{1}{\sum_{i \neq k} \underline{X}_i}$. Finally, Eq. (8d) guarantees that only one binary variable is active for the *b-th* place in the power representation of $\hat{\sigma}^{\alpha}_{k,a,b}$.

Similarly, together with Eq. (7b) the following equalities and inequalities are included:

$$x_i = \sum_{d} \sum_{a} a \cdot 10^d \cdot y^{x}_{i,a,d}, \tag{9a}$$

$$\sigma_k = \sum_{a} \hat{\sigma}^{x}_{k,i,a,d}, \qquad : \forall d \tag{9b}$$

$$0 \leq \hat{\sigma}^{x}_{k,i,a,d} \leq \overline{S}_k \cdot y^{x}_{i,a,d} \qquad : \forall a, \forall d \tag{9c}$$

$$\sum_{d} y^{x}_{i,a,d} = 1, \qquad : \forall d \tag{9d}$$

$$y^{x}_{i,a,d} \in \{0, 1\}. \qquad : \forall a, \forall d \tag{9e}$$

with $a \in \{0, 1, ..., 9\}$ and $d \in \{\psi_d, ..., \eta_d\}$. The two parameters ψ_b and ψ_d are chosen according to the desired decimal precision, e.g. $\psi_b = \psi_d = -5$ denote a precision of 10^{-5}, while η_b and η_d are determined by the magnitude of α_k and x_i, respectively. For example, the upper bound of α_k is $\alpha - \underline{X}_k$; if $\alpha = 300$, η_b must be equal to or greater than 2.

After the linearization, problem (4) is recast into:

$$\min_{\Gamma} \sum_{i=1}^{n-1} \sum_{c=i+1}^{n} |x_i - x_c| \tag{10a}$$

$$\text{s.t. } (4b) - (4c) \tag{10b}$$

$$(5a) \qquad : \forall k \tag{10c}$$

$$(7a),\ (8a) - (8e) \qquad : \forall k \tag{10d}$$

$$(7b),\ (9a) - (9e) \qquad : \forall i, \forall k \tag{10e}$$

$$(6) \tag{10f}$$

with $\Gamma = \{x, \hat{\sigma}^{\alpha}, \hat{\sigma}^{x}, y^{\alpha}, y^{x}\}$. Problem (10) is now a Mixed Integer Linear Problem (MILP) and can be solved with commercial and open-source MILP solvers (e.g. Gurobi, Mosek or GLPK).

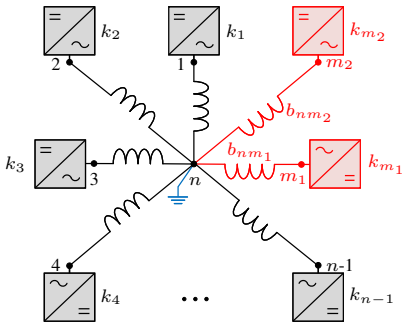

Fig. 4. Example of a network of n converter nodes. Node n is grounded following the approach in [27]. Two additional converter nodes m_1 and m_2, highlighted in red, are included in the system to study its dynamic performance with equal or different droop gains.

C. Dynamic Performance of Frequency Droop Control

As explained in section III-B, the objective of the optimization problem is to minimize the distance between the droop gains of the converters. To motivate this choice, we now evaluate the performance of primary frequency control when offshore converters have equal or different frequency droop values, using as a metric the H_2 norm of the system, i.e. root-mean-square of the impulse response of the system.

The simplified model used in this section, depicted in Fig. 4, considers an AC system with n nodes "formed" by grid-forming converters. Similar to [26] (that also considers an AC network with multiple grid-forming converters and loads), the AC system is described by linear power flow and Kron-reduced network models. Several wind farms are connected to the system, modelled as negative constant loads. Under the assumptions of linear power flow model (i.e. voltage magnitude are considered constant and cable capacitance negligible), any constant power load can be represented by a constant impedance load and, under the assumption of Kron-reduced network model, included in the impedances of the cables. Since the frequency is regulated by the grid-forming converters, the frequency control dynamics can be described as:

$$\dot{\theta}_i = \omega_i \tag{11}$$

$$T_{p_i}\dot{\omega}_i = -\omega_i + \omega_{\text{ref}} + k_{f_i}(P_i^{\text{ref}} - P_i) \tag{12}$$

where T_{p_i} represents the delay for measuring the active power P_i at the PCC of the grid-forming converter. Based on the linear power flow assumptions, $P_i = \sum_j b_{ij}\,(\theta_i - \theta_j)$, where b_{ij} is the susceptance of the cable connecting node i to node j and θ_i, θ_j are the voltage angles at node i and j.

For the dynamic performance analysis, it is assumed that the system is subject to persistent amplitude noise (wind fluctuation), modelled as an additive disturbance $w(t)$. Similar to [24], the system output $y(t)$ is the frequency deviation $\omega(t)$ at the terminal of grid forming converters, since the focus of the analysis is on the impact of the frequency droop gains on the frequency fluctuations and, thus, active power oscillations.

Considering a second-order frequency droop control model for inverter-based networks [26], the state-space model of the system model can be described as follows:

$$\begin{bmatrix}\dot{\theta}\\ \dot{\omega}\end{bmatrix} = \underbrace{\begin{bmatrix}0 & I\\ -T_p^{-1}K_fL_B & -T_p^{-1}\end{bmatrix}}_{A}\begin{bmatrix}\theta\\ \omega\end{bmatrix} + \underbrace{\begin{bmatrix}0\\ -T_p^{-1}K_f\end{bmatrix}}_{B} w \tag{13a}$$

$$y = \underbrace{\begin{bmatrix}0 & I\end{bmatrix}}_{C}\begin{bmatrix}\theta\\ \omega\end{bmatrix} \tag{13b}$$

where $T_p = \text{diag}(T_{p_i})$, $K_f = \text{diag}(k_{f_i})$ and L_B is the b_{ij}-weighted Laplacian matrix. We assume that all the time delays are equal, i.e. $T_{p_i} = \tau\ \forall i$, and that the grid-forming converters do not provide an inertia effect. To evaluate the dynamic performance of the system with a certain set of droop gains, the H_2 norm of the system is computed. The H_2 norm, which gives an interpretation of how the gains affect the frequency and active power response after an active power disturbance, is calculated as follows:

$$||H||_{\mathcal{H}_2}^2 = \text{tr}(B^T X B) \tag{14}$$

where X is the observability Gramian computed by solving the Lyapunov equation:

$$A^T X + XA = -C^T C \tag{15}$$

1) Performance analysis: We first look at how the dynamic performance of the system is affected by different parameters, such as the number of grid-forming converters, the value of the droop gains and the inertia effect of the converters. Following the approach in [27], we use a reduced model of the system described by (13). The reduced order model is based on the change of variables:

$$\theta = U\theta' \quad \text{and} \quad \omega = U\omega' \tag{16}$$

where U is the unitary matrix that diagonalizes L_B. This change aims at eliminating the zero eigenvalue contained in the matrix A. The physical interpretation of the reduced system is that one of the nodes in the network is considered grounded.

Assuming that all the droop gains are equal, i.e. $k_{f_i} = k\ \forall i$, the state-space model describing the reduced model is:

$$\begin{bmatrix}\dot{\theta}'\\ \dot{\omega}'\end{bmatrix} = \begin{bmatrix}0 & I\\ -\frac{k}{\tau}\widetilde{L}_B & -\frac{1}{\tau}I\end{bmatrix}\begin{bmatrix}\theta'\\ \omega'\end{bmatrix} + \begin{bmatrix}0\\ -\frac{k}{\tau}I\end{bmatrix}w' \tag{17a}$$

$$y' = \begin{bmatrix}0 & I\end{bmatrix}\begin{bmatrix}\theta'\\ \omega'\end{bmatrix} \tag{17b}$$

From (14), the H_2 norm of the system is calculated as:

$$||\widetilde{H}||_{\mathcal{H}_2}^2 = (n-1)\,\frac{(k)^2}{2\tau} \tag{18}$$

The following observations can be made for the H_2 norm: (i) it is directly proportional to the value of the frequency droop gain k, (ii) it decreases with increasing time delay τ and (iii) it increases with increasing number of grid-forming converters. The first observation is related to the responsiveness of the controller: the higher the frequency droop gain, the faster the response of the converter and, thus, the higher the oscillations in the frequency. The second observation has to do with the inertia effect provided by the grid-forming converters: the higher the time delay, the higher the inertia effect and,

thus, the smaller the frequency fluctuations. Finally, the third observation suggests that the droop gains should be adjusted in case a grid-forming converter is added/removed from the system to preserve the performance of the frequency droop control strategy.

2) Comparison between equal and different gains: To study how the dynamic performance of the system is affected by selecting different droop gains for the converters, we consider two additional nodes $m_1 = n+1$ and $m_2 = n+2$ connected to the grounded node (for simplicity node n). Two grid-forming converters, with droop gains k_{m_1} and k_{m_2} respectively, are connected to these nodes. Similar to the other nodes, also the new converters are subject to persistent amplitude noise, respectively w_{m_1} and w_{m_2}. The new system $\widehat{H}$ consists of system $\widetilde{H}$ described by (17) and two subsystems formed by the two grid-forming converters, respectively H_{m_1} and H_{m_2}. The state-space model of these subsystems can be written as:

$$\begin{bmatrix} \dot{\theta}_m' \\ \dot{\omega}_m' \end{bmatrix} = \begin{bmatrix} 0 & 1 \\ -\frac{k_m}{\tau} b_{nm} & -\frac{1}{\tau} \end{bmatrix} \begin{bmatrix} \theta_m' \\ \omega_m' \end{bmatrix} + \begin{bmatrix} 0 \\ -\frac{k_m}{\tau} \end{bmatrix} w_m' \tag{19a}$$

$$y_m' = \begin{bmatrix} 0 & 1 \end{bmatrix} \begin{bmatrix} \theta_m' \\ \omega_m' \end{bmatrix} \tag{19b}$$

where $m \in \{m_1, m_2\}$. As described in [27], system $\widehat{H}$ can be decoupled into three subsystems, $\widehat{H} = \text{diag}(\widetilde{H}, H_{m_1}, H_{m_2})$. It follows that the squared H_2 norm of system $\widehat{H}$ can be computed as:

$$||\widehat{H}||_{\mathcal{H}_2}^2 = ||\widetilde{H}||_{\mathcal{H}_2}^2 + ||H_{m_1}||_{\mathcal{H}_2}^2 + ||H_{m_2}||_{\mathcal{H}_2}^2. \tag{20}$$

Similar to (18), the sum of the squared norms of subsystems H_{m_1} and H_{m_2} can be calculated as follows:

$$||H_{m_1}||_{\mathcal{H}_2}^2 + ||H_{m_2}||_{\mathcal{H}_2}^2 = \frac{(k_{m_1})^2}{2\tau} + \frac{(k_{m_2})^2}{2\tau} = \frac{\varepsilon}{2\tau} \tag{21}$$

where ε is equal to the sum of the squared frequency droops values k_{m_1} and k_{m_2}.

Let us now assume that the frequency droop gains sum to a fixed value σ, which corresponds to fixing the SSFD to a specific value. If $k_{m_1} > k_{m_2}$, it follows that $||H_{m_1}||_{\mathcal{H}_2}^2 > ||H_{m_2}||_{\mathcal{H}_2}^2$, which indicates that the performance of the frequency controller of converter m_1 is worse compared to the one of m_2. Moreover, the relation between ε and σ is given by:

$$\varepsilon = \sigma^2 - 2k_{m_1}k_{m_2}. \tag{22}$$

Equation (22) clearly shows that the minimum value of the sum of the squared H_2 norm of the two subsystems corresponds to the situation where $k_{m_1} = k_{m_2}$, meaning that the dynamic performance of the system is improved when all the converters have the same droop gain.

IV. Simulation and Results

The test system used for the validation of the proposed methodology is inspired by the NSWPH project, and represents an offshore energy island configuration for massive integration of offshore wind power. Ten wind farms, with a total installed capacity of 9 GW, are connected to the island through 400 kV HVAC cables. Six point-to-point HVDC links connect the island to the onshore grids, as depicted in Fig. 5. The rated power of each offshore and onshore converter is 1850 MVA, and the base power of the system is S_b = 1850 MVA. More details about the converters' control structure and the models of power system components can be found in [4]. All the dynamics simulations presented in this section have been performed with DIgSILENT PowerFactory [28].

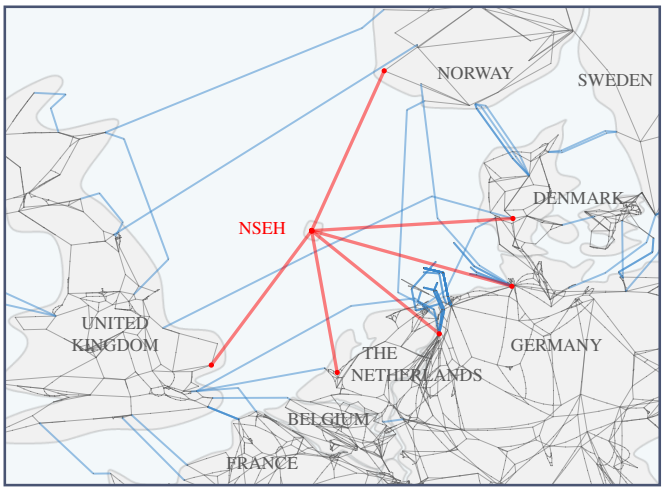

Fig. 5. Connections between the offshore island and the onshore grids. The electrical networks correspond to the 400 kV transmission networks of the respective countries.

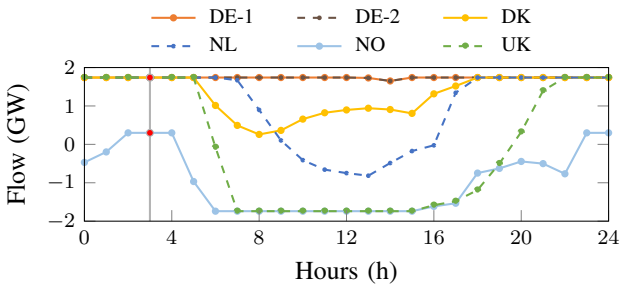

Fig. 6. Flows over the HVDC interconnectors.

A market model representing the European electricity market in 2030 is used to determine the power flows from the island to each country for a period corresponding to one year. In order to highlight the problems arising with static equal droops, the market is first cleared without considering the N-1 security criterion, i.e. without limitations on the available transmission capacity. Subsequently, the compliance with the N-1 criterion is checked before clearing the market and transmission capacities are decreased if necessary. The market is then cleared again to highlight the benefit of the proposed methodology. An example of the power flows during one day (24 hours) is plotted in Fig. 6. From this representative day, the hour with the most critical set of flows has been selected for the dynamic simulations, which corresponds to hour 3 when most of the converters are operated close to their limits. All the market simulations presented in this section have been performed using YALMIP [29] and Gurobi [30].

The remainder of this section is divided into three parts.

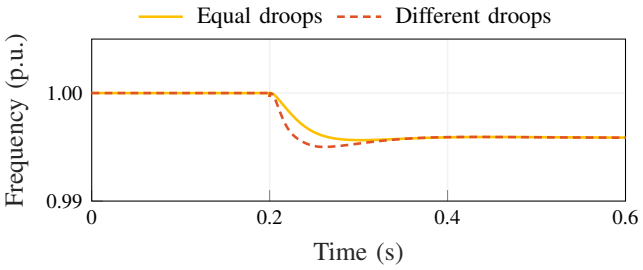

Fig. 7. Average frequency deviation following a step decrease of wind power in case of equal and different droops.

In Section IV-A, we compare the dynamic performance of the frequency droop controllers with equal and different frequency droop gains in case of a sudden variation of the wind. This is to highlight that equal droop gains better perform in terms of dynamic response. In Section IV-B, we evaluate the performance of the proposed methodology, considering a converter outage and the corresponding system response with static and adaptive gains. Finally, in Section IV-C, we assess the benefits of the proposed methodology in terms of increased transmission capability for market operation.

Without loss of generality, in all the simulations in Section IV-B and IV-C, we consider that the offshore converter at outage corresponds to the HVDC-link connecting the NSWPH to UK, with an active power output of 1740 MW. Thus, the loss of this converter is equivalent to an increase of active power (1740 MW) that must be shared among the other converters. It should be mentioned that, at the pre-fault state, all the converters control the voltage at their PCC, which is equal to 1 pu. This leads to a reactive power absorption in the range of 0-150 MVAr for all converters, which corresponds to an initial reactive current less than 0.08 pu. Finally, due to space limitations, the legend is omitted in the next plots; the reader is referred to the legend of Fig. 6.

A. Dynamic Performance

In the first simulation, a step decrease (250 MW) of the wind power output is applied to the system. Fig. 7 shows the frequency deviations of the grid-forming converters. The stiffness of the system is the same in both simulations ($\alpha = 600$); however, in the first case all the droop coefficients are equal, while in the second case they are different. As expected, the average steady-state frequency deviation in the system is the same in both cases. This confirms that the SSFD only depends on the stiffness of the system and it is not affected by individual droop values. Moreover, it is evident that the average frequency deviation of the system is higher in case of different gains. This confirms that the dynamic performance of the system is worse when grid-forming converters have different gains, as described in Section III-C2.

B. Validation of the Proposed Methodology

In the second simulation, the effectiveness of the proposed frequency controller with adaptive droop gains is demonstrated. Two cases are analyzed: (i) frequency droop values are static gains and are all equal and (ii) frequency droops

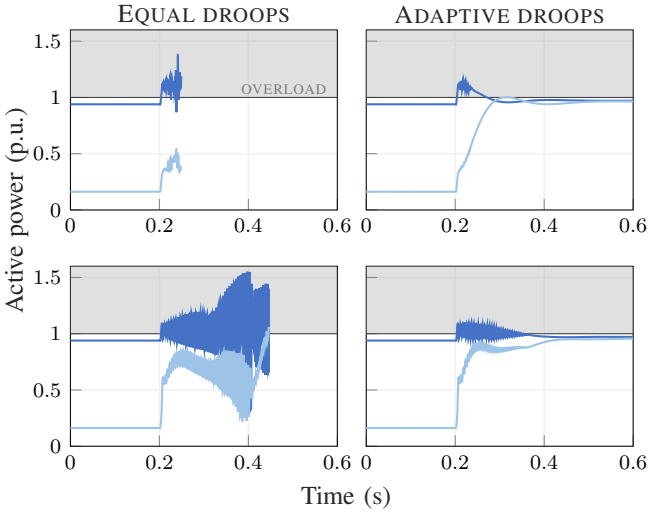

Fig. 8. System response to an offshore converter outage. The two left figures show the power set-point of two remaining converters (NL and NO) with equal droops, while the two right figures are obtained with adaptive droops. In both cases, the two current limiting techniques in [31] (upper figures) and [32] (lower figures) are used with $I_{max} = 1.1$ pu. The overload region is represented with the gray area.

are updated based on the optimization problem presented in Section III every time the HVDC set-points are changed. Moreover, two different current limiting controllers, presented respectively in [31] and [32], are implemented for each case. This is done in order to show that the presented results are independent on the implemented current limiting strategy.

Fig. 8 shows the system response to the trip of the converter connected to UK (1740 MW); for a better visualization, only the converters connected to NL and NO are displayed. During the first milliseconds after the outage, the power that was previously flowing to UK is redirected to the other converters. In the case of equal frequency droops, it can be seen that during the first few hundred milliseconds the converters are saturated to 1.1 pu, which is the maximum saturation current. However, we can see that afterwards the converters lose synchronous stability with both the current limiting controllers. More details about the instability mechanisms in case of the dynamic virtual impedance current limiting controller and d-axis priority based current saturation algorithm, can be found in [19] and [31], respectively.

In case of adaptive frequency droops, the system response initially triggers the applied current limiting schemes. However, due to the different gains, a big portion of the active power initially absorbed by the converter at outage is directed towards the offshore converter which had the largest headroom at pre-fault state. That "relieves" the offshore converters that were saturated immediately after the outage. As shown in Fig. 8, with the proposed frequency droop controller the active power absorbed by the remaining converters stays below its nominal value also at post-fault state regardless of what current limiting technique is implemented. This demonstrates that the effectiveness of the proposed method is not dependent on the current limiting strategy and that the power imbalance is distributed according to the available power headroom, ensuring N-1 security at every time interval.

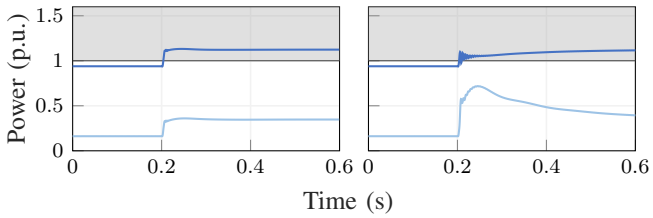

Fig. 9. System response to an offshore converter outage using the current limiting technique in [31] (left) and [32] (right). Both figures shows the power set-point of two of the remaining converters (NL and NO) with equal droops and $I_{max} = 1.2$ pu.

C. Impact of the Proposed Methodology on Market Operation

In the third simulation, the value at which the current saturates, I_{max}, is increased from 1.1 pu to 1.2 pu. This is done to show that, in case of contingency, the system remains stable if converters do not saturate. Fig. 9 shows the system response in case of equal droops with the two current limiting techniques. During the first milliseconds after the outage, all the offshore converters share equally the current of the converter at outage, which is distributed according to the frequency droop gains. Given that most of the converters were operating close to their limits (except NO), the active power limits of most of the converters are violated (we only represent NL as the other converters have the exact same behavior). Since now I_{max} is increased, all the converters remain synchronised, which shows that the system is stable when the converters are not saturated. However, exceeding the active power limit of the converters violates the N-1 criterion. Thus, in case of equal droops, system operators would have to decrease the available transmission capacity in order to ensure that the converters will operate within the operating region after the contingency.

In order to understand what are the implications of reducing the available transmission capacity given to the market, the market simulations are run again now considering the N-1 criterion. In other words, the market is cleared and then the obtained flows are used to check the compliance with the N-1 security criterion. In both situations, with fixed equal droops and adaptive droops, the capacity is decreased (50 MW steps) on those converters whose power limits are violated in case of converter outage, and the market is cleared again with the new capacities. This is repeated until the N-1 criterion is fulfilled. This procedure could be intended as the offline calculation performed by TSOs to ensure the stability of the system before communicating the available transmission capacity to the market operator. Fig. 10 shows the available transmission capacities (shaded areas) between DE and NSWPH (upper graphs) and NL and NSWPH (lower graphs) and the resulting flows (red dots). These graphs show the duration curve of the capacities, meaning the values of the capacity have been rearranged in descending order. With fixed equal droops, the N-1 security criterion is often violated and the full capacity is allowed only for less than 30% of the time. It is interesting to observe that the full capacity is only allowed when it is not actually needed, as shown by the flows which are always below the maximum value. On the contrary, with adaptive droops, the gains are calculated in order to take advantage

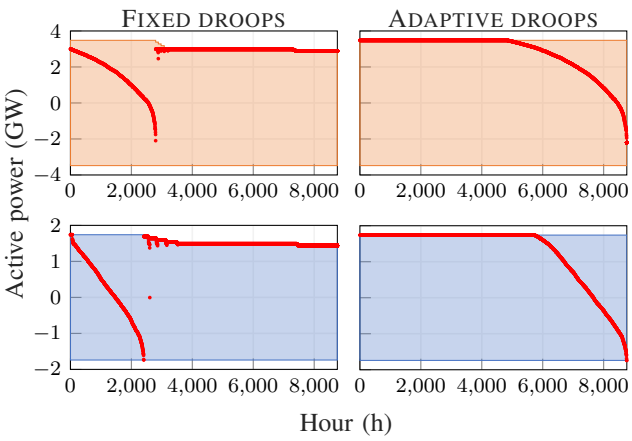

Fig. 10. Available transmission capacity (shaded area) and corresponding flows (red dots) to DE (upper plots) and NL (lower plots). In the left graphs, the available capacity has been calculated based on fixed/equal droop gains while, in the right ones, based on adaptive droop gains.

of the different headrooms, and the N-1 criterion is always satisfied. The reduction of transmission capacity in case of fixed droops results in more than 350 GWh of curtailed wind energy which, in turn, increase the total system costs by 85 million Euros. This could be avoided either by oversizing the converters, increasing the investment costs, or by adjusting the droop gains with the proposed methodology.

V. Conclusion

In this paper, challenges with respect to active power sharing in zero-inertia systems have been discussed and a method for deriving and updating frequency droop gains has been developed, ensuring active power sharing in the system after a large disturbance in compliance with the N-1 security criterion.

The simulation results show that, in the event of an offshore converter outage, current limiting strategies lead to instability in case the converters are saturated. Thus, the N-1 criterion cannot be guaranteed. By considering the headroom of each converter when calculating the frequency droop gains, the proposed approach distributes the power among the converters while taking into consideration their safe operating regions. As a consequence, the proposed methodology avoids converter saturation and preserves their synchronization to the rest of the grid. Moreover, by enforcing upper bounds on the frequency droop gains, also the small-signal stability of the system is guaranteed. As a result, the proposed methodology allows for greater loadability of the offshore converters at pre-fault state and guarantees their safe operation in the event of any power imbalance. Finally, from an operational point of view, the additional capacity given to the market results in a better utilization of the interconnectors, avoids wind curtailment and reduces the total system costs without oversizing of the converters.

References

[1] North Sea Wind Power Hub - Consortium Partners. (2017) Power hub as an island. [Online]. Available: https://northseawindpowerhub.eu/wp-content/uploads/2017/11/Concept-Paper-3-Hub-as-an-Island.pdf

[2] North Sea Wind Power Hub Consortium. (2019) Cost evaluation of north sea offshore wind post 2030. [Online]. Available: https://northseawindpowerhub.eu/wp-content/uploads/2019/07/Cost-Evaluation-of-North-Sea-Offshore-Wind-1.pdf

[3] D. Van Hertem, O. Gomis-Bellmunt, and J. Liang, *Modeling and control of offshore AC hub*, 2016, pp. 451–471.

[4] G. Misyris *et al.*, "North sea wind power hub: System configurations, grid implementation and techno-economic assessment," 2020.

[5] D. Van Hertem, O. Gomis-Bellmunt, and J. Liang, *Power system operations with HVDC grids*, 2016, pp. 213–237.

[6] L. Harnefors, M. Hinkkanen *et al.*, "Robust Analytic Design of Power-Synchronization Control," *IEEE Trans. Ind. Electron.*, vol. 66, no. 8, pp. 5810–5819, Aug 2019.

[7] P. Vorobev, P. Huang *et al.*, "High-Fidelity Model Order Reduction for Microgrids Stability Assessment," *IEEE Trans. Power Syst.*, vol. 33, no. 1, pp. 874–887, Jan 2018.

[8] S. D'Arco, J. A. Suul, and O. B. Fosso, "A Virtual Synchronous Machine implementation for distributed control of power converters in SmartGrids," *Electric Power Systems Research*, vol. 122, pp. 180 – 197, 2015.

[9] N. Pogaku, M. Prodanovic, and T. C. Green, "Modeling, Analysis and Testing of Autonomous Operation of an Inverter-Based Microgrid," *IEEE Trans. Power Electron.*, vol. 22, no. 2, pp. 613–625, March 2007.

[10] T. Qoria, F. Gruson *et al.*, "Inertia effect and load sharing capability of grid forming converters connected to a transmission grid," *IET Conference Proceedings*, pp. 79 (6 pp.)–79 (6 pp.)(1), January 2019.

[11] T. Qoria, F. Gruson *et al.*, "Tuning of Cascaded Controllers for Robust Grid-Forming Voltage Source Converter," in *2018 Power Systems Computation Conference (PSCC)*, June 2018, pp. 1–7.

[12] A. Tayyebi, D. Groß *et al.*, "Frequency stability of synchronous machines and grid-forming power converters," *IEEE Journal of Emerging and Selected Topics in Power Electronics*, vol. 8, no. 2, pp. 1004–1018, 2020.

[13] Hitachi ABB. (2019) KriegersFlak Master Controller (MIO). [Online]. Available: http://www.multi-dc.eu/wp-content/uploads/2019/10/20190919-KriegersFlak-Master-Controller_R03.pdf

[14] R. Eriksson, "Current Sharing in Multiterminal DC Grids—The Analytical Approach," *IEEE Trans. Power Syst.*, vol. 33, no. 6, pp. 6278–6288, Nov 2018.

[15] N. R. Chaudhuri and B. Chaudhuri, "Adaptive droop control for effective power sharing in multi-terminal dc (mtdc) grids," *IEEE Transactions on Power Systems*, vol. 28, no. 1, pp. 21–29, 2013.

[16] J. Beerten and R. Belmans, "Analysis of Power Sharing and Voltage Deviations in Droop-Controlled DC Grids," *IEEE Trans. Power Syst.*, vol. 28, no. 4, pp. 4588–4597, Nov 2013.

[17] J. Beerten, R. Eriksson, and D. V. Hertem, "A new approach to hvdc grid voltage control based on generalized state feedback," in *2014 IEEE PES General Meeting — Conference Exposition*, July 2014, pp. 1–5.

[18] J. Rocabert, A. Luna, F. Blaabjerg, and P. Rodríguez, "Control of Power Converters in AC Microgrids," *IEEE Trans. Power Electron.*, vol. 27, no. 11, pp. 4734–4749, Nov. 2012.

[19] T. Qoria, F. Gruson *et al.*, "Critical clearing time determination and enhancement of grid-forming converters embedding virtual impedance as current limitation algorithm," *IEEE Journal of Emerging and Selected Topics in Power Electronics*, pp. 1–1, 2019.

[20] L. Zhang, "Modeling and Control of VSC-HVDC Links Connected to Weak AC Systems," Ph.D. dissertation, KTH, Electrical Machines and Power Electronics, 2010, qC20100607.

[21] ABB, "HVDC Light - It's time to connect," Tech. Rep., 2017.

[22] E. Barklund, N. Pogaku *et al.*, "Energy management in autonomous microgrid using stability-constrained droop control of inverters," *IEEE Transactions on Power Electronics*, vol. 23, no. 5, pp. 2346–2352, 2008.

[23] G. Misyris, S. Chatzivasileiadis, and T. Weckesser, "Zero-inertia systems: Sufficient conditions for phasor modeling," 2020.

[24] E. Mallada, "idroop: A dynamic droop controller to decouple power grid's steady-state and dynamic performance," in *2016 IEEE 55th Conference on Decision and Control (CDC)*, 2016, pp. 4957–4964.

[25] J. Teles, P. Castro, and H. Matos, "Multi-parametric disaggregation technique for global optimization of polynomial programming problems," *Journal of Global Optimization*, vol. 55, no. 5, pp. 227–251, Feb. 2013.

[26] E. Tegling, M. Andreasson, J. W. Simpson-Porco, and H. Sandberg, "Improving performance of droop-controlled microgrids through distributed pi-control," in *2016 American Control Conference (ACC)*, 2016, pp. 2321–2327.

[27] E. Tegling, B. Bamieh, and D. F. Gayme, "The price of synchrony: Evaluating the resistive losses in synchronizing power networks," *IEEE Transactions on Control of Network Systems*, vol. 2, no. 3, pp. 254–266, 2015.

[28] DIgSILENT, "PowerFactory 2021 - Integrate Power System Analysis Software," Nov. 2020.

[29] J. Löfberg, "YALMIP : A Toolbox for Modeling and Optimization in MATLAB," in *Proc. CACSD Conference*, Taipei, Taiwan, 2004.

[30] Gurobi Optimization, LLC, "Gurobi optimizer reference manual," 2020. [Online]. Available: http://www.gurobi.com

[31] H. Xin, L. Huang *et al.*, "Synchronous instability mechanism of p-f droop-controlled voltage source converter caused by current saturation," *IEEE Transactions on Power Systems*, vol. 31, no. 6, pp. 5206–5207, 2016.

[32] A. D. Paquette, M. J. Reno, R. G. Harley, and D. M. Divan, "Sharing transient loads : Causes of unequal transient load sharing in islanded microgrid operation," *IEEE Industry Applications Magazine*, vol. 20, no. 2, pp. 23–34, 2014.

[Pub. F] Grid-forming Converters: Sufficient Conditions for RMS Modeling

Authors:
G. S. Misyris, S. Chatzivasileiadis and T. Weckesser

Submitted to:
Electric Power Systems Research

Grid-forming Converters in Transmission Grids: Parameter Constraints & Appropriatness of RMS Modeling for a Subset of Disturbances

George S. Misyris, Spyros Chatzivasileiadis, and Tilman Weckesser

Copenhagen, Denmark

Abstract

Time-domain simulations are a critical tool for power system operators. Depending on the instability mechanism under consideration and the system characteristics, such as the time constants of controllers, either phasor or Electro-Magnetic Transient (EMT) models should be employed. On the one hand, EMT models provide a detailed-modeling of the system dynamics, thus increase the reliability of stability analysis; on the other hand, using these models increase the computing time of simulations, slowing down the security assessment process. To decrease computational time, system operators could resort to phasor-mode simulations for a subset of disturbances. This paper investigates the appropriateness of phasor-approximation models on simulating events related to power supply and balance stability when grid-forming converters are employed for providing frequency support. Moreover, it provides sufficient conditions and bounds for the control parameters of a grid-forming converter under which the phase-approximation modeling of the component is still valid. The control design is carried out using a simple transfer function approach. Time-domain simulation are performed to validate the transfer function analysis using different control settings and different line impedance characteristics.

Keywords: Electro-magnetic Transient (EMT) model, RMS modeling, Voltage Source Converters (VSCs), low-inertia systems.

1. Introduction

The dynamic nature of the electric power system undergoes a period of significant changes. A major part of these changes is associated with the replacement of synchronous generators with converter-based resources, which lead to the so-called low-inertia systems [1, 2, 3, 4, 5]. Due to this transition, transmission system operators encounter critical stability challenges for stabilizing the frequency

of the system, since in the absence of synchronous generators, the maximum frequency deviation and rate of change of frequency become larger. To preserve a minimum amount of inertia, transmission system operators will rely on new converter control strategies, which can potentially address these issues [6]. These control strategies can be categorized based on the operating mode of the converter [7]. There are two main categories, namely grid-following and grid-forming converter. Considering that grid-following converters rely on a strong grid with high short circuit ratio and penetration of synchronous generation, they cannot be used as a potential control strategy for participating in active power balance [8]. Thus, in this work the focus is on the control strategies for grid-forming converters.

In traditional power systems, the dynamics of transmission lines is usually neglected and an algebraic model of the transmission network is used, i.e. algebraic relationship between the line currents and bus voltages. This neglecting of the dynamic nature of the network line dynamics is valid since the characteristic time constants of the synchronous generators are much greater. However, the characteristic time-constants of the converter-based resources are much smaller, thus there is no distinct time-scale separation between converter control loops and eigen-frequencies in power network. As a result, the influence that network line dynamics have on system stability is growing and the quasi-static modeling of transmission lines, i.e. RMS modeling [9, 10], becomes inappropriate for determining the stability boundaries of the system. Consequently, to analyze fast power components, such as Power Electronic (PE) devices, the electro-magnetic dynamics (network line dynamics) are vital for system stability. However, taking electro-magnetic dynamics into account drastically increases the computational time for solving the system of differential algebraic equations which describes the power system dynamics (since the number of state variables increases).

This creates a limitation for online security assessment, since EMT simulations are considerably slower than RMS simulations. To assess the problem of the computation time of simulation, we first need to understand when RMS modeling is appropriate for simulating zero-inertia systems. As a result, neglecting the line dynamics can lead to incorrect results, such as the RMS model predicting stability while in reality the system is unstable [11]. Several works have focused on parametric constraints for the control settings of grid forming converters considering the influence of network line dynamics on the stability of the converter. While most of the existing work focuses on eigenvalue, bode plot and Nyquist analyses [12, 13, 14, 15] for the control tuning of the converter, few researchers have studied the appropriateness of quasi-static modeling of network line dynamics [16, 17, 18]. In [16], the authors examined the appropriateness of RMS modeling by means of singular perturbation techniques. In particular, they focused on the timescale of the line and load dynamics in order to neglect the fast dynamics and define a reduced order model which preserves the state variables of the slower dy-

namics. However, they did not provide any bounds on the control parameters of the outer controllers of the grid-forming converters. Similar approach which only focuses on neglecting the electromagnetic dynamics and fast inner loops based singular perturbation theory have also been presented in [11] and [19]. In [17], the authors use tools both from singular perturbation and Lyapunov theory to derive sufficient conditions on the frequency and voltage droop gains of the converters that guarantee the stability not only of the EMT model but also for the RMS model. However, the bounds for the control gains are quite conservative, due to the employment of Lyapunov theory, which is also highlighted and demonstrated in the results section. It should be also mentioned that the aforementioned works only focus on microgrids where the X/R ratio of the grid impedance is low, which improves significantly the resonance at the nominal frequency. Finally, the authors in [18] propose sufficient conditions, based on transfer function analysis, for a virtual synchronous generator to ensure the stability and the validity of RMS modeling of the grid-forming converter. However, these conditions only focus on the phase crossover frequency of the open loop system and the ratio between the damping and inertia term of the active power controller of the grid forming converter.

The scope of this paper is to identify the appropriateness of RMS modeling of a class of grid-forming converters, namely power synchronization loop and virtual synchronous generator [7], which are the most commonly used in literature. Our goal is to assess under which conditions RMS modeling (used by simulation tools, such as PowerFactory DigSilent, PSSE, etc.) can still be used for performing power system dynamic security assessment in power grids with high penetration of grid-forming converters. The motivation is that system operators could continue using the RMS for monitoring the active power sharing in systems, as long as the mismatch between the RMS and the EMT models are within acceptable limits. The contributions of this paper are the following:

1. We provide sufficient conditions and upper bounds for the control gains of the outer controllers of grid-forming converters that preserve the time-scale separation properties between the outer control loop and the network line dynamics. We also provide sufficient conditions for the stability of the fully detailed model. To extract the sufficient conditions, transfer function analysis is employed.
2. We present an analytical control tuning of the grid-forming converters, that enable to define the control gains based on minimum phase margin and gain margin requirements for the open loop system of the active power controller.
3. We make use of the gain margin and the phase margin as performance metrics for evaluating the appropriateness of neglecting the effect of the transmission-line dynamics when monitoring the active power balance of the system. This can allow transmission system operators to enforce certain

requirements to vendors regarding the control truing and design of converter operating in grid-forming mode. To this end, we present a transfer function for the relation between the angle and the active power that accounts for the impact of voltage droop on the angle dynamics. This allows us to quantify the impact of the voltage droop on the gain and phase margin of the open-loop system of the active power controller and reducing the coupling between the active and reactive power.

4. We demonstrate the effectiveness of the conditions using two different simulation tools, namely Matlab and PowerFactory.

The rest of the paper is organized as follows. In Section II, we present a description of the outer loop controller of a grid-forming converter. In section III, we derive sufficient conditions for the control gains of the controllers of the grid-forming converter using transfer function analysis. Section IV verifies the conditions derived in section III using time-domain simulations. Conclusions are drawn in Section VI.

2. Grid-forming converter

As described in [7], grid-forming converters are equipped with a two-loop control system, which is illustrated in Fig. 1. The inner loop is designed to be much faster than the outer loop and the control gains are chosen according to the tuning procedure presented in [20], so that we achieve a time-scale separation between the network line and outer loop dynamics. Similar time-scale separation has been also observed with the inner gains proposed in [13, 19]. This enables to study only the impact of the network line dynamics on the outer loop's control gains, that are the ones defining the power regulation in a future low-inertia grid. Therefore, the dynamics presented in this section only concern the outer loops.

2.1. dq and xy frame

Similar to [21], we define two rotating frames: i) the dq rotating frame and ii) the xy rotating frame. The angular speed of the dq frame is equal to the frequency of the i^{th} converter ω_i, whereas the angular speed of the xy frame is equal to the frequency of the grid ω_g. Similar to [22], the converter dq frame leads the xy frame by the angle $\Delta\theta$, which is given by:

$$\frac{d\Delta\theta}{dt} = (\omega_i - \omega_g)\omega_b \tag{1}$$

where $\omega_b = 2\pi f_{\text{nom}}\ rad/s$ is the base angular speed, where f_{nom} is the grid's nominal frequency. The transformation from the xy to dq coordinates is given by:

$$\boldsymbol{x} = \boldsymbol{x}^{\mathbf{c}} e^{-j(\theta_0 + \Delta\theta)} \tag{2}$$

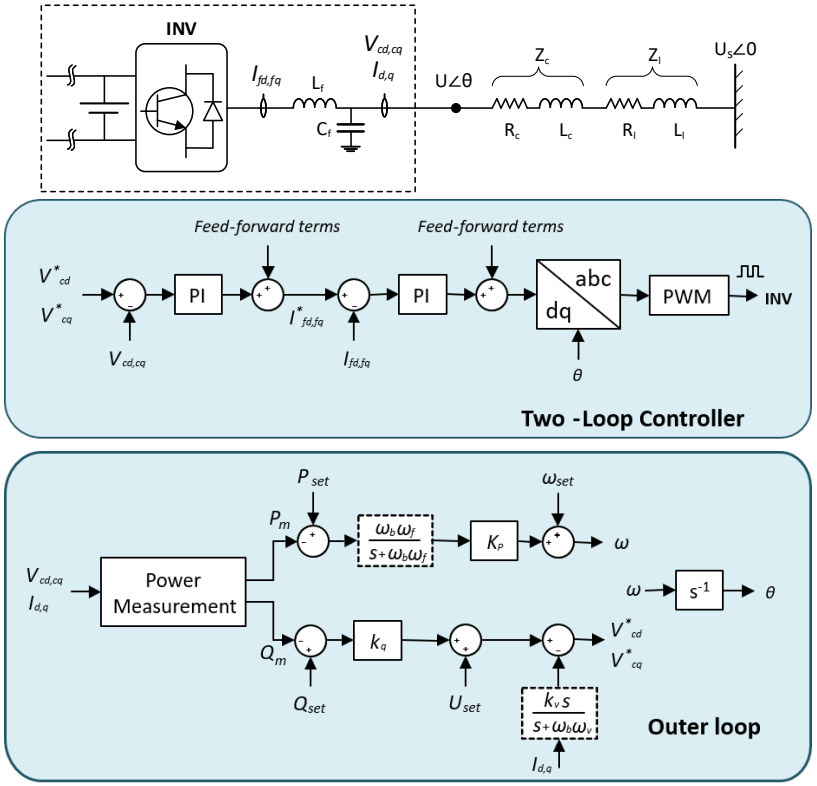

Figure 1: Control structure of grid forming converter. Dashed blocks are either considered or disregarded depending on the class of the grid forming converter.

where the superscript c denotes the xy frame. The corresponding dq frame is denoted without a superscript, e.g., x. The quantities in dq- and xy frame are described in complex space vector form as:

$$\boldsymbol{x} = x^d + jx^q \tag{3a}$$
$$\boldsymbol{x}^c = x^x + jx^y. \tag{3b}$$

2.2. Phase reactor and transformer

As depicted in Fig. 1, the circuit model consists of a Voltage Source Converter (VSC) connected through an RL impedance to the rest of the grid. L_c and L_l represent the transformer and grid inductances, respectively. R_c and R_l represents the transformer and grid resistances, respectively. For the rest of this paper, we consider that $R_g = R_c + R_l$ and $L_g = L_c + L_l$. The relation between the current

flowing through the RL circuit and the voltages U and U_s, expressed in the dq frame, is given by:

$$U = U_s^c e^{-j(\theta_0+\Delta\theta)} + [R_g + (s + j\omega_i)L_g]\boldsymbol{i} \tag{4}$$

where L_g and R_g are expressed in p.u. and s is the Laplace complex variable. U_s^c is the grid voltage expressed in the xy frame and U is the converter terminal voltage in the dq frame.

2.3. Voltage-vector control

A voltage set-point is used to control the output voltage U of the converter at its effective terminal bus. An additional voltage droop is employed for regulating the voltage set point based on the reactive power injected. Apart from setting the voltage at the converter terminal, the voltage-vector control unit must also be able to provide damping of poorly-damped resonances. To this end, a high-pass filter current control is incorporated to increase the damping of high frequency modes [23]. To this end, the voltage-vector control can be expressed as:

$$\boldsymbol{U} = U_{\text{set}} - \underbrace{\frac{k_v s}{s + \omega_v}}_{H_{\text{hp}}(s)} \boldsymbol{i} + K_q(Q_{\text{set}} - Q) \tag{5}$$

where k_v determines the damping effect on the poorly-damped eigenfrequencies. The cut-off frequency of the high-pass filter ($H_{\text{hp}}(s)$) is determined by the value of ω_v, which according to [22] takes values in the range $0.1\omega_1 \rightarrow 0.2\omega_1$, where ω_1 is the reference angular speed chosen to be 1.0 p.u. The outer voltage control loop is also equipped with a QV droop characteristic, where K_q is the voltage droop which determines the amount of reactive power change after a voltage deviation at the Point of Common Coupling (PCC).

2.4. Active power control schemes

Two frequency control schemes are considered and described in the following, namely power synchronization loop and virtual synchronous generator.

2.4.1. Power synchronization loop

The active power droop control regulates the angular speed ω_i; the controller acts by adjusting the voltage angle θ_i based on deviations of the injected/absorbed active power P with respect to a given reference value P_{ref}. The equations de-

scribing the imposed frequency and angle at the converter terminal are given by:

$$\omega_i = \omega_1 + K_p(P_{\text{ref}} - P) \tag{6a}$$

$$\Delta\theta = (\omega_i - \omega_g)\frac{\omega_b}{s} \tag{6b}$$

where the frequency droop K_p is used to regulate the frequency ω_i based on the power mismatch between the power reference point and the power output.

2.4.2. Virtual synchronous generator

A low pass filter is placed on the the active power measurement, as depicted in Fig. 1, that emulates the inertia response of the synchronous generators. The equation describing the imposed frequency and angle at the converter terminal are given by:

$$\omega_i = \frac{\omega_f \omega_b}{s + \omega_f \omega_b}\left(\omega_1 + K_p\left(P_{\text{ref}} - P\right)\right) \tag{7}$$

where ω_f is the cut-off frequency of the low-pass filter. It should be mentioned that this grid-forming scheme is same with the one presented in [18], for $K_p = \frac{1}{D}$ and $\omega_f = \frac{D}{M}$, where D is the damping and M the virtual inertia.

2.5. Neglecting the inner-loop and filter dynamics

To justify the neglecting of the inner loop and filter dynamics of the converter, we demonstrate the coupling between the state variables corresponding to the inner loop and filter dynamics and the active power signal. We focus only on the active power signal, since in this paper we want to evaluate the appropriateness of RMS modeling for monitoring the active power regulation. However, the framework presented in this section can be applied for evaluating the coupling of the state variables of the system to any algebraic variable, e.g. reactive power and voltage signal. we make use of the approach presented in [24], to the participation of algebraic variables in power system modes and investigate how they couple with the state variables of the system. Using the same notation as presented in [24], we consider the following set of differential algebraic equations describing the EMT model of a grid-forming converter:

$$\dot{\boldsymbol{x}} = \boldsymbol{f}(\boldsymbol{x}, \boldsymbol{y}) \tag{8}$$

$$\boldsymbol{0} = \boldsymbol{g}(\boldsymbol{x}, \boldsymbol{y}) \tag{9}$$

Table 1: Contribution of the active power signal to system modes - Power Synchronization Loop

y_k [pu]	$\text{—}\pi_{k,i}\vert_{\max}$	Mode	$x-\text{dom}$	$\vert p\vert$
P [pu]	0.50529	-96.2 $\pm$ j312	I_d, I_q	0.5052
			I_{fd}, I_{fq}	0.0458
			ξ_d, ξ_q	0.0439
			θ	0.020

Table 2: Contribution of the active power signal to system modes - Virtual Synchronous Generator

y_k [pu]	$\text{—}\pi_{k,i}\vert_{\max}$	Mode	$x-\text{dom}$	$\vert p\vert$
P [pu]	0.4983	-102 $\pm$ j315	I_d, I_q	0.4983
			I_{fd}, I_{fq}	0.0462
			ξ_d, ξ_q	0.0443
			$M_{\text{ad}}, M_{\text{aq}}$	0.0146

where x is a vector matrix containing the system state variables, and y is a vector matrix containing the algebraic variables. To obtain the participation matrix $\boldsymbol{P}_x$ we first linearize the system around the operating point $(\boldsymbol{x_0}, \boldsymbol{y_0})$ as follows:

$$\Delta\dot{\boldsymbol{x}} = \boldsymbol{f_x}\Delta\boldsymbol{x} + \boldsymbol{f_y}\Delta\boldsymbol{y} \tag{10}$$

$$\boldsymbol{0} = \boldsymbol{g_x}\Delta\boldsymbol{x} + \boldsymbol{g_y}\Delta\boldsymbol{y} \tag{11}$$

where $\boldsymbol{f_x}$, $\boldsymbol{f_y}$, $\boldsymbol{g_x}$ and $\boldsymbol{g_y}$ are the Jacobian matrices evaluated at the operating point $(\boldsymbol{x_0}, \boldsymbol{y_0})$. The participation factors of the algebraic states, (the active power signal is an algebraic state of the system) can be calculated by the following expression:

$$\Pi_{(\boldsymbol{y})} = -\boldsymbol{g_y}^{-1}\boldsymbol{g_x}\boldsymbol{P}_x \tag{12}$$

where $\Pi_{(\boldsymbol{y})}$ is the participation matrix of the algebraic states in system modes included in the DAE model, with $\pi_{k,i}$ being the elements of the matrix (k denotes the k-*th* algebraic variable, i denotes the i-*th* mode) and provides information about for the coupling between the algebraic and state variables of the system. Table 1 shows the mode with the highest contribution from the active power signal $|\pi_{k,i}|_{\max}$, as well as the contribution from the state variables of the system $|p|$. The state variables corresponding to the line currents presents the highest contribution

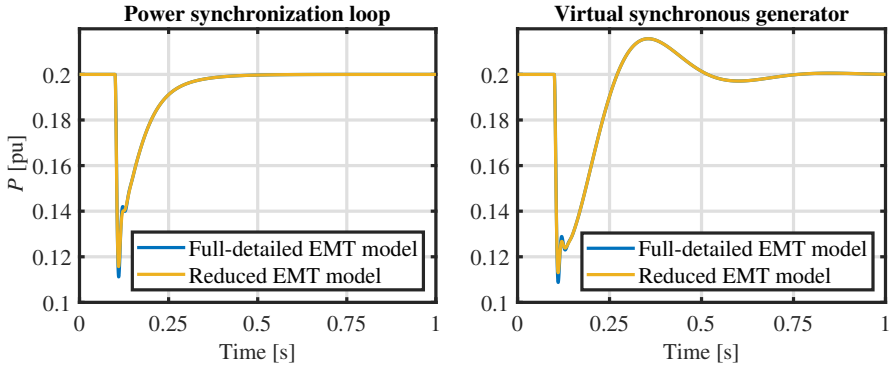

Figure 2: Trajectory of the active power signal for a step change the SCR from 5 to 3. The difference between the full-detailed EMT model and the reduced-one is that in the latter the inner loop and the filters (phase reactor and capacitance) are disregarded.

to that mode. The state variables (I_{fd}, I_{fq}), (ξ_d, ξ_q) and θ, corresponding to the phase reactor currents, inner voltage control loop and phase angle, respectively, present a small participation to the model. Similar observations, can be made for the virtual synchronous machine, see Table 2. The main difference is that instead of the phase angle, the state variables corresponding to the high pass filter of the virtual impedance controller slightly contribute to the active power signal. Based on this analysis we omit the inner loop, the phase reactor and the filter capacitance dynamics.

Fig. 2 shows a comparison between the full-detailed EMT model and the reduced EMT model (only accounts for the network line dynamics, the outer loops and the virtual impedance controller). For the comparison, we consider a line outage, i.e. sudden drop of the short circuit ratio from 5 to 3. As it can be seen the difference between the EMT models is negligible even for large disturbances, which implies the limited effect of the inner loops and filters on the active power signal. We would like again to remind that for very high SCR, the inner loop is expected to influence more the active power signal. However, since the focus is on transmission level, such a study is omitted in this paper. In one of your later remarks we provide additional simulation results to show the impact of the virtual impedance controller on the appropriateness of RMS modeling in case of line outage.

To summarize, this paper investigates the control tuning of the outer loop and virtual impedance controllers and suggests values for which the bandwidth of the active power controller is limited, in order to ensure that its effect on the line resonance is minimized and improve the damping ratio of the mode at $s = -\frac{R}{L} \pm j\omega_b$, which is the one that affects significantly the trajectory of the active power signal.

3. Sufficient Conditions for Phasor-approximation modeling

In this section, we identify the control gains and parametric constraints, under which the line dynamics can be disregarded. For the analysis, the system depicted in Fig. 1 is used. The constraints will allow system operators to rely on the RMS modeling of grid-forming converters and not use the EMT model for monitoring the active power sharing in the power grid. For the analysis we use the theory of loop-shaping control design and Nyquist's criterion. In particular, we employ the gain and phase margin g_m and ϕ_m, respectively, which are relative measures of the distance of the Nyquist curve to the critical point (-1,0) [25].

To derive the sufficient conditions, we consider the transfer function of the open loop system $L(s)$. The open loop transfer function $L(s)$ consists of the transfer functions $P(s)$ and $C(s)$, which describe the plant and controller dynamics, respectively:

$$L(s) = P(s)C(s), \tag{13}$$

where $C(s) = \frac{K_p}{s}$ in the case of power-synchronization loop and $C(s) = \frac{K_p}{s}\frac{1}{s+\omega_f}$ in the case of the virtual synchronous machine. $P(s) = G_{\theta P}(s)$ is the transfer function of the plant. The transfer function can be found in the appendix. The gain margin is calculated as follows:

$$g_m = -\frac{1}{|L(j\omega_{180})|}, \tag{14}$$

where ω_{180} is the phase crossover frequency and is the lowest frequency where the Nyquist plot intersects the negative real axis. The gain margin indicates how much the controller gain can be increased before reaching the stability limit. Similarly, the phase margin is defined as:

$$\phi_m = \pi + \arg L(j\omega_c), \tag{15}$$

where ω_c is the gain crossover frequency where the loop transfer function $L(s)$ has unit magnitude and indicates the amount of phase lag required to reach the stability limit.

To derive the sufficient conditions and provide meaningful expressions, we initially consider that the converter is at no load condition, which yields that i_{q0} and i_{d0} are equal to zero. Later in this section, we will show how the active and reactive currents affect the parametric constraints. Moreover, we will analyze the impact of the control and system parameters on the frequency droop value K_p, as well as on the inertia effect that can be provided by the converter.

From control design perspective, minimizing the differences between the RMS and EMT models of a grid-forming converter can be considered as the problem

of minimizing the effect of the network line dynamics on the outer loops of the converters. A reasonable control design requirement is to tune the control gains of the converters in such a way that the bandwidth of the active power controller is less than $0.1\omega_1$ [18, 26], where ω_1 is the nominal frequency of the power grid. This yields the following condition for the gain crossover frequency of the open loop system of the active power controller, $\omega_c \leq 0.1\omega_1$. This requirement is due to the line resonance at nominal frequency (modes are at $-\frac{R_g}{L_g} \pm j\omega_1$). By limiting the bandwidth of the controller, we first mitigate the effect of line resonance (increasing the gain margin of the open loop system), but also enable the time-scale separation between the network line dynamics and the outer loop. This ensures that the RMS model of the grid-forming converter is a good approximation of the full-detailed model. However, as it will be presented in Section 3.2, an additional condition is required based on the gain margin of the open loop system in order to improve this approximation.

To this end, we first investigate the properties of the open loop system of the power-synchronization control loop and then the virtual synchronous generator one.

3.1. Power synchronization loop

At no-load condition, the transfer function of the open loop system can be expressed as follows:

$$G_{\mathrm{ol}}(s) = \underbrace{\frac{K_p}{s}}_{C(s)} \underbrace{\frac{\left(K_q + \omega_1 L_g\right) U_{\mathrm{set}}^2}{K_q \omega_1 L_g + (\omega_1 L_g)^2 + (H_{\mathrm{hp}}(s) + R_g + sL_g)^2}}_{G_{\theta P}(s)} \tag{16}$$

We first calculate the phase crossover frequency from setting the imaginary part of the open loop system equal to zero ($\Im(L(j\omega_{180}))$=0).

$$\omega_{180} = \frac{\sqrt{(R_g + k_v)^2 + L_g^2\omega_1^2 + K_q\omega_1 L_g}}{\omega_1 L_g}. \tag{17}$$

Having calculated the phase crossover frequency, we can now express K_p as a function of the gain margin, network line parameters and the active damping controller parameters. This is given by:

$$K_p = 2\left(k_v + R_g\right)\left(\frac{1}{g_m U_{\mathrm{set}}^2} + \frac{\frac{(k_v+R_g)^2}{\omega_1 L_g}}{g_m (K_q + \omega_1 L_g) U_{\mathrm{set}}^2}\right) \tag{18}$$

where K_p and g_m are inversely proportional to the voltage droop K_q and directly proportional to the damping coefficient k_v. An analytical condition for the stability

of the grid-forming converter and the maximum value of the frequency droop is obtained when $g_m = 1$. As described earlier, in order to mitigate the impact of the line resonances, the gain crossover frequency of the open loop system must be less than 0.1 of the nominal frequency ($\omega_c \leq 0.1\omega_1$). This condition allows for a sufficient phase margin close to 90^o, since the impact of the pole $-\frac{R_g}{L_g} \pm j\omega_1$ on the phase angle of the open loop system is negligible for $\omega \leq \omega_c$ [25], making the open loop system behaving as an integrator for $\omega \leq \omega_1$. It should noted that the phase margin of the RMS model is 90^o since the open loop system is a static gain (see Appendix) In order to determine the gain crossover frequency, the expression (15) is used with $C(s) = \frac{K_p}{s}$ and $P(s) = G_{\theta P}(s)$. The Laplace complex variable s is set to $j\omega_c$ and $|L(j\omega_c)| = 1$ is solved for ω_c. This yields the following expression for the gain crossover frequency:

$$\omega_c \approx \frac{K_p U_{\text{set}}^2}{\omega_1 L_g + \frac{R_g^2}{\omega_1 L_g + K_q}} \tag{19}$$

$$K_p \leq \frac{0.1}{U_{\text{set}}} \left(\omega_1 L_g + \frac{R_g^2}{K_q + \omega_1 L_g} \right) \tag{20}$$

It is evident that for small resistances the impact of the voltage droop on the frequency droop value is negligible. Substituting (20) into (18) we obtain the following inequalities (21a)-(21c).

$$k_v \geq \frac{g_{m,\min}}{20} L_g - R_g \tag{21a}$$

$$K_q \geq 0 \tag{21b}$$

$$g_m \geq 20 \frac{k_v^3 + 3\beta_2 k_v^2 + \beta_1 k_v + \beta_0}{(\omega_1 L_g)^3 + K_q(\omega_1 L_g)^2 + \omega_1 L_g R_g^2} \tag{21c}$$

where $g_{m,\min}$ is a minimum value for the gain margin of the open loop system, which is selected in order to mitigate the line resonance, $\beta_2 = R_g$, $\beta_1 = \left(K_q \omega_1 L_g + (\omega_1 L_g)^2 + 3R_g^2\right)$ and $\beta_0 = \left(K_q \omega_1 L_g R_g + \omega_1 L_g^2 R_g + R_g^3\right)$. It is worth mentioning that $g_m > g_{m,min}$, due to the fact that the high pass filter is not a static gain. In case $H_{\text{hp}}(s) = k_v$, then $g_m = g_{m,min}$. We can notice that by selecting $\omega_c \leq 0.1\omega_1$, the lowest obtainable value of the gain margin is equal to 2 ($g_m \geq 2$), which is equivalent to neglecting the active damping controller. Additionally, from (21a) we can infer that for low X/R ratio the active damping controller $H_{\text{hp}}(s)$ can be disregarded, e.g. for $g_{m,\min} = 10$ and X/R=1 the lower bound of k_v becomes negative meaning that the mode $-\frac{R_g}{L_g} \pm j\omega_1$ is well damped

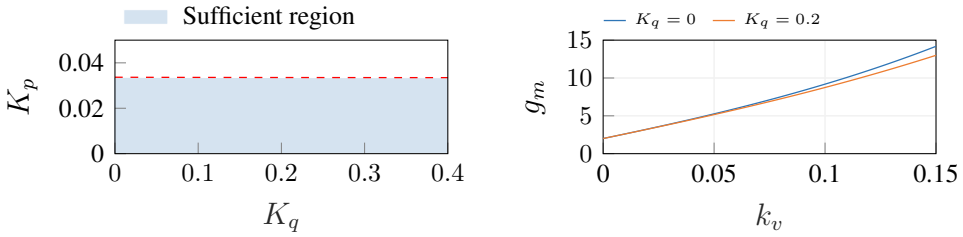

Figure 3: Left: sufficient region defined by the values of K_p and K_q. Right: impact of damping coefficient k_v and K_q on the gain margin.

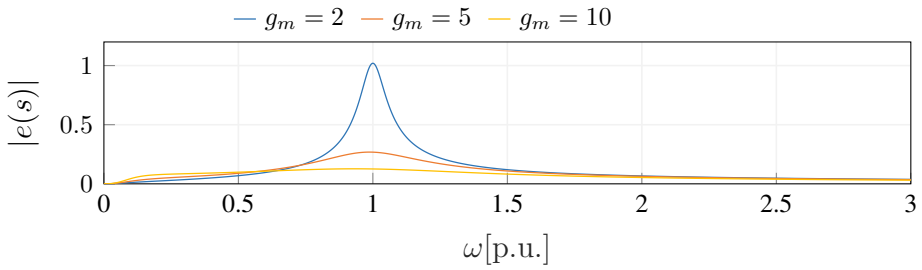

Figure 4: Singular values of $e(s)$ transfer function for different values of the gain margin.

and not additional damping is required.

3.1.1. Illustrative case

The following example will help us understand better the sufficient conditions (21a)-(21c). It should be noted that the regions shown in Fig. 5 do not represent the stable region of the system, but the region that establish the timescale separation between the network line and the angle dynamics. The considered system parameters are: $R_g = 0.033$, $L_g = 0.33$, $\omega_1 = 1$ and $V_{\text{set}} = 1$.

Fig. 3 (left figure) depicts the sufficient region for the frequency and voltage droops (derived using (20)), that provide a good approximation of the RMS model. As it can be seen from the figure the impact of the voltage droop on the frequency droop is negligible. It should be noted that this occurs due to the high X/R ratio of the grid impedance. As it will be presented in Section 3.3, low X/R ratio increases the influence of the voltage droop on the maximum value of the frequency droop. Fig. 3 (right figure) shows the gain margin for different values of the control parameters k_v and K_q. Based on the proposed control design, the impact of the voltage droop on the gain margin is negligible compared to k_v.

Fig. 4 depicts the Bode magnitude plot of the transfer function $e(s)$. $e(s)$ describes the error between the RMS and EMT model. K_p is equal to the upper

bound defined by (20), $K_q = 0$ and k_v is determined by (21a). As it can be seen in the figure, for small values of g_m, the magnitude of $e(s)$ is of significance around the nominal frequency of the system. This indicates that the power signal captured by the RMS model will present an important error with respect to the actual power signal (captured by the EMT model). Increasing the gain margin decreases the approximation error, as shown in the same figure. We can also notice that for $\omega \leq 0.1\omega_1$, the impact from increasing the gain margin and consequently k_v on the amplitude of $e(s)$ is limited. This indicates that the value of the frequency droop is the one that primarily affects the phase shift of the open loop system and consequently the time response of the active power controller. Moreover, it can be seen that the gain margin is a useful metric for analyzing the H_∞ norm of the $e(s)$. By selecting a high gain margin we can limit the error between the RMS and EMT not only within the range of $[0, \omega_c]$ but also over the whole frequency spectrum. Lastly, as shown in the figure, the singular values $e(s)$ at steady state, $\omega = 0$, are equal to zero, which was expected since the RMS model is able to preserve the dc-gain of the EMT state-space model. It is also depicted that during a dynamic event $\omega > 0$, the RMS model presents a mismatch with respect to the EMT model.

To summarize the results, we show that by selecting a high gain margin leads to a good-approximation of the RMS model over the whole frequency spectrum, where, on the other hand, by limiting the gain crossover frequency, the RMS and EMT models have the same phase shift at the frequencies at which the plant is supposed to track its reference signal ($[0, \omega_c]$).

3.2. Virtual synchronous generator

Until now, we have neglected the filter constant and its impact on both the stability of the closed loop system and the time-scale separation between the frequency and the network line dynamics. In this section, we investigate its impact on the stability of the closed loop system, as well as on the selection of the frequency droop value. The main advantage of using a low-pass filter is that we can decouple the network line dynamics from the frequency dynamics by placing the cut-off frequency at $0.1\omega_1$. The advantage of placing a low-pass filter on the measurement is that it increases the damping of the line resonance. As a result, the active damping controller it could be disregarded, which implies that $k_v = 0$.

We first calculate the phase crossover frequency. To determine the gain crossover frequency, (15) is used with $C(s) = \frac{K_p}{s}\frac{\omega_f}{s+\omega_f}$. The Laplace complex variable s is set to $j\omega_{180}$ and $\Im(L(j\omega_{180}))$=0 is solved. This yields the expression in (22). We continue by determining the gain crossover frequency: the Laplace complex variable s is set to $j\omega_c$ and $|L(j\omega_c)| = 1$ is solved for ω_c. To realize the calculation of ω_c and obtain analytical expressions for the phase margin and gain parameters, we perform Taylor series expansion of the transfer function describing the plant

dynamics, $G_{\theta P}(s)$, which yields the following expression: $G_{\theta P}(s) = B - B_t s$. As indicated also in [11], this approximation is valid for $\omega \leq 0.1\omega_1$, i.e. the expression $G_{\theta P}(s) = B - B_t s$ is not valid for $\omega >> 0.1\omega_1$. The mathematical expression for ω_c is given by (23).

$$\omega_{180} = \sqrt{\frac{K_q L_g \omega_1 + (L_g \omega_1)^2 + R_g^2}{L_g(2\frac{R_g}{\omega_f} + L_g)}}. \tag{22}$$

$$\omega_c = \frac{\sqrt{-\omega_f^2\left(1 - (B_{\mathrm{t}}K_p)^2\right) + \omega_f\sqrt{4\left(BK_p\right)^2 + \omega_f^2\left(1 - (B_{\mathrm{t}}K_p)^2\right)^2}}}{\sqrt{2}} \tag{23}$$

where

$$B_{\mathrm{t}} = 2R_g L_g U_{\mathrm{set}}^2 \frac{K_q + \omega_1 L_g}{\left(K_q\omega_1 L_g + (\omega_1 L_g)^2 + R_g^2\right)^2}$$

$$B = U_{\mathrm{set}}^2 \frac{K_q\omega_1 L_g + \omega_1 L_g}{K_q\omega_1 L_g + (\omega_1 L_g)^2 + R_g^2}$$

In contrast to the power synchronization, where the value of the phase crossover frequency is larger than $\omega_{180} > \omega_1$, the phase crossover frequency of the virtual synchronous generator's open loop system can get values lower than ω_1. From (22), we realize that when ω_f decreases the value of ω_{180} also decreases. To remove the effects of line resonance on the active power regulation we choose the gains of K_p, K_q and ω_f, so that the $\omega_c \leq 0.1\omega_{180}$. The motivation behind this constraint is that it ensures a minimum gain margin of 10, since the slope for $\omega_c \leq \omega_{180}$ is at least -1/decade (-20dB/decade) due to the two poles at zero and $-\omega_f$ [25]; it also minimizes the impact of the pole corresponding to the network line dynamics on the phase shift, since the complex conjugate poles, associated with the network line dynamics, start influencing the phase of the open loop system at $\omega = \frac{\omega_n}{10^\zeta}$ where ω_n is the natural frequency and ζ the damping ratio of the complex. This ensures an almost linear decrease of the phase until -180^o. Using

Mathematica, we extract the following conditions which satisfy $\omega_c \leq 0.1\omega_{180}$.

$$K_p \leq \frac{\omega_c}{\omega_f}\sqrt{\frac{\omega_c^2+\omega_f^2}{(B^2+B_{\mathrm{t}}^2\omega_c^2)}} \tag{24a}$$

$$\omega_c \leq 0.1\omega_1 \tag{24b}$$

$$\omega_f = \frac{\alpha_{\mathrm{pm}}B\omega_c + B_{\mathrm{t}}\omega_c^2}{B - \alpha_{\mathrm{pm}}B_{\mathrm{t}}\omega_c} \tag{24c}$$

$$\alpha_{\mathrm{pm}} \geq \frac{\omega_c c_1}{c_2+c_3+c_4}\omega_1 L_g R_g \tag{24d}$$

$$\alpha_{\mathrm{pm}} < \frac{K_q L_g + L_g^2 + R_g^2}{2L_g R_g \omega_c} \tag{24e}$$

where

$$\begin{aligned}
c_1 &= 0.66\left(K_q L_g\omega_1 + R_g^2 + (L_g\omega_1)^2(1+\omega_c^2)\right)\\
c_2 &= \frac{1}{300}\left((K_q L_g\omega_1 + R_g^2)^2\right)\\
c_3 &= \frac{1}{300}\left(L_g^4(1-100\omega_c^2) + (R_g L_g\omega_1)^2(2+300\omega_c^2)\right)\\
c_4 &= \frac{1}{300}(K_q(L_g\omega_1)^3(2-100\omega_c^2))
\end{aligned}$$

and the variable α_{pm} is the ratio $\frac{\Im(L(j\omega))}{\Re(L(j\omega))}$. Lastly, to evaluate the impact of the control and system parameters on the gain margin of the open loop system, we substitute ω_{180} into (14). This yields the following expression:

$$\begin{aligned}
K_p = &\frac{2R_g}{g_m(L_g^2\omega_1)}\frac{\left((L_g\omega_1)^2+R_g^2\right)\left((R_g+L_g\omega_f)^2+(L_g\omega_1)^2\right)}{U_{\mathrm{set}}^2(2R_g+L_g\omega_f)^2\,(K_q+\omega_1 L_g)}\\
&+\frac{2R_g K_q L_g\omega_1\left(K_q L_g\omega_1 + (R_g+L_g\omega_f)^2 + R_g^2 + 2(L_g\omega_1)^2\right)}{U_{\mathrm{set}}^2(2R_g+L_g\omega_f)^2\,(K_q+\omega_1 L_g)}
\end{aligned} \tag{25}$$

An analytical condition for the stability of the grid-forming converter and the maximum value of the frequency droop is obtained when $g_m = 1$. It should be noted that in case we want to further increase the damping of the line resonance and employ the active damping controller, the above expressions can be used for $\omega_v = 0$ and $R_g = R_g + k_v$. This means that the active damping controller would add as a pure resistance. In case, $\omega_v = 0.1\omega_1$, the conditions (23)-(25) remain the

same, but the transfer function of the plant changes $G_{\theta P}(s) = B - B_t s$ (by the Taylor expansion). B and B_t are now different and are expressed as follows:

$$B_{\mathrm{t}} = 2R_g L_g U_{\mathrm{set}}^2 \frac{K_q + \omega_1 L_g}{\left(K_q \omega_1 L_g + (\omega_1 L_g)^2 + R_g^2\right)^2}$$
$$B = U_{\mathrm{set}}^2 \frac{K_q \omega_1 L_g + \omega_1 L_g}{K_q \omega_1 L_g + (\omega_1 L_g)^2 + R_g^2}$$

It should be mentioned that as $\omega_v \to 0$, the approximation of the transfer function describing the plant dynamics becomes less accurate since $B_t \to \infty$. However, as mentioned above ω_v is usually chosen in the range [$0.1\omega_1$, $0.2\omega_1$].

3.2.1. Illustrative case

The following example will help us understand better the sufficient conditions (24a)-(24e). Similar to the previous case, the sufficient regions shown in Fig. 5 do not represent the stable region of the system, but the region that establish a good approximation of the RMS model of the grid-forming converter. Since in Section 3.1 we show that the voltage droop does not reduce the sufficient region defined by the control gains, we consider that $K_q = 0$. Fig. 5 shows the sufficient regions for the control parameters, the gain crossover frequency and the phase margin, extracted using (24a)-(24e). In the left figure, we show the sufficient region for the control parameters ω_f and K_p that enables the decoupling between the network line and frequency dynamics. We can see that by increasing ω_f, the maximum value of the frequency droop increases. In the right figure, we show the minimum value required for the phase margin, in order to mitigate the impact of network line dynamics on the active power controller. As ω_c approaches $0.1\omega_1$, the minimum required phase margin increases and so does the value of ω_f. Consequently, we can infer that the inertial effect of the grid-forming converter drastically reduces, when ω_c is close to $0.1\omega_1$.

Fig. 6 shows how the control and system parameters affect the gain margin of the open loop system and consequently the damping ratio of the mode associated with the line resonance. It can be seen that the gain margin of the open loop system remains larger than 2, if K_p and ω_f are chosen within the sufficient region defined by (24a)-(24e). Last but not least, it can seen that as ω_c approach $0.1\omega_1$, and consequently $\omega_f \to 1$ the gain margin of the system decreases significantly. It should be noted that the value of the gain margin is significantly affected by the X/R ratio of the grid impedance. For lower values of the X/R ratio the gain margin is expected to be larger, however for larger resistances the influence on the phase of the open loop system becomes larger [11].

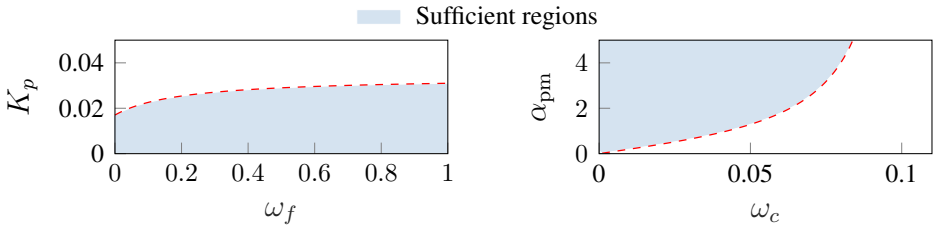

Figure 5: Sufficient regions for the phase margin and the control parameters of the grid-forming converter.

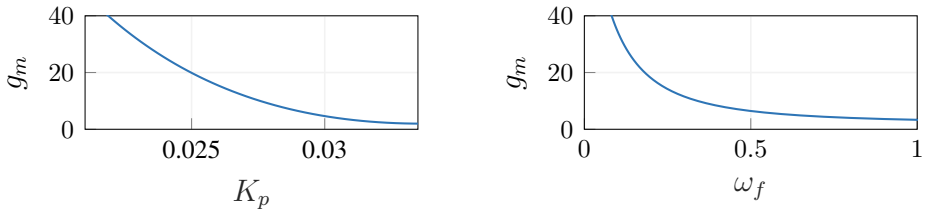

Figure 6: Sufficient gain margin for different values of K_p (left) and ω_f (right).

3.3. Transmission-line length & X/R ratio

We now investigate the impact of the transmission-line length and X/R ratio on the sufficient regions defined by the control parameters of the grid-forming converter. Fig. 7 shows how the different levels of X/R ratio affect the sufficient regions for the control parameters. For the comparison, we consider that $L_g = 0.333$. We consider that, the X/R ratio is the ratio $\frac{L_g}{R_g}$. The left figure indicates that the lower the value of the X/R ratio the higher the impact of the voltage droop on the maximum value of the frequency droop. Moreover, it can be seen that the lower the X/R ratio the higher the maximum value for the frequency droop becomes. From the right figure, we observe that the maximum value of the frequency droop is similar for low values of the $\omega_f < 0.2$ and the different levels of X/R ratios. In the case of X/R=1, the maximum value for K_p increases, as $\omega_f \to 1$, which is not the case for higher levels of X/R.

Fig. 8 shows how different levels of Short Circuit Ratio (SCR) affect the sufficient regions for the control parameters. For the comparison, we consider that the X/R is equal to 10, which allows us to consider that $L_g \approx \frac{1}{SCR}$. The left figure indicates that the lower the value of the SCR, the higher the relative value of the frequency droop becomes. This shows that increase of transmission-line length extends the sufficient region, in which the quasi-static approximation of the network line dynamics is valid. We can also observe that the impact of the

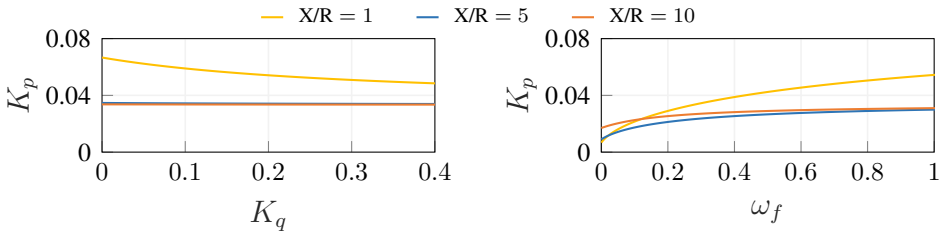

Figure 7: Left: sufficient region for (K_q, K_p) for different X/R ratios. Right: sufficient region for (ω_f, K_p) for different X/R ratios.

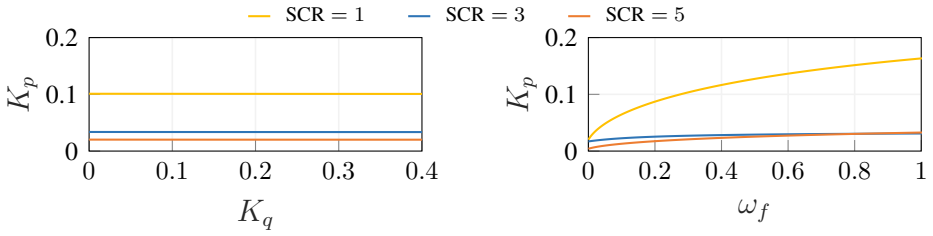

Figure 8: Left: sufficient region for (K_q, K_p) for different values of SCR. Right: sufficient region for (ω_f, K_p) for different values of SCR.

voltage droop on the frequency droop is negligible, since the maximum relative value for the frequency droop does not change. In the right figure, it is depicted the impact of the SCR on the sufficient region defined by the control gains K_p and ω_f. We can observe that the maximum relative value of the frequency droop increases for lower values of the SCR. Moreover, it can be seen that for low values of ω_f, the maximum value of the frequency droop is relatively small compared to the case where the low-pass filter is disregarded.

3.4. Impact of active and reactive currents

Fig. 9 and Fig. 10 demonstrate the impact of active and reactive currents, respectively, on the sufficient region defined by the control gains of the grid-forming converter. As it can be seen from the figures, the sufficient region slightly reduces, when the grid-forming converter absorbs reactive power. It should be noted that the increase of the sufficient region indicates that the bandwidth of the closed loop system of the active power controller decreases when the converter is initialized at different operating point. This means that in case of a small droop value, the active power controller might not be able to track the reference signal, which is something that was also highlighted in [22].

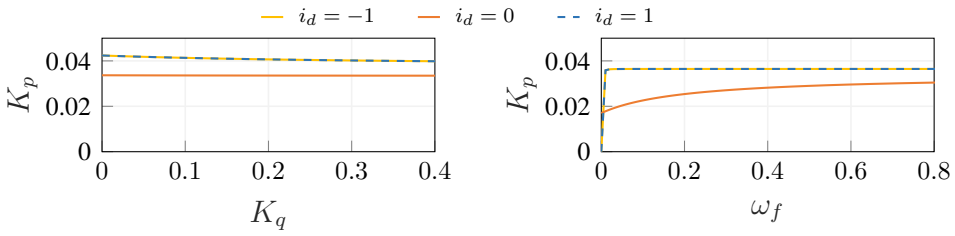

Figure 9: Impact of active current on the sufficient region for the control gains of the power synchronization loop and virtual synchronous generator. For the virtual synchronous generator we consider that $K_q = 0$.

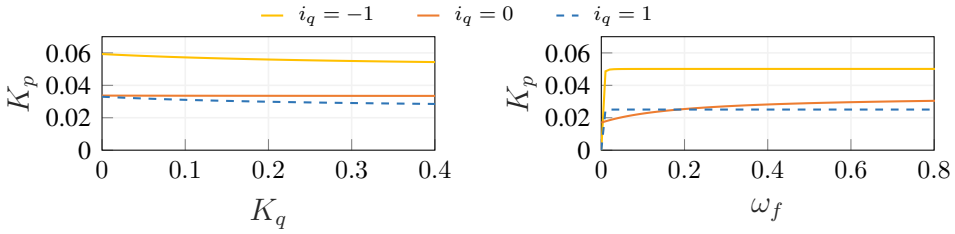

Figure 10: Impact of reactive current on the sufficient region for the control gains of the power synchronization loop and virtual synchronous generator. For the virtual synchronous generator we consider that $K_q = 0$.

4. Simulation and Results

In this section, we verify using time-domain simulations the sufficient regions extracted in the previous section. Our goal is to compare the active power response, obtained by the fully detailed model and the proposed reduced order models for different control and system parameters. For the analysis, we consider that the rated power of the converter is 1000 MVA.

4.1. Validation on 2-Bus system - Step change of the active power set-point

The presented sufficient conditions are evaluated on the 2 bus system depicted in Fig. 1. For the analysis we consider $L_g = 0.333$ and $R_g = 0.0333$. The control parameters for the inner loop control and the values of the phase reactor and filter capacitance can be found in the appendix.

4.1.1. Power synchronization loop

For the frequency droop-based control, we consider the following set of parameters in order to evaluate the accuracy of the reduced order model which corresponds to the phasor-approximation model.

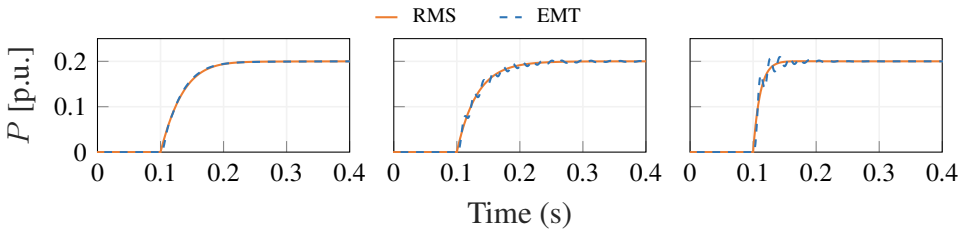

Figure 11: Active power response of power synchronization loop. Left figure: Case 1, Middle figure: Case 2, Right figure: Case 3

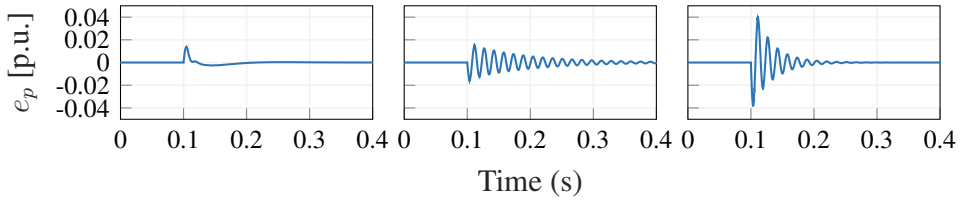

Figure 12: Active power error between RMS and EMT - Power synchronization loop. Left figure: Case 1, Middle figure: Case 2, Right figure: Case 3

- Case 1: $K_p = 0.0335$, $K_q = 0.2$, $k_v = 0.12$
- Case 2: $K_p = 0.0335$, $K_q = 0.2$, $k_v = 0.0$
- Case 3: $K_p = 0.1$, $K_q = 0.2$, $k_v = 0.1$

For the good approximation case, the selection of the control gains is based on the conditions (20)-(21c). For the poor approximation case, we choose the frequency droop according to (20) and we neglect the active damping controller, which leads to reduced gain margin and poor damping of the line resonance. For the third case, we consider a high value of frequency droop which increases the bandwidth of the active power controller and a smaller value of damping resistor k_v.

Fig. 11 shows the converter's response for the step change of the P_{ref} and Fig. 12 the active power error between the RMS and EMT model for the 3 different cases. For the case where the frequency droop was selected based on the sufficient conditions, it can be seen that the difference between the RMS and EMT models is insignificant. For this case, the root mean squared error between the RMS and EMT model during the transient period is equal to 0.0036. Moreover, for the case where the active damping controller is neglected it can be seen that the impact of the line resonance on the system response increases, which was expected due to the poor gain margin of the open loop system. However, the time response of the

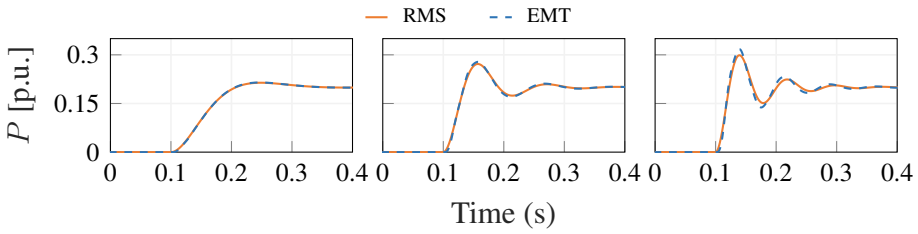

Figure 13: Active power response of virtual synchronous generator. Left figure: Case 1, Middle figure: Case 2, Right figure: Case 3

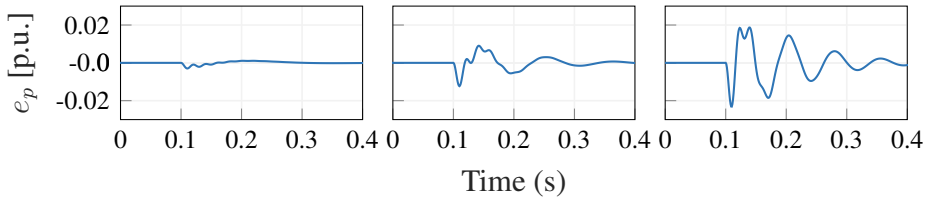

Figure 14: Active power error between RMS and EMT - Virtual synchronous machine. Left figure: Case 1, Middle figure: Case 2, Right figure: Case 3

RMS and EMT model matches, since the K_p is tuned according to (20). For this case, the relative mean square error between the RMS and EMT model during the transient period is equal to 0.0062 . It can be seen that the active power signal is oscillatory with the frequency of oscillations being equal to ω_{180} (see (17)). In the case we use a high frequency droop value and a relative small value for the k_v, it can be seen that the maximum active power error between the RMS and EMT model is higher compared to the other cases, which indicates that the impact on the estimation error is higher when $\omega_c > 0.1\omega_1$. For this case, the relative mean square error between the RMS and EMT model during the transient period is equal to 0.0153.

4.1.2. Virtual synchronous generator

We consider the following set of parameters in order to evaluate the accuracy of the phasor approximation model. We consider three cases for the control parameters K_p and ω_f, where we gradually increase the frequency droop value, which consequently decreases the phase margin. For case 1, the control gains have been selected based on the sufficient conditions. For the considered cases, we consider that $K_q = 0$ and $k_v = 0$.

- Case 1: $K_p = 0.0230, \omega_f = 0.1108$

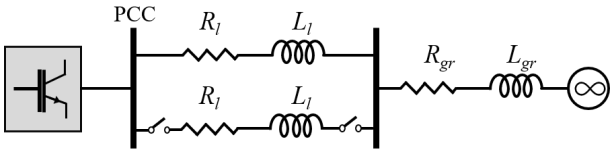

Figure 15: Test case system containing a single-line diagram of a converter connected to an infinite bus via two parallel transmission lines.

- Case 2: $K_p = 0.1$, $\omega_f = 0.1108$
- Case 3: $K_p = 0.2$, $\omega_f = 0.1108$

Fig. 13 demonstrates the active power response and Fig. 14 the active power error between RMS and EMT for the three different cases. Apart from the poor phase margin and the oscillatory response of the active power due to the decrease of the phase margin, it can be noticed that the maximum error between the RMS and EMT models is relatively higher for the 2^{nd} and 3^{rd} cases. This indicates that the phase margin predicted by the RMS model appear rather optimistic compared to the EMT model. Moreover, it can be seen that by increasing the frequency droop, the gain margin of the open loop system deteriorates, which leads to a higher influence of the line resonance on the angle dynamics. Lastly, compared to the power synchronization loop, we can observe that the error between the RMS and EMT is similar for the 1^{st} and 2^{nd} cases, where it is relatively higher for the 3^{rd} case.

4.2. Validation on 2-Bus system - Line outage

To further validate the conditions, we consider a line outage in the system depicted in Fig. 15, which is simulated as a step decrease of the SCR value, while the X/R remains the same.

4.2.1. Power synchronization loop

Fig. 16 shows the active power signal for a change of the SCR from 3 to 1 in the case of power-synchronization loop control scheme. We want to show the effect of the damping resistor control gain k_v on the mismatch between the RMS and EMT modeling of the converter. In Fig. 16, we show the trajectory of the active power signal. In the left figure, k_v is equal to 0.1333 and in the right figure k_v is equal to 0.4. As it can be seen, the mismatch between the RMS and EMT model is higher in the left figure where the value of k_v is smaller and the RMS model of the converter is inadequate of capturing the maximum active power deviation. This comes to show the effect of damping ratio of the mode associated with the line dynamics. In particular, using the expression $g_{m,\min} =$

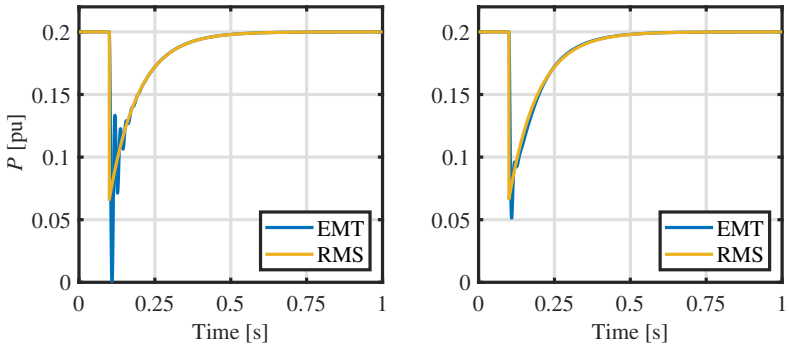

Figure 16: Trajectory of the active power signal for a sudden drop of the SCR from 3 to 1 - Power synchronization loop. In the left figure the value of k_v = 0.1333 and in the right k_v=0.4.

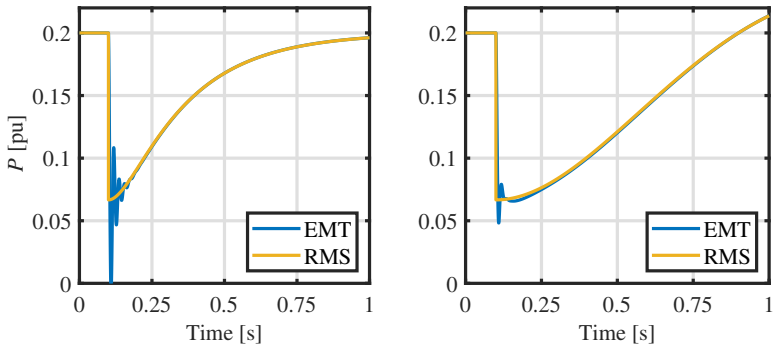

Figure 17: Trajectory of the active power signal for a sudden drop of the SCR from 3 to 1 - Virtual synchronous generator. In the left figure the value of k_v = 0.1333 and in the right k_v=0.4.

$(k_v + R_g)\frac{20}{L_g}$, where $R_g = 0.0333$ and $L_g = 0.333$ at pre-fault state and $R_g = 0.1$ and $L_g = 1$ at post-fault, we can calculate the minimum gain margin of the open loop system $G_{ol}(s)$. For $k_v = 0.133$, although the gain margin is sufficiently large ($g_{m,\min} = 10$) at pre-fault state, it decreases significantly $g_{m,\min} = 4.66$ due to the event. For $k_v = 0.4$, the value of the gain margin is higher than 10 both at pre- and post-faults, which improves significantly the damping of the line resonance and therefore minimizing the error between the RMS and EMT model. Moreover, it can be seen that higher value of k_v limits the maximum active power deviation and consequently improves the dynamic performance of the system. It should be mentioned, however, that large values of k_v can decrease the bandwidth of the active power control and also deteriorate the phase margin of the open loop system [22], which implies that there is a trade-off between transient performance and

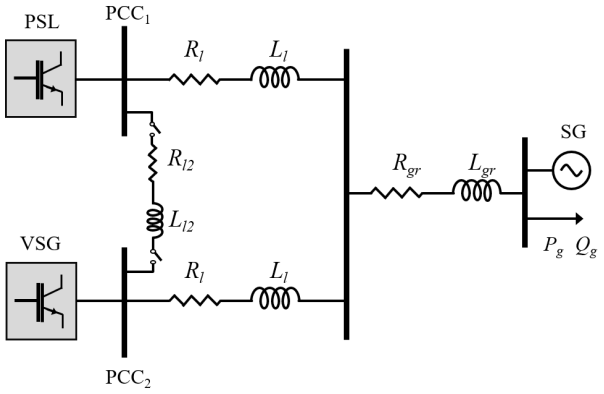

Figure 18: Test case system containing a single-line diagram of two grid-forming converters, one using Power Synchronization Loop (PSL) active power control and the other the Virtual Synchronous Generator (VSG). The grid-forming converters are connected to an equivalent variable frequency AC grid and a load.

maximum bandwidth of the active power controller of the grid-forming converter.

4.2.2. Virtual synchronous generator

Similar observations can be made in the case of the virtual synchronous generator control scheme, see Fig. 17. As it can be seen the mismatch between the RMS and EMT model is higher in case of a smaller k_v value. Also it can be noticed from the left figure that the settling time of the active power signal increases. This is due to the fact that higher value of k_v decreases the phase margin of the open loop system and consequently the damping ratio corresponding to the modes associated with the active power controller deteriorates.

4.3. Multi-converter topology

To validate if the conditions are valid in case of nearby connections of grid-forming converters, we consider the grid topology depicted in Fig. 18. Two events are realized: (i) line outage at t=0.1 s and (ii) generation loss equal to 1000 MW at t=0.55 s. Before the line outage, the output impedance for both of the converters is equal to $L_g = 0.415$ and $R_g = 0.0366$ and after the line outage is equal to $L_g = 0.48$ and $R_g = 0.0453$. Both converters are of identical rated power. The converter utilizing the power synchronization loop operates with an active power equal to 0.2 pu at pre-fault state and the virtual synchronous generator with an active power equal to 0.5 pu. The control settings of the active power control loop for the converters are as follows:

- PSL: K_p = 0.0417, K_q = 0.2 and k_v = 0.197

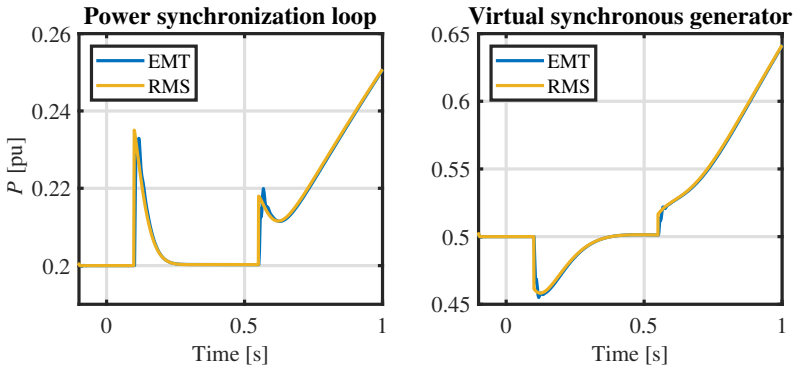

Figure 19: Trajectory of the active power signal of the two converters.

- VSG: $K_p = 0.0135$, $\omega_f = 0.074$, $K_q = 0.2$ and $k_v = 0.197$

From Fig. 19, it can be concluded that the mismatch between the RMS and EMT models of the system is negligible (a bit higher in the case of power synchronization loop) when considering events that may occur in the transmission grid, as long as the control parameters are selected based on the conditions presented in Section 3 of the paper.

4.4. Validation on Large system

The presented sufficient conditions are evaluated on a modified version of the IEEE 39 bus system, which is depicted in Fig. 20. The system parameters, the control gains and the components comprising the test case can be found in [27]. A grid-forming converter is placed on bus 40. For the analysis and the validation of the phasor approximation model, we simulate a step change of P_{ref} from 0 to 200 MW. The simulations have been performed in PowerFactory, using the RMS and EMT simulation methods [28].

4.4.1. Power synchronization loop

Fig. 21 depicts the active power response for the 3 different cases. Similar to the previous case and the 2 bus system, it is evident that the active damping controller mitigates the effect of the line resonance on the angle dynamics. Consequently, the mismatch between the RMS and EMT simulation methods is insignificant. As in the 2 bus system, for high values of frequency droop and smaller value of k_v the mismatch between the RMS and EMT model of the converter is significantly larger.

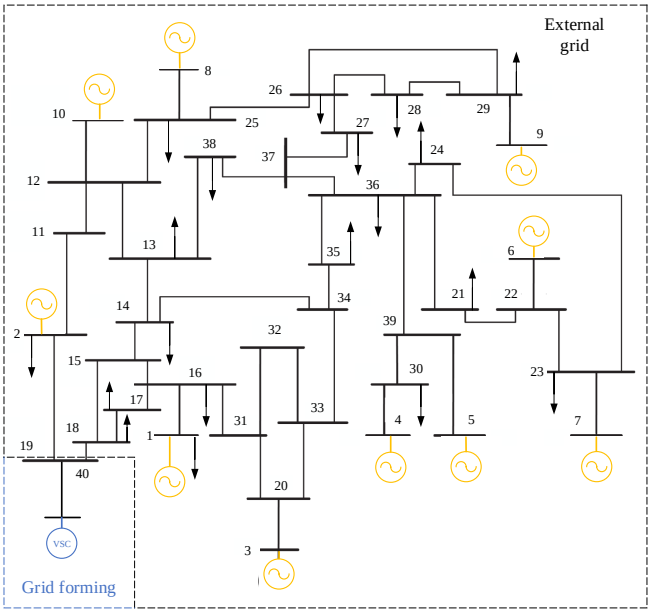

Figure 20: Modified version of IEEE 39 Bus system. Disturbance location is indicated by red symbol

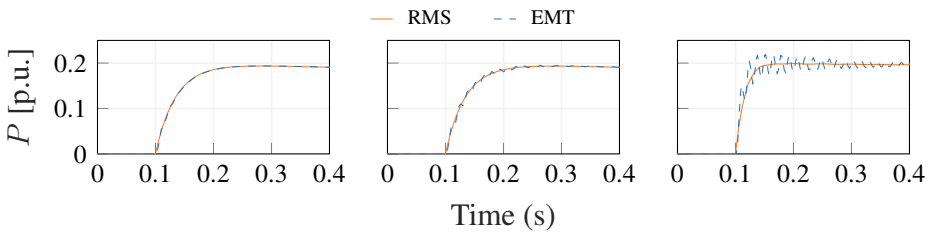

Figure 21: Active power response of power synchronization loop - Powerfactory. Left figure: Case 1, Middle figure: Case 2, Right figure: Case 3

4.4.2. Virtual Synchronous Generator

For the analysis three cases have been considered; the control parameters ω_f and K_p are the ones that are used for the one bus system configuration. Fig, 22 depicts the active power response of the synchronous generator. As it can be seen the higher the frequency droop, the smaller becomes the phase margin of the open loop system, which leads to high low frequency oscillations, as well as decrease of the gain margin of the open loop system. Similar to the previous case and the 2 bus system, we can observe a mismatch between the RMS and EMT models in the

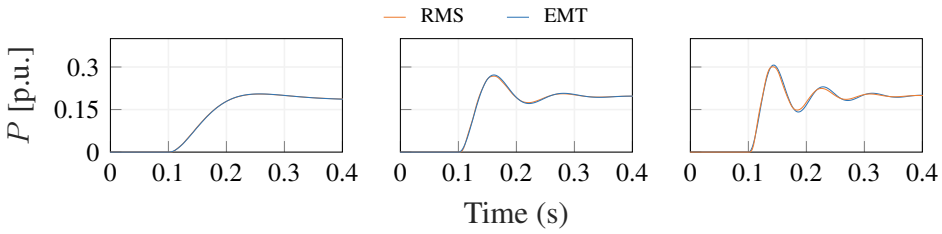

Figure 22: Active power response of virtual synchronous generator - Powerfactory. Left figure: Case 1, Middle figure: Case 2, Right figure: Case 3

maximum value of the active power signal, as well as a small phase shift between the two responses.

5. Conclusion

In this paper, we study the appropriateness of phasor-approximation models when simulating grid-forming converters. We present sufficient conditions for the control gains of outer loops of the grid-forming converter, that enable transmission system operators to use the RMS model of the grid-forming converter for monitoring its active power exchange with the grid. We also provide sufficient bounds for the control gains that ensure the stability of the full-detailed model. We provide expressions that can be used for sufficient damping of the line resonance and mitigation of the impact of network line dynamics on angle dynamics. Lastly, we demonstrate that in the case of the power synchronization loop, the RMS model is unable to detect the system instability for relative small value of the frequency droop, as long as the active damping controller is neglected. On the contrary, for the virtual synchronous generator, the RMS and EMT models can differ on the phase response (depending on the ratio of the damping and inertia parameter), as well as on the maximum active power deviation caused by the poor gain margin of the open loop system.

Future work is intended to investigate the impact of a slower voltage droop controller (low pass filter on the reactive power) and different classes of grid-forming converters on the appropriateness of RMS modeling.

Appendix A. Derivation of the transfer function describing the plant dynamics

We derive the transfer function describing the relation between $\Delta\theta$ and $\Delta\boldsymbol{i}$, while accounting for the impact of voltage droop on the active power regulation.

We consider that $\boldsymbol{U} = U_{\text{set}} + \Delta\boldsymbol{U}$ and $\boldsymbol{U_s}^c = U_s$ at steady state. Using perturbation quantities of θ, $\boldsymbol{U}$ and $\boldsymbol{i}$, (4) is expressed as:

$$U_{\text{set}} + \Delta\boldsymbol{U} - \Big(R + [s + j(\omega_1 + \dot{\Delta}\theta)]L_g\Big)\,(\boldsymbol{i_0} + \Delta\boldsymbol{i}) = U_s e^{-j(\theta_0 + \Delta\theta)}. \tag{A.1}$$

where, $\Delta\boldsymbol{U} = -H_{\text{hp}}(s)\Delta\boldsymbol{i} + K_q\Delta i_q$ if neglect the term $\Delta\boldsymbol{U}\Delta i_q = 0$. The term $e^{-j\Delta\theta} \approx 1 - j\Delta\theta$. The approximation stands for small variation of $\Delta\theta \approx 0$, since $\cos(\Delta\theta) \approx 0$ and $\sin(\Delta\theta) \approx \Delta\theta$. This can be explained by:

$$e^{-j\Delta\theta} = \underbrace{\cos(\Delta\theta)}_{1} - \underbrace{j\sin(\Delta\theta)}_{j\Delta\theta}. \tag{A.2}$$

After these simplifications (A.1) is expressed as:

$$\begin{aligned} -Kq\Delta i_q + [R_g + H_{\text{hp}}(s) + (s + j\omega_1)L_g]\Delta\boldsymbol{i} = j(U_s e^{-j\theta_0} - sL\boldsymbol{i_0})\Delta\theta \\ \underbrace{+U_{\text{set}} - (R_g + j\omega_1 L_g)\boldsymbol{i_0} - U_s e^{-j\theta_0}}_{=0} \end{aligned} \tag{A.3}$$

where $U_{\text{set}} - (R_g + j\omega_1 L_g)\boldsymbol{i_0} - U_s e^{-j\theta_0} = 0$ (steady state condition). Using (A.3), we can derive the relation between $\Delta\theta$ and $\Delta\boldsymbol{i}$:

$$\begin{aligned} \underbrace{\begin{bmatrix} H_{\text{hp}}(s) + R_g + L_g s & -K_q - \omega_1 L_g \\ \omega_1 L_g & H_{\text{hp}}(s) + R_g + L_g s \end{bmatrix}}_{A} \Delta\boldsymbol{i} = \\ \underbrace{\begin{bmatrix} \omega_1 L_g i_{d0} + i_{q0}(R_g + L_g s) \\ \omega_1 L_g i_{q0} - i_{d0}(R_g + L_g s) + U_{\text{set}} \end{bmatrix}}_{B} \Delta\theta. \end{aligned} \tag{A.4}$$

where $A^{-1}B$ provides the relationship between $\Delta\theta$ and $\Delta i_{d,q}$ and is a vector of two rows and one column. We consider that $G_{\theta i_d}(s) = \frac{\Delta i_d}{\Delta\theta}$, $G_{\theta i_q}(s) = \frac{\Delta i_q}{\Delta\theta}$ and $G_{\theta\Delta i}(s) = [G_{\theta i_d}(s)\ G_{\theta i_q}(s)]^T$. Similar to [22], by using perturbation variables we can express the active power variation of the VSC as:

$$\Delta P = \Re(U_{\text{set}}\Delta\boldsymbol{i}^* + \boldsymbol{i_0^*}\Delta\boldsymbol{U}). \tag{A.5}$$

Substituting (A.4) into (A.5) and considering that $\Delta\boldsymbol{U} = -H_{\text{HP}}(s)\Delta i + K_q\Delta i_q$ yields:

$$\Delta P = \underbrace{\Re(U_{\text{set}}G^*_{\theta\Delta i}(s) - \boldsymbol{i_0^*}H_{\text{hp}}(s)G_{\theta\Delta i}(s)) + \boldsymbol{i_0^*}K_q G_{\theta i_q}(s)}_{G_{\theta P}(s)}\,\Delta\theta. \tag{A.6}$$

Lastly, to extract the transfer function of the plant dynamics corresponding to the RMS model, we set the Laplace operator s in (A.3) equal to zero. We do that in order to extract the transfer function $e(s)$ which represents the difference between the RMS and EMT model of the active power controller.

Appendix B. Grid-forming converter parameters

Table B.3: Converter parameters

Parameter	Value	Parameter	Value
Rated power	1000 MVA	filter inductance	0.15 pu
Rated AC voltage	320 kV	filter capacitance	0.066 pu
Rated DC voltage	640 kV	filter resistance	0.005 pu
Switching frequency	5 kHz	Current controller proportional gain	2.3873
Current controller integral gain	25	Voltage controller proportional gain	0.59
Voltage controller integral gain	736	Voltage/current feed-forward terms	1

References

[1] F. Milano, F. Dörfler, G. Hug, D. J. Hill, G. Verbič, Foundations and challenges of low-inertia systems (invited paper), in: 2018 Power Systems Computation Conference (PSCC), 2018, pp. 1–25. doi:10.23919/PSCC.2018.8450880.

[2] U. Markovic, et al., Understanding stability of low-inertia systems, 2019. URL: engrxiv.org/jwzrq. doi:10.31224/osf.io/jwzrq.

[3] C. Collados-Rodriguez, M. Cheah-Mane, E. Prieto-Araujo, O. Gomis-Bellmunt, Stability analysis of systems with high vsc penetration: Where is the limit?, IEEE Transactions on Power Delivery (2019) 1–1. doi:10.1109/TPWRD.2019.2959541.

[4] G. S. Misyris, S. Chatzivasileiadis, T. Weckesser, Robust frequency control for varying inertia power systems, in: 2018 IEEE PES Innovative Smart Grid Technologies Conference Europe (ISGT-Europe), 2018, pp. 1–6. doi:10.1109/ISGTEurope.2018.8571607.

[5] G. S. Misyris, J. A. Mermet-Guyennet, S. Chatzivasileiadis, T. Weckesser, Grid supporting vscs in power systems with varying inertia and short-circuit capacity, in: 2019 IEEE Milan PowerTech, 2019, pp. 1–6. doi:10.1109/PTC.2019.8810979.

[6] A. Crivellaro, A. Tayyebi, C. Gavriluta, D. Groß, A. Anta, F. Kupzog, F. Dörfler, Beyond low-inertia systems: Massive integration of grid-forming power converters in transmission grids, 2019. arXiv:1911.02870.

[7] J. Rocabert, A. Luna, F. Blaabjerg, P. Rodríguez, Control of power converters in ac microgrids, IEEE Trans. Power Electron. 27 (2012) 4734–4749. doi:10.1109/TPEL.2012.2199334.

[8] M. Farrokhabadi, et al., Microgrid stability definitions, analysis, and examples, IEEE Transactions on Power Systems 35 (2020) 13–29. doi:10.1109/TPWRS.2019.2925703.

[9] P. Kundur, N. J. Balu, M. G. Lauby, Power system stability and control, volume 7, McGraw-hill New York, 1994.

[10] T. Demiray, Simulation of Power System Dynamics using Dynamic Phasor Models, Ph.D. thesis, ETH Zurich, 2008. doi:10.3929/ethz-a-005566449.

[11] P. Vorobev, P. Huang, M. Al Hosani, J. L. Kirtley, K. Turitsyn, High-fidelity model order reduction for microgrids stability assessment, IEEE Trans. Power Syst. 33 (2018) 874–887. doi:10.1109/TPWRS.2017.2707400.

[12] T. Qoria, et al., Tuning of cascaded controllers for robust grid-forming voltage source converter (2018).

[13] S. D'Arco, J. A. Suul, O. B. Fosso, A virtual synchronous machine implementation for distributed control of power converters in smartgrids, Electric Power Systems Research 122 (2015) 180 – 197. doi:https://doi.org/10.1016/j.epsr.2015.01.001.

[14] X. Wang, F. Blaabjerg, Harmonic stability in power electronic-based power systems: Concept, modeling, and analysis, IEEE Transactions on Smart Grid 10 (2019) 2858–2870.

[15] X. Wang, Y. W. Li, F. Blaabjerg, P. C. Loh, Virtual-impedance-based control for voltage-source and current-source converters, IEEE Transactions on Power Electronics 30 (2015) 7019–7037.

[16] V. Mariani, F. Vasca, J. C. Vásquez, J. M. Guerrero, Model order reductions for stability analysis of islanded microgrids with droop control, IEEE Transactions on Industrial Electronics 62 (2015) 4344–4354.

[17] S. Baros, C. N. Hadjicostis, F. O'Sullivan, Stability analysis of droop-controlled inverter-based power grids via timescale separation, 2020. arXiv:2003.11934.

[18] J. Chen, T. O'Donnell, Parameter constraints for virtual synchronous generator considering stability, IEEE Transactions on Power Systems 34 (2019) 2479–2481.

[19] L. Luo, S. V. Dhople, Spatiotemporal model reduction of inverter-based islanded microgrids, IEEE Transactions on Energy Conversion 29 (2014) 823–832.

[20] S. D'Arco, J. A. Suul, O. B. Fosso, Automatic tuning of cascaded controllers for power converters using eigenvalue parametric sensitivities, IEEE Transactions on Industry Applications 51 (2015) 1743–1753. doi:10.1109/TIA.2014.2354732.

[21] L. Papangelis, M. Debry, T. Prevost, P. Panciatici, T. Van Cutsem, Stability of a voltage source converter subject to decrease of short-circuit capacity: A case study, in: 2018 Power Systems Computation Conference (PSCC), 2018, pp. 1–7. doi:10.23919/PSCC.2018.8442773.

[22] L. Harnefors, M. Hinkkanen, U. Riaz, F. M. M. Rahman, L. Zhang, Robust analytic design of power-synchronization control, IEEE Trans. Ind. Electron 66 (2019) 5810–5819. doi:10.1109/TIE.2018.2874584.

[23] L. Zhang, Modeling and Control of VSC-HVDC Links Connected to Weak AC Systems, Ph.D. thesis, KTH, Electrical Machines and Power Electronics, 2010. QC20100607.

[24] G. Tzounas, I. Dassios, F. Milano, Modal participation factors of algebraic variables, IEEE Transactions on Power Systems 35 (2020) 742–750. doi:10.1109/TPWRS.2019.2931965.

[25] S. Skogestad, I. Postlethwaite, Multivariable Feedback Control: Analysis and Design, John Wiley & Sons, 2005.

[26] National Grid, Effects of VSM / Option 1 (Grid Forming) Converter Control on Penetration Limits of Non-Synchronous Generation (NSG) in the GB Power System, ???? URL: https://www.nationalgrid.com/sites/default/files/documents/GC0100%20Annex%209%20%20VSM_0.pdf.

[27] T. Athay, R. Podmore, S. Virmani, A practical method for the direct analysis of transient stability, IEEE Transactions on Power Apparatus and Systems PAS-98 (1979) 573–584.

[28] F. Gonzalez-Longatt, J. L. Rueda, PowerFactory Applications for Power System Analysis, Springer Publishing Company, Incorporated, 2014.

[Pub. G] Physics-Informed Neural Networks for Power Systems

Authors:
G. S. Misyris, A. Venzke and S. Chatzivasileiadis

Published in:
2020 IEEE Power & Energy Society General Meeting

DOI:
10.1109/PESGM41954.2020.9282004

Physics-Informed Neural Networks for Power Systems

George S. Misyris, Andreas Venzke and Spyros Chatzivasileiadis
Center for Electric Power and Energy
Technical University of Denmark
{gmisy, andven, spchatz}@elektro.dtu.dk

***Abstract*—This paper introduces for the first time, to our knowledge, a framework for physics-informed neural networks in power system applications. Exploiting the underlying physical laws governing power systems, and inspired by recent developments in the field of machine learning, this paper proposes a neural network training procedure that can make use of the wide range of mathematical models describing power system behavior, both in steady-state and in dynamics. Physics-informed neural networks require substantially less training data and can result in simpler neural network structures, while achieving high accuracy. This work unlocks a range of opportunities in power systems, being able to determine dynamic states, such as rotor angles and frequency, and uncertain parameters such as inertia and damping at a fraction of the computational time required by conventional methods. This paper focuses on introducing the framework and showcases its potential using a single-machine infinite bus system as a guiding example. Physics-informed neural networks are shown to accurately determine rotor angle and frequency up to *87 times faster* than conventional methods.**

***Index Terms*—deep learning, neural network, power system dynamics, power flow, system inertia.**

I. Introduction

Machine learning techniques demonstrate impressive results for a range of highly complex tasks, especially where an accurate mathematical representation of the problem cannot be obtained. Applications include image recognition, robotics, weather forecasting, and others [1]. In power systems, decision trees and neural networks have been shown to solve computational problems both in dynamics and optimization at a fraction of the time required by traditional approaches, being up to three order of magnitude faster [2]–[6].

Up to this point, however, machine learning methods applied to power systems (and other physical systems) were largely agnostic to the underlying physical model. This made them heavily dependent on the quality of the training data, it required large training datasets, and oftentimes complex neural network structures. Despite recent efforts for efficient creation of datasets with encouraging results [7], [8], generating the required training dataset size still requires substantial computational effort. In this work, inspired by [9], [10], we reduce the dependency on training data and complex neural network structures by exploiting *inside the neural network training* the underlying physical laws described by power system models.

This is the first work, to our knowledge, that proposes physics-informed neural networks for power system applications. It introduces a neural network training framework that can exploit the underlying physical laws and the available power system models both for steady-state and dynamics. Following recent approaches reported in [9], [10], we incorporate the power system differential and algebraic equations inside the training procedure. Exploiting advances in automatic differentiation [11] that are implemented in Tensorflow [12], we can directly compute derivatives of neural network outputs during training, such as the rotor angle, and build neural networks able to accurately capture the rotor angle and frequency dynamics. Our approach (i) requires less initial training data, (ii) can result to smaller neural networks, while (iii) demonstrating high performance.

Physics-informed neural networks introduce a novel technology that may lead to a new class of numerical solvers [10] as well as dynamic state estimation techniques [13]. Within power systems, they have the potential to solve systems of differential-algebraic equations at a fraction of computational time required for conventional methods, are able to directly determine the value of state variables at any time instant t_1 (without the need to integrate from t_0 to t_1), and can handle directly higher-order differential equations without the need to introduce additional variables to solve a first-order system.

In this paper, we present the main principles for the application of physics-informed neural networks of [10] in power systems, focusing on power system dynamics and using the swing equation as an example. Besides obtaining solutions to ordinary differential equations, we demonstrate how the same methods can be used to estimate uncertain parameters such as inertia and damping. The contributions of our work are:

1) We propose physics-informed neural networks to (i) accurately determine solutions of differential equations and, thus, values of power system dynamic states, such as rotor angle and frequency, and (ii) identify uncertain power system parameters. Contrary to previous approaches, physics-informed neural networks utilize the underlying physical model, lead to significantly reduced computation time and need less training data.
2) For the single machine infinite bus (SMIB) system, we show that physics-informed neural networks (i) predict system dynamics with high accuracy at a fraction of the computational time required by conventional approaches (28-87 times faster in our study), and (ii) can identify with high accuracy uncertain system parameters such as inertia and damping.

This paper is structured as follows: Section II describes the employed power system model and introduces the architecture of physics-informed neural networks. Section III presents simulation results demonstrating the performance of physics-informed neural networks. Section IV discusses the challenges and the opportunities emerging from the successful application of this concept. Section V concludes. The code to reproduce

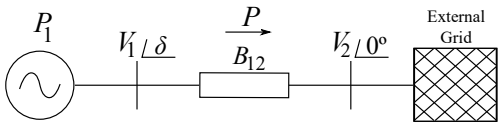

Fig. 1. Single machine infinite bus system

the simulation results is available online [14].

II. Methodology

A. Physical Model for Power System Dynamics

Power system dynamics, in their simplest and most common form, are described by the swing equation, neglecting transmission losses and bus voltage deviations. For each generator k, the resulting system of equations can then be represented by [15], [16]:

$$m_k\ddot{\delta_k} + d_k\dot{\delta_k} + \sum_j B_{kj}V_kV_j\sin(\delta_k - \delta_j) - P_k = 0 \quad (1)$$

where m_k defines the generator inertia constant, d_k represents the damping coefficient, B_{kj} is the $\{k, j\}$-entry of the bus susceptance matrix, P_k is the mechanical power of the k^{th} generator, V_k, V_j are the voltage magnitudes at buses k, j and δ_k, δ_j represent the voltage angles behind the transient reactance. $\dot{\delta}_k$ is the angular frequency of generator k, often also denoted as ω_k.

1) Single Machine Infinite Bus (SMIB) System: The single-machine infinite-bus system, shown in Fig. 1, has been widely used to understand and analyze the fundamental dynamic phenomena occurring in power systems. As the focus of this paper is on the introduction of physics-informed neural networks for power systems, we will use this system as a guiding example. Note though that our proposed framework is general. Future work will focus on larger, more complex systems. The swing equation (1) for the SMIB system is given by:

$$m_1\ddot{\delta} + d_1\dot{\delta} + B_{12}V_1V_2\sin(\delta) - P_1 = 0 \quad (2)$$

In the rest of this paper, we will show how physics-informed neural networks can accurately estimate both rotor angle δ and frequency $\dot{\delta}$ while P_1 varies within $[P_{\min}, P_{\max}]$, and can identify uncertain parameters such as m_1 and d_1.

B. Physics-Informed Neural Networks

In the following, we explain the general architecture of physics-informed neural networks, and detail its application to the SMIB system. Feed-forward neural networks are composed of the input layer, fully connected hidden layers having a non-linear activation function at each neuron, and the output layer. Between each layer a weight matrix $\mathbf{W}$ and bias $\mathbf{b}$ is applied. During training, weight matrices and biases are optimized to minimize an objective function which usually penalizes the deviation of the neural network prediction from the training data. Neural networks are universal function approximators as they can, in theory, learn any unknown function between some inputs and outputs. Therefore, neural networks could be used to directly learn the nonlinear mapping between the inputs and the outputs of differential equations, such as (2). Not taking into account the underlying physical model, however, will require large amounts of training data and a large neural network size. The work in [10] introduced a framework for physics-informed neural networks which we will rely on in the following. Considering physical laws during training allows to bound the space of admissible solutions to the neural network parameters, which translates to a lower requirement in both the amount of training data and neural network size.

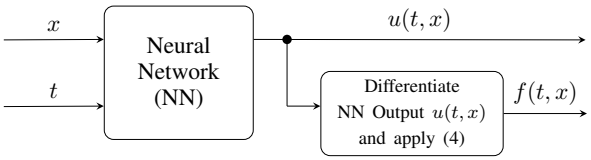

Fig. 2. General structure of a physics-informed neural network: it predicts the output $u(t, x)$ given inputs x and t. Then, using automatic differentiation [11] of the same neural network, the partial derivatives of $u(t, x)$ are computed, and $f(t, x)$ is evaluated. The parameters λ are either assumed to be known, or are optimized as part of the neural network training. During training, the neural network weights and biases are adjusted according to loss function (5), which minimizes the deviation of both the output prediction $u(t, x)$ from ground truth and $f(t, x)$ from 0.

Following notation similar to Ref. [10], the general form of the functions that the physics-informed neural network can approximate is:

$$\frac{\partial u}{\partial t} = -N[u;\lambda]\,,\ x \in \Omega,\ t \in [0, T] \quad (3)$$

where $u(t, x)$ is the solution and $N[u; \lambda]$ is a nonlinear operator connecting the state variables u with the system parameters λ. The term t denotes time and x the system input. The domain Ω can be bounded based on prior knowledge of the dynamical system and $[0, T]$ is the time interval within which the system evolves. The model parameters λ can be constant or unknown. In case λ is unknown, the problem of approximating function (3) becomes a problem of system identification, where we seek parameters λ for which the expression in (3) is satisfied. To enforce the physical law describing the dynamical system we define the physics-informed neural network $f(t, x)$:

$$f(t,x) = \frac{\partial u}{\partial t} + N[u,\lambda] \quad (4)$$

Note that if the system parameters λ are known the nonlinear operator $N[u, \lambda]$ simplifies to $N[u]$. The overall architecture is shown in Fig. 2. A neural network is used to predict $u(t, x)$ based on the inputs t and x. To determine $f(t, x)$, we use automatic differentiation [11] of the components of the neural network predicting $u(t, x)$. Based on this, we compute the required derivatives of $u(t, x)$ with respect to time t and system inputs x. As a result, the neural network predicting $f(t, x)$ has the same parameters compared to the neural network predicting $u(t, x)$, but different activation functions. The shared parameters of the two neural networks are optimized by minimizing the loss function:

$$MSE = \underbrace{\frac{1}{N_u}\sum_i^{N_u} |u(t_u^i, x_u^i) - u^i|^2}_{MSE_u} + \underbrace{\frac{1}{N_f}\sum_i^{N_f} |f(t_f^i, x_f^i)|^2}_{MSE_f} \quad (5)$$

where MSE_u denotes the mean squared error loss corresponding to the initial data, N_u is the total number of training data, MSE_f is the mean squared error at a finite set of collocation points and N_f is the total number of collocation points. The

number of collocation points and training data influence the prediction accuracy and the computational time to optimize the loss function. The error MSE_u enforces the boundary conditions of the independent variables x and MSE_f enforces the physics of the dynamical system imposed by the condition (3), i.e. it penalizes deviations of the predicted physical law. Given a training data set and known system parameters λ, we seek to find the parameters (weights and biases) of the neural networks which minimize (5). If the parameters λ are unknown, we train for the same objective but consider the system parameters as additional variables.

1) Physics-informed neural networks capturing power system dynamics: We show how physics-informed neural networks can be used to derive δ and $\omega = \dot{\delta}$ of the swing equation (2) at any time instant t and for a range of mechanical power P_1. We assume that the system parameters $\lambda := \{m_1, d_1, B_{12}\}$ are known and the voltages V_1 and V_2 are fixed. As a result the system input is defined as $x := \{P_1\}$. In contrast with conventional numerical solvers, which require the conversion of higher-order ordinary differential equations (ODEs) to first-order in order to solve them (by introducing additional variables), physics-informed neural networks can directly incorporate higher-order ODEs, as we show in (7).

Incorporating (2) to the neural network, function (4) is given by:

$$u(t, x) := \delta(t, P_1), \tag{6}$$

$$f_\delta(t, P_1) = m_1\ddot{\delta} + d_1\dot{\delta} + B_{12}V_1V_2\sin(\delta) - P_1, \quad P_1 \in [P_{\min}, P_{\max}], \quad t \in [0, T] \tag{7}$$

The interval $[0, T]$ can be defined based on the time period of interest for the dynamic simulation. The domain Ω of the input P_1 is restricted to $[P_{\min}, P_{\max}]$. The neural network output is $\delta(t, P_1)$. After the training phase, the frequency signal $\omega := \dot{\delta}$ is extracted as a function of the estimated angle δ. As a result, the prediction error of the frequency ω depends on the prediction error of the angle δ and the differential method. In the rest of the paper, we refer to this neural network structure as NN_δ.

2) Data-driven discovery of inertia and damping coefficients: Information about power system parameters such as system inertia is of significant importance for system operators to prevent large frequency deviations and maintain frequency stability. As described in [16], due to varying generation of converter-connected renewable energy sources, the inertia level of power systems becomes uncertain and has to be estimated (or predicted) at regular time intervals [17]. Physics-informed neural networks can be used to address the problem of system identification and data-driven discovery of partial differential equations. For this case, we define m_1 and d_1 as unknown parameters in (7). The structure of the physics-informed neural network remains the same, with the only difference that a subset of the system parameters λ are now treated as additional variables when minimizing (5) during neural network training.

III. Simulation & Results

A. Simulation Setup

Besides an initial training set, to assess the neural network performance we also need an extensive test data set. To create the training and test data sets we use the numerical solver $ode45$ in MATLAB with a time step of $0.1s$ and time interval $T = [0, 20s]$, resulting in 201 time steps for each trajectory. The voltage magnitudes V_1 and V_2 are equal to 1 p.u. and B_{12} = 0.2 p.u. In our first case study, we assume system inertia and damping are known, and that the system is not at an equilibrium. Assuming an uncertain active power input in the range $P_1 = [0.08, 0.18]$ and initial values for δ and ω equal to 0.1 rad and 0.1 rad/s, we generate 100 trajectories. As a result, our entire test and training dataset consists of $20'100$ samples. We consider the interval from $[0.08, 0.18]$ to show the capability of the physics-informed neural network to accurately predict trajectories for uncertain power injections. For values larger than 0.18, the system becomes unstable, and for values lower than 0.08 multiple oscillations occur. For these regimes, we observe lower prediction accuracy, and different trained physics-informed neural networks could be used to achieve high accuracy in each of these regimes.

In our second case study, inertia and damping are also unknown parameters. Given scattered observed data about active power, frequency and angle measurements, our goal is to identify the parameters m_1 and d_1 of (7), as well as to obtain the trajectory of δ. Considering that the levels of inertia and damping vary, we assign 10 different values to m_1 and d_1 that lie within the range of $[0.1, 0.4]$ and $[0.05, 0.15]$, respectively. To this end, for each of the 10 pairs $\{m_1, d_1\}$ we generate 40 trajectories.

Next, before starting the training procedure, as usual for neural networks, we need to determine an appropriate number of hidden layers and number of neurons per layer, the amount of training data N_u and the number of collocation points N_f. We carried an extensive investigation of the appropriate values for each of those parameters, assessing the relative L_2 error between the predicted and the exact solution of $\delta(t, P_1)$ and $\omega(t, P_1)$ for a range of different configurations. In the case studies, we report results only for the most suitable configuration, which achieved the lowest L_2 error. Similar to [10], as the required amount of training data N_u is very small (only 40 data points), we use a gradient-based optimization algorithm to optimize the loss function $MSE = MSE_u + MSE_f$ in (5). We perform neural network training and testing in TensorFlow on a laptop (Intel Core i7 3.9 GHz, 32-GB RAM, single NVIDIA GeForce 940MX 2-GB). The hidden layers of the neural network use hyperbolic tangent activation functions. The code to reproduce the results is available online [14].

B. Data-driven solution of frequency dynamics through physics-informed neural networks

The following parameters were selected to obtain the lowest L_2 error on the test data: we select a set of N_u = 40 randomly distributed initial and boundary data across the entire spatio-temporal domain, N_f = $8'000$ collocation points, and a 5-layer neural network with 10 neurons per hidden layer. Observe that compared to conventional neural network approaches, we only need a very small amount of samples (N_u = 40). Increasing N_u in our simulations, led to over-fitting to the training data. Training took 223 seconds and the relative L_2 error between exact and predicted solutions on the $11'600$-points test dataset is $1.34 \cdot 10^{-2}$. Fig. 3 depicts the comparison between the predicted and the actual trajectory of the angle $\delta(t)$ and the frequency $\omega(t)$. The best and worst $\{\delta, \omega\}$ estimation during different active power inputs P_1 in terms of L_2 error on both

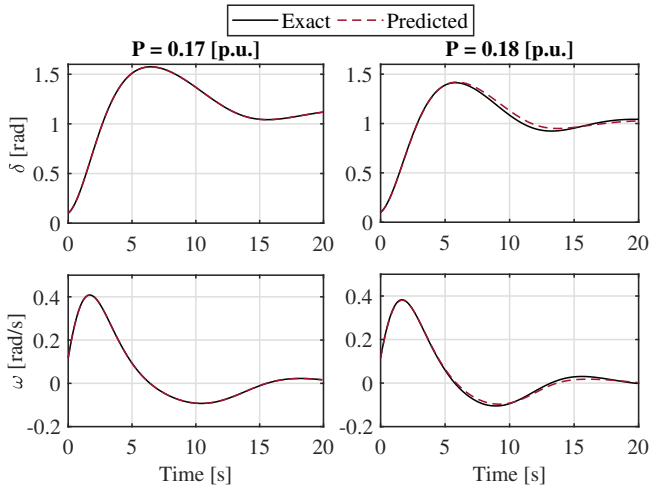

Fig. 3. Comparison of the predicted and exact solution for the angle $\delta(t)$ and frequency $\omega(t)$ with the physics-informed neural network NN_δ. Note that to compute the frequency $\omega(t)$ we perform numerical differentiation of the angle $\delta(t)$ using a Newton method. In the left figures, we show the most accurate estimation of the trajectory of $\delta(t)$ and $\omega(t)$, with a relative L_2 error of $2.37 \cdot 10^{-2}$. In the right figures, we show the least accurate estimation of the trajectory of $\delta(t)$ and $\omega(t)$, with a relative L_2 error of $2.55 \cdot 10^{-4}$.

training and test sets are depicted in the left and right side of the figure, respectively. To extract the frequency ω we differentiate the signal associated with the angle δ. To this end, we numerically approximate the derivative of a function as: $\omega(t) = \lim_{h \to 0} \frac{\delta(t+h)-\delta(t)}{h}$. The value of h depends on the simulation time step. In this study, we generated the trajectories with a fixed step of $h = 0.1s$. In future work, we will use automatic differentiation [11] to extract the frequency directly from the physics-informed neural network. It can be observed that the physics-informed neural network is able to predict the trajectory of the angle $\delta(t)$ with high accuracy, and that the frequency signal $\omega(t)$ can be successfully recovered using numerical differentiation.

After training, we evaluate the neural network performance in terms of computational speed required for solving the differential equation defined by (2). For 100 different initial conditions of (2), the $ode45$ solver takes on average 0.45 s to solve the differential equations and the neural network only 0.016 s, resulting to a speed-up of factor of 28. We expect that for larger systems the computational speed-up will be even higher, as solving large-scale differential equations is computationally very expensive, whereas the evaluation of a trained neural network remains computationally low even for large network sizes. Additionally, and most importantly, the physics-informed neural network can directly determine δ at any specified time step $\delta(t_1, P_1)$, whereas numerical methods always have to start integrating from the boundary conditions at $t = t_0$ until they reach $t = t_1$. The computational time for evaluating any random time step (e.g. at $t_1 = 10$ s) is $4 \cdot 10^{-3}$ s, whereas integrating from $t_0 = 0s$ up to $t_1 = 10$ s with the $ode45$ solver takes 0.35 s, resulting to a *substantial speed-up of almost two order of magnitude* for the physics-informed neural network (87 times to be exact). This illustrates the capability of physics-informed neural networks to predict directly the solution to higher-order differential equations with high accuracy and low computational cost, offering significant advantages over classical numerical integration tools.

1) Predicting both angle δ and frequency ω as separate neural network outputs: Within our investigations, we also attempted to train a physics-informed neural network that considers δ and ω as separate outputs, essentially setting $f_\omega = \dot{\delta} - \omega$ and $f_\delta = m_1\dot{\omega} + d_1\omega + B_{12}V_1V_2\sin(\delta) - P_1$. To obtain the lowest L_2 error in this case, we had to select again a set of N_u = 40 randomly distributed initial and boundary data, a 5-layer neural network with 10 neurons per hidden layer, but a set N_f = $50'000$ collocation point (instead of $8'000$ in the previous case) . The model training took approximately 30 minutes as more collocation points N_f are required to obtain a satisfactory prediction error. Considering that $\delta(t)$ and $\omega(t)$ are predicted as separate outputs, the relative L_2 errors between the exact and predicted solutions are $9.43{\cdot}10^{-2}$ and $1.51{\cdot}10^{-1}$, respectively, and are higher than for the NN_δ structure. It becomes obvious that the neural network architecture with the single output δ (and subsequent numerical differentiation to determine ω) is preferable in terms of training time and predictive accuracy.

C. Data-driven discovery of inertia and damping coefficients through physics-informed neural networks

In this subsection, we evaluate the performance of the physics-informed neural network to predict system inertia and damping from observed trajectories. In this case study, we assume that m_1 and d_1 are unknown, and instead we have a set of limited training datapoints $\{t, P_1, \delta\}$. Contrary to the usual practice of first training a neural network and then using it, our objective here is exploit the physics-informed neural network training procedure to determine m_1 and d_1. To illustrate the effectiveness of this approach, we perform this analysis for 10 different pairs of $\{m_1, d_1\}$ and evaluate the average predictive accuracy. We select a set of N_u = 100 randomly distributed points across the spatio-temporal domain from the exact solutions of (2) for each inertia level. A 5-layer neural network with 30 neurons per hidden layer is trained for each inertia level with the corresponding trajectories in order to predict the system parameters and $\delta(t)$. The resulting average errors for predicting m_1 and d_1 over the 10 different cases are 0.74% and 1.28%, respectively. The average training time of the neural network to identify the system parameters was less than 60 seconds. This means that with a limited training dataset, and within 60 seconds, we can accurately predict the inertia and damping level of a system. Considering that the swing equation (2) is often used to approximate the aggregate dynamic behavior of large power systems, these results demonstrate that physics-informed neural network show substantial potential to not only accurately derive δ and ω but also predict both system inertia and damping. Last but not least, the relative L_2 errors between the exact and predicted solutions for the phase angle are less than 10^{-1} over the 10 different cases of $\{m_1, d_1\}$. This shows the potential of physics informed neural networks to be used as a dynamic state estimator, when the model parameters are unknown [13].

IV. Discussion and Outlook

This work introduces for the first time in power systems a neural network training procedure that explicitly considers the underlying differential and algebraic equations describing power system behavior. This unlocks a series of opportunities in power systems, as physics-informed neural networks may

be able to accurately determine the solution of differential-algebraic sets of equations several orders of magnitude faster than traditional methods relying on numerical integration. Still, to unlock this potential, there are several challenges to be addressed.

a) Number of training data: Besides the limited number of training data, physics-informed neural networks as described in this paper need to generate a substantial number of collocation points. In our case studies, we used $N_u = 40$ points as input data and $N_f = 8'000$ collocation points. It is expected that for larger systems, a much larger number of collocation points will be necessary, which will result to a longer training time. In our future work, we plan to investigate methods using Runge-Kutte integration schemes such as the ones proposed in [10] which can eliminate the need for collocation points.

b) Scalability: Although the swing equation is a good first approximation for first-swing instability, and single-machine infinite-bus systems are still used as aggregate models of large power systems, we still need to explore what are the computational needs if we were to apply these methods in large scale power systems and how to address the associated challenges related to the neural network training. Particularly, the comparison with numerical solvers and approximation techniques like polynomial fits will serve as a benchmark.

c) Range of applications: As shown in this paper, physics-informed neural networks can determine two orders of magnitude faster the rotor angle and frequency at any time instant for uncertain power inputs. At the same time, they can accurately identify uncertain parameters such as inertia and damping. Future applications must also assess cases that include both stable and unstable equilibria, a wide range of different dynamic phenomena, including small-signal stability, voltage stability and converter dynamics [18], discrete events, such as protection actions, as well as power system optimization, among numerous others. In our simulation study, we observed high accuracy for a single stable swing prediction, but for different regimes such as multiple oscillations or unstable conditions, different physics-informed neural networks might have to be trained. We also need to examine if such neural networks can capture discrete events, such as protection actions, or if we need to develop a hybrid approach, using physics-informed neural networks as a numerical solver only during the continuous dynamics before and after a discrete event. For power system applications, physics-informed neural networks can (and should) be combined with neural network verification methods, see [19]. In this way, they would no longer be considered a black box, but instead we would be able to extract formal guarantees for their behavior.

V. Conclusions

To the best of our knowledge, for power system applications, this is the first paper to propose physics-informed neural networks. Explicitly considering the power system governing equations, we are able to determine the solution of differential-algebraic systems of equations at a fraction of the time required for conventional numerical approaches. Physics-informed neural networks require substantially less training data, while achieving high accuracy, due to the inclusion of the underlying swing equation. This paper introduces the general framework and presents results for a single-machine infinite-bus system. In our case studies, we demonstrate how physics-informed neural networks can accurately determine the rotor angle and frequency *87 times* faster than conventional numerical methods. We further demonstrate their successful identification of uncertain system parameters such as inertia and damping from a limited set of input data. Our results showcase the potential for successful application of these methods in larger systems, unlocking a series of opportunities for power system security and optimization, achieving good accuracy and high computational speed. Future work will explore a series of possible applications and potential improvements in the training procedure.

Acknowledgement

This work is supported by the multiDC project funded by Innovation Fund Denmark, Grant No. 6154-00020B.

References

[1] Y. LeCun, Y. Bengio, and G. Hinton, "Deep learning," *Nature*, vol. 521, no. 7553, pp. 436–444, 2015.

[2] L. A. Wehenkel, *Automatic learning techniques in power systems*. Springer Science & Business Media, 2012.

[3] B. Donnot, I. Guyon, M. Schoenauer, P. Panciatici, and A. Marot, "Introducing machine learning for power system operation support," *CoRR, arXiv preprint arXiv:1709.09527*, 2017.

[4] M. Sun, I. Konstantelos, and G. Strbac, "A deep learning-based feature extraction framework for system security assessment," *IEEE Transactions on Smart Grid*, vol. 10, no. 5, pp. 5007–5020, Sep. 2019.

[5] J. H. Arteaga, F. Hancharou, F. Thams, and S. Chatzivasileiadis, "Deep learning for power system security assessment," in *2019 IEEE Milan PowerTech*, June 2019, pp. 1–6.

[6] F. Fioretto, T. W. K. Mak, and P. V. Hentenryck, "Predicting ac optimal power flows: Combining deep learning and lagrangian dual methods," *arXiv preprint arXiv:1909.10461*, 2019.

[7] F. Thams, A. Venzke, R. Eriksson, and S. Chatzivasileiadis, "Efficient database generation for data-driven security assessment of power systems," *IEEE Transactions on Power Systems*, pp. 1–1, 2019.

[8] A. Venzke, D. K. Molzahn, and S. Chatzivasileiadis, "Efficient creation of datasets for data-driven power system applications," *arXiv preprint arXiv:1910.01794*, 2019.

[9] T. Q. Chen, Y. Rubanova, J. Bettencourt, and D. K. Duvenaud, "Neural ordinary differential equations," in *Advances in neural information processing systems*, 2018, pp. 6571–6583.

[10] M. Raissi, P. Perdikaris, and G. Karniadakis, "Physics-informed neural networks: A deep learning framework for solving forward and inverse problems involving nonlinear partial differential equations," *Journal of Computational Physics*, vol. 378, pp. 686 – 707, 2019.

[11] A. G. Baydin, B. A. Pearlmutter, A. A. Radul, and J. M. Siskind, "Automatic differentiation in machine learning: a survey," *Journal of machine learning research*, vol. 18, no. 153, 2018.

[12] M. Abadi *et al.*, "Tensorflow: Large-scale machine learning on heterogeneous distributed systems," *arXiv preprint arXiv:1603.04467*, 2016.

[13] J. Zhao *et al.*, "Power system dynamic state estimation: Motivations, definitions, methodologies, and future work," *IEEE Trans. on Power Syst.*, vol. 34, no. 4, July 2019.

[14] G. S. Misyris, A. Venzke, and S. Chatzivasileiadis, "Online Appendix: Physics-Informed Neural Networks for Power Systems," 2019. [Online]. Available: https://github.com/gmisy/Physics-Informed-Neural-Networks-for-Power-Systems/

[15] S. Chatzivasileiadis, T. L. Vu, and K. Turitsyn, "Remedial actions to enhance stability of low-inertia systems," in *IEEE Power and Energy Society General Meeting 2016, Boston, MA, USA*, July 2016, pp. 1 –5.

[16] G. S. Misyris, S. Chatzivasileiadis, and T. Weckesser, "Robust frequency control for varying inertia power systems," in *2018 IEEE PES Innovative Smart Grid Technologies Conference Europe*, 2018, pp. 1–6.

[17] D. Zografos and M. Ghandhari, "Power system inertia estimation by approaching load power change after a disturbance," in *2017 IEEE Power and Energy Society General Meeting*, 2017, pp. 1–5.

[18] G. S. Misyris, J. A. Mermet-Guyennet, S. Chatzivasileiadis, and T. Weckesser, "Grid supporting vscs in power systems with varying inertia and short-circuit capacity," in *2019 IEEE Milan PowerTech*, June 2019, pp. 1–6.

[19] A. Venzke and S. Chatzivasileiadis, "Verification of neural network behaviour: Formal guarantees for power system applications," *arXiv preprint arXiv:1910.01624*, 2019.

Department of Electrical Engineering
Center for Electric Power and Energy (CEE)
Technical University of Denmark
Elektrovej, Building 325
DK-2800 Kgs. Lyngby
Denmark

www.elektro.dtu.dk/cee
Tel: (+45) 45 25 35 00
Fax: (+45) 45 88 61 11
E-mail: cee@elektro.dtu.dk